Quantum properties of Bose-Einstein Condensates coupled to semiconductor heterojunctions

by

Germán Alfredo Sinuco León

Thesis submitted to the School of Physics and Astronomy of the
University of Nottingham in partial fulfilment
of the requirements for the degree of
Doctor of Philosophy
May 2010

Abstract

Quantum properties of Bose-Einstein Condensates coupled to semiconductor heterojunctions

Germán Alfredo Sinuco León
School of Physics and Astronomy, University of Nottingham,
Nottingham, United Kingdom
Advisor: T. M. Fromhold
Thesis submitted for the degree of Doctor of Philosophy
at the University of Nottingham
December 2009

In this thesis, we present a theoretical study of the effects that a current-carrying Two-Dimensional Electron Gas (2DEG) produce on a neighbouring magnetically trapped Bose-Einstein Condensate of alkali atoms (BEC). We suggest that technology used for magnetic micro-controlling of cold gases could be improved by replacing or combining the metallic wires used in such structures with 2DEG-based conductors or quantum electronic devices. All calculations presented in this thesis consider parameters attainable with present technology, suggesting that experimental realization of the scenarios proposed here is already feasible.

In Chapter one we present the general context in which this thesis is developed. It includes a definition of the Bose-Einstein condensate state, a description of the principles of magnetic trapping and a brief review of the developments in the area of micro-manipulation of atomic BECs. Chapter two is devoted to describe the characteristics of the heterojunction considered in the thesis, and a simple model used to evaluate the electron flow in the 2DEG it contains. Chapter three shows in detail the properties of magnetic trapping configurations considered afterwards.

We study two simple applications that can be developed by bringing a BEC near to a current carrying 2DEG. Firstly, in Chapter four, we demonstrate the feasibility of

creating magnetic trapping potentials using a current-carrying 2DEG and an external magnetic field. We identify the advantages of such a 2DEG-based trap over traditional metal-based traps and the conditions needed for operability.

Recently developed techniques of magnetic field microscopy with BECs motivate our second considered application, namely, using a Bose-Einstein Condensate to probe the electron transport in 2DEGs and structural characteristics of the heterojunction. In Chapter five, we demonstrate how the quantization of conductance occurring in Quantum Point Contacts (QPC) fabricated from the heterojunction in the 2DEG, can be detected through a localized depletion of the BEC caused by a small inhomogeneity of the magnetic field that originates from a current through the QPC.

In addition, we show that the electron density fluctuations in the 2DEG can be measured by detecting the corresponding inhomogeneous magnetic field produced when current flows, via modulation of the BEC's density. We establish the conditions under which a sensitive response of the BEC to the magnetic field is possible. We also derive a general relation between the modulation of the magnetic field affecting the BEC and the distribution of ionized donors in the heterojunction.

Creating semiconductor-cold-atom hybrid systems, where electrons in the semiconductor and atoms in the BEC are coupled to each other, requires a full understanding of the properties of both systems. Since typical micro-traps have an elongated geometry, in Chapter six we present a study of phase correlations of BECs in such geometries. To do this, we use a recently proposed effective one-dimensional equation that takes into account the 3D character of the BEC.

Finally, in Chapter seven, we conclude and identify directions for future work emerging from this thesis.

Acknowledgements

With these lines, I would like to thank all people that made this thesis possible.

First and foremost I would like to thank Prof. Mark Fromhold for giving me the great opportunity to join the Condensed Matter group in the University of Nottingham. Through his brilliant ideas, dedication and passion for physics he gave me not only good advice but also encouraged me to perform most of the work presented in this thesis. It has been a pleasure to work with and learn from his experience in relevant aspects of physics as science and social activity. His ideas, suggestions and careful reading of the manuscript were really valuable for the development of this thesis. Nonetheless, mistakes, inaccuracies and misspelling present in the text are entirely my responsibility.

I also want to thank all people in the group whom I have many physics-related chats. I want to thank specially to Tao Ya, with who I discussed several common problems, pointed to usually by his critical thinking. He also provide me with useful ideas for the solution of several issues I had with the coding. I also want to thank Robin Scott for taking part of his time to read and comment about Chapter six of this work. Thanks are also due to Andrew Henning for dragging me to the pub to share a couple of pints from time to time.

I cannot leave without mention to Anton Piccardo-Selg for providing me the skeleton for several figures, being this a substantial aid for the presentation of this thesis. I also want to acknowledge the support of Prof. Peter Krüger during the writing period.

I cannot forget to thank Prof. Joseph Fortágh. He gave me the opportunity to spend three wonderful months in his experimental group in Tuebingen, and also visiting them a couple of times, being each one a completely delightful experience.

Finally, I owe my deepest thanks to my family - my mother, my father, my sisters and my brother, and to my girlfriend Lucia. They have always stood by me in good and bad times. I really owe all my achievements to them; without their love and support, the completion of this work would not have been possible.

To Mum and Dad
with gratitude and love

Contents

Glossary and constants

Symbol	Definition
$\boldsymbol{A}$	Bold-symbols are used for vectors
μ	Chemical potential
T	Temperature
η	Density (donor, electron or atomic)
m	Atomic mass
m_e^*	Electron effective mass
N_i	Number of particles in state i
ϕ_i	Wave-function of the i^{th} single-particle state
$\rho_{(1)}$	One-body reduced density matrix operator
$\Psi, \hat{\Psi}$	Annihilation and creation boson operators
$\psi_0 = \sqrt{N_0}\phi_0$	Condensate wave-function
$\hat{\boldsymbol{\mu}}_F$	Magnetic moment operator
m_F	Total angular momentum projection quantum number
g_F	Landé g-factor
z_0	Trap position
B	Magnetic field
I	Electric current
ϵ	Relative permittivity
d	Separation between donor and 2DEG planes in a hetero-junction

Name	Symbol	Value
Boltzmann constant	k_B	1.3807×10^{-23} J/K
Planck's constant/2π	$\hbar$	1.05457×10^{-34} J s
Planck's constant	h	6.6261×10^{-34} J s
Bohr magneton	μ_B	9.2740×10^{-24} J T^{-1}
Vacuum Permeability	μ_0	$4\pi \times 10^{-7}$ N A^{-2}
Vacuum Permittivity	ϵ_0	8.8542×10^{-12} C V^{-1} m^{-1}
Electron's electric charge	e	1.602×10^{-19} C

Introduction

According to the spin-statistic theorem, the quantum states of a system composed of particles with half-integer spin (Fermions), cannot be occupied by more than one particle (Pauli's exclusion principle). If the particles have integer spin (Bosons), such a constraint is relaxed. Both statements have impressive consequences for dynamics of many-particle systems at low temperatures, where the population of the quantum states can be strongly influenced by the bosonic or fermionic nature of the system components (degenerate regime) [1].

As an example of such consequences, Fermionic systems in the degenerate regime have a significant amount of energy due to the distribution of particles over many states. This internal energy produces an associated pressure, whose origin comes from the inability to have more than one particle in the same quantum state. This pressure is, for example, responsible for the stability of some massive stars against gravitational collapse. In a Bosonic system in the same regime, a large proportion of the particles are in the same quantum state, forming what is known as a Bose-Einstein condensate [2].

Modern techniques of magnetic trapping of neutral particles and of laser and evaporative cooling, all developed during the last thirty years of the 20^{th} century, provide the tools needed to create dilute atomic gases in which the degenerate regime can be reached by cooling the system to nano-Kelvin temperatures. This technique gave rise to the experimental realization of an atomic Bose-Einstein condensate in 1995 [3, 4, 5] and enabled the observation of effects associated with Fermi statistics in 1999 [6].

Magnetic trapping offers almost perfect isolation of a gas from external perturbations, creating convenient environments to investigate physics under controllable conditions. The case of degenerate Bosonic gases or Bose-Einstein condensate (BEC), which this thesis focuses on, has been particularly successful and several theoretically predicted phenomena have been already observed, including: interference fringes of matter waves [7], quantised vortices [8], vortex lattices [9, 10], Feshbach resonances [11, 12], BCS-BEC crossover [12, 13, 14, 15], quantum reflection [16], soliton waves [17, 18, 19], and the Berezinskii-Kosterlitz-Thouless transition in quasi-2D geometries [20], among many

other examples.

In addition to interesting fundamental physics, BECs are also suitable for developing applications that take advantage of their quantum nature. Due to the isolation conditions mentioned, such applications could offer sensitivities and efficiencies beyond the limits reached by semiconductor-based technology. The realization of simple devices, like a matter-wave interferometer [21], high sensitivity and resolution field microscope setups [22] and a miniaturised atomic clock [23], suggests a promising future in this direction.

Along these lines, the last decade has seen the appearance of the "atom chip" as a standard setup used to control the dynamics of BECs. Using micron-sized sources of magnetic field, the atom chip produces controllable potentials useful for manipulating atomic gases and registering their state. The high precision and flexibility in the design of microstructured patterns have made possible the creation of a wide range of trapping potentials as well as some analogues to optical devices such as matter-wave splitters and interferometers. With the miniaturization of the trapping potential, other areas of interest have appeared; including low dimensional systems (quasi-1D and quasi-2D), matter-wave interferometry [21], high precision sensors of force and atom-surface interactions [22], BECs in disordered potentials [24], quantum information processing [25], integrated atom-optics [26]. In analogy with the development of semiconductor technology, miniaturization of the atom-chip has become a key element for the success of applications [26, 27].

Microtraps in atom-chips usually hold about $10^4 - 10^6$ atoms at distances above 10 μm from the surface over which the magnetic sources are deposited [26, 27]. At smaller separations, processes like spin flips induced by Johnson Noise in the surface [28], surface absorption due to the attractive Casimir-Polder potential [29], fabrication imperfections [30] and technical noise [31], strongly restrict the possibilities for coherent manipulation, and therefore the functionality of the system.

A potential breakthrough in this context would be the integration of semiconductor structures with devices that are either able to control the atomic behaviour or whose properties depend sensitively in the atom-semiconductor interaction. Apart from adding new features, such structures could produce a simple solution to the problems mentioned above, improving the prospects for developing applications. Also, the quality of the atom-chip would be improved by using established techniques for fabricating structures with nanometre precision, such as deep and shallow etching, gate depletion or ion implantation [32]. Hybrid systems could use a large range of solid-state devices, including quantum dots, quantum point contacts, ferromagnetic semiconductors, spin-polarised currents or 2DEG-superconductor devices, to manipulate and detect single atoms or atomic clouds. Currently, integration of semiconductor technology for atom manipulation is restricted by the typically large atom-surface separation, making the direct coupling between an electron (or hole, if the semiconductor device is p-type) and atomic magnetic moments

very weak: to our knowledge no example of such direct coupling currently exists.

In this work, as a first step towards the integration of semiconducting devices into atom chips, we consider how currents through a Two-Dimensional Electron Gas (2DEG), embedded in a semiconductor device, affect a neighbouring Bose-Einstein condensate (BEC). We demonstrate the feasibility of creating magnetic trapping potentials using currents in a 2DEG and identify their advantages over traditional metal-based traps. We show that properties and effects occurring in the 2DEG, like electron density fluctuations and quantization of the conductance, can be measured through modulation of a BEC's density by the inhomogeneous magnetic field produced. We also establish the conditions under which a sensitive response of the BEC to this magnetic field is possible.

Finally, we use an effective 1D model to describe the phase fluctuations of elongated BECs in different regimes of confining. This study has two motivations: firstly, understanding the phase properties of BEC is a key element to successfully developing applications, and secondly, typical atom chip configurations creates elongated atom clouds, almost of 1D character, whose dynamic is dominated by the phase the condensate wave function.

New materials useful in scientific and technological applications are discovered very frequently. It is worth evaluating how these can be incorporated into atom-chip configurations to understand the physics of both systems and to develop applications. An example of such a situation is the 2DEG-BEC hybrid system considered in this thesis.

CHAPTER 1

Bose-Einstein condensation (BEC) in micro-trap potentials

A system of bosons is said to form a Bose-Einstein condensate (BEC) if, qualitatively speaking, a large portion of its particles are in the same quantum-mechanical state. By extending the ideas of S. Bose on the statistics of photons, in 1925 A. Einstein predicted this condensed state for a gas of massive non-interacting particles, where a macroscopic occupation of the ground state can occurs below a finite critical temperature.

Experiments with helium at low temperatures showed the first evidence of Bose-Einstein condensation. In particular, in 1938 F. London [33] suggested that the superfluid transition observed in ^{4}He was the equivalent of the BEC transition of the ideal gas, occurring in a strongly interacting system. Subsequent theoretical work by Landau [34, 35], Bogoliubov [36], Landau and Lifshitz [37], Penrose [38] and Penrose and Onsager [39], established the superfluid-BEC relation suspected by London, and rigorously extended the notion of Bose-Einstein condensation to the case of interacting particles. Theory and experiments demonstrated that due to the strong interaction between helium atoms in liquid ^{4}He well below the superfluid critical temperature, the lowest energy state is occupied only by $\sim 8\%$ of the total number of atoms [39].

It took about 70 years after Einstein's prediction to observe experimentally the spectacularly large condensed fraction characteristic of the non-interacting case. In 1995, two groups reported the creation of BEC in dilute atomic gases: the team lead by W. Ketterle condensed 5×10^5 ^{23}Na atoms at a temperature below 2 μK (MIT-USA, [4]), while the research group at JILA, led by C. E. Wieman and E. A. Cornell, reached a degenerate state of 2×10^4 ^{87}Rb atoms at a temperature of 170 nK [3]. Since then, at least 75 research groups around the world have reported the achievement not only of

the Bose condensed state, but also of the Fermionic gases in the degenerate regime [1]. So far, the Bose-Einstein condensed state has been reached with vapour gases of alkali atoms of ^{7}Li, ^{23}Na, ^{41}K, ^{52}Cr, ^{85}Rb, ^{87}Rb, ^{133}Cs and ^{174}Yb [40].

This huge experimental success rekindled theoretical interest in the field of quantum degenerate gases [2, 40]. Finite temperature mean field methods, established by Bogoliubov in the 1950's, provide a satisfactory description of many features observed at temperatures well below the transition temperature (T_c). Currently, the extension to regimes where the mean field approach is no longer valid is attracting great attention from the scientific community [41]. Additionally, modern computing facilities allow the simulation of complex situations, getting close to reproducing many of the experimental conditions, and considerable effort has also been devoted to this area [42].

The aim of this Chapter is to introduce the terminology and conventions used in this thesis, as well as the general framework in which this work has been developed. Section 1.1 establishes the definition of the Bose-Einstein condensed state. A brief introduction to the concept of magnetic trapping is presented in Section 1.2. Finally, some developments in the area of micromanipulation of BECs are (very) briefly reviewed in Section 1.3.

1.1 Definition of BEC and the Gross-Pitaevskii equation

In fermionic systems (composed of particles with semi-integer spin), the Pauli exclusion principle implies the single occupancy of any single-particle state. This limitation over the occupancy of levels does not apply for systems made up of particles with integer spin (Bosons). In Bosonic systems at very low temperatures, a macroscopic proportion of the particles can occupy the quantum state with lowest energy, creating what is known as a Bose-Einstein condensate (BEC).

To illustrate how the transition from a thermal gas to a BEC occurs, consider N non-interacting Bosons in a large volume. According to the Bose-Einstein distribution [1], the average number of particles in a state i is given by:

$$N_i = \frac{1}{\exp([E_i - \mu]/k_B T) - 1} \tag{1.1}$$

where E_i is the energy of the state and μ is the system's chemical potential, which is fixed by the total number of particles, N, and the temperature, T, of the system according to:

$$N = \sum_i \frac{1}{\exp([E_i - \mu]/k_B T) - 1} \tag{1.2}$$

[1] http://ucan.physics.utoronto.ca/News

In the non-interacting case, the energy eigenstates are obtained by solving the single-particle time-independent Schrödinger equation, and it is convenient to change the summation over states into a summation over the energy spectrum:

$$N = \sum_n \frac{g_n}{\exp([E_n - \mu]/k_B T) - 1} \tag{1.3}$$

where g_n is the number of states with energy E_n. For a large volume system, the spacing between energy levels tends to zero and the summation over n can be replaced by integration over the energy:

$$N = \int dE \frac{g(E)}{\exp([E - \mu]/k_B T) - 1} \tag{1.4}$$

where $g(E)dE$ is the number of states within the energy interval $[E, E + dE]$.

The simplest situation occurs when particles, of mass m, are free to move in a 3D box of volume V. The density of states is then [1]:

$$g(E) = V \frac{m^{3/2} E^{1/2}}{\pi^2 \hbar^3 \sqrt{2}} \tag{1.5}$$

Substituting Eq. (1.5) into Eq. (1.4) yields a relation between the particle density $\eta = N/V$ and the chemical potential, μ:

$$\eta \lambda^3 = g_{3/2}(z) \tag{1.6}$$

with the standard definitions:

$$\lambda = \sqrt{\frac{2\pi\hbar^2}{m k_B T}} \tag{1.7}$$

$$z = \exp(\mu/k_B T) \tag{1.8}$$

$$g_k(z) = \sum_{\ell=1}^{\infty} \frac{z^\ell}{\ell^k} \tag{1.9}$$

for the thermal wavelength (λ), the fugacity ($z = \exp(\mu/kT)$) and the Bose function $g_k(z)$, respectively [1].

A plot of $g_{3/2}(z)$ is shown in Figure 1.1(a). This function is well defined for $z \leq 1$ and its slope becomes infinite at $z = 1$. As a consequence, the right hand side of Eq. (1.6) has an upper bound equal to $g_{3/2}(1) \simeq 2.612$, which imposes a limit to the product $\eta\lambda^3$. In other words, Eq. (1.6) can be solved only if the condition:

$$\eta \lambda^3 \leqslant g_{3/2}(1) \tag{1.10}$$

is satisfied. This *critical condition* can be violated either if the temperature is very small, making $\lambda \to \infty$ according to Eq. (1.7), or, if the particle density is large enough for a given temperature.

Notice that by replacing the summation in Eq. (1.3) by an integral in Eq. (1.4), the density of states corresponding to the zero momentum state is completely neglected ($g_{3/2}(0) = 0$), and therefore Eq. (1.6) counts the particles with momentum *different from zero*. Violation of Eq. (1.10) means that, in accordance with the Bose distribution, the number of particles with non-zero momentum is smaller than the total number of particles *by a finite fraction*. If the total number of particles is conserved, the remaining finite fraction should be accommodated in the zero momentum ($\boldsymbol{p} = 0$) state. The number of such condensed particles depends on how far the system is from satisfying Eq. (1.10), and saturates at $T = 0$ when all particles are in the zero momentum state.

Eq. (1.10) can be used to define conditions under which Bose-Einstein condensation occurs in the ideal gas. Assuming a fixed density, the critical temperature T_c below which the number of particles in the $p = 0$ state becomes macroscopic is:

$$T_c = \frac{2\pi\hbar^2}{mk_B}\left[\frac{\eta}{g_{3/2}(1)}\right]^{2/3} \tag{1.11}$$

and, assuming a given critical temperature T_c, Eq. (1.10) defines the critical density:

$$\eta_c = g_{3/2}(1)\left[\frac{mk_BT_c}{2\pi\hbar}\right]^{3/2} \tag{1.12}$$

Below T_c, the fraction of particles with zero momentum, N_0, becomes [1]:

$$\frac{N_0}{N} = 1 - \left(\frac{T}{T_c}\right)^{3/2} \tag{1.13}$$

In the thermodynamic limit, considered here by replacing the summation over energy by an integral, the condensation occurs as a second order phase transition at a finite temperature T_c, as seen by the discontinuity in the condensate fraction shown in Figure 1.1(b) [40]. The discontinuities of the thermodynamic functions in this limit, smooth out when the system only contains a finite number of particles, but still change dramatically near the critical temperature [43, 44].

At this point, two remarks deserve mention. First, the potential energy acting on the bosons, and the dimensionality of the system, both influence the character and presence of BEC by defining the density of states (see Eq. (1.4)) [40]. For example, true condensates are not present in the thermodynamic limit of 2D and 1D uniform systems at any finite temperature [2]. Second, the previous definition of BEC cannot be applied directly to an interacting system because single-particle energy levels are only defined for the non-interacting case. However, generalisation of the BEC concept can be done by considering eigenstates of the one-particle reduced density matrix [39], as described in the next Section.

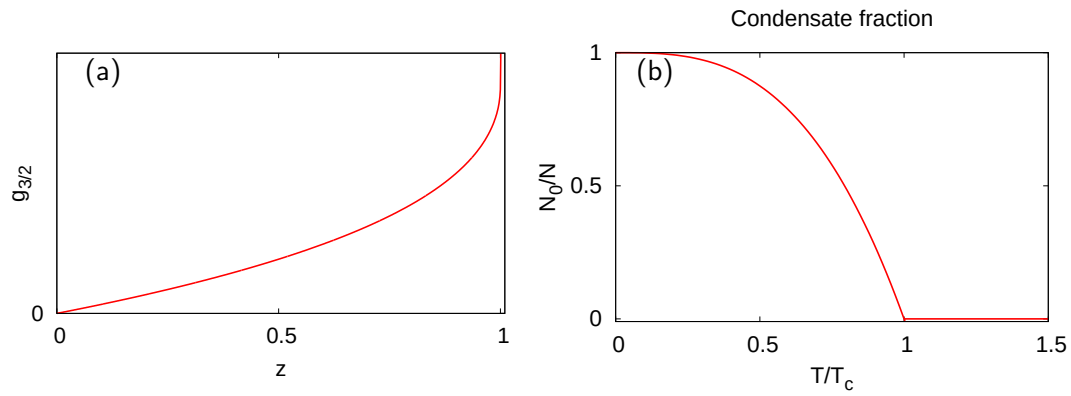

Figure 1.1: (a) Right hand side of Eq. (1.6). This function has an infinite slope at $z = 1$, which implies that Eq. (1.10) has no solutions for $z \geq 1$ (b) Fraction of particles in the zero momentum state for a non-interacting Bose gas. Below the critical temperature, T_c, a macroscopic fraction populates this state.

1.1.1 Definition of BEC for interacting systems

The general definition of the Bose-Einstein condensation phenomenon was originally introduced by R. Penrose and L. Onsager [39]. Using the properties of the one-particle reduced density matrix, they generalised the notion of the ideal BEC in a non-interacting and free gas, to interacting and trapped cases. Their approach also provides a suitable framework for describing the system's dynamics in terms of its excitation spectrum, as done initially by Bogoliubov [36]

Consider a system of N bosons in thermal equilibrium in the many-particle state $|\Psi\rangle$. The one body reduced density matrix is defined by:

$$\hat{\rho}_{(1)} = N \ \mathrm{Tr}_{2\ldots N} \, |\Psi\rangle \langle\Psi| \tag{1.14}$$

where $\mathrm{Tr}_{2\ldots N}$ means the trace is taken with respect to particles $2 \ldots N$ but not particle 1. In the spatial-coordinate representation, the eigenvalues of this operator are defined by the integral equation:

$$\int d\boldsymbol{r'} \rho_{(1)}(\boldsymbol{r}, \boldsymbol{r'}) \phi_i(\boldsymbol{r'}) = N_i \phi_i(\boldsymbol{r}) \tag{1.15}$$

where N_i is the occupation number of the single-particle state ϕ_i. The eigenfunctions, ϕ_i, define an orthonormal and complete basis of the system's Hilbert space, and the density operator can be written as:

$$\rho_{(1)}(\boldsymbol{r}, \boldsymbol{r'}) = \sum_i N_i \phi_i(\boldsymbol{r}) \phi_i^*(\boldsymbol{r'}) \tag{1.16}$$

Bose-Einstein condensation occurs when one of the single-particle states, ϕ_0, is macroscopically occupied while the other single-particle states have an occupation of order

1. This condition is equivalent to establishing positive upper and lower bounds for the fraction of particles in a single-particle state ϕ_0 [39].

Under this condition, the major contribution to the density matrix Eq. (1.16) comes from the macroscopically occupied state, ϕ_0. Therefore, it is convenient to separate out it from Eq. (1.16), which can be written as:

$$\rho_{(1)}(\boldsymbol{r},\boldsymbol{r'}) = N_0\phi_0(\boldsymbol{r})\phi_0^*(\boldsymbol{r'}) + \sum_{i\neq 0} N_i\phi_i(\boldsymbol{r})\phi_i^*(\boldsymbol{r'}) \tag{1.17}$$

In general, the second term involves a superposition of functions with all possible length scales, and tends to zero for large separation $|\boldsymbol{r}-\boldsymbol{r'}| \to \infty$ [2, 39]. The first term gives a finite contribution up to distances fixed by the extension of the function $\phi_0(\boldsymbol{r})$, making $\rho_{(1)}(\boldsymbol{r},\boldsymbol{r'}) \neq 0$ for all relevant distances in the system. This characteristic of the density matrix is known as long-range order and under Bose-Einstein condensation *all* relevant non-diagonal elements of the density matrix of a system are finite, in contrast with the situation in a non-condensed state, where they tend to zero [2].

1.1.2 The Gross-Pitaevskii Equation

The Gross-Pitaevskii equation (GPE) corresponds to the mean-field approximation of a system of weakly interacting bosons at $T = 0$. It differs from the Schrödinger equation by a non-linear term proportional to the local density of the system. The GPE enables the system's dynamics to be described in terms of a reduced set of parameters with a clear physical meaning [40, 45]. Phenomena like the creation of sound waves, solitons and vortices are described with great accuracy by the GPE [40].

To obtain the Gross-Pitaevskii equation in its usual form, consider a system of N interacting particles, described in the many-body representation by the Hamiltonian operator:

$$\begin{aligned}\hat{H} &= \int d\boldsymbol{r}\hat{\Psi}^\dagger(\boldsymbol{r},t)\left[-\frac{\hbar^2}{2m}\nabla^2 + V_{\text{ext}}(\boldsymbol{r})\right]\hat{\Psi}(\boldsymbol{r},t) \\ &\quad + \frac{1}{2}\int d\boldsymbol{r}\int d\boldsymbol{r'}\hat{\Psi}^\dagger(\boldsymbol{r},t)\hat{\Psi}^\dagger(\boldsymbol{r'},t)V(\boldsymbol{r}-\boldsymbol{r'})\hat{\Psi}(\boldsymbol{r},t)\hat{\Psi}(\boldsymbol{r'},t)\end{aligned} \tag{1.18}$$

where $\hat{\Psi}(\boldsymbol{r},t)$ and $\hat{\Psi}^\dagger(\boldsymbol{r},t)$ are the Boson field operators for annihilation and creation of a particle at position $\boldsymbol{r}$, respectively, and $V(\boldsymbol{r}-\boldsymbol{r'})$ is the two-body interaction potential.

Defining the Bose-Einstein condensed state in terms of the single-particle density matrix and its eigenstates allows us to identify the single-particle states for both the interacting and non-interacting cases. These functions can be used to expand the field operators, $\hat{\Psi}(\boldsymbol{r},t)$ and $\hat{\Psi}^\dagger(\boldsymbol{r},t)$ respectively, in terms of single-particle annihilation and creation operators :

$$\hat{\Psi}(\boldsymbol{r},t) = \phi_0(\boldsymbol{r},t)\hat{\phi}_0 + \sum_{i\neq 0}\phi_i(\boldsymbol{r},t)\hat{\phi}_i \tag{1.19}$$

where the contribution associated with a macroscopically occupied single-particle state ϕ_0 has been separated out. The annihilation and creation operators satisfy the usual relations:

$$\hat{\phi}_i^\dagger |N_0 N_1 \dots N_i \dots\rangle = \sqrt{(N_i+1)}\, |N_0 N_1 \dots N_i + 1 \dots\rangle \tag{1.20}$$

$$\hat{\phi}_i |N_0 N_1 \dots N_i \dots\rangle = \sqrt{N_i}\, |N_0 N_1 \dots N_i - 1 \dots\rangle \tag{1.21}$$

$$\left[\hat{\phi}_i, \hat{\phi}_j^\dagger\right] = \delta_{i,j};\ \left[\hat{\phi}_i, \hat{\phi}_j\right] = 0;\ \left[\hat{\phi}_i^\dagger, \hat{\phi}_j^\dagger\right] = 0 \tag{1.22}$$

If the system has a large number of particles and most of them are in a single-particle state ϕ_0, the action of the corresponding creation and annihilation operators on the equilibrium state can be approximated by the c-number, composed of the real factor $\sqrt{N_0}$ times an arbitrary phase factor [2]. This is equivalent to ignoring the non-commutativity of the operators $\hat{\phi}_0$ and $\hat{\phi}_0^\dagger$ and considering the main contribution to the field operator as a classical entity. The field operator then can be split in the form:

$$\hat{\Psi}(\boldsymbol{r}, t) = \psi_0(\boldsymbol{r}, t) + \hat{\Psi}'(\boldsymbol{r}, t) \tag{1.23}$$

where $\psi_0(\boldsymbol{r}, t) = \sqrt{N_0}\phi_0(\boldsymbol{r})$ is a complex function normalised to:

$$\int |\psi_0(\boldsymbol{r}, t)|^2 d\boldsymbol{r} = N_0 \tag{1.24}$$

and plays the role of an order parameter. Substituting Eq. (1.23) into the Heisenberg equation of motion for $\hat{\Psi}$ and dropping second order terms gives:

$$i\hbar\partial_t \psi_0(\boldsymbol{r}, t) = \left\{ -\frac{\hbar^2}{2m}\nabla^2 + V_{\text{ext}}(\boldsymbol{r}) + \int \psi_0^*(\boldsymbol{r'}, t) V(\boldsymbol{r} - \boldsymbol{r'}) \psi_0(\boldsymbol{r'}, t) d\boldsymbol{r'} \right\} \psi_0(\boldsymbol{r}, t) \tag{1.25}$$

In dilute gases, only the low energy binary collisions are relevant and the interaction potential can be characterized by a single parameter, the s-wave scattering length (a_s) [40]. The two body interaction can be then represented by a δ-function potential energy:

$$V(\boldsymbol{r'} - \boldsymbol{r}) = \frac{4\pi\hbar^2 a_s}{m} \delta(\boldsymbol{r'} - \boldsymbol{r}) \tag{1.26}$$

Within this approximation, the time evolution of $\psi_0(\boldsymbol{r}, t)$ is governed by the equation:

$$i\hbar\partial_t \psi_0(\boldsymbol{r}, t) = \left\{ -\frac{\hbar^2}{2m}\nabla^2 + V_{\text{ext}}(\boldsymbol{r}) + \frac{4\pi\hbar^2 a_s}{m} |\psi_0(\boldsymbol{r}, t)|^2 \right\} \psi_0(\boldsymbol{r}, t) \tag{1.27}$$

which is known as the *Gross-Pitaevskii* Equation (GPE) [47]. The total energy of the interacting system described by the condensed wave function $\psi_0(\boldsymbol{r})$ is given by:

$$E[\psi] = \int d\boldsymbol{r} \left[\frac{\hbar^2}{2m} |\nabla\psi(\boldsymbol{r})|^2 + V_{\text{ext}}(\boldsymbol{r}) |\psi(\boldsymbol{r})|^2 + \frac{1}{2}\frac{4\pi\hbar^2 a_s}{m} |\psi(\boldsymbol{r})|^4 \right] \tag{1.28}$$

[2] This procedure is known as the Bogoliubov shift [46]. By choosing a fixed phase of the condensate wave-function, the gauge symmetry of the Schrödinger Equation is broken.

To obtain the equilibrium configuration, the energy functional Eq. (1.28) must be minimised, subject to the normalisation condition Eq. (1.24). This leads to the time-independent Gross-Pitaevskii equation:

$$\mu\psi_0(\boldsymbol{r}) = \left\{-\frac{\hbar^2}{2m}\nabla^2 + V_{ext}(\boldsymbol{r}) + \frac{4\pi\hbar^2 a_s}{m}\left|\psi_0(\boldsymbol{r})\right|^2\right\}\psi_0(\boldsymbol{r}) \tag{1.29}$$

where μ is the Lagrange multiplier associated with the normalisation condition Eq. (1.24) and coincides with the system's chemical potential.

1.2 Trapping neutral Bosons

Bose-Einstein condensation in atomic gases has been achieved by combining techniques of magnetic and optical trapping (1980's) [48] with laser and evaporative cooling procedures developed during the 1990's [4]. As magnetic trapping is a central topic in this thesis, its general principles are now presented.

Under appropriate conditions, the coupling of the atomic magnetic moment to external magnetic fields can be used to confine the motion of atoms with low kinetic energy (*cold atoms*) into small spatial regions (mm – μm). This is a flexible mechanism because the two main ingredients can be controlled experimentally with high precision. A desired atomic magnetic moment[3] can be induced by shining laser fields with the appropriate frequencies. In addition, almost arbitrary spatial magnetic field profiles can be produced by an appropriate distribution of sources (electric currents and/or permanent ferromagnets).

Consider an atom in the state $|F, m_F\rangle$ moving through an inhomogeneous magnetic field ($\boldsymbol{B}(\boldsymbol{r})$), where F is the quantum number corresponding to the total angular momentum, and m_F is its projection along one chosen spatial direction. The interaction potential is given by [2]:

$$\hat{V}(\boldsymbol{r}) = -\hat{\boldsymbol{\mu}}_F \cdot \boldsymbol{B}(\boldsymbol{r}) \tag{1.30}$$

where $\hat{\boldsymbol{\mu}}_F$ is the operator for the magnetic moment of the atom.

When the atom's translational energy is small enough, the atomic magnetic moment follows adiabatically the direction of the magnetic field and its projection on the local direction of the magnetic field remains constant along the trajectory of the atom. This adiabatic condition can be expressed using a classical model for the atomic magnetic moment as follows: The spatial translation of the atom should be much slower than the precession of its spin around the magnetic field local direction. Under this condition, Eq. (1.30) becomes:

$$\hat{V}(\boldsymbol{r}) = m_F g_F \mu_B \left|\boldsymbol{B}(\boldsymbol{r})\right| \tag{1.31}$$

[3] Of course, one that is allowed by quantum mechanics

where m_F is the projection of the atomic magnetic moment along the direction of $\boldsymbol{B}$ and g_F is the Landé g-factor.

In terms of the atomic energy level structure, the trapping mechanism can be explained as follows. Consider an alkali atom whose valence electron is in an S orbital and with total angular momentum:

$$\hat{\boldsymbol{F}} = \hat{\boldsymbol{I}} + \hat{\boldsymbol{S}} \tag{1.32}$$

where $\hat{\boldsymbol{I}}$ corresponds to the nuclear angular momentum and $\hat{\boldsymbol{S}}$ the electronic spin. The interaction between nuclear and electronic spins lifts the degeneracy of the S orbital with respect to the total angular momentum (hyperfine splitting), and the states $|F = I + 1/2, m_F\rangle$ and $|F = I - 1/2, m_F\rangle$ have different energy, $E_{F=I\pm1/2}$. Coupling the nuclear and electronic spins to an external magnetic field, $\boldsymbol{B}$, lifts the remaining degeneracies; this is the Zeeman effect. At low magnetic fields, the Zeeman splitting is linear and small compared with the hyperfine splitting. In this case the atomic energy is given by:

$$E = E_F + m_F g_F \mu_B |\boldsymbol{B}| \tag{1.33}$$

The key feature of equations (1.31) and (1.33) is that the energy depends on the magnitude of the magnetic field, $|\boldsymbol{B}|$, whose spatial dependence creates a potential landscape for the atomic motion. The equilibria points will coincide either with maxima or minima of this quantity, according to the sign of the magnetic moment, $m_F g_F \mu_B$. We can conclude, therefore, that states with negative magnetic moment will be attracted towards regions of low field intensity (*low field seeker states*) whilst atomic states with a positive magnetic moment are attracted towards regions of high field (*high field seeker states*).

The time-independent Maxwell equations prohibit the creation of a local maximum of magnetic field in free space, but do not forbid a minimum being attained [49, 50]. The task of producing a trapping potential for cold atoms therefore translates into creating a magnetic field distribution with localized regions of low magnetic field.

A basic setup to create a magnetic trap consists of combining the magnetic field produced by a thin and infinitely long wire, carrying a current I:

$$B = \frac{\mu_0}{2\pi}\frac{I}{r} \tag{1.34}$$

with a uniform bias magnetic field ($\boldsymbol{B}_{\text{Bias}}$) orthogonal to the current flow [26, 50, 51, 52], as shown in Figure 1.2(a).

Assuming the bias field is applied parallel to the y axis in Figure 1.2, the total magnetic field has a minimum along z axis, located at a distance:

$$z_0 = \frac{\mu_0 I}{2\pi B_{\text{Bias}}} \tag{1.35}$$

from the wire. The position of minimum magnetic field is also referred to as the trap position. The total magnetic field distribution produces an ideal side trap where the

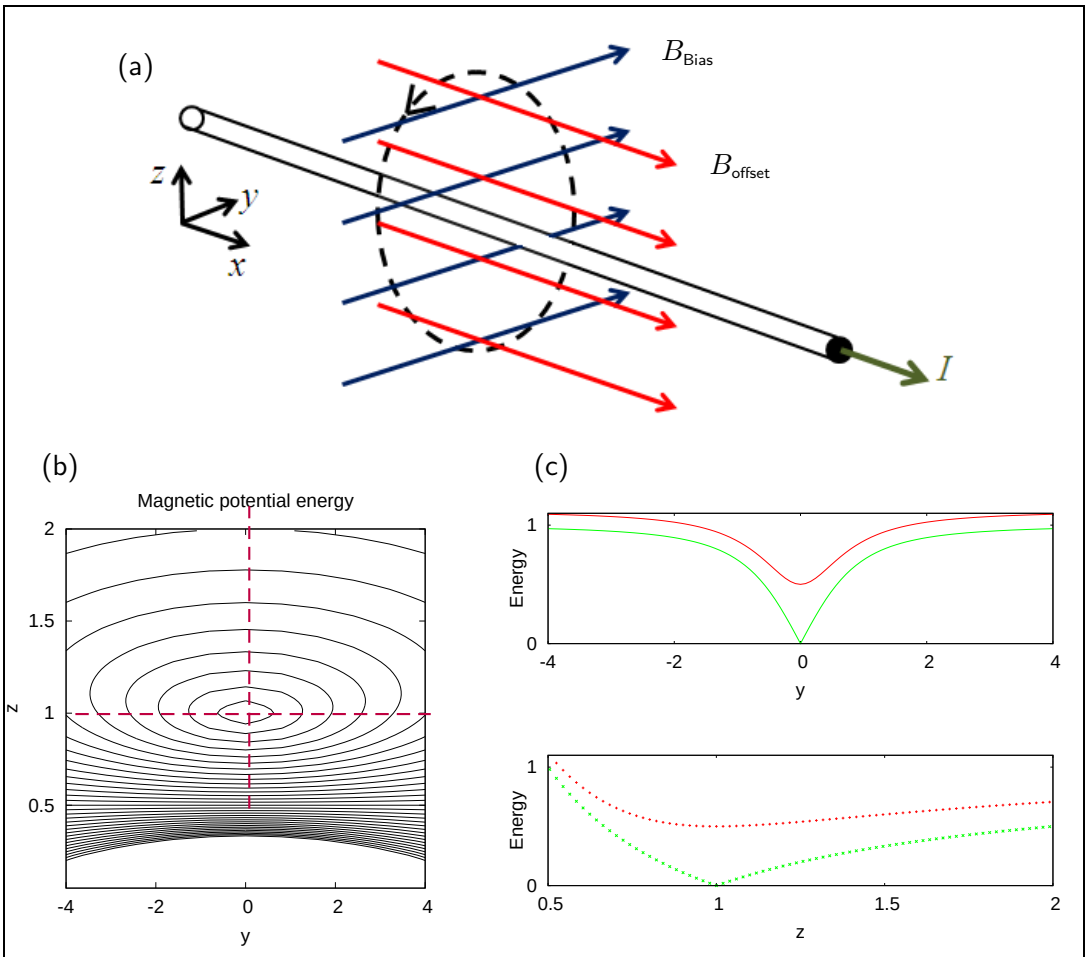

Figure 1.2: (a) Geometry of a simple magnetic trap setup. The bar represents a long and thin current carrying conductor. External uniform fields are represented by blue (bias field) and red (offset field) arrows. The dashed circle indicates the magnetic field produced by the wire. (b) Isopotential curves for the waveguide configuration in (a). Energy contours are equally spaced by $0.0625 B_{\text{Bias}}$. (c) Potential energy Eq. (1.31) along the axes crossing the trap position. Notice that when an offset field is added, the potential energy rounds off near the minimum (red lines). In a typical setup, the trap is located at few tens of micrometre, $z \sim 10$ μm and the fields has an intensity of a few tens of Gauss, $B_{\text{Bias}}, B_{\text{offset}} \sim 10$ G.

atoms are free to move parallel to the wire but their motion in the orthogonal plane is restricted. In Figure 1.2, panel (b) shows potential energy curves (Eq. (1.31)) in the plane transverse to the wire, and panel (c) plots the energy along the y and z axes, shown as purple lines in panel (b). Notice that when the minimum potential energy equals zero, the potential energy increases linearly with distance to the minimum position (green lines).

In panels (b) and (c) of Figure 1.2, the length scale have been set to the distance between the centre of the wire and z_0. In typical experiments with atom chips, such

a distance is in the range of 10μm – 100μm. For experiments is also common using micron-sized conductors that support currents of a few hundreds of mA up to 1 A, creating magnetic fields of a few tens of Gauss. As the distance between the source of magnetic field is comparable with its size, finite size effects have to be included to evaluate the distribution of magnetic field. In order to simplify the presentation, such an effect is ignored in this chapter and the wire is considered as infinitely long and thin.

Near the trap position z_0, the components of the magnetic field in the $y-z$ plane, $\boldsymbol{B}_\perp$, are well approximated by a quadrupole distribution [40]:

$$\boldsymbol{B}_\perp = (B_y, B_z) = \alpha(z - z_0, y) \tag{1.36}$$

where α is the gradient of the magnetic field evaluated at the trap centre z_0. In an ideal quadrupole distribution, the magnetic field varies linearly with the distance to the point where it vanishes. For comparison, the ideal quadrupole and the exact magnetic field distributions of the ideal side trap are shown in Figures 1.3(a) and 1.3(b), respectively.

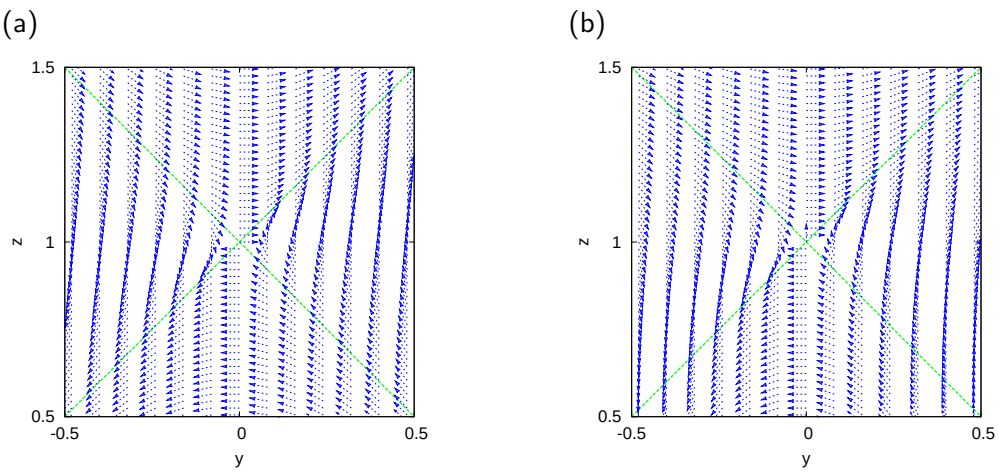

Figure 1.3: (a) Ideal quadrupole magnetic field distribution. (b) Magnetic field distribution in a side trap produced by an ideal wire plus a Bias field, shown in Figure 1.2. Similarly to Figure 1.2, the length scale here is typically ~ 10 μm.

The quadrupole trap has two orthogonal axes (dashed lines in Figure 1.3). Along one of them the magnetic field points towards the position of zero magnetic, while along the other the magnetic field points in the opposite direction (see arrows along the dashed lines in Figure 1.3(a)). Comparing with Figure 1.2(b), it can be seen by inspection that the magnetic field in the ideal side trap has approximately the same properties as the ideal quadrupolar magnetic field distribution, Eq. (1.36).

Atoms can escape from the magnetic trap due to its thermal motion or to transitions involving electronic spin-flips transition to untrapped states. These processes are particularly common at places where the magnetic field is zero because there the electron spin does not have a preferred direction to be projected. Also, at positions where $|\boldsymbol{B}| = 0$,

the adiabatic condition over the atomic motion cannot be satisfied because there is no spin precession [40].

In order to reduce atom losses in a trap like the one in Figure 1.2, due to the absence of magnetic field at the minimum, it is common to apply uniform magnetic field parallel to the wire (usually called offset field: $\boldsymbol{B}_{\text{offset}}$). With this additional field, the position of the minimum of the total magnetic field does not change (Eq. (1.35)), but the value of B at z_0 becomes equal to $B_{\text{offset}} \neq 0$. The additional offset field fixes a quantization axis, which the spin of all trapped atoms projects over, reducing significantly the probability of atomic transitions involving spin flips.

The presence of the offset field does not modify the validity of the quadrupole approximation, Eq. (1.36), for the components of the magnetic field in the $y - z$ plane. The offset field adds non-linearly to the total potential energy, Eq. (1.31), rounding off the potential energy near the minimum, as can be seen in Figure 1.2(c) (red lines). Therefore, the potential energy is no longer a linear function of the distance from the minimum of magnetic field, and the next level of approximation is a quadratic or harmonic potential, being now its curvature (translated into frequency) the appropriate quantity to describe the tightness of the trap.

1.3 BEC in micro-trap potentials

The use of microstructured surfaces has enabled the control of cold atom clouds on a micrometre scale. The principle of operation relies on the interaction of the atom's magnetic moment with a controllable external magnetic field, whose sources commonly are current carrying wires and/or permanent magnets. A brief review of some developments in the area of micro-manipulation of cold atoms is presented below.

Micro-traps offers a broad range of possible applications, many of them the subject of ongoing development and study. Amongst others, the following can be mentioned: dynamics of low-dimensional quantum gases, effects of disordered potentials [53], atom optics (interferometry [54], quantum reflection [16, 55], diffraction of matter waves [56, 57]), quantum information processing [58, 59], force and field sensors [60].

In comparison with the first setups used in the MIT and JILA experiments, production of micro-trapped atomic Bose-Einstein condensates is simplified by the proximity of microstructures [61, 62, 63, 64]. Very strong trapping potentials can be easily produced by small currents in micro-wires in particular when the atom-wire distance is in the micrometre range. The tight confinement reduces the time scale of the collisions in the trapped cloud and accelerates the forced evaporation stage. In addition, a surface close to a thermal atomic cloud acts like a thermal knife, removing the hottest atoms by the action of an attractive potential towards the surface (Casimir-Polder force). As a consequence of these two effects, the vacuum conditions needed for BEC preparation

are relaxed compared with the requirements of pioneering experiments [50].

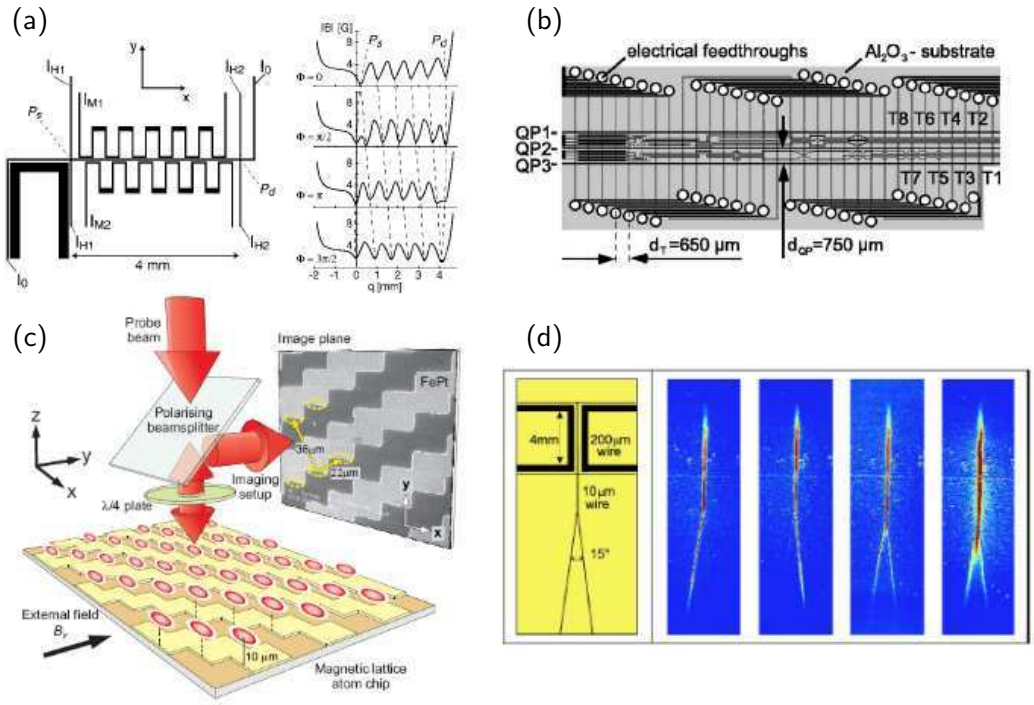

Figure 1.4: Several setups developed for atom manipulation. (a) Conveyor belt by Reichel, *et al.* [61]. Left panel: layout of the chip; right panel: potential energy at different times. The motion of the potential wells is indicated by dashed lines. (b) Atom chip by Günter *et al.* [65]. Axial confinement is provided by a set of vertical wires separated by 650 µm, such that the position of the trap can be displaced horizontally by adjusting the current in those wires. (c) Atomic shift register by Whitlock *et al.* [66]. A patterned FePt magnetic film is used to trap atom clouds at micrometre distances (~ 10 µm). The position of the trap can be translated by modifying the direction of the external field . (d) Y junction on a chip by Cassettari *et al.* [67]. Left panel: schematic of the wire layout showing the Y-shaped guide. Right panel: images of guided atoms showing it is possible to control the splitting

Precise *positioning and displacement* of trapped atoms can be performed relatively easily by using microtrapping setups. Different schemes have been applied to transport trapped clouds across a few cm with velocities of a few mm/s. For example, Reichel *et al.* [61] and Hänsel *et al.* [62, 68] developed an Archimedean screw analogue to transport cold atoms. By combining segments of wires carrying ac-currents out of phase, they created a train of moving trap potentials wells that can transport atoms at a speed of ~ 10mm/s (see Figure 1.4(a)).

An alternative approach was developed by Günther *et al.* [65]. They used a set of

parallel conductors orthogonal to the main trapping structure. By using an appropriate set of time-dependent currents in the parallel wires, the barriers producing the lateral confinement are displaced smoothly, thus enabling arbitrary control of the trapping position (see Figure 1.4(b)).

A completely different transport mechanism was demonstrated by Whitlock *et al.* [66] (see Figure 1.4(c)). They used a lattice of permanent magnets plus external uniform fields to create a 2D array of trapping wells. Then, by smoothly changing the orientation of one external field, the trapping positions can be shifted simultaneously, and the trapped atoms are driven to adjacent sites of the periodic potential. This setup demonstrates a way to perform operations on a large number of individual clouds as required for possible quantum computing applications.

A more advanced feature of microtrap devices is the possibility to perform so-called *atom optics*. Careful design of the magnetic field distribution can produce effects on the trapped atoms similar to those that optical devices produce on light. The atomic wave nature can be exploited in this way and coherent manipulation of atomic clouds has been already demonstrated [69]. Such optical-like setups can be built by bending the current carrying wires, adding time-dependent magnetic fields, using laser light, or using microstructured solid state surfaces from which quantum reflection can occur [16].

A *beam splitter* for matter-waves can be produced by a Y junction of current carrying wires (see Figure 1.4(d)). Adding a uniform magnetic field to this setup produces a trap where a single branch splits into two following the shape of the junction. A slowly moving BEC approaching the junction from the single branch region, can be split or deflected into one of the junction arms, by controlling the current in the wires. An experimental demonstration of such a switch has been reported by Cassettari *et al.* [70].

Closing the Y junction on the opposite side of the structure produces a matter-wave Mach-Zehnder interferometer device [74] (see Figure 1.5(a)). In this case, a cloud slowly approaching the junction is split in two. Then, each part moves along the branches of the interferometer and are finally recombined by an inverted Y junction. The state of the atom cloud at the end of the interferometer arm depends on the relative phase acquired by the two interfering clouds. This relative phase can originate from localized forces along the interferometer arms (see Anderson and Kasevich [74]). T. Müller *et al.* [75] have proposed an interferometer device based on a superconducting atom chip. Up to now, however, no experimental realization of this interferometer has been reported.

Continuous transformation of a single well trapping potential into a double-well can be used to create a different interferometric device [26]. A cloud can be split by slowly increasing a central potential barrier. Each part of the split cloud can then be exposed to different external effects inducing a phase difference that shapes the interference pattern produced when the clouds are recombined by lowering the barrier [76].

Diffraction of matter waves has been demonstrated by Günter *et al.* [56, 65]. They

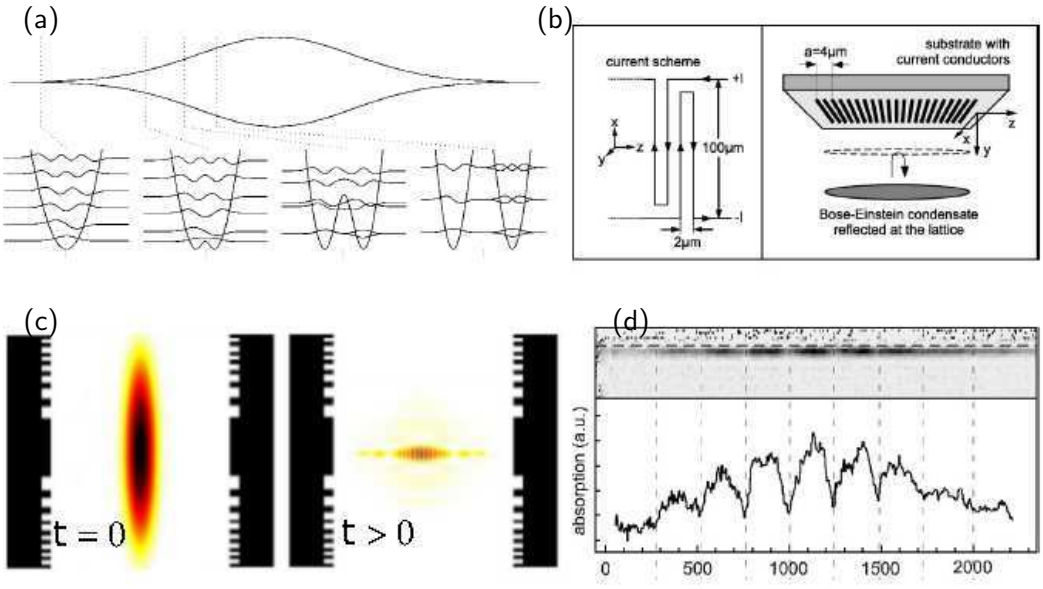

Figure 1.5: (a) Schematic of a matter-wave Mach-Zehnder interferometer. The figure shows the wire geometry needed (upper panel) and the guiding potential as well as some eigenfunctions at different positions along the interferometer. This scheme was proposed by Anderson and Kasevich [71]. (b) Sketch of the experiment of diffraction of matter waves, by Günter *et al.* [56]. Left panel: current scheme used to create a magnetic lattice. Right panel: procedure followed to imprint a phase pattern into a BEC. (c) Numerical simulation of focusing an atomic cloud by reflecting it from a patterned surface. Left panel: original condensate. Right panel: condensate after reflection from the side pattern surfaces. Figures produced by Tom Montgomery [72]. (d) Fragmentation of ultra-cold cloud of ^{85}Rb trapped at ~ 45 µm from a electro-plated conductor. Taken from Kraft *et al.* [73]. All figures were taken from the indicated references.

used an array of parallel wires carrying currents in alternating directions to create a periodic magnetic potential (see Figure 1.5(b)). Then, a BEC was held for a short period of time near the current pattern, causing it to acquire a spatially dependent phase. The phase pattern is revealed later when the cloud is left to expand freely, forming an interference pattern. A theoretical model shown by the same authors explains the observed pattern in terms of the superposition of several orders of diffraction [56, 77]. Judd *et al.* [78] then produced a more complete model by performing full 3D solutions of the GPE and establishing the effect of inter-atomic interactions on the diffraction process.

A recently proposed setup for matter-wave manipulation is based on the quantum reflection effect [55]. Numerical evidence shows that lithographically sculptured surfaces can be used as lenses for matter waves, for example to focus coherent atomic clouds.

Simulation of the 3D Gross-Pitaevskii equation shows that two parallel sets of Fresnel rings can focus a freely expanding BEC into an area of few a nm [72] (see Figure 1.5(c)). This is potentially useful for nano-fabrication processes, if the focused cloud can be deposited on top of a semiconductor substrate for subsequent treatment and production [79]

Research on fundamental aspects of the light-matter interaction is also possible using microtrapping setups. In typical experimental situations, atoms are held at small distances from the field sources. When the atom-surface distance is of the order of a few tens of micrometres, the trapping potential becomes affected by defects in the trapping elements or from the surface itself.

Distortion of the magnetic field sources corrugates the trapping potential and produces fragmentation of the trapped clouds (see Figure 1.5(d)) [30, 60, 80]. This effect is greatly reduced by optimising the fabrication process of the conducting elements [22], or by polishing the conductor edges [81].

Also, at short distances, the trapping potential becomes affected by the fluctuating magnetic field surrounding the trapping elements [31, 82, 83]. The source of this field is the Johnson noise in the material, which, at thermal equilibrium, produces a fluctuating field whose spectral density depends on the shape of the elements and on their temperature and conducting properties.

The fluctuating field can induce spin flips promoting losses of the trapped atoms [84, 85]. To develop future applications, it is therefore important to understand these effects deeply. Several proposals have been made to reduce the magnetic noise, including the use of metal alloys [86], anisotropic materials [87], carbon nano-tubes [88], permanent ferromagnets [89, 90] and superconductors [85, 91, 92, 93, 94], as trapping elements, but only the last two have been experimentally realized so far.

The next generation of microtraps should expand the already high flexibility of atom-chips, from which a small sample has been given above. One of the major problems to overcome its to understand the effects of the atom-surface interactions and, if possible, to exploit them as a tool for manipulating the atoms. Also, solid state structures, like semiconductors, ferromagnets, graphene, superconductors, meta-materials may in due course to be used in microtrapping and micro-manipulating technologies. The present work is expected to contribute to such advances.

CHAPTER 2

The Two-Dimensional Electron Gas (2DEG)

Schottky barriers, p-n junctions, field effect transistors and laser-diodes are devices made by combining layers of materials with different conducting properties [95]. The working principle of such devices relies on the fact that abrupt changes of the band structure, occurring at layer interfaces, produce a carrier redistribution which can be can be controlled by external electric or magnetic fields [96].

This chapter describes the origin and properties of a Two Dimensional Electron Gas (2DEG), formed near the interface between layers of (AlGa)As and GaAs. The typical layer structure of this heterojunction is described in Section 2.2. The model used to evaluate the effect of ionized donors over the motion of electrons in the 2DEG is presented in Section 2.3.

The description presented here is used in Chapters 4 and 5 to the determine the effects of a magnetic field produced by current flows in a 2DEG, over a BEC magnetically trapped near the heterojunction.

2.1 Some features of semiconducting materials

The one-electron model [97] has been used successfully to predict the electrical properties of some semiconductor materials. In this model, solids are considered as crystalline structures with atomic nuclei rigidly fixed to crystal sites and valence electrons moving under an effective potential, origining from the electron-electron and electron-nuclear interaction. The energy levels of the system form a band structure associated with each representation of the translation symmetry group [97]. Each eigenstate is identified

by two indices: one related to crystal momentum, $\boldsymbol{k}$, and the other to the level band index, n. The variation of the energy with the crystal momentum, $E_n(\boldsymbol{k})$, known as the dispersion relation of the n^{th} band, determines the response of the system to applied electromagnetic fields. The band structure of GaAs is shown in Figure 2.1 (from [95]).

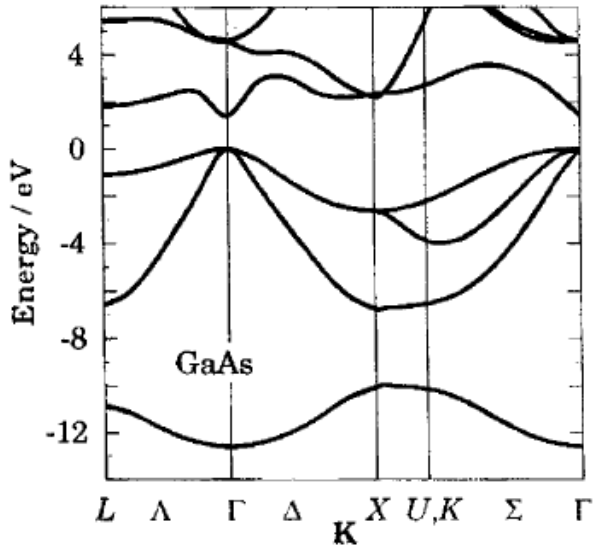

Figure 2.1: Energy band structure for GaAs. Adapted from [95]

Once the band structure of the material is known, the electric properties can be obtained by distributing the valence electrons in the allowed states, satisfying the Pauli exclusion principle. The occupied band with the highest energy is defined as the *valence band* and the empty band immediately above it is known as the *conduction band*. Depending on the total number of valence electrons, materials can be classified into four categories: If all bands are completely full, then the crystal behaves as an insulator. If one band is partially filled, the system behaves as a metal. Semimetal or semiconducting behaviour is present when one band is slightly empty or filled [97].

Material	Lattice constant (Å)	E_g (eV)	m_e^*/m_e^0
Si	5.43	1.11	0.33
Ge	5.65	0.66	0.22
AlAs	5.66	2.23	0.26
GaAs	5.65	1.42	0.067

Table 2.1: Properties of technologically important semiconductor materials at room temperature (300 K). E_g is the calculated energy gap between the conduction and valence band. m_e^* is the electronic effective mass, expressed as a fraction of the free electron mass m_e^0.

Relevant properties of some technologically important semiconductor materials are shown in Table 2.1. The elements Ge, Si and compounds GaAs and AlAs have eight valence electrons per unit cell, which completely fills four bands (2 electrons per state if they are spin-degenerate). Typically, the distance between the top of the valence band and the bottom of the conductance band is a few eV, corresponding to a temperature scale of 12000 K. At zero temperature, the conduction band remains completely empty and electrical conduction is not possible. At finite temperature, though, some electrons can be thermally transferred to the conduction band making electrical transport possible, but with a large resistance compared with normal metals like gold (Au), silver (Ag) or copper (Cu) [97].

By doping semiconductor materials with alien species added to the crystalline structure, the number of charge carriers can be increased, modifying the conducting properties with respect to the pure crystal. In GaAs, for example, one atom of Ga can be replaced by Si, which has five valence electrons. Assuming that the crystal structure is not heavily modified, the extra valence electron becomes only weakly attached to the Si nucleus, occupying an energy level just below the bottom of the conduction band. This extra electron is easily transferred thermally to the conduction band, where it behaves as a free charged particle with a material dependent effective mass m_e^* [97].

Electrons in the conduction band can transfer energy to the lattice through inelastic scattering with crystal vibrations, imperfections and boundaries. In response to a low external electric field ($\boldsymbol{E}$), such scattering events produce a finite current density following, in a linear approximation, the Ohm's law:

$$\boldsymbol{j} = \sigma \boldsymbol{E} \tag{2.1}$$

where the conductivity of the material, σ, depends on the density of electrons in the conduction band, the temperature and scattering process of electrons with the crystal and impurities [97].

2.2 The GaAs/(AlGa)As heterojunction and the 2DEG

Electronic devices are designed using materials whose electrical characteristic can be controlled by applied external fields. Semiconductors are natural elements for this task because current technology makes possible to engineer the way as their transport properties depend on controllable external fields. This section briefly describes the origin and properties of a two-dimensional electron gas at the interface between two semiconductor materials.

GaAs is a semiconductor with a direct band gap of $E_{g,\mathrm{GaAs}} = 1.42$ eV at room temperature and located at the Γ point of the reciprocal space (see Figure 2.1). The alloy $\mathrm{Al}_x\mathrm{Ga}_{1-x}\mathrm{As}$ is obtained from GaAs by replacing a fraction x of the Ga atoms by

Al. Its band gap depends on x and lies between the AlAs ($E_{g,\mathrm{AlAs}} = 2.23$ eV) and GaAs band gaps. The direct character of the band gap is broken when $x = 0.45$ is exceeded [98].

A typical GaAs/$Al_xGa_{1-x}As$ heterojunction is a four layers device with an optional metallic gate. The first two layers are a *substrate*, made of ultrapure GaAs, and a n-doped $Al_xGa_{1-x}As$ alloy. The third layer, known as the $spacer$, consist of un-doped $Al_xGa_{1-x}As$. The structure is completed by a cap layer of GaAs. The equilibrium state between the components of the heterojunction is reached by charge transfer between them, accompanied by bending of the conductance band determined by Poisson's equation. At equilibrium, a 2DEG forms near the interface between the GaAs and $Al_xGa_{1-x}As$ spacer layers. The spatial variation of conduction band edge energy across the heterojunction is shown in Figure 2.2. The optional metallic gate, grown on top of the substrate, can be used to control the bending of the conductance band across the heterojunction and thus the density of the 2DEG near the interface between the *substrate* and the *spacer* layers.

All numerical calculations for the 2DEG presented in this thesis were performed for a heterojunction prepared by Prof. Mohamed Henini in the Semiconductor Physics Group of the University of Nottingham, identified as NU2239. The structure, shown schematically in Figure 2.2, consists of a 20 nm thick cap layer, doped and undoped spacer layers each 400 nm thick, grown on a substrate of ultrapure GaAs. The potential energy at the cap-vacuum interface is pinned by the surface states to 0.770 eV and the doped region contains 1.3×10^{24} m^{-3} Si atoms.

The process responsible for the appearance of an electron gas can be described as follows: Electrons in the conduction band at the n-$Al_xGa_{1-x}As$ side (high conduction band edge energy) migrate into regions of lower potential energy, i.e., the GaAs material (Figure 2.3). These electrons cannot go too far into the GaAs because of their attraction to the ionized Si atoms left behind them. Once the electrons leave their original material, they cannot easily return because the offset between the conduction band edge energy of the two materials acts like a barrier. The electron flow stops once equilibrium is established between the chemical potential in the $Al_xGa_{1-x}As$ and GaAs layers. This is achieved by the band bending created by the transfer of electrons from the donors to the 2DEG. The transferred electrons are free to move in the plane parallel to the interface but not along the direction orthogonal to it, where they are confined.

The transport properties of the heterostructure NU2239 have been determined experimentally by standard Hall bar measurements, and are summarised in Table 2.2 [96]. This sample was chosen for the present work because it represents a standard setup in the sense that the properties of typical high mobility heterojunctions are in the same range.

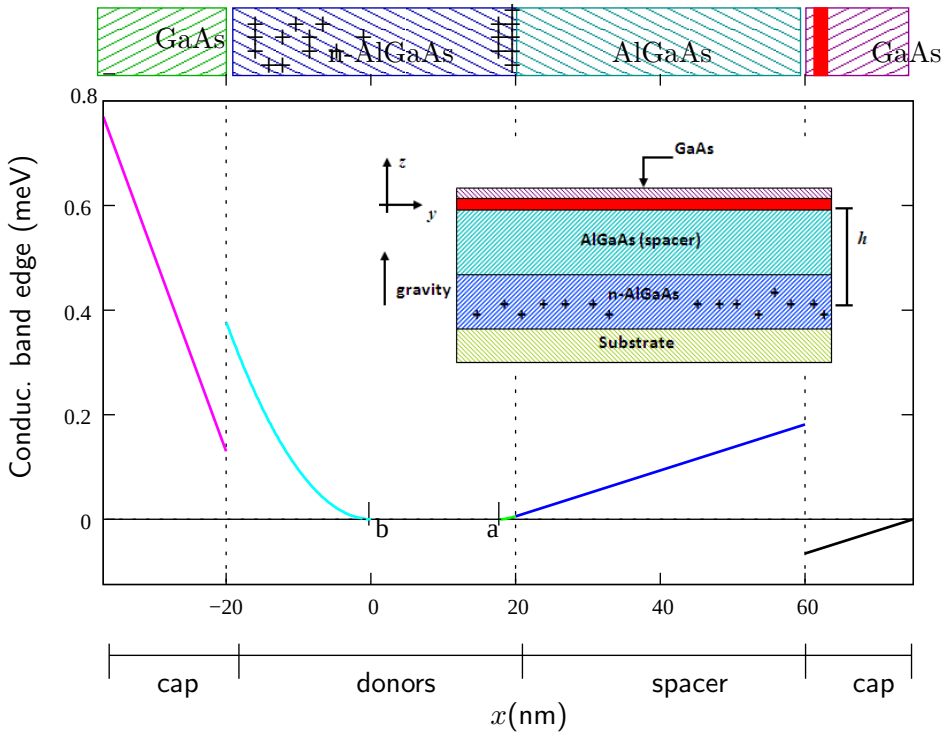

Figure 2.2: Layer structure and conduction band profile calculated for the GaAs-n-AlGaAs-AlGaAs-GaAs heterojunction modelled in this thesis. The 2DEG forms near the right-hand edge of the structure and is indicated by a red rectangle. The inset shows the standard layer diagram of the heterojunction.

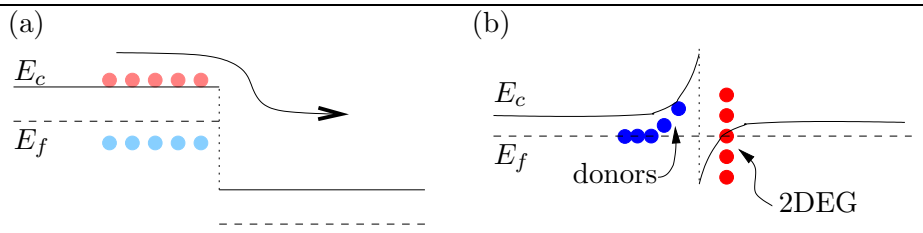

Figure 2.3: Process of formation of a 2DEG. Electrons in the $Al_xGa_{1-x}As$ material with the higher conduction band edge energy migrate to the adjacent GaAs. Flux stops once the equilibrium condition is reached, leaving a thin sheet of electrons (indicated by red filled circles) close to the interfaces and a positively charged region in the material of origin (blue filled circles). The dotted line corresponds to the Fermi level (a) before equilibrium (b) at equilibrium

2.2.1 Limits for the current density in a 2DEG

Typically, heterostructures with a 2DEG embedded can sustain small current densities producing power dissipation of not more than a few 10^6 W/m^2 [99]. An estimate of the maximum current density supported by a 2DEG can therefore be made as follows:

Property	value
Electron density (η_e)	3.3×10^{15} m $^{-2}$
Fermi energy (E_f)	11.79 meV
Fermi wavelength (λ_F)	4.3635×10^{-8} m
Fermi velocity (V_F)	2.49×10^{5} m/s
Scattering time (τ_m)	5.33×10^{-11} s (1.9047×10^{-13} s)
Scattering length (L_m)	13.29×10^{-6} m (4.747×10^{-7} m)
Mobility (μ)	140 $\mathrm{m}^2(\mathrm{Vs})^{-1}$ (0.5 $\mathrm{m}^2(\mathrm{Vs})^{-1}$)
Conductivity (σ)	7.4×10^{-2} Ω^{-1} (2.644×10^{-4} Ω^{-1})
Donor -2DEG distance (h)	500 nm

Table 2.2: Properties of the 2DEG in the NU2239 sample, determined at liquid Helium temperatures. Values in parentheses correspond to room temperature.

it is expected that an electron travelling a distance of the order of the scattering length, L_m, loses an energy equal to a fraction of the Fermi energy $\Delta E = \epsilon E_f, \epsilon \in [0, 1]$. This consideration implies that, to produce a stationary electron flow, the maximum electric field that can be applied is $\Delta E/(eL_m)$, corresponding to a maximum current density of $j_{\max} = \sigma(\epsilon E_F)/(eL_m)$.

Applying this consideration to the NU2239 heterostructure at liquid Helium temperature (see Table 2.2) and assuming $\epsilon = 1/3$, [1] the maximum allowed current density is $j_{\max} = 0.296$ mA/μm, which corresponds to a power density dissipation of $P = 1.2 \times 10^6$ W/m^2 and is comparable with the peak power reported in [99]. For the same sample, this consideration imposes a maximum applied electric field of $|\boldsymbol{E}_{\max}| = 4.0$kV/m (4.0 mV/μm).

For the purposes of this thesis, it is important to establish the operational conditions which allow the largest possible current density to be obtained for a small electric field. The electric current induced by an external electric field is determined by its mobility tensor. For an isotropic 2DEG at the interface of the GaAs/Al$_x$Ga$_{1-x}$As heterostructure, the mobility depends on the temperature and the intensity of the electric field as shown in figure 6.1 [99]. From the data shown in Figure 6.1 (a), we can conclude that by increasing the electric field, the mobility remains constant for samples at room temperature, but falls very fast for cooled systems. Similarly, from Figure 6.1 (b), it can be observed that the mobility at low temperature is much larger than at room temperature. This can be explained by the suppression of e^-–phonon scattering [100] at low temperatures. In conclusion, combining low temperatures and a low electric field $|E| << 1$kV/cm optimises the electrical conductivity of the 2DEG and hence the maximum possible

[1] Meaning that after three momentum relaxation periods, electrons lose an energy equivalent to the 2DEG Fermi energy, E_F.

current flow [99].

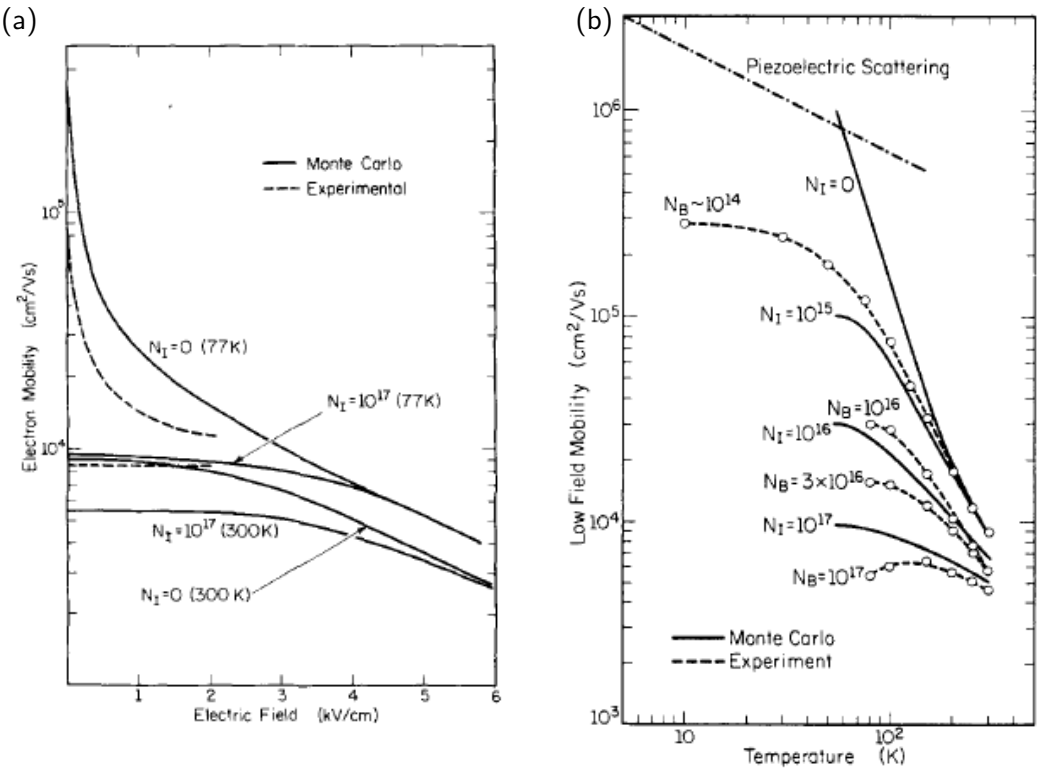

Figure 2.4: (a) Calculated (solid line) and measured (dashed line) electron mobility of a 2DEG as function of electric field for different donor impurity concentrations (N_I) and at room and liquid nitrogen temperatures. (b) Measured electron mobility in a 2DEG at different temperatures (dashed lines). Current versus electric field characteristics were measured in the dark at several temperatures, between 77 K and 300 K. Solid line corresponds to the calculated mobility for bulk GaAs containing different donor impurity concentrations, N_I and 300 K. Taken from reference [99].

2.3 The ionized-donor potential

State of the art technology can produce 2DEGs with mobilities as large as $\mu = 3100$ $m^2s^{-1}V^{-1}$ [101], but typical ones, like in NU2239, are in the range of a few hundred $m^2s^{-1}V^{-1}$ at liquid Helium temperatures and ~ 1 $m^2s^{-1}V^{-1}$ at room temperature. At low temperatures (< 77 K) lattice modes are strongly suppressed and the main electron scattering mechanism corresponds to the interaction of the electrons with their parental ionized donors at the opposite side of the interface. This section presents calculations of the potential landscape experienced by an electron in the 2DEG and the effect that the ionized donors has on the electron distribution and electric current.

Suppose that the ionized donors are distributed randomly in an infinitesimally thin layer positioned at a distance d from the 2DEG plane. Also assume that the number of ionized donors and electrons in the 2DEG coincide. In this case, the length scale and strength of the spatial fluctuations in the donor potential felt by electrons in the 2DEG depends on both the statistical distribution of donors and on the donor-2DEG distance.

If the separation between the 2DEG and the donor layer is large enough and the charge density within these layers is also large, the electrostatic donor potential is effectively screened by the 2DEG. Using a linear screening approximation, the effective (screened) potential that an electron in the 2DEG experiences is given by [102]:

$$\Phi_{\text{screened}}(\boldsymbol{r}) = \frac{e^2}{4\pi\epsilon\epsilon_0}\int e^{-kd}\frac{\eta_d(\boldsymbol{k})e^{i\boldsymbol{k}\cdot\boldsymbol{r}}}{k+k_s}d\boldsymbol{k} \tag{2.2}$$

where $\boldsymbol{r} = (x, y)$ is a position vector in the plane of the 2DEG, $\boldsymbol{k} = (k_x, k_y)$, $k = \sqrt{k_x^2 + k_y^2}$, $\eta_d(\boldsymbol{k})$ is the 2D Fourier Transform of the donor density, $\eta_d(\boldsymbol{r})$, ϵ is the relative permittivity of GaAs and

$$k_s = \frac{e^2 m_e^*}{2\epsilon\epsilon_0\pi\hbar^2} \tag{2.3}$$

is the screening wave vector, with m_e^* the electron effective mass.

Linear screening model applies when the concentration of electrons is large compared with the changes in the concentration brought about by fluctuations in the bare electrostatic potential produced by the ionized donors. This approximation is valid if the relevant values of k in the integral Eq. (2.2) are much smaller than the screening wavelength k_s [102], which is certainly the case for structures with a large spacer layer (d) compared to the screening length of the 2DEG, $\lambda_s = 2\pi/k_s$. For the AlGaAs heterostructure $k_s = 2.1 \times 10^8 \text{m}^{-1}$

Fig. 2.5(a) shows a typical donor density profile calculated assuming a random uncorrelated distribution, characterized by the ensemble average $\langle\eta_d(\boldsymbol{r})\eta_d(\boldsymbol{r'})\rangle = \eta_d^2\delta(\boldsymbol{r}-\boldsymbol{r'})$. This distribution can obtained by positioning N_d donors on a regular array of M cells, defined in a region of total area A. Two independent random generators provide each one of the components of the position for each donor $\boldsymbol{r}_d = (x_d, y_d)$. Once all donors are distributed, the local density is then calculated as the ratio between the number of donors in each cell and its area, A/M. For the calculations presented here, there is no restriction over the number of donors that can be in each cell.

Figure 2.5(b) shows the amplitude of the 2D Fourier transform, $|\Phi_{\text{screened}}(k_x, k_y)|$, of the screened potential. For clarity, a section of this Fourier transform is presented in Figure 2.5(c). Notice the amplitude of $\Phi_{\text{screened}}(0, k_y)$ decays very fast as $k_y \to \infty$, satisfying the condition required to apply Eq. (2.2), i.e., the major contributions to integral Eq. (2.2) correspond to small values of k compared with k_s

The electron density in the 2DEG can be calculated assuming local equilibrium and

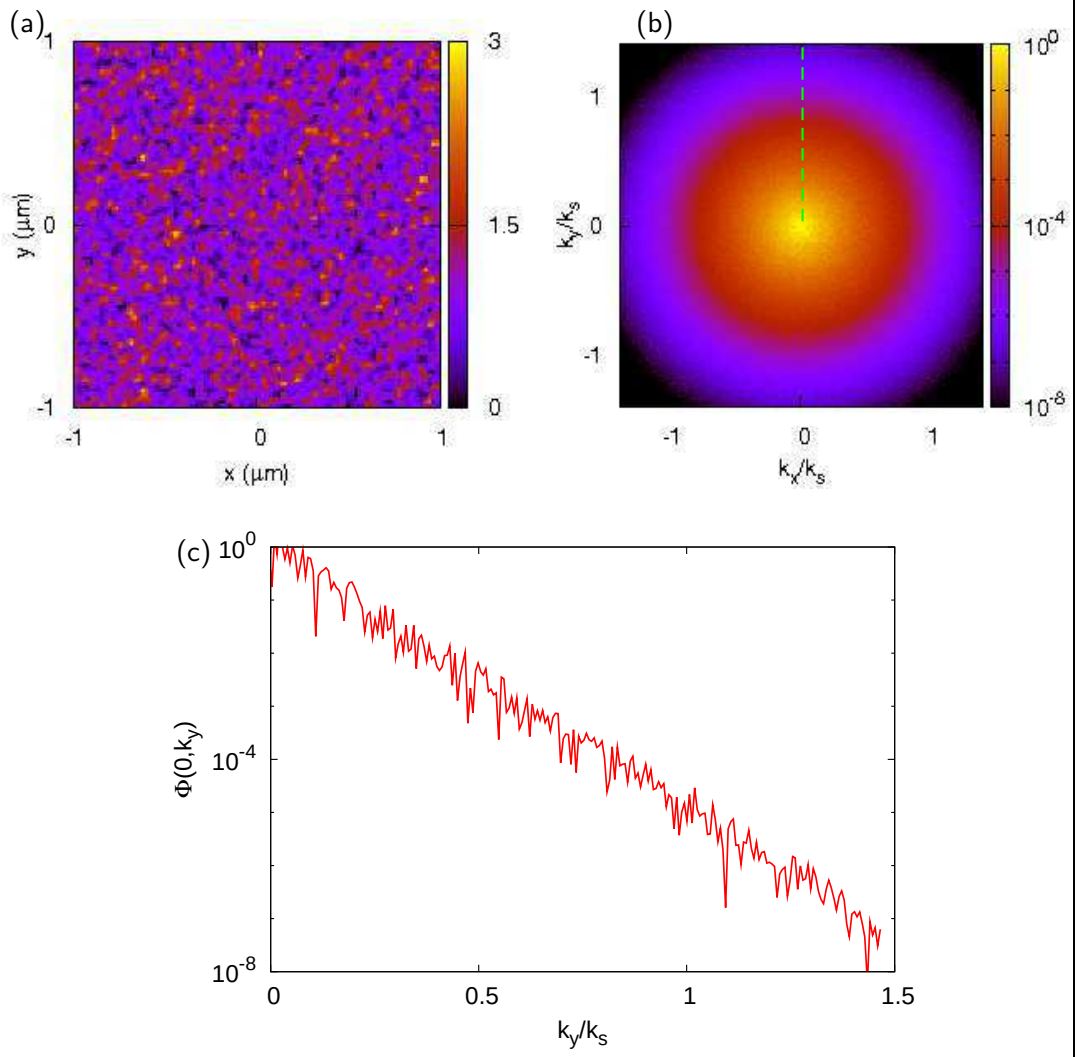

Figure 2.5: (a) Typical donor density profile calculated for the NU2239 heterostructure. The colour scale at the right is in units of 3.3×10^{15}donors/m^2. (b) Amplitude of the 2D Fourier transform of the screened potential, $|\Phi_{\text{screened}}(k_x, k_y)|$, due to the donor distribution shown in (a). Arbitrary units are employed. (c) A section of $\Phi_{\text{screened}}(k_x, k_y)$ along the line $\boldsymbol{k} = (0, k_y)$ (dashed line in panel (b)). The exponential decay constant is given by the 2DEG-donor distance.

using the Thomas-Fermi approximation. Combining these two assumptions results in [102]:

$$\eta_e(\boldsymbol{r}) = \frac{m_e^*}{\pi\hbar^2}(E_f - \Phi_{\text{screened}}(\boldsymbol{r}))\theta(E_F - \Phi_{\text{screened}}(\boldsymbol{r})) \tag{2.4}$$

where $\theta(x)$ is the Heaviside step function, $\Phi(\boldsymbol{r})$ is given by (2.2) and E_f is the Fermi energy of the system (or chemical potential).

If all donors are ionized, the number of electrons in the 2DEG is equal to the number

of donors and the Fermi level in Eq. (2.4) can be evaluated by:

$$N_d = N_e = \int_{\text{Area}} \eta_e(\boldsymbol{r}) d^2\boldsymbol{r} \tag{2.5}$$

The electron density profile in the 2DEG can be calculated for a given distribution of donors by combining Eqs. (2.2), (2.4) and (2.5). Typical results of this model applied to the NU2239 heterojunction are shown in Figures 2.6(a) and 2.6(b).

The randomness of the distribution of the ionized donors affects the density profile of the 2DEG. For the case presented here, the electric potential experienced by an electron in the 2DEG fluctuates on an energy scale $\approx 10\%$ of the Fermi energy. Consequently, η_e is not uniform and exhibits similar percentile inhomogeneity. Finally, the length scale of these spatial fluctuations are of the same order of magnitude as the 2DEG-donor layers separation ~ 0.5 µm. Fluctuations on a shorter length scale are suppressed by the e^{-kd} term in Eq. (2.2)

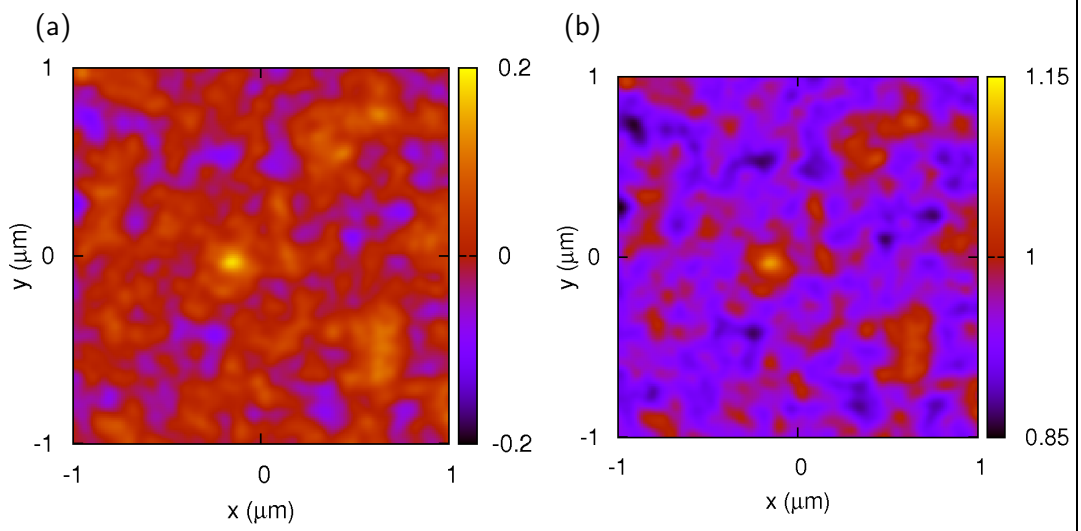

Figure 2.6: (a) Calculated screened potential and (b) electron density, both for a small sample (2×2 µm^2) of the NU2239 heterojunction. The colour scale on the right are 10 mV and 3.3×10^{15} m^{-2} respectively.

The potential energy fluctuations created by the ionized donors affect the trajectory that an electron follows when a uniform electric field is applied to the 2DEG. Instead of moving in a straight line, the electron path is deflected by the valleys and hills of the electrostatic potential. Ignoring boundary conditions defining a finite sample, the current flow then can be described by two contributions:

$$\boldsymbol{j} = \sigma_0 \boldsymbol{E} - \sigma_0 \vec{\nabla} \frac{\Phi_{\text{screened}}(\boldsymbol{r})}{e} \tag{2.6}$$

The first term on the right corresponds to the uniform flow generated by an applied homogenous electric field. The second term corresponds to the current inhomogeneities

created by the potential fluctuations associated with the remote ionized donors. The properties of the inhomogeneous component are determined by the donor distribution, the electron density and the donor-2DEG distance.

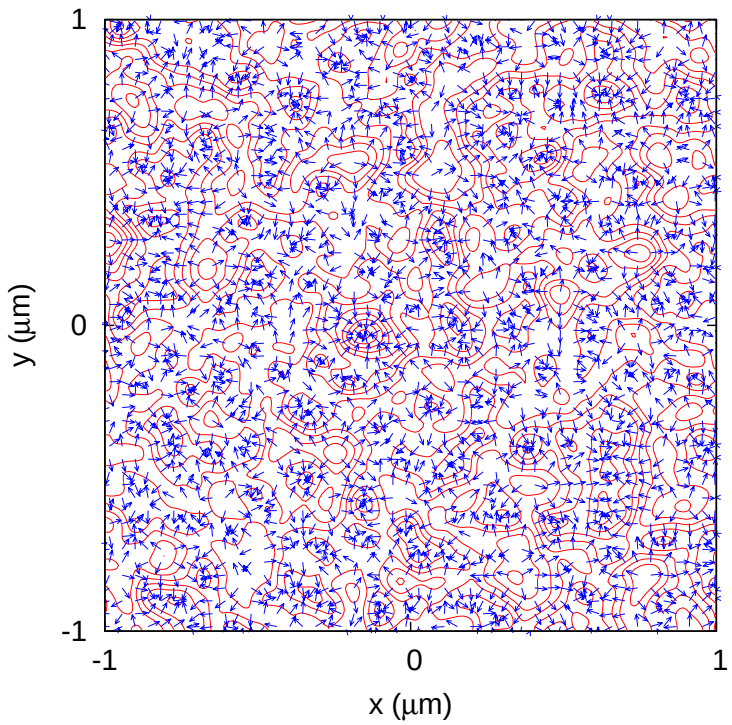

Figure 2.7: Contours of the screened potential, Φ_{screened}, for a 2.0 μm square sample. Contours are 0.25 meV apart. The vector field corresponds to $-\vec{\nabla}\Phi_{\text{screened}}$, which, according to Eq. (2.6), determines the inhomogeneities of the current in the 2DEG.

Near the 2DEG, the magnetic field produced by the current in Eq. (2.6) reflects the properties of the electron gas. This can be quantified by combining Eqs. (2.2 - 2.6) with the Biot-Savart law. The impact of this inhomogeneous current on the the magnetic field profile close the 2DEG is explored in Chapters 4 and 5.

2.4 Summary

Materials with different band structures can be combined to create a low dimensional electron gas near one of the interfaces, whose density is determined by equilibration of the chemical potential, and can be manipulated by externally applied fields. In the case of the GaAs/AlGaAs heterojunction, a 2DEG appears next to the interface on the GaAs side. The current flow in such a 2DEG is limited by energy dissipation considerations, and typically cannot exceed $j_{\max} = 0.295$ A/m^2.

In the model presented here, the electric transport properties of the 2DEG are de-

termined by the distribution of ionized donors, the distance between the donor and the 2DEG layers, and the density of electrons. The presence of the parental ionized donors affects the trajectory of electrons in the 2DEG, making them deviate from ideal straight paths, as quantified by combining Eqs. (2.2) and (2.6).

The non-uniform electron flow in a 2DEG creates an equally inhomogeneous magnetic field, whose characteristics reflect the properties of the heterojunction. This magnetic field is the quantity of interest in subsequent Chapters in this thesis.

CHAPTER 3

Simple setups for magnetic microtrapping

The coupling of the dipole moments of an atom with external fields can be used to confine slow atoms into regions of inhomogeneous magnetic and/or electric fields. Assuming that the atomic moment can be selected by shining laser light tuned to the right frequency, the task of designing a trap reduces to finding an appropriate distribution of sources of electric and/or magnetic fields.

Quantum degenerate gases can be produced by trapping neutral atoms through the interaction between their intrinsic magnetic moment and external inhomogeneous magnetic fields. At the beginning of this century, several groups implemented magnetic microtraps for ultra-cold alkali atoms, recently reviewed in [26, 50], establishing the nowadays standard setup for microtrapping: the atom chip. It combines the inhomogeneous magnetic field produced by current-carrying wires or permanent magnets microfabricated on a substrate, with magnetic fields and laser light produced by external sources.

Due to the vector nature of the magnetic field, although the Biot-Savart law is well known, designing a magnetic trap is not a trivial matter and, apart from using a purely numerical approach, several analytic methods have been developed for this purpose [103, 104]. Depending on the complexity of the required system, and its intended task, determining an appropriate grid of current carrying elements and/or permanent ferromagnets, easily can become a computationally heavy task.

This chapter contains general definitions and summarizes the relevant aspects of trapping configurations needed for the work presented in Chapters 4 and 5. Definitions of relevant trapping characteristics are presented in Section 3.1. Effects associated with the finite size of the current elements are explained in Section 3.2. Finally, the trapping

properties of setups relevant in this thesis, are described in Sections 3.3, 3.4 and 3.5.

3.1 Magnetic traps on a chip: The atom chip

In section 1.2 we show that the potential energy of a slow atom in an inhomogeneous magnetic field depends on its magnetic moment and the intensity of the magnetic field so that:

$$V(\boldsymbol{r}) = m_F g_F \mu_B |\boldsymbol{B}(\boldsymbol{r})| \tag{3.1}$$

Atomic states with $m_F g_F > 0$ are attracted towards regions of low magnetic field. The strength of the attraction and subsequent trapping depends on the gradient of the magnetic field, which is determined by the shape and intensity of the sources.

An *atom chip* is a circuit-shaped array of current carrying miniaturized conductors, whose magnetic field is used to trap and manipulate ultra-cold atoms[1]. These setups can be designed to produce magnetic profiles with almost arbitrary geometry on the micrometre scale, which can be made time-dependent by controlling the current over different sections of the array.

The atom chip configuration enables fast manipulation of trapped atomic clouds, currently at the milli-second scale, due to the tight confining potentials they provide. Also, atom chips are suitable for incorporating devices to control and register the trapped atomic clouds, thus allowing complex tasks to be performed like precise control of atom position, transporting the trapped particles and splitting and merging of atomic clouds. Some of these tasks were briefly mentioned in Section 1.3. Other applications, currently under development, include studies of low dimensional quantum gases, disordered systems, quantum information processing, matter-wave dynamics, precision sensors (force, magnetic and gravitational fields, accelerometers), amongst others (see [26]).

Practical limitations relating to material properties and fabrication techniques should be taken into account to design a magnetic microtrap. For example, melting the wires should be avoided by limiting the current density to a maximum value, $j_{\max}$, determined by the thermal coupling between the conductor and the environment. This restriction affects the achievable strength of the trap since the intensity of the magnetic field is proportional to the current in the wires. On the fabrication side, limits on the resolution and size of the defined structures affect the shape of the trap. These limitations have not, however, prevented the creation of flexible setups using combinations of current-carrying wires.

Two effects limit the operational distance between the chip surface and the trapped atoms to about 1 μm, adding difficulty to the development of advanced applications,

[1] They can also include micrometre permanent ferromagnets as sources of magnetic field and other devices used to register/modify the atomic behaviour.

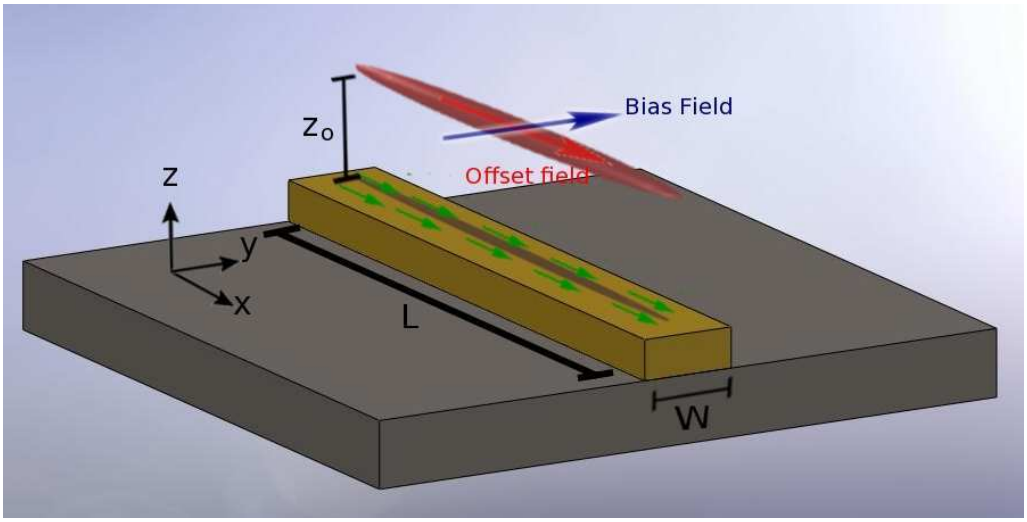

Figure 3.1: Sketch of the basic building block of an atom chip microtrap. A current carrying wire (current flow direction indicated by green arrow) produces a magnetic field which is combined with two other magnetic fields: a compensating bias field (blue arrow) orthogonal to the current flow and an offset field (red arrow) parallel to it. The x axis is oriented along the current flow in the trapping wire. The bias field is the component of the external magnetic field used to compensate the magnetic field created by the central wire. The offset field produces a global shift of the potential energy and is also oriented along the x axis. The bias field cancels the wire's magnetic field above the wire, at z_0. L and W are the length and width for the wire, respectively. The red bubble indicates a cloud of trapped atoms.

in particular creating strong confinement. First, thermal fluctuations of the field near the chip surface and its components (see Chapter 4) induce losses of atoms due to transitions to untrapped states with $m_F g_F < 0$. Proposals to reduce the amplitude of such fluctuations includes the use of alloys [86], conductors with anisotropic conductivity [87] and superconductors [92]. The second effect originates from the inevitable attraction force between any surface and a nearby atom. At distances $\lesssim 5$ µm from the surface, the Casimir-Polder surface-atom attraction has a strong impact in the trapping potential, causing many atoms to escape from the part of the trap nearest to the surface [29].

Figure 3.1 shows a sketch of the atom chip fundamental building block and conventions for the coordinate system, the bias and offset field, used in this thesis. A current carrying micron-sized wire deposited on a substrate produces a magnetic field, which, when compensated by the bias field, creates a magnetic trap located above the wire itself, at a distance z_0.

3.1.1 Depth, gradient and frequency of a magnetic trap

The ionisation threshold of an atom and the work function of a metal are two parameters that indicate how strongly an electron is trapped in those physical systems. In the context of trapped cold atoms, the trapping properties refer to a set of parameters (depth, gradient and frequency) that indicate how strongly a particle is confined into a spatial region of inhomogeneous magnetic field.

These parameters determine the degree of stability of the trap with respect to processes that can kick particles out of the trapping region. The relative importance of such processes can be established by comparing the atom's intrinsic energy and time scales with those of the trapping potential[2].

Although definitions of trapping properties can be done for arbitrary configurations [50], here the discussion is restricted to traps made by combining the magnetic field produced by several parallel current carrying wires, with homogenous externally applied magnetic fields, as shown in Figure 3.1.

The magnetic field in these kinds of traps can be decomposed as:

$$\boldsymbol{B} = (B_{\text{offset}}, \boldsymbol{B}_{\perp}) \tag{3.2}$$

where B_{offset} is a homogenous component of the magnetic field, which is orthogonal to the 2D vector $\boldsymbol{B}_{\perp}$, defined in the $y-z$ plane shown in the Figure 3.1.

Combining Eqs. (3.1) and (3.2), the potential energy becomes:

$$V = m_F g_F \mu_B (B_{\text{offset}}^2 + |\boldsymbol{B}_{\perp}|^2)^{1/2} \tag{3.3}$$

The trap position, $\boldsymbol{r}_0 = (x_0, y_0, z_0)$, is defined as the place where the transverse components of the magnetic field become zero, i.e. $\boldsymbol{B}_{\perp} = 0$. As shown in Chapter 1, near $\boldsymbol{r}_0$, the magnetic field can be approximated by $\boldsymbol{B}_{\perp} \sim (\alpha(z - z_0), \alpha(y - y_0))$ and therefore the potential energy Eq. (3.3) exhibit an approximate cylindrical symmetry.

The magnetic trap can be characterized by studying the potential energy, Eq. (3.3), along a line orthogonal to the chip plane and passing through the trap position $\boldsymbol{r}_0$. Figure 3.2 shows a typical potential energy curve along such a line, corresponding to the z direction in Figure 3.1. The red and green curves correspond to the potential energy when $B_{\text{offset}} = 0$ and $B_{\text{offset}} \neq 0$, respectively.

Figure 3.2 motivates the definition of three parameters to describe the trap produced by a setup like the one in Figure 3.1. The rate of transitions to untrapped states is determined by the strength of the trap, expressed in terms of the gradient of magnetic

[2] The quality of an atom chip operation is then characterized by the rates of atom loss, heating and decoherence. In this thesis, only properties related with the first aspect are discussed. These rates depend on the distance from the atom chip's surface (trap height) and on the strength of the trapping.

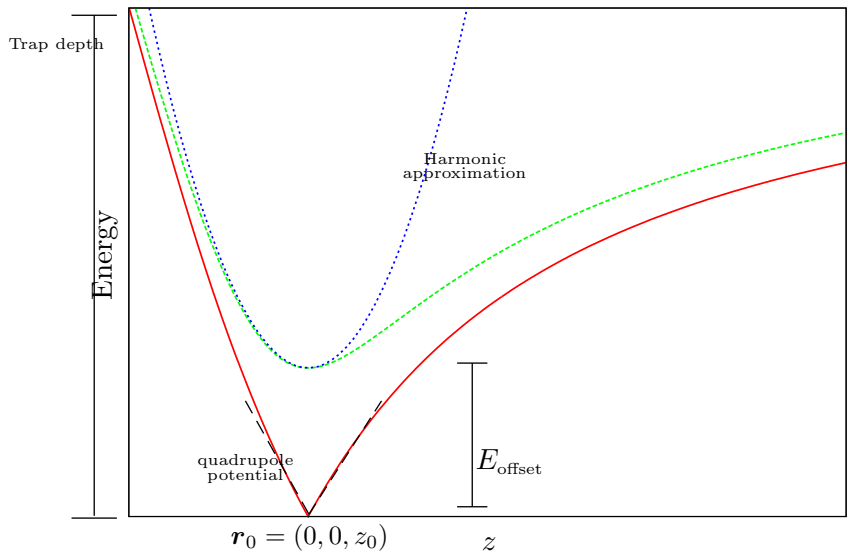

Figure 3.2: Definition of the trapping properties considering the potential energy along the z axis in Figure 3.1. Red and green lines show the potential energy without and with offset magnetic field, respectively. The black and blue lines approximate the field profiles near the minimum at $\boldsymbol{r}_0 = (0, 0, z_0)$, for the same cases. Note the chip surface is at $z = 0$.

field at the trap position. The definitions of these parameters are given below, along with a short discussion of typical values they have in actual atom chips.

1. **Depth**

   The trap depth is the energy difference between the bottom of the trapping potential and its maximum inside the region of interest.

   $$\Delta V = m_F g_F \mu_B (|\boldsymbol{B}_{\max}| - |\boldsymbol{B}_{\min}|) \tag{3.4}$$

   Atoms near a surface can collapse against it due to the Casimir-Polder atom-surface attraction [26], and the trapping potential Eq. (3.3) should, therefore, provide a barrier large enough to counteract such attraction and effectively avoid the tunnelling of the atoms towards the chip surface.

   This potential barrier is given by the difference of potential energy at the trap position $\boldsymbol{r}_0 = (0, 0, z_0)$ and at the chip surface $\boldsymbol{r} = (0, 0, 0)$, as shown in Figure 3.2. This is the definition of trap depth adopted in this thesis.

   In general, a small rate of atom losses due to thermal motion requires a large ΔV compared with the thermal energy $k_B T$. Typically, microtrap setups have a depth of a few μK, restricting the trapping possibilities to such low temperature atoms.

2. **Gradient (or Restoring force)**

   If the chip is oriented with the z axis parallel to the gravitational field, as is usually the case, the force associated with the potential energy Eq. (3.1) should counteract the weight of the atom:

$$-g_F \mu_B m_F \frac{d}{dz}|\boldsymbol{B}| > mg \tag{3.5}$$

   In particular, when the magnetic field near the trap position has an approximate quadrupole distribution (Eq. 1.36), the potential energy along the z axis becomes:

$$V(0,0,z) = g_F \mu_B m_F |\alpha(z - z_0)| \tag{3.6}$$

   and condition Eq. (3.5) gives:

$$-g_F \mu_B m_F \alpha > mg \tag{3.7}$$

   To have an idea of the order of the magnitude involved in this condition, note that the gravitational force on a ^{87}Rb atom is $\sim 10^{-24}$N which can be compensated by a magnetic field gradient of ~ 15 Gauss/cm.

   If near the bottom of the trap the potential energy is approximated by a harmonic potential, the gravitational attraction on the atoms causes a displacement of the trap position.

3. **Trap frequency**

   According to Eq. (3.3), the offset magnetic field affects the potential energy in a non-linear way, and has two different effects on the trap. First, the magnetic field at the trap centre becomes non-zero, fixing a quantization axis for the projection of the atomic angular momentum. Second, the potential energy around the equilibrium position, z_0, can be approximated by a harmonic potential:

$$V(y,z) = \frac{m\omega_y^2}{2} y^2 + \frac{m\omega_z^2}{2}(z - z_0)^2 + |m_F g_F \mu_B B_{\text{offset}}| \tag{3.8}$$

   where m is the atomic mass and the frequencies are given by:

$$\omega_{y,z}^2 = \frac{m_F g_F \mu_B}{m} \frac{1}{B_{\text{offset}}} \left(\partial_{y,z}|\boldsymbol{B}_\perp|\right)^2\Big|_{\boldsymbol{r}_0} \tag{3.9}$$

   When the magnetic field $\boldsymbol{B}_\perp$ behaves like a quadrupole field, the trap frequencies Eq. (3.9) simplifies to:

$$\omega_z^2 = \omega_y^2 = \frac{m_F g_F \mu_B}{m} \frac{1}{B_{\text{offset}}} \alpha^2 \tag{3.10}$$

   Note that when $B_{\text{offset}} = 0$, these frequencies diverge. This is expected because in this limit the harmonic trap transforms into a quadrupole trap, and the potential

energy, instead of having quadratic dependence, varies linearly with distance from the trap centre.

The frequencies $\omega_{y,z}$ are good indicators of the strength of the trap. Trapping potentials with elongated geometry are very common. They have large frequencies ($\sim$kHz) in two spatial directions and a small frequency ($\sim$Hz) along the remaining direction.

4. **Majorana losses**

   The atomic translation motion in the trapping region can induce spin flips, thereby driving the atom to a high-field seeking state. Such processes are known as Majorana spin flips and are due to the loss of the adiabaticity of the motion in the trapping potential.

   The probability of such transitions is small if, in the atom's reference frame, the direction of the magnetic field changes slowly enough for the spin to follow adiabatically the local field direction. The rate of Majorana flips of a single atom in a harmonic trap is given by [26, 105]:

$$\Gamma_{MF} = \frac{\pi}{2\sqrt{e}}\omega \exp\left(-\frac{\hat{\omega}^3}{\omega^3}\right) \tag{3.11}$$

   where ω is the trapping frequency and $\hat{\omega}$ is a critical frequency defined by:

$$\hat{\omega} = \left[\frac{(m_F g_F \mu_B)^2 (\partial_z |\boldsymbol{B}_\perp||_{\boldsymbol{r}_0})^2}{\hbar m}\right]^{1/3} \tag{3.12}$$

   where $\partial_z |\boldsymbol{B}_\perp||_{\boldsymbol{r}_0}$ is the magnetic field gradient at the centre of the trap when the offset field is absent.

   A low rate of spin flips occurs if $\omega \gg \hat{\omega}$. Using Eq. (3.10), this condition imposes the following lower bound on the offset field:

$$\left|\boldsymbol{B}_{\text{offset}}^{\min}\right| = \left[\frac{\hbar m^{1/3}}{(m_F g_F \mu_B)^{1/2}}\, \partial_z B_y|_{\boldsymbol{r}_0}\right]^{2/3} \tag{3.13}$$

   In typical experiments, the value of the offset field is a few tens of Gauss, and in most situations this is enough to satisfy Eq. (3.13) [26].

According to the previous definitions, the key quantity to characterize the trap strength is the gradient of the magnetic field, $\partial_{x_i} |\boldsymbol{B}_\perp||_{\boldsymbol{r}_0}$, with $x_i = x, y, z$

3.2 Magnetic field of a planar wire

By definition, low field seeker states are attracted towards regions of low magnetic field (see Section 1.2) and the equilibrium point in the potential energy coincides with the position where the magnetic field is minimum. As seen in Chapter 1, a magnetic field distribution with a localized minimum can be produced by superposing the magnetic field due to a single current carrying ideal wire with a homogeneous magnetic field transverse to the current flow.

Real-life conductors have a finite cross section and length. When the distance to the magnetic field sources is comparable to, or less than, any of its dimensions, the magnetic field distribution is affected by the finite size of the conductors. This situation is common in the microtrapping context, where the atom-conductor distance and the dimensions of the conductors are both in the range $1 - 100$ μm. In this section, planar geometry is considered (Figure 3.3), since it is a good approximation to wires of rectangular cross section with small height/width ratios.

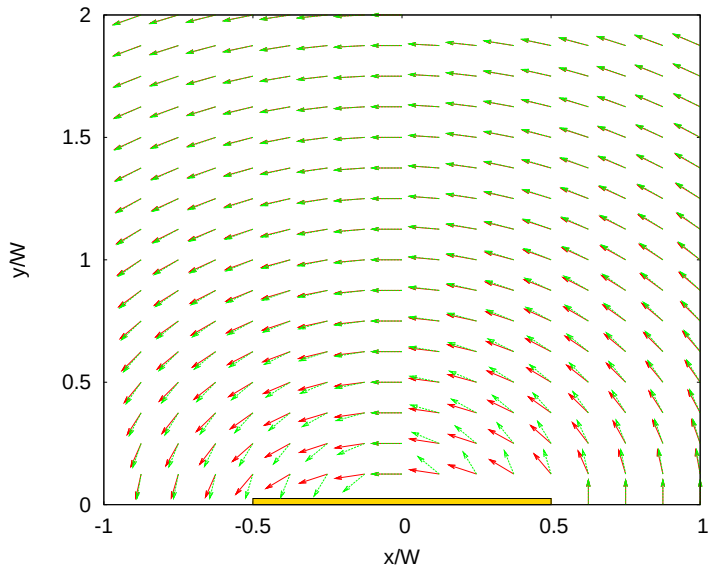

Figure 3.3: Comparison between the magnetic field produced by a planar conductor (conductor in yellow, field shown by red arrows) and the magnetic field corresponding to current through an ideal wire located at the origin (green arrows). Notice that these fields differ mainly near the conductor and rapidly become indistinguishable as the distance from the conductor increases. Length is scaled to the width of the wire, W.

In this case, the Biot-Savart law is restricted to an integration over a rectangular planar region:

$$\vec{B}(\boldsymbol{r}) = \frac{\mu_0}{4\pi} \int_{-\frac{W}{2}}^{\frac{W}{2}} \int_{-\frac{L}{2}}^{\frac{L}{2}} \frac{\boldsymbol{j}(\boldsymbol{r'}) \times (\boldsymbol{r} - \boldsymbol{r'})}{|\boldsymbol{r} - \boldsymbol{r'}|^3} d^2\boldsymbol{r'} \tag{3.14}$$

where $\boldsymbol{j}$ is the current density distribution, $\boldsymbol{r'}$ is a vector position in the plane of the conductor and $\boldsymbol{r}$ is a vector position in 3D space. L, W and the axes orientation are defined in Figure 3.1. If the current flows along the x-axis, the integral Eq. (3.14) gives us:

$$B_y = \frac{\mu_0 j}{4\pi}\left\{\arctan\left(\frac{[x+x_0][y+y_0]}{z[(x+x_0)^2+(y+y_0)^2+z^2]^{1/2}}\right)\right\}\Bigg|_{(x_0,y_0)=(L/2,-W/2),(-L/2,W/2)}^{(x_0,y_0)=(-L/2,W/2),(L/2,-W/2)} \tag{3.15}$$

$$B_z = \frac{\mu_0 j}{4\pi}\log\left([x+x_0]+[(x+x_0)^2+(y+y_0)^2+z^2]^{1/2}\right)\Bigg|_{(x_0,y_0)=(L/2,W/2),(-L/2,-W/2)}^{(x_0,y_0)=(L/2,-W/2),(-L/2,W/2)} \tag{3.16}$$

where the notation $f(x)|_{(x=c,d)}^{(x=a,b)}$ is shorthand for $f(a)+f(b)-f(c)-f(d)$.

In the limit of an infinitely long wire ($L\to\infty$), this reduces to:

$$\begin{aligned} B_y &= \frac{\mu_0 j}{2\pi}\left\{\arctan\left(\frac{[y+W/2]}{z}\right)-\arctan\left(\frac{[y-W/2]}{z}\right)\right\} \\ B_z &= \frac{\mu_0 j}{4\pi}\log\left(\frac{[y+W/2]^2+z^2}{[y-W/2]^2+z^2}\right) \end{aligned} \tag{3.18}$$

Several features differ from the magnetic field produced by an ideal wire (infinitely long and infinitesimally thin). In the former case, the magnetic field does not diverge at any position in the space. It reaches a maximum on the plane of the conductor ($z=0$), equal to the uniform magnetic field generated by an infinite plane with the same current density $B_s=\mu_0 j/2$. In addition, the magnetic field decreases at a lower rate up to distances of about $2W$, and at larger distances the magnetic field produced by the plane converges to that generated by a thin wire. Finally, at the conductor surface ($z=0$), the gradient of the magnetic field has a finite value, in contrast to the case of an ideal wire where it is also divergent. All these characteristics are shown in Figure 3.4. Notice that the finite value of both the gradient and the magnetic field limits the achievable trap depth of a setup like that in Figure 3.1.

Eq. (3.18) indicates that the intensity of the magnetic field is proportional to the product $B_s=\mu_0 j/2$ and the length scale of its variations is fixed by the wire's width W. In what follows, unless otherwise indicated, reduced units for the magnetic field $\tilde{B}=B/B_s$, length $\tilde{x}=x/W$, and energy $\tilde{E}=E/E_0$ with $E_0=g_F\mu_B m_F B_s$ are used. Table 3.1 summarizes these definitions along with typical values of this parameters.

Using this scaling, Eqs. (3.18) results in:

$$\begin{aligned} \tilde{B}_y &= \frac{1}{\pi}\left\{\arctan\left(\frac{[\tilde{y}+1/2]}{\tilde{z}}\right)-\arctan\left(\frac{[\tilde{y}-1/2]}{\tilde{z}}\right)\right\} \\ \tilde{B}_z &= \frac{1}{2\pi}\log\left(\frac{[\tilde{y}+1/2]^2+\tilde{z}^2}{[\tilde{y}-1/2]^2+\tilde{z}^2}\right) \end{aligned} \tag{3.19}$$

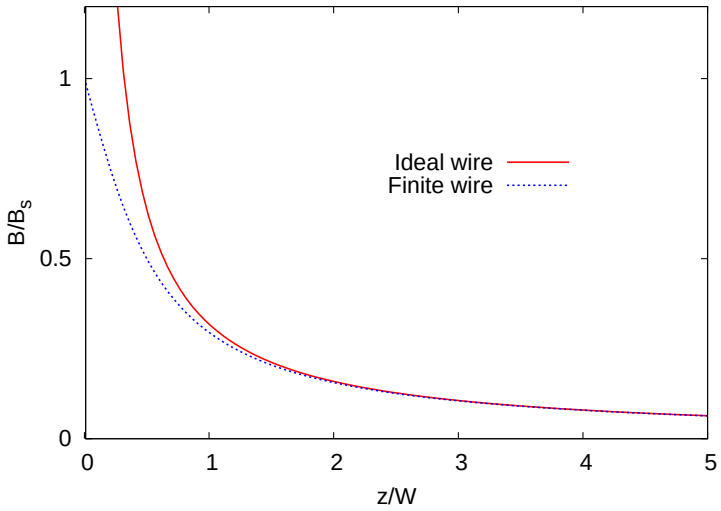

Figure 3.4: Comparison between the magnetic field of an ideal thin wire (solid, red) and a wide wire (dotted, blue). Notice that at $z = 0$, the magnetic field corresponding to the wide wire has an non-zero value and gradient.

Dimension	scale	Typical Value
Length Scale	W	1 μm
Magnetic field at surface	$B_s = \mu_0 j/2$	1 G
Energy scale	$E_0 = g_F \mu_B m_F B_s$	10 μK
Frequency Scale	$\omega_0 = (\frac{\lvert\boldsymbol{\mu}\rvert B_s}{\pi^2 m W^2})^{1/2}$	$2\pi \times$ 1KHz
Gradient Scale	B_s/W	10 Gauss/cm

Table 3.1: Definition of the scaling factors.

and the potential energy Eq. (3.1) becomes:

$$\begin{aligned} \tilde{V}(\tilde{y},\tilde{z}) &= |\tilde{\boldsymbol{B}}| \\ &= (\tilde{B}_x^2 + \tilde{B}_y^2 + \tilde{B}_z^2)^{1/2} \end{aligned} \tag{3.20}$$

If the magnetic field can be split as in Eq. (3.2), the potential energy can be written as:

$$\tilde{V}(\tilde{y},\tilde{z}) = (\tilde{B}_{\text{offset}}^2 + |\tilde{\boldsymbol{B}}_\perp|^2)^{1/2} \tag{3.21}$$

Finally, the trap properties previously defined transform to:

- **Depth**

$$\tilde{V}_{\max} - \tilde{V}_{\min} = (|\tilde{\boldsymbol{B}}_{\max}| - |\tilde{\boldsymbol{B}}_{\min}|) \gg k_B T/E_0 \tag{3.22}$$

- **Gradient**

$$-\frac{d}{d\tilde{z}}|\tilde{\boldsymbol{B}}| > \frac{mgW}{E_0} \tag{3.23}$$

- **Frequency**

$$\tilde{\omega}^2_{\tilde{y},\tilde{z}} = \frac{1}{\tilde{B}_{\text{offset}}} \left(\partial_{\tilde{y},\tilde{z}} \tilde{B}_{\tilde{z},\tilde{y}}\right)^2 \Big|_{\tilde{\boldsymbol{r}}_0} \tag{3.24}$$

- **Majorana flips (Lower bound for the offset field)**

$$\left|\tilde{\boldsymbol{B}}^{\min}_{\text{offset}}\right| = \left(\frac{\hbar\omega_0}{\pi^2 m W^2}\right)^{2/3} \left(\partial_{\tilde{z}} \tilde{B}_y\right)^{4/3} \Big|_{\tilde{\boldsymbol{r}}_0} \tag{3.25}$$

These definitions are now applied to different trapping setups.

3.3 Case 1: Magnetic trap using a single wire plus external field

Figures 3.1 shows the sketch of the simplest possible magnetic micro-trapping setup. A current conductor is placed in a homogenous bias magnetic field, resulting in a line of vanishing magnetic field. This forms a quadrupole trap for paramagnetic atoms ($g_F m_F > 0$). The addition of an offset field ($\tilde{B}_{\text{offset}}$), transforms the quadrupole trap into an Ioffe trap, with a non-zero magnetic field along the trap axis and a spatial profile that is well approximated by a quadratic potential near the trap axis.

Assuming the coordinate system in Figure 3.1 and applying Eq. (3.19), the total magnetic field is:

$$\tilde{B}_x = \tilde{B}_{\text{offset}} \tag{3.26}$$

$$\tilde{B}_y = \tilde{B}_{\text{bias}} + \frac{1}{\pi}\left\{\arctan\left(\frac{[\tilde{y}+1/2]}{\tilde{z}}\right) - \arctan\left(\frac{[\tilde{y}-1/2]}{\tilde{z}}\right)\right\} \tag{3.27}$$

$$\tilde{B}_z = \frac{1}{2\pi}\log\left(\frac{[\tilde{y}+1/2]^2+\tilde{z}^2}{[\tilde{y}-1/2]^2+\tilde{z}^2}\right) \tag{3.28}$$

Note that the magnetic field can be split as in Eq. (3.2)

In absence of the offset field, there is a line of zero magnetic field at $\tilde{z}_0$ satisfying:

$$\tilde{z}_0 = \frac{1}{2}\tan\left(\frac{2}{\pi \tilde{B}_{\text{bias}}}\right) \tag{3.29}$$

The potential energy of an atom in this magnetic field can be evaluated by combining Eq. (3.26)-(3.28) with Eq. (3.21). A qualitative description of the trap produced can be made using the isoenergy curves, the magnetic field variation and the potential energy curves along different directions as shown in Figure 3.5. The parameters in this figure have been adjusted to create a trap near $\tilde{z}_0 = 1$.

In this figure, the isopotential curves indicate the presence of a local minimum along the z axis. The trap strength, estimated by the distance between different contours, depends on the spatial direction, indicating that the cylindrical symmetry is only approximate due to the wire's finite width.

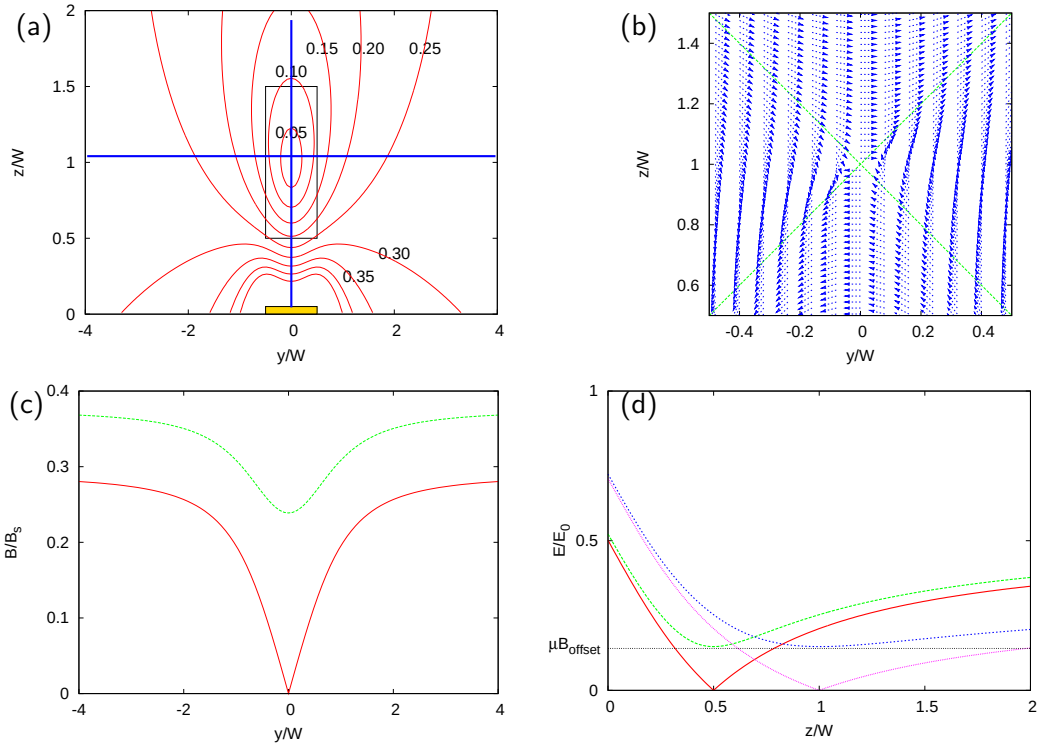

Figure 3.5: (a) Energy contours for the trapping configuration shown in Figure 3.1 (single wire plus external fields with $B_{\text{offset}} = 0$). The conductor slab is schematically shown in yellow. Energy contours are equally spaced by $0.05E_0$ as indicated. The bias field was set to produce a minimum of potential energy at $y/W \sim 1$. (b) Magnetic field near the position of the trap ($y/W \sim 1$, enclosed region in panel (a)). Note that along the ideal quadrupole axis (green lines), the field is nearly parallel to them, demonstrating that the magnetic field distribution is well approximated by a quadrupole field. (c) Potential energy along the y axis (horizontal blue line in panel (a)) with and without an offset field (red and green line, respectively). Notice that in the former case, the minimum and the curvature of the potential are non-zero at $y = 0$. (d) Potential energy along the z axis (vertical blue line in panel (a)), for two bias fields set to produce a trap at $z/W \sim 1$ and $z/W \sim 0.5$, and with or without an offset field (red/green and blue/magenta lines).

Figure 3.5(b) shows the magnetic field distribution near the trap position. Observe that $\tilde{\boldsymbol{B}}_\perp$ (arrows) are almost aligned with the ideal quadrupole axes (green lines), indicating that it can be approximated by a quadrupole distribution $\tilde{\boldsymbol{B}}_\perp \sim \tilde{\alpha}(\tilde{z} - \tilde{z}_0, \tilde{y} - \tilde{y}_0)$.

The presence of an offset field does not modify the previous statements. Its effects on the trap can be seen in Figure 3.5(c)-(d), where the energy along the $\tilde{y}$ axis, centred on the trap position $\tilde{z}_0$, and along the $\tilde{z}$ axis are shown. The offset field modifies the energy curve and the original quadrupole potential is rounded off near $\tilde{z}_0$.

The previous statements can be quantified, according to the definitions given in the previous section, as follows:

1. **Depth**

   The trap depth, defined as the difference between the potential at the centre of the wire $\tilde{\boldsymbol{r}} = (0,0,0)$ and the trap position, $\tilde{\boldsymbol{r}}_0 = (0,0,\tilde{z}_0)$, is obtained by applying Eqs. (3.26)-(3.28) to Eq. (3.20):

$$\begin{aligned} \Delta\tilde{V} &= |\tilde{\boldsymbol{B}}(0,0,0)| - |\tilde{\boldsymbol{B}}(0,0,\tilde{z}_0)| \\ &= (1 - \tilde{B}^2_{\text{Bias}} + \tilde{B}^2_{\text{offset}})^{1/2} - \tilde{B}_{\text{offset}} \end{aligned} \tag{3.30}$$

   The position of the trap depends on the bias field through Eq. (3.29), which, combined with (Eq. (3.30)), gives:

$$\Delta\tilde{V} = \left(1 - \frac{4}{\pi^2}\arctan^2\left(\frac{1}{2\tilde{z}_0}\right)^2 + \tilde{B}^2_{\text{offset}}\right)^{1/2} - \tilde{B}_{\text{offset}} \tag{3.31}$$

   Figure 3.6 shows the trap depth for different trapping positions. Compared with the quadrupole trap, the potential barrier at the wire surface ($\tilde{z} = 0$) is reduced by the presence of the offset field.

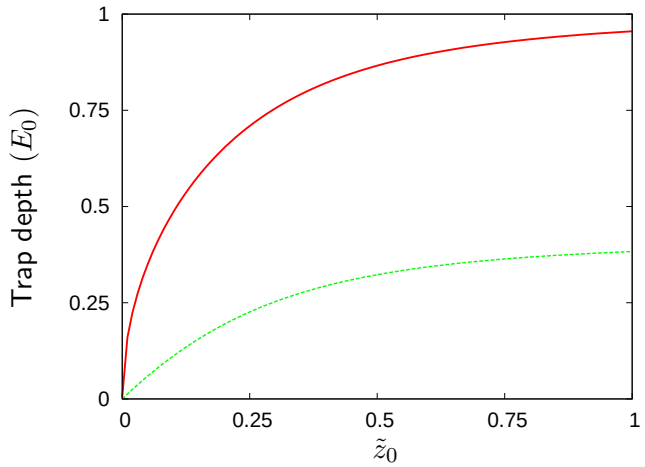

Figure 3.6: Trap depth as a function of its position. The solid (red) curve corresponds to the depth when $\tilde{B}_{\text{offset}} = 0$. Turning on the offset field reduces the trap depth, as indicated the dotted (green) curve.

2. **Gradient:**

   Using Eqs. (3.26)-(3.28) and (3.20), the potential energy along the z axis is:

$$\tilde{V}(\tilde{z}) = \left(\tilde{B}^2_{\text{offset}} + (\tilde{B}_{\text{Bias}} + \frac{2}{\pi}\arctan^2(1/2\tilde{z}))\right)^{1/2} \tag{3.32}$$

and its gradient at the trap position $\tilde{z}_0$ is:

$$\frac{d}{dz}\tilde{V}(\tilde{z})\bigg|_{\tilde{z}_0} = \frac{1}{\pi}\left[\tilde{z}_0^2 + \frac{1}{4}\right]^{-1} \tag{3.33}$$

As shown in Figure 3.7, the gradient has a Lorentzian dependence with respect to the trap position, which saturates as the trap position approaches the wire's plane ($\tilde{z}_0 = 0$) [26].

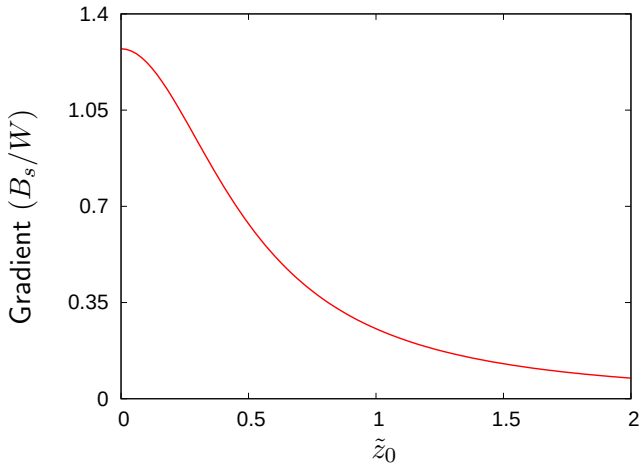

Figure 3.7: The gradient of the potential energy as function of the trap position.

3. **Curvature and trap frequency**

   Substituting Eq. (3.33) into Eq. (3.9), the frequency of the trap obtained by applying an offset field is given by:

$$\tilde{\omega}_z = \left(\frac{1}{\tilde{B}_{\text{offset}}}\right)^{1/2}\left[\tilde{z}_0^2 + \frac{1}{4}\right]^{-1} \tag{3.34}$$

   It has the same dependence as the gradient. High frequencies are reached by small offset fields. Similar to the gradient, the frequency has a Lorentzian dependence with the trap position and saturates approaching to the wire's surface, i.e. as $\tilde{z}_0 \to 0$.

4. **Majorana Losses**

   According to Eq. (3.25), reducing significantly the Majorana spin flips, requires an offset field that depends on the position of the trap as:

$$\tilde{B}_{\text{offset}} = \frac{B_{\text{offset}}}{B_s} \gg \left(\frac{\hbar^2}{\pi^2 W^2 \mu m B_s}\right)^{1/3}\left[\tilde{z}_0^2 + \frac{1}{4}\right]^{-2/3} \tag{3.35}$$

3.4 Case 2: On chip biased trapping configuration

From the experimental point of view, the source of the compensating bias magnetic field is better controlled when it is located in the same plane as the trapping wire, allowing a better knowledge of the trap geometry [26].

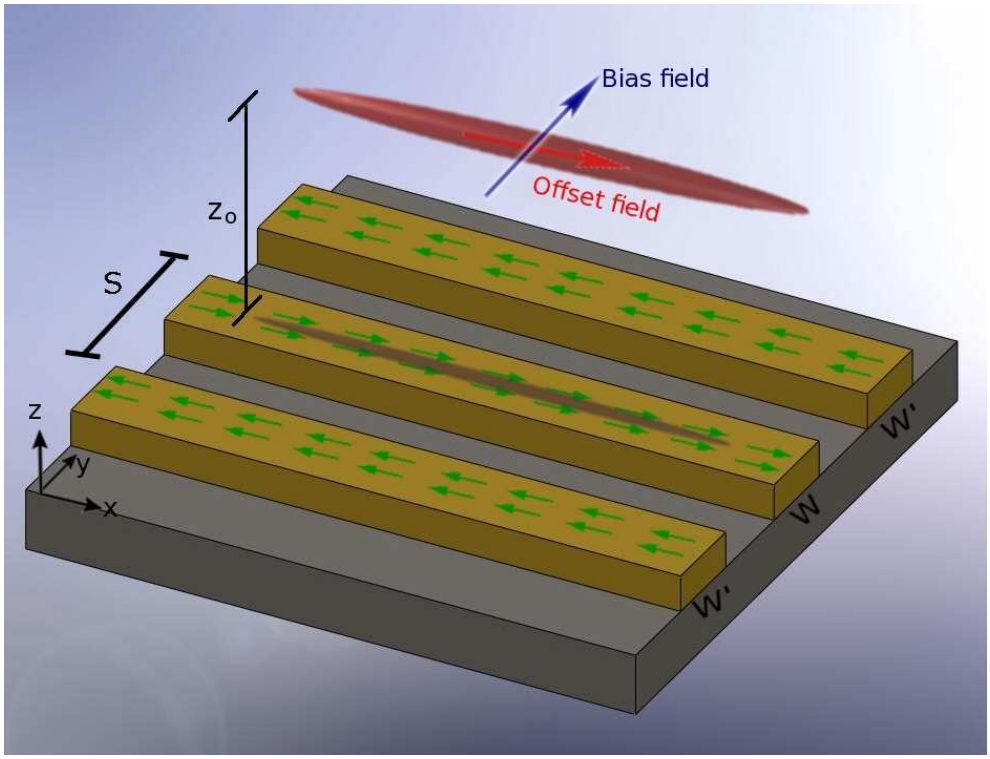

Figure 3.8: Simple geometry with an on-chip bias field. The green arrows indicate the current direction in each wire.

Here, we consider a trapping setup made of three wires. In addition to a central trapping wire, this configuration contains two long side wires carrying parallel currents. The additional magnetic field generated plays the role of the uniform bias field in the single wire configuration presented in the previous section (see Figure 3.8).

The symmetric configuration where the side wires have the same width and carry the same current density is considered here. The convention of signs and coordinates are shown in Figure 3.8. Due to the homogeneity of the system along the x axis, the dependence on x can be ignored and the magnetic field and the trap properties are evaluated at points in the plane $x = 0$ (or equivalently the $y - z$ plane).

In addition to the width, W, of the central wire and the current density, j, it carries, three other parameters are needed to characterize this setup: the width of the side wires, W', their current densities j' and their centre-to-centre distance, S, from the trapping wire (see Fig. 3.8). As in the case of a single wire trap, all trap properties are given in terms of scaled quantities defined with respect to the central wire dimensions, and

indicated in Table 3.1.

Using Eq. (3.17) centred at each wire and the scaling factors defined in Table 3.1, the combined magnetic field is:

$$\begin{aligned}
\tilde{B}_x(\tilde{y},\tilde{z}) &= \tilde{B}_{\text{offset}} \\
\tilde{B}_y(\tilde{y},\tilde{z}) &= \frac{1}{\pi}\Bigg(\beta \arctan\frac{\tilde{y}+\tilde{S}-\tilde{W}'/2}{\tilde{z}} - \beta\arctan\frac{\tilde{y}+\tilde{S}+\tilde{W}'/2}{\tilde{z}} \\
&\qquad +\beta\arctan\frac{\tilde{y}-\tilde{S}-\tilde{W}'/2}{\tilde{z}} - \beta\arctan\frac{\tilde{y}-\tilde{S}+\tilde{W}'/2}{\tilde{z}} \\
&\qquad -\arctan\frac{\tilde{y}+1/2}{\tilde{z}} + \arctan\frac{\tilde{y}-1/2}{\tilde{z}}\Bigg) \\
\tilde{B}_z(\tilde{y},\tilde{z}) &= \frac{1}{\pi}\Bigg(\beta\log\frac{(\tilde{y}+\tilde{S}-\tilde{W}'/2)^2+\tilde{z}^2}{(\tilde{y}+\tilde{S}+\tilde{W}'/2)^2+\tilde{z}^2} - \beta\log\frac{(\tilde{y}-\tilde{S}-\tilde{W}'/2)^2+\tilde{z}^2}{(\tilde{y}-\tilde{S}+\tilde{W}'/2)^2+\tilde{z}^2} \\
&\qquad +\log\frac{(\tilde{y}-1/2)^2+\tilde{z}^2}{(\tilde{y}+1/2)^2+\tilde{z}^2}\Bigg)
\end{aligned} \tag{3.36}$$

where β is the ratio between the current densities in the wire, $\beta = j'/j$. The contributions from each wire, to the total magnetic field, are easy to identify in Eq. (3.36).

Along the line of symmetry, $\tilde{y} = 0$, the magnetic field component $\tilde{B}_z$ cancels out and the magnetic field $\tilde{B}_y$ is given by:

$$\tilde{B}_y(0,\tilde{z}) = \frac{2}{\pi}\left(\beta\arctan\frac{\tilde{S}-\tilde{W}'/2}{\tilde{z}} - \beta\arctan\frac{\tilde{S}+\tilde{W}'/2}{\tilde{z}} - \arctan\frac{1}{2\tilde{z}}\right) \tag{3.37}$$

The trap is centred at the point where the magnetic field of the three wires compensates exactly, $\boldsymbol{r_0} = (0,\tilde{z}_0)$, where z_0 satisfies:

$$\beta\left[\arctan\frac{\tilde{S}-\tilde{W}'/2}{\tilde{z}_0} - \arctan\frac{\tilde{S}+\tilde{W}'/2}{\tilde{z}_0}\right] = \arctan\frac{1}{2\tilde{z}_0} \tag{3.38}$$

Again, qualitative characteristics of this trap can be deduced by plotting the potential energy and magnetic field. Figures 3.9(a)-(d) show isopotential curves, the magnetic field distribution near the trap position and the potential energy along different directions in the $y-z$ plane.

The properties of this trap are similar to those exhibited by the single wire configuration, as can be concluded from comparing Figures 3.9(a)-(b) with 3.5(a)-(b). For example, the magnetic field near z_0 can be approximated by a quadrupole field, as can be verified qualitatively from Figures 3.9(b) where the ideal quadrupole field axes are also shown.

Figure 3.9(c) and 3.9(d) show the potential energy Eq. (3.20), evaluated along the z and y axes, using different combinations of parameters in the same way as for the

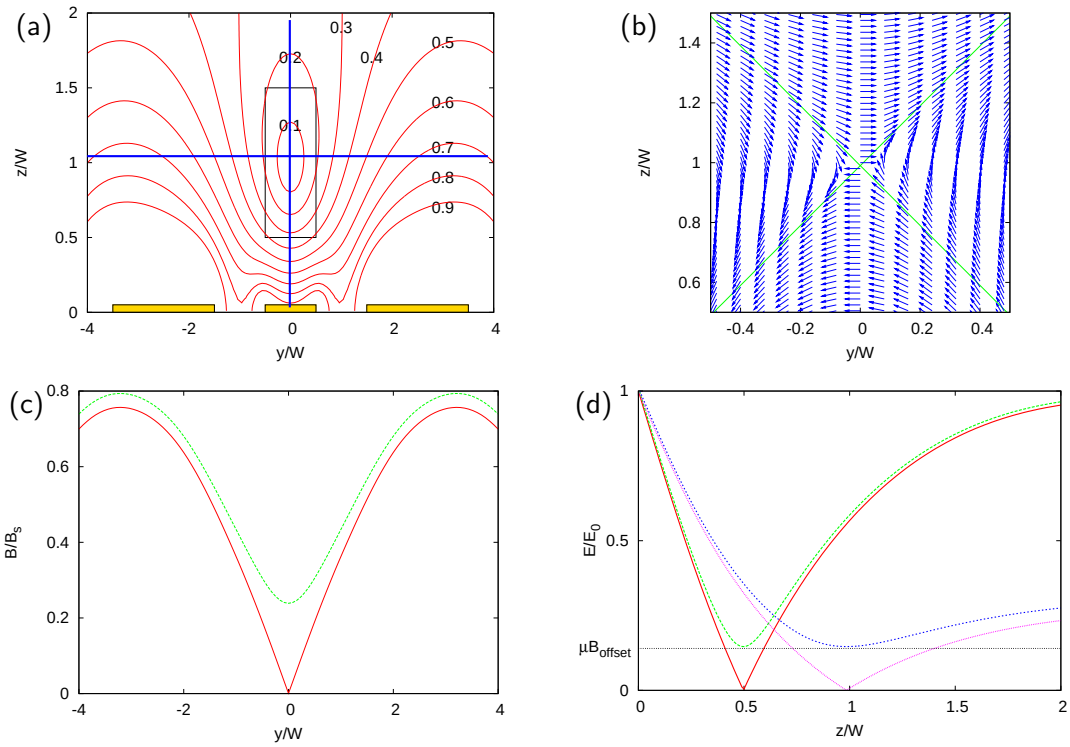

Figure 3.9: (a) Typical energy contours for the trapping configuration made by a three wire setup (Figure 3.8). Conductor slabs, schematically shown in yellow, have relative widths $\tilde{W}' = W'/W = 2$ and the centre-to-centre distance from the central conductor to side ones is $\tilde{S} = S/W = 2.5$. The relative currents were set to produce a trap located at $z/W \sim 1$ and energy contours are equally spaced by $0.1E_0$, as indicated. (b) Magnetic field near the position of the trap ($z/W \sim 1$, enclosed region in panel (a)). Similar to the single conductor case, along the ideal quadrupole axis (green lines), the field is nearly parallel to them, demonstrating that the magnetic field distribution is well approximated by a quadrupole field. (c) Potential energy along the y axis (horizontal blue line in panel (a)) with and without offset field (red and green line, respectively). Notice that in the former case, the minimum and the curvature of the potential are non-zero at $y = 0$. (d) Potential energy along the z axis (vertical blue line in panel (a)), for two bias fields set to produce a trap at $z/W \sim 1$ and $z/W \sim 0.5$, and with or without an offset field (red/green and blue/magenta lines).

single wire trap. Using Eqs. (3.36) and (3.20) the characteristics of the trap presented here are:

1. **Depth**

   The potential energy Eq. (3.20) evaluated using Eq. (3.36) has a minimum at $\boldsymbol{r}_0 = (0, \tilde{z}_0)$, equal to $\tilde{V}(0, \tilde{z}_0) = |\tilde{B}_{\text{offset}}|$. As shown in Figure 3.2(a) and (b), there

are two symmetric maxima along the y axis, and two maxima along the z axis, one of them in the middle of the central wire at $\boldsymbol{r} = (0,0)$ in the $y-z$ plane. The last two become approximately equal as the trap approaches to the chip surface.

In the middle of the central wire, $\boldsymbol{r} = (0,0)$, the contributions to the magnetic field coming from the side wires cancel exactly and the total magnetic field becomes $\tilde{\boldsymbol{B}}(0,0) = (\tilde{B}_{\text{offset}}, 1, 0)$ (see Eq. (3.36)). Therefore, the trap depth, relative to the magnetic potential energy at the central wire, becomes:

$$\begin{aligned} \Delta\tilde{V} &= \tilde{V}(0,0) - \tilde{V}(0,\tilde{z}) \\ &= \left(1 + \tilde{B}_{\text{offset}}^2\right)^{1/2} - |\tilde{B}_{\text{offset}}| \end{aligned} \tag{3.39}$$

From Eq. (3.39), we conclude that the maximum depth occurs in the absence of an offset field and that it is independent of the trap position, z_0.

2. **Gradient**

As mentioned previously, in the absence of an offset field, the magnetic field distribution can be approximated by a quadrupole field centred at the trap position. The gradient of the potential along the z axis, centred at the trap position, is calculated by differentiating Eq. (3.36):

$$\partial_{\tilde{z}}\tilde{V}(0,\tilde{z})\Big|_{\tilde{z}_0} = \frac{2}{\pi}\left(\frac{2}{1+4\tilde{z}_0^2} - \beta\,\frac{\tilde{S}^2 - \tilde{W}'^2/4 - \tilde{z}_0^2}{(\tilde{S}^2 + \tilde{W}'^2/4)^2 + \tilde{z}_0^2(2\tilde{S}^2 + \tilde{W}'^2/2) + \tilde{z}_0^2}\right) \tag{3.40}$$

Notice that as the trap position has a non-trivial dependence on the system parameters, $\tilde{z}_0 = \tilde{z}_0(\beta, \tilde{S}, \tilde{W}')$, the full dependence of the potential energy gradient on all the parameters is not explicit in Eq. (3.40).

3. **Trap frequency**

Again, using a harmonic approximation, the potential energy near z_0 is given by:

$$\tilde{V}(\tilde{y},\tilde{z}) = \frac{\tilde{\omega}_{\tilde{y}}^2}{2}\tilde{y}^2 + \frac{\tilde{\omega}_{\tilde{z}}^2}{2}(\tilde{z}-\tilde{z}_0)^2 + \tilde{B}_{\text{offset}} \tag{3.41}$$

where, applying Eq. (3.9), the trap frequency is:

$$\tilde{\omega}_{\tilde{z}} = \left(\frac{1}{\tilde{B}_{\text{offset}}}\right)^{1/2}\partial_{\tilde{z}}\tilde{B}_{\tilde{y}} \tag{3.42}$$

An explicit formula can be obtained by replacing Eq. (3.40) into the previous expression.

4. **Majorana Losses**

To make the rate of spontaneous spin flips small, the offset field should satisfy the condition Eq. (3.25). The result of combining this condition with Eq. (3.42) is:

$$\frac{B_{\text{offset}}}{B_s} \gg \left(\frac{4\hbar^2}{\pi^2 \mu m B_s W^2}\right)^{1/3} \frac{w}{B_s}\frac{\pi}{2}\partial_{\tilde{z}}\tilde{B}_{\tilde{z}}|_{\tilde{\boldsymbol{r}}_0} \tag{3.43}$$

3.5 Case 3: Full 3D trapping

The single and three wire configurations shown previously provide confinement in the plane orthogonal to the current flow but not along the wire's axis. By bending the wires, e.g. forming U or Z shapes, as in Figure 3.10(a) and 3.11(a), confinement along the trap axis can be achieved.

In these configurations, external uniform magnetic fields produce effects similar to those described above: an offset field parallel to the current flow at the centre of the structure controls the trapping strength, and the trapping position is defined by a bias field transverse to the same current flow.

If the length of the central wire (L) is much larger than its width W, a good approximation to the total magnetic field can be obtained by splitting the wire into rectangular sections and then using Eq. (3.17) for each one. This procedure, which ignores the bending of the current occurring at the corners of the wire, is accurate enough to estimate the magnetic field near the centre of the trap, in a region smaller than the dimensions of the wire.

This thesis uses a purely numerical approach to evaluate the magnetic field distribution produced by the array of current elements and the properties of the trap produced. Typical features of the potential energy in these configurations are shown in Figures 3.10 and 3.11.

In both cases, the bending of the wires breaks the cylindrical symmetry, which was present, to a good approximation, in the previous trapping configurations. Figures 3.10(b)–(c) and 3.11(b)–(c) show the contours of potential energy in the planes $(0, y, z)$ and (x, y, z_0). The presence of closed contours demonstrates asymmetric trapping along the three spatial directions. In the U-shaped case, the trap is not centred above the central wire, but is shifted away from it. In the Z-shaped wire, the trap is tilted along the central wire (see Figure 3.11(b)).

Figures 3.10(d)–(e) and 3.11(d)–(e) show the potential energy along the lines $(0, 0, z)$ and $(x, 0, z_0)$, again for the U and Z-shaped wires, respectively. The nature of the resulting trapping potential in the U and Z geometries is quite different. In the Z geometry, the orthogonal segments produce a magnetic field parallel to the current flow, which is nearly uniform at the centre of the wires. This magnetic field plays a similar role to the offset field defined in previous section. The resulting potential is smooth along the three spatial directions, and can be approximated by a harmonic function near the position

of the potential minimum. With the U shape geometry, the magnetic field at the trap position is zero, and the trap has a quadrupole-like dependence.

All the definitions given here to characterize the strength of the trapping potential can be straightforwardly applied to the present case and extended to all three spatial directions. Although, Eq. (3.17) can be used to obtain approximate analytic expressions for the harmonic trapping potential, the results are very complex and do not make clear the properties of such traps. Therefore, in this thesis we do not used this procedure for trapping configurations that include bended wires, limiting ourselves to a numerical approach.

3.6 Summary

Magnetic trapping of cold atoms is possible because particles with negative magnetic moment are attracted towards regions where the magnetic field is small. Magnetic field distributions with a localized minimum can be built by combining different field sources that locally cancel each other.

The strength of the trapping is characterized by the absolute value of the potential energy (depth), and its gradient, evaluated at the position of the minimum. Analytic expressions for such properties have been found for trapping setups relevant to this thesis.

Confinement along the three spatial directions can be provided by bending the central trapping structure. In this case, the total magnetic field can be calculated by adding the contributions associated with the different sections of the wire.

The analysis presented here will be used to establish the possibility of preparing trapping potentials with current flows through two-dimensional electron gases, and the general conditions demanded to achieve a useful trapping potential.

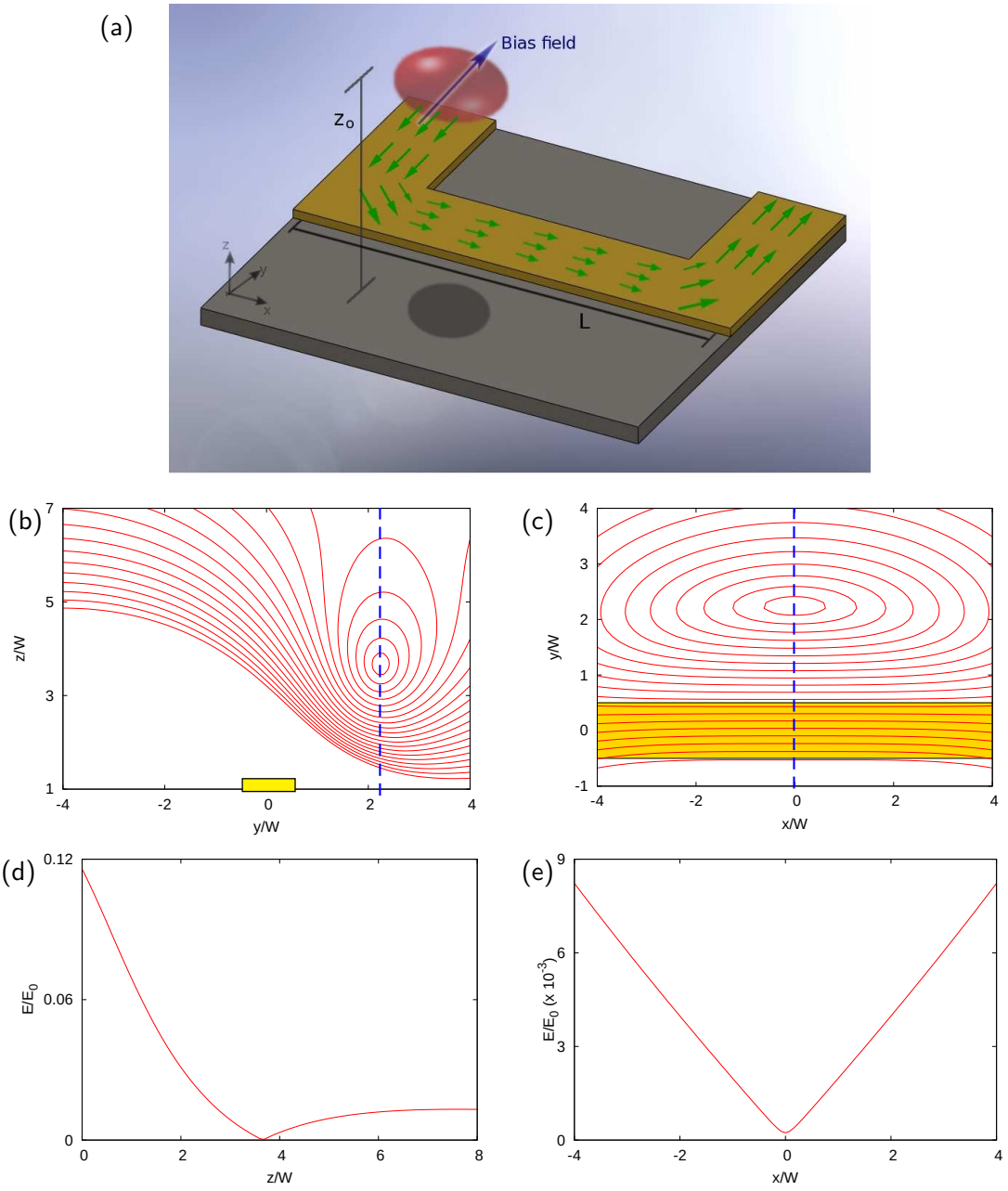

Figure 3.10: (a) Schematic diagram of a U-wire magnetic trap setup. Note that the wire's bending provides confinement along the central wire axis, and pushes away the trap position from the centre of the wire. Other panels show the potential energy of an atom in the magnetic field produced by a current in an U-shaped wire and an external bias field. (b) Iso-potential energy curves in the $y-z$ plane, spaced by $0.05E_0$. (c) Contours of the potential energy in $x-y$ plane, spaced by $0.0025E_0$. (d) and (e) shows the potential energy along the z and x axis (blue lines in panels (b) and (c), respectively). No offset field is considered in this configuration.

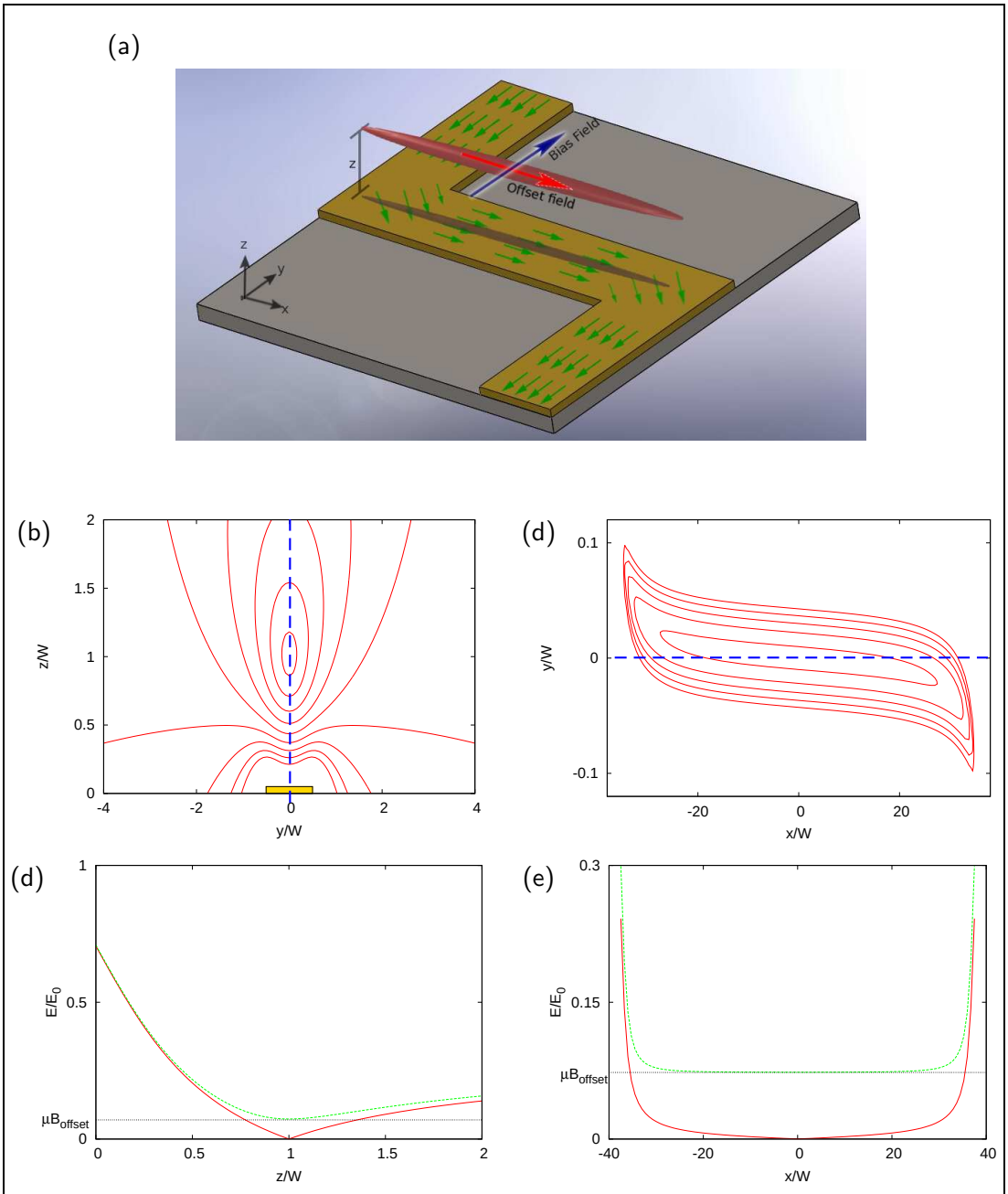

Figure 3.11: (a) Schematic diagram of a Z-wire magnetic trap setup. Note that the wire's bending provides confinement along the central wire axis and an intrinsic offset field at the centre of the trap. Other panels show the potential energy of an atom in the combined magnetic field produced field produced by a current in an Z-shaped wire and an external magnetic field. (b) and (c) show contours of the potential energy in $y-z$ and $x-y$ planes respectively. Panels (d) and (e) corresponds to the potential energy along the z and x axis with origin at the centre of the setup. It can be observed that the offset field has the same effect previously discussed.

CHAPTER 4

Magnetic trap fabricated using a Two-Dimensional Electron Gas wire

Good conductors, like gold or copper, have been the preferred material to use in atom chips setups like that shown in the previous chapter. These materials support large current densities with low heating rates, making possible the production of strong magnetic fields and, consequently, strong magnetic traps. The production of atom-chips has also benefitted from the ability to create intricate webs of wires with micrometre resolution, by using standard techniques of deposition/etching over semiconducting substrates [106].

The material properties and fabrication techniques limit the flexibility and quality of the traps that can be built with metallic conductors. As an example of this, thermal damage of the atom chip components should be avoided by limiting the current density in the wires to below a certain value, $j_{\max}$, determined by the thermal properties of the conductor, substrate interfaces and boundary conditions [107]. This maximum current density sets the smallest possible wire cross section and/or the maximum current ($I_{\max}$) that a wire can support, therefore limiting the strength of the trapping potential. In general, establishing the optimal distribution of elements in the atom chip, thereby obtaining an effective sink of the heat dissipated by the current flow[1], is a complex problem [26].

On the other hand, the quality of the magnetic trap can be affected by defects in the wires originating from the production process [30, 60, 80]. Geometrical imperfections and finite grain size are sources of corrugation that can deviate the current flow from

[1] Typical microtraps use current densities in the range of $10^{10} - 10^{12}$ mA/μm^2, which produce a power of a few Watts along the whole wire [50].

idealised paths. This may cause the trapped clouds to break up into fragments along the length of a current carrying wire. The extent of the fragmentation is then dictated by the wire quality and is typically observed for a large range of atom-wires distances, e.g. at ~ 10 μm for lithographically formed wires, and ~ 100 μm from electro-plated wires [26].

Neighbouring surfaces have important effects on the trapped atoms. At micrometre atom-surface separations, the interaction of the atoms with magnetic field fluctuations, created by the surface become relevant and the rate of induced spin-flip transitions, decoherence and heating of the trapped clouds is greatly increased [60] compared with their rates in vacuum. The temperature of the surface, the amount of material below it and its conductivity, determine the intensity, time and length scales of such effects, and impose limits on the quality of the trapping potential [31, 80].

Limitations associated with using metallic materials for atom trapping and manipulation are nowadays well understood [26]. It is interesting, therefore, to explore different materials which can open other possibilities. Proposals of using superconducting wires [85, 91], metallic alloys [86] and materials with anisotropic conductivity [87], have already been made but only the first one has been experimentally tested.

This chapter explores the possibility of using a 2DEG as a conducting material for microtrapping. As motivation, a prediction of the life-time of trapped states near dielectric surfaces is presented in Section 4.1. The conditions required for operation of a simple 2DEG-based trapping configuration with acceptable strength are established in Section 4.2. To perform this analysis, results of Sections 3.3 and 3.4, are applied considering that, in this context, the only relevant differences between a metallic material and a 2DEG are their conductivities and thickness.

The potential landscape experienced by an electron in a 2DEG has inhomogeneities that cause deviations in the electron's trajectory, as explained in Chapter 2. In turn, this creates inhomogeneities of the generated magnetic field. In Section 4.3 we show how this inhomogeneous magnetic field distribution corrugates the trapping potential and modulates the density of a trapped BEC.

The last section summarizes this chapter and discusses the feasibility and potential advantages/disadvantages of using 2DEGs for ultra-cold atom trapping.

4.1 Lifetime of trapped states near a dielectric body

The thermal motion of charges inside any body generates a fluctuating electromagnetic field near its surface, determined by the electrical properties of the material, the shape of the body and its temperature. So far, two equivalent approaches have been used to compute the magnetic component of this fluctuating field [83]. One of them [108], uses

an application of Nyquist's Theorem [1], whereby the distribution of current fluctuations in the body is evaluated and then the magnetic field can be worked out through Maxwell's equations. The second method evaluates directly the spectrum of the magnetic field by using the relation given by the Fluctuation-Dissipation theorem [1], between the magnetic field (fluctuation) and the material dynamic permeability (dissipation) [82, 83, 109].

An atom near the surface of a body can be strongly affected by the fluctuating field associated with the thermal motion of the charges at and below the surface. If an atom in the state $|F, m_f\rangle$ is magnetically trapped (see Eq. (3.1)), the fluctuations of the magnetic field field can drive spin flips to states with lower m_f, which are weakly trapped and more likely to escape [31].

The rate of the process $|F, m_i\rangle \rightarrow |F, m_f\rangle$ (Γ_{if}) is given by Fermi's golden rule and involves the spectral density of the magnetic fluctuation at the frequency of the transition ($\hbar w_{fi} = E_f - E_i$) and the matrix elements of the interaction operator [28, 31, 85]:

$$\Gamma_{if}(\boldsymbol{r}) = \sum_{\alpha\beta} \frac{\langle i|\,\mu_\alpha\,|f\rangle\,\langle f|\,\mu_\beta\,|i\rangle}{\hbar^2} S_B^{\alpha\beta}(\boldsymbol{r}; -w_{fi}) \tag{4.1}$$

where μ_α, $\alpha = x, y, z$ are the components of the magnetic moment operator and $S_B^{\alpha\beta}(\boldsymbol{r}; -w_{fi})$ is the spectral density of the magnetic field, which depends on the imaginary part of the dielectric function of the surface material and on the surface shape [109].

The purpose of this section is to estimate the transition rate, or equivalently the lifetime, of atoms trapped near a heterostructure containing a near-surface 2DEG and compare it with the rates for atoms near a good conducting material. A schematic diagram of the geometry considered is shown in Figure 4.1.

In this geometry, three length scales determine the rate of transitions: the atom-surface distance (z_0), the thickness of the conducting layer (h) and its skin depth, given by:

$$\delta = \sqrt{\frac{2\rho_{3D}}{\mu_0 \omega_{fi}}} \tag{4.2}$$

where ρ_{3D} is the 3D resistance of the material and ω_{fi} is the transition frequency.

Analytic results for several regimes have been reported [26, 28, 85] and can be summarised as follows [85]:

$$\tau = \left(\frac{8}{3}\right)^2 \frac{\tau_0}{n_{th}+1} \left(\frac{\omega_{fi}}{c}\right)^3 \times \begin{cases} \frac{z_0^4}{3\delta} & \delta \ll z_0, h \\ \frac{\delta^2 z_0}{2} & \delta, h \gg z_0 \\ \frac{\delta^2 z_0^2}{2h} & \delta \gg z_0 \gg h \end{cases} \tag{4.3}$$

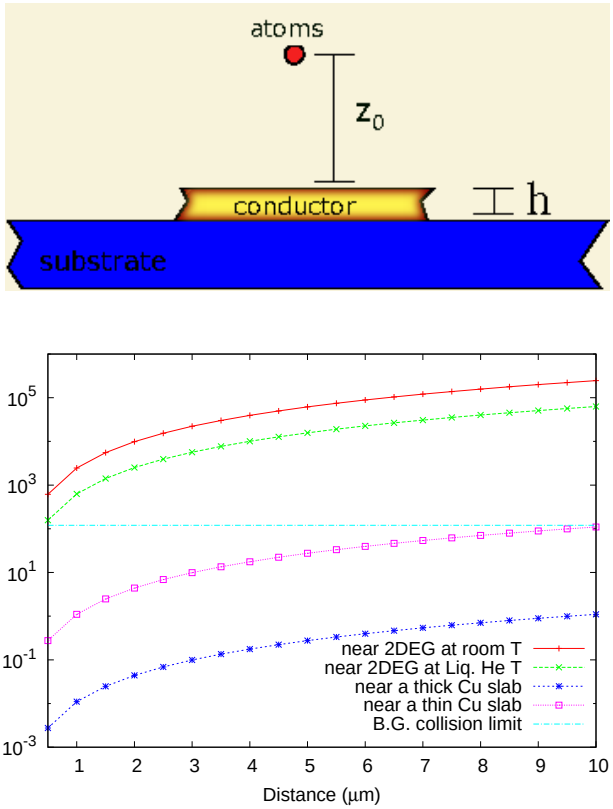

Figure 4.1: (a) Typical geometry for trapping atoms near surfaces. The thick slab (in blue) represents a dielectric substrate, over which there is a conducting slab of thickness h (in yellow). Atoms are trapped at a distance z_0 from the surface [26, 85, 28] (b) Expected lifetime of the atomic state $|f = 2, m_F = 2\rangle$, near 2DEG and copper wires. We assume a ^{87}Rb in a uniform magnetic field of $B \sim 0.2$G, corresponding to a Larmor precession frequency of 279.92 kHz. Only spin-flip transitions due to the thermal fluctuating electromagnetic field near the materials have been considered [85].

where $n_{th} = [\exp(\hbar\omega_{fi}/k_BT) - 1]^{-1}$ is the Bose factor, τ_0 is the lifetime in free space:

$$\tau_0 = \frac{3\pi\hbar c^3}{\mu_0\omega_{fi}^3 \sum_{\alpha=x.y,z} \mu_B^2 g_F^2 \left|\langle f|\, \hat{F}_\alpha\, |i\rangle\right|^2} \tag{4.4}$$

in which $\hat{F}_\alpha$,$(\alpha = x, y, z)$ are the Cartesian components of the total angular momentum operator.

Typical experimental situations with atoms trapped by an atom chip configuration correspond to the third case in Eq. (4.3) ($\delta \sim$ a few hundreds of μm $\gg z_0 \sim$ a few tens of μm $\gg h \sim$ a few μm). From the same equation, it can be concluded that long lifetimes of trapped states are favoured by using thin conductors and/or by keeping the atoms far from any metal surface [26].

To quantify the possible benefit of trapping atoms using a 2DEG-based atom chip, consider a ^{87}Rb atom in a magnetic trap with an offset field $B_{\text{offset}} = 0.2$ G, and compare the transition rate of the process $|F = 2, m_F = 2\rangle \rightarrow |F = 2, m_F = 1\rangle$, when it occurs close to a 2DEG and to a thin copper slab [84]. In this case, the transition frequency, ω_{fi} coincides with the Larmor frequency of the spin precession around the offset magnetic field axis, $\omega_{fi} = g_F \mu_B |B|/\hbar \sim 2\pi \times 0.3$ MHz.

Figure 4.1(b) shows the calculated lifetime of the trapped state above a 2DEG, with the properties shown in Table 2.2, at 300 K (top curve) and 4.2 K (green curve) and also next to a 1.0 μm thick copper slab (cyan curve) and a 10 nm copper layer (blue curve), both at room temperature. The lifetime limit due to collision with the background gas is also shown [26]. Table 4.1 shows the properties of copper and the 2DEG considered here, and compares the lifetime of a trapped atom located at 1 μm above these materials.

Material	Resistance (Ω)	δ (μm)	Thick (h)	$\delta^2/2h$ (m)	τ at 1 μm (s)
2DEG (300 K)	3.78×10^{-5}	5649.4	10 nm	1595.8	2.465×10^{3}
2DEG (4.2 K)	1.35×10^{-7}	337.6	10 nm	5.7	6.289×10^{2}
Cu (300 K)	1.69×10^{-8}	119.5	1 μm	0.00714	1.101×10^{-2}
Cu (300 K)	1.69×10^{-8}	119.5	10 nm	0.7	1.101

Table 4.1: Comparison between the properties of copper and a 2DEG at different temperatures, and lifetime of a trapped atom held 1 μm above them.

Due to its small conductance and thickness, magnetic field fluctuations near a 2DEG are weaker than close to a normal metal. Consequently, the lifetime of trapped states is largely increased and becomes limited only by collisions with background atoms (typically a hundred seconds [29]) even at sub-micrometre distances. Notice the apparent contradiction that the lifetime above a 2DEG a room temperature is larger than when it is cooled to 4.2 K. This occurs because the enhancement of the magnetic fluctuations occurring with increasing temperature (Bose factor in Eq. (4.3)) is overcome by a reduction driven by the enhancement of the material resistance ($\delta^2 \propto \rho_{3D}$ in Eq. (4.2)).

Traps with long lifetimes would present great advantages for the manipulation and storage of cold atoms, which is a strong motivation to explore the possibilities that a 2DEG offers as a trapping structure.

4.2 Feasibility of a 2DEG-based microtrap for cold atoms

This section establishes the conditions required to produce a magnetic trap using a 2DEG as the conducting material, for the single-wire and on-chip biased setups explained in Sections 3.3 and 3.4. The magnitude of the bias/offset magnetic fields and the current density are restricted according to the limitations on the current density that can flow

through a 2DEG, as explained in subsection 2.2.1.

In order to be potentially useful, a trap produced by a current carrying 2DEG should have characteristics comparable with that typically found in experiments on atom-chips with metallic conductors [26]. In particular, it should have a minimum located at a distance between $1-10$ μm from the main trapping structure, transverse frequencies in the range of $1-10$ kHz and a depth of a few tens of μK. The conditions needed to get such a trap and a discussion about how those conditions can be achieved/tolerated by using a high-mobility 2DEG are discussed in this section.

For a 2DEG-based atom trap, the wire's size is of the order of 1 μm (both width and length). As the Fermi wave length of electrons in the 2DEG (10 nm) is much smaller than those dimensions, effects due to the quantisation of energy levels associated with the wire geometry can be neglected and the 2DEG is simply considered as a slab of conducting material with a thickness of a few tens of nano-meters [95]. However, we mention in passing that the interaction between ultra-cold atoms and quantised electronic states in heterostructures may be of interest in its own right, and currently remains a poorly studied topic.

4.2.1 Single wire trapping

Consider the single wire trapping setup described in Section 3.3. To quantify the achievable trapping strength, we must first set the values of current flow and the dimensions of the wire. As shown in section 2.2.1, a 2DEG can tolerate a maximum current of the order of $j_{\max} \sim 0.3$ mA/μm. For illustration, consider a smaller flow $j = 0.16$ mA/μm $\simeq j_{\max}/2$, which yields a magnetic field of $B_s = 1$ G at the wire surface. For this current, the trap parameters, defined in Section 3.3 (Eqs. (3.29) - (3.35)), scale according to (see Table 3.1):

Quantity	Symbol	value
Wire's width	W	10 μm
Magnetic field at surface	B_s	1 G
Energy scale	E_0	67.2 μK
Frequency Scale	$\nu_0 = \omega_0/2\pi$	404 Hz
Gradient factor	B_s/W	10 T/m $= 0.1$ G/m

Table 4.2: Scaling factors of the trapping properties associated with a plausible single-wire setup including a 2DEG as conducting material

Once the width of the trapping wire is fixed, all properties of the trapping potential depend only on the ratios B_{Bias}/B_s and B_{offset}/B_s (as shown in Figure 4.2) scaled by an appropriate factor. For the set of parameters in Table 4.2, the trapping potential has the following properties:

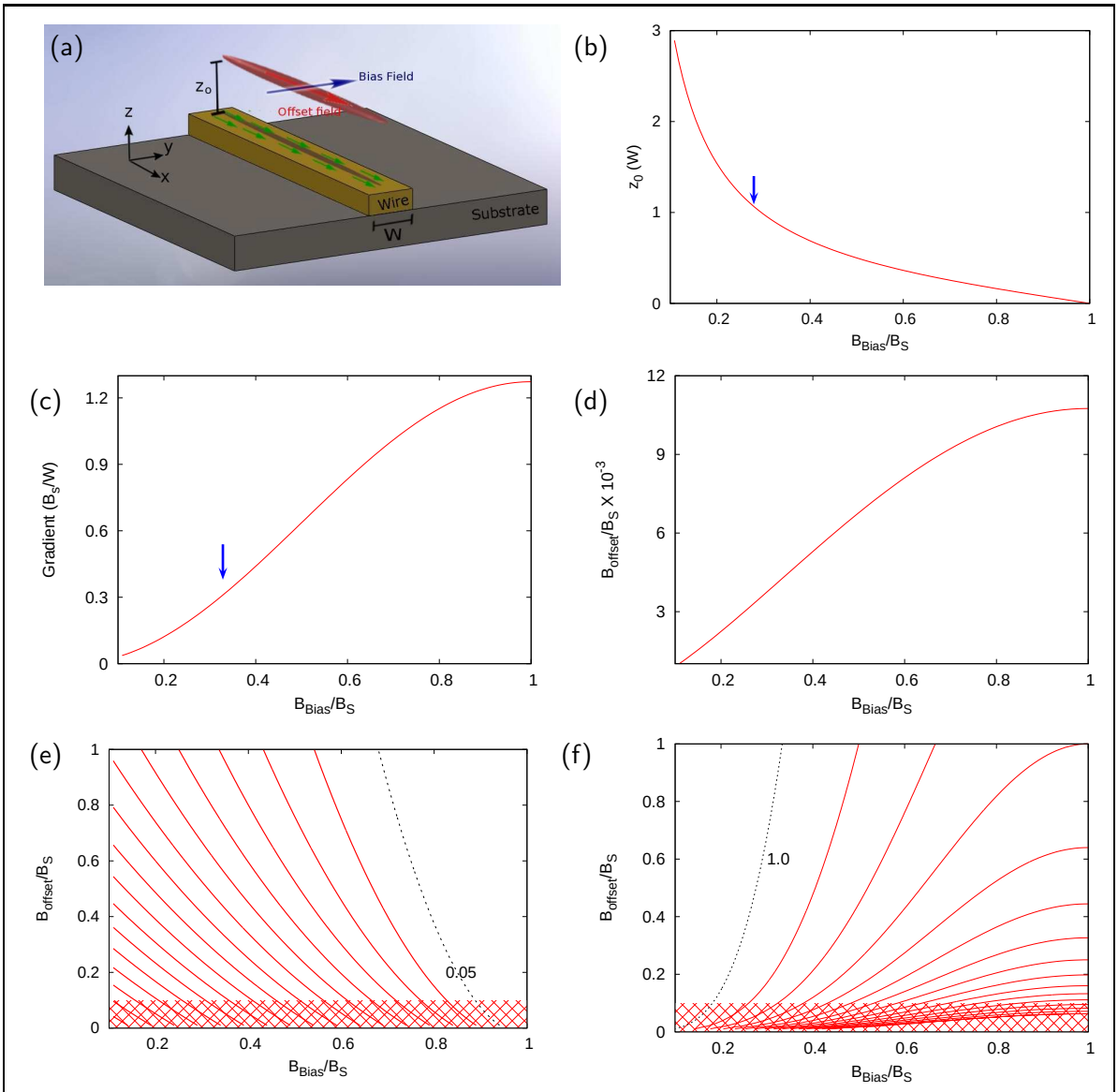

Figure 4.2: Characteristics of the trapping potential generated by a single planar wire plus external homogenous fields (panel (a)). All quantities are scaled according to the definitions in Table 3.1. (b) Vertical position of the trap (z_0) as function of magnetic bias field. (c) Trap gradient (d) Minimum value of the offset field needed to satisfy the adiabatic condition Eq. (3.25). (e) Contours of the trap depth versus offset and bias fields. Contours are separated each $0.05E_0$ (starting with the dotted curve at $0.05E_0$) (f) Trap frequency as function of offset and bias fields. Contours are separated by $1.0\nu_0$ (starting with the dotted curve at ν_0). The dashed region in (e) and (f) corresponds to values of B_{offset} that do not satisfy the adiabatic condition, according to panel (d).

1. Trap positions below $W \sim 10$ μm can be obtained by a bias field satisfying $B_{\text{Bias}}/B_s \geq 1/3$ (indicated by the arrow in Figure 4.2(b)), which, according to Table 4.2, corresponds to $B_{\text{Bias}} \geq 300$ mG.

2. The trap depth ($\Delta\tilde{V}$) and radial frequency ($\tilde{\omega}_z$) are functions of both the bias and the offset fields (see Eq. (3.31) and (3.34) respectively). Contour curves of shown in Figures 4.2(e) and 4.2(f). From Figure 4.2 and using the scaling factors in Table 4.2, it can be conclude that using magnetic fields in the ranges $B_{\text{offset}} \in [0.1, 1]$ G and $B_{\text{Bias}} \in [0.3, 1]$ G, produces traps with satisfactory depth ($\sim 10\mu$) and frequency (~ 1 KHz).

3. In the absence of an offset field, the trap can be approximated by a quadrupole configuration with a gradient (α in Eq. (1.36)) larger than 3 T/m $\sim 0.3B_s/W$ (arrow in Figure 4.2(c)), which is strong enough to compensate the gravitational attraction on an ^{87}Rb atom.

4. Eq. (3.35) provides a lower bound for the offset field required to avoid Majorana spin flips. In dimensionless units, this lower bound is $B_{\text{offset}}^{\text{minimum}} \sim 10^{-3}B_s$, which, according to Table 4.2, corresponds to $B_{\text{offset}}^{\text{minimum}} \sim 1$ mG.

The order of magnitude of all relevant trap parameters, for the single wire trap configuration, are summarized in Table 4.2. Quantifying such properties can be done by combining this scaling with results shown in Figures 4.2(b) - 4.2(f), which corresponds to Eqs. (3.29) - (3.35). Notice that by using external bias and offset magnetic fields of a few hundred mG, produces at trap at the position and with the strength required. For example, using $B_{\text{Bias}} = 550$ mG and $B_{\text{offset}} = 500$ mG creates a trap located 5 μm above the 2DEG plane, with transversal frequency of 1.2 kHz and a depth of 13.4 μK.

This particular set of parameters illustrates the order of magnitude of the trap characteristics that can be achieved by using 2DEG as conducting elements in atom chips. These results are comparable with those realized in current experiments (see [26]) and encourage us to explore a more complex system: the on-chip biased trap.

4.2.2 On-chip biased trap.

Consider a three wire configuration like that in Section 3.4, with a $W = 10$ μm wide central wire and $W' = 10$ μm wide side wires with a centre-to-centre separation of $S = 40$ μm (see Figure 4.3 (a)). Once the geometry is fixed, the position of the trap is determined by the ratio between the currents, j and j' of the central and side wires, respectively. For example, as can be seen in Figure 4.3 (b), positioning the trap below $W = 10$ μm requires a ratio satisfying $j'/j \gtrsim 3$.

The length scales of the system are set by the width of the central wire and the strength of the trapping potential depends only on the ratio j'/j and the applied offset

field, as can be seen from Eqs. (3.39) - (3.43) in section 3.4. Using the same scaling parameters in Table 4.2, the trapping properties can be summarized as follows:

1. In Figure 4.3(b), observe that locating the trap a few micrometres above the central wire, by using micrometre wide wires, requires $j'/j \gtrsim 3$.

2. According to Eq. (3.39), in this configuration the trap depth is independent of the current in the side wires, j', and only depends on the ratio between the offset field and B_S. The depth can be several tens of μK ($\Delta\tilde{V} \in [0.1, 1]$) if the offset field varies between 100 mG and 4 G ($B_{\text{offset}}/B_s \in [0.1, 4]$).

3. Similarly to the single wire case, the ratio B_s/W corresponds approximately to 10 T/m. According to Figure 4.3(c), the gradient of the quadrupole (Eq. (3.40)) trap is several T/m, and therefore the gravitational attraction can be compensated by this setup.

4. The trap frequency depends on the ratio j'/j and on the offset field. Contours of $\nu(B_{\text{offset}}, j'/j)$ are shown in Figure 4.3(f). Frequencies of a few kHz are achieved for combinations of $B_{\text{offset}} \in [0.1, 4]$ G and $j'/j \in [3, \infty)$.

5. The adiabatic condition Eq. (3.43), plotted in Figure 4.3(d), is satisfied if the offset field is larger than $0.01B_S \sim 10$ mG.

The considerations presented here enable us to identify the order of magnitude of the parameters and conditions needed to create a trap useful for atom manipulation, by using current flows through a 2DEG. A current producing a magnetic field at the surface of 1G combined with bias and offset magnetic fields of ~ 100 mG, can create a potential strong enough to trap condensed atoms.

To guarantee low levels of power dissipation during the operation of the trap, the 2DEG must have a high electrical conductivity, which can be achieved by keeping the sample cooled to cryogenic temperatures ~ 4.2 K. Such low temperatures complicates the experimental setup, but certainly the design would not be very different from the experiments already made using superconductors as trapping structures [93, 94]. In the next chapter, we show that BECs can be used to probe the electronic properties of 2DEG-base components such as quantum wires and dots. Since these structures often only exhibit quantum phenomena at 4.2 K or below, a natural way to probe such effects using a BEC microscope would be to use the 2DEG to fabricate both the trapping wires an the components to be probed.

Finally, considerations about the three-wire configuration suggest that hybrid systems, combining currents through metal conductors and semiconductor materials, are needed to produce strong trapping. Specifically, in the example presented, to obtain a trap at a micrometre distance, $\sim 1 - 10$ μm, from the surface, the current in the side

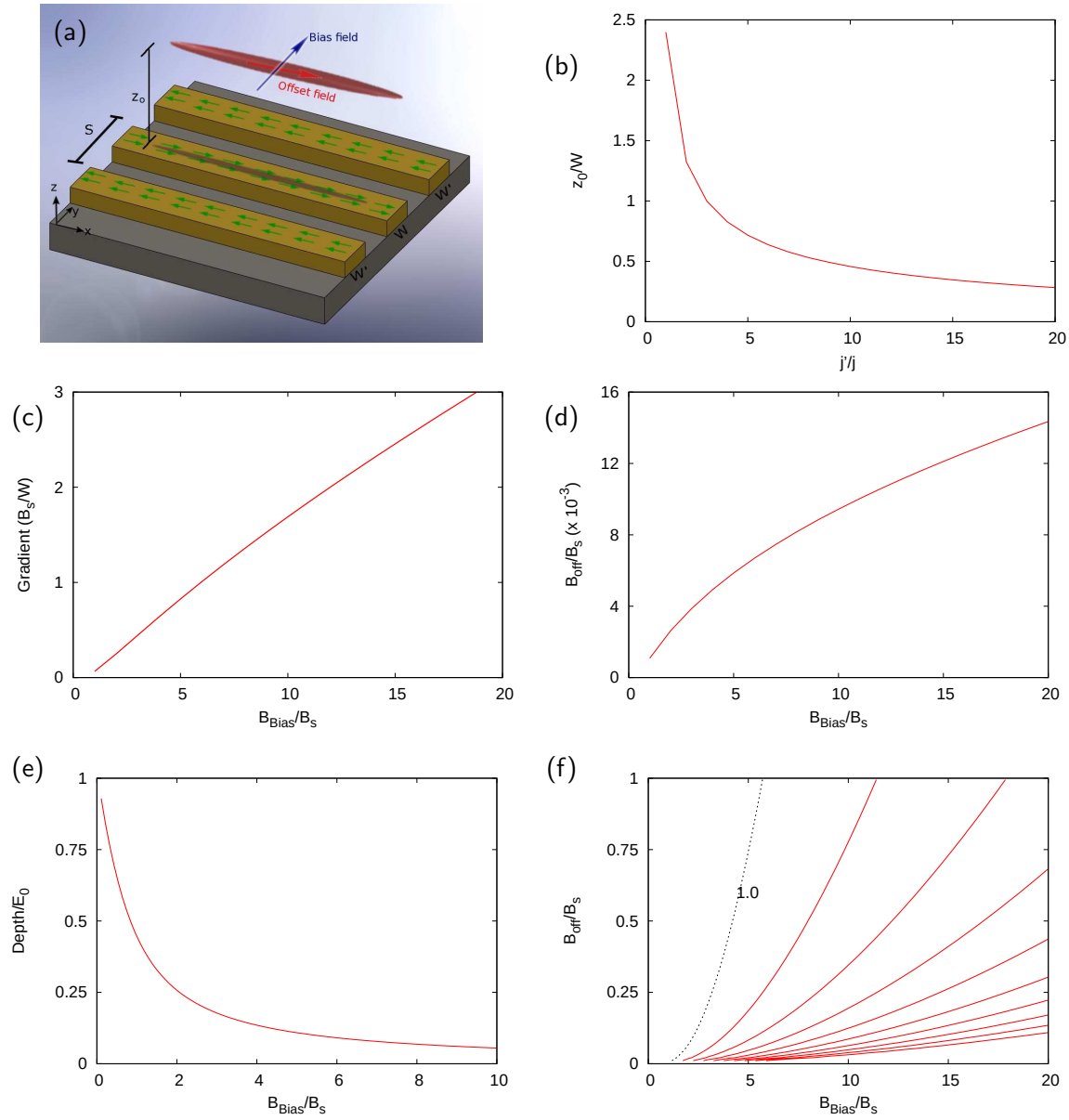

Figure 4.3: Characteristics of the trapping potential generated by a three wire configuration (panel (a)). All quantities are scaled following the definitions in Table 3.1 (b) Vertical position of trap position versus magnetic bias field. Note that to reach trapping distances lower than 10 µm requires a bias field larger than 0.3 times B_s. (c) Trap gradient (d) Minimum value of the offset field needed to satisfy the adiabatic condition Eq. (3.25). (e) Trap depth as a function of offset field. (f) Trap frequency versus offset and bias fields. Contours are separated by ν_0 (starting with the dotted line $= 1.0$).

wires must be three times that in the central wire, which can easily exceed the maximum tolerable current in a 2DEG, thus requiring metallic side wires.

4.3 Trap corrugation due to current flow in a 2DEG

The previous section considered trapping setups where the current flow is homogeneous. Defects in the definition of the wire edges and local changes in the properties of the conductor can locally deviate the current and produce a corrugation of the trapping potential. This corrugation is then imprinted in the density distribution of trapped atoms [22, 80, 110].

As mentioned in Chapter 2, 2DEGs at low temperatures have large mobilities, limited mainly by the interaction of the electrons with their parent ionized donors. The donor-electron potential leads to a long-range and small angle scattering of the electron path, creating a branched flow pattern [111, 112], like that illustrated in Figure 2.6.

The effect of inhomogeneity of a 2DEG used to form a Z-trap (Section 3.5) is evaluated in this section. It is assumed that, along the central portion of a Z-shaped wire, the current has a uniform contribution $\boldsymbol{j} = (j, 0)$ along the x direction and an inhomogeneous component $\Delta\boldsymbol{j} = (\Delta j_x, \Delta j_y)$. The inhomogeneous component $\Delta\boldsymbol{j}$ is calculated from Eqs. (2.2) and (2.6) as follows: Eq. (2.2) is used to determine the screened donor potential in a region the same size as the central portion of the Z-trap. Then, the current distribution is obtained using Eq. (2.6). The total magnetic field profile is then evaluated from the Biot-Savart law Eq. (3.14).

Each component of $\Delta\boldsymbol{j}$ affects the trapping potential in a different way. This can be seen most easily by assuming that the magnetic field at a given point (x, y, z) is mainly due to the current element just below it. Then Δj_x shifts the trapping position because the magnetic field acquires an extra contribution, which changes the vertical position (i.e. along z) where the applied B_{Bias} is exactly compensated. On the other hand, Δj_y shifts the bottom of the potential energy because it creates a magnetic field along the x axis that locally changes the offset field.

As explained in Section 3.5, the superposition of a uniform magnetic field and the inhomogeneous magnetic field produced by the current through a wire bent into a Z shape produces a 3D trapping potential. Simulations presented here consider parameters that are attainable in current experiments (see Table 4.3).

As shown in Table 4.3, by choosing different external bias and offset fields the trap position and frequency can be set to selected values. To study the form of the confined atom cloud, we calculate the ground state of a BEC made of 10^5 ^{87}Rb atoms in the $|F = 2, m_f = 2\rangle$ state is in traps located at different distances from the 2DEG plane. An imaginary-time evolution of the Gross-Pitaevskii Equation within a Crank-Nicolson

scheme was the numerical method used to evaluate the atom density distribution of the ground state (see Appendix A). Figure 4.3 shows the result of this procedure.

Parameters of the 2DEG Z-trap	
Length	1.0 mm
Width	20 μm
Mobility	140 $\mathrm{m^2 s^{-1} V^{-1}}$
Applied electric field	11.1 mV/μm
current	0.12 A
B_{offset}	0.2 G

Different configurations of a 2DEG-based trap			
B_{bias} (G)	2.27	3.2	4.2
z_0 (μm)	10	5	3
$\omega_\perp/2\pi$ (Hz)	412.3	1020	2410
$\omega_x/2\pi$ (Hz)	6.6	7.5	10.3

Table 4.3: Full set of parameters used to create a trapping potential from a Z-shaped 2DEG wire. The parameters to the left define the geometry of the trap. To the right we show several combination of parameters and properties of the trap (position and frequency).

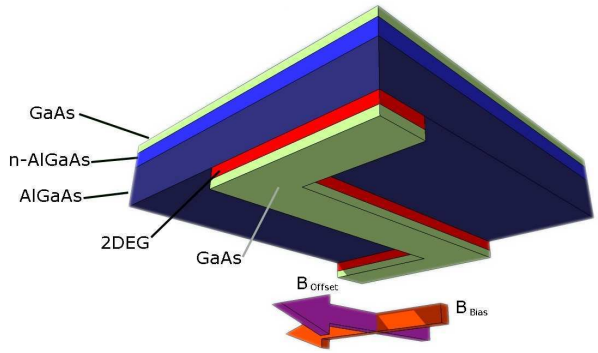

Figure 4.4: Geometry of the proposed trapping configuration using a 2DEG as the conducting element

The inhomogeneity of the potential imprints itself on the density of atoms. The length scale of the corrugation is of the order of the 2DEG-BEC distance and its amplitude increases as the distance to the 2DEG is reduced. The effect on a trapped Bose-Einstein condensate is large if the potential inhomogeneities are comparable with

the chemical potential of the BEC. In the simulation presented here, very weak modulation occurs at a distance above 5 μm ($< 10\%$) (Figures 4.3(a) and 4.3(b)) while at 1 μm the atomic cloud has a strong modulation and the condensate breaks apart (Figure 4.3(c)).

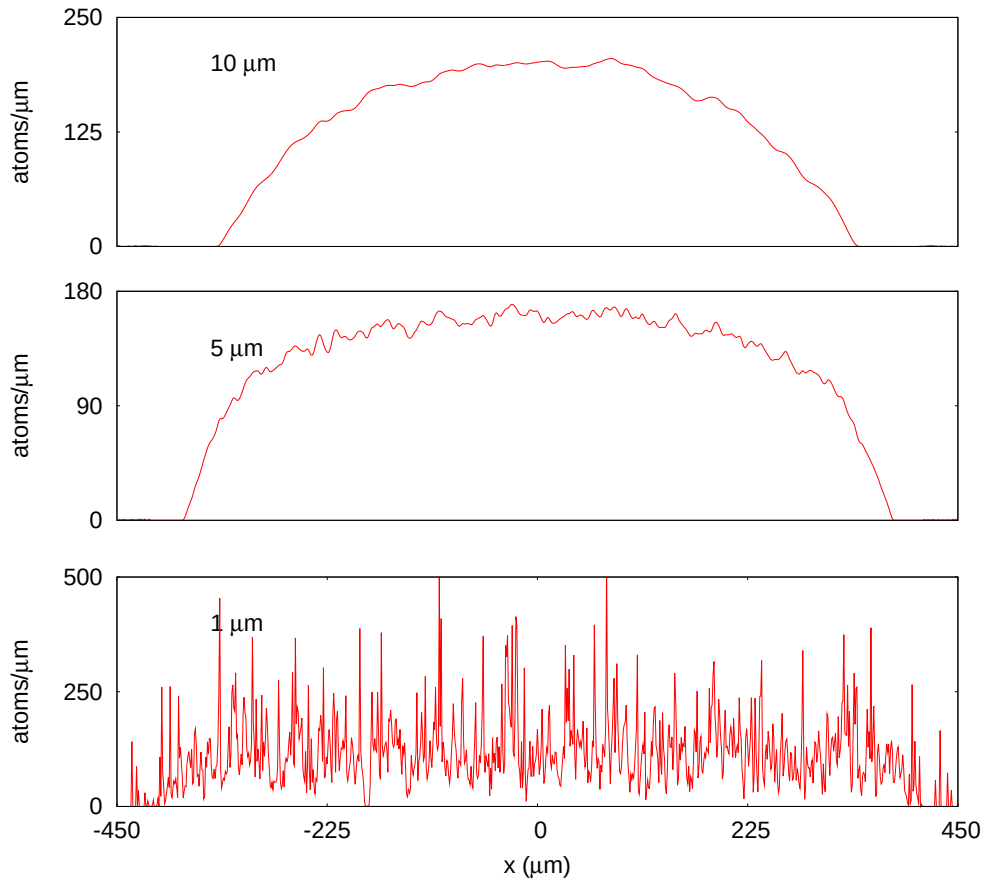

Figure 4.5: Ground state of 10^5 ^{87}Rb atoms at different distances from a 2DEG trapping wire. Effects of the inhomogeneities in the electron density are appreciable at distances around 1 μm. The trap configurations are detailed in Table 4.3

The calculations shown so far demonstrate that, using a 2DEG as the main trapping structure, it is possible to produce magnetic traps with strength similar to those used in experiments that use current carrying metal wires (for example [22, 113]). Trapping configurations employing 2DEG would have several advantages: firstly, the lifetime of trapped states would be restricted only by collisions with the background atoms present in the experiment, even when the atoms are located at submicrometre distances of the heterojunction surface. Secondly, as it is possible to pattern to 2DEG with submicrometre resolution, a higher spatial control of the atomic cloud is possible. Thirdly, using this semiconductor structures for trapping and control leaves the surface free for

other components such as metal gates, improving the quality of the trapping potential and introducing a additional degree of freedom in the design of the atom chip. Finally, the large inhomogeneity at very short distances between the trap and the 2DEG can be reduced by applying time dependent currents, as has been proposed and demonstrated already in atom chips experiments [22, 113].

4.4 Summary

This Chapter has explored the possibility of using a 2DEG as the conducting material for the microtrapping setups discussed in Chapter 3. To demonstrate the feasibility of such a trapping device, all calculations were performed using parameters accessible in present experiments.

The initial motivation for this study was the prediction of long lifetimes for the trapped states, due to the small amplitude of the electromagnetic noise near a 2DEG. Ignoring other mechanisms that induce spin flips in trapped atoms, the predicted improvement is such that the lifetime near a 2DEG would be limited only by collisions with background atoms, even at sub-micrometre distances (Figure 4.1).

In general, it would be possible to produce traps located at distances between $1 - 10$ μm from the 2DEG plane and with frequencies up to a few kHz (see un-dashed region in Figure 4.2 and 4.3). The weakness of the trapping potential due to the low peak current that can pass through a 2DEG, can be compensated by using small external fields. Table 4.3 illustrates a particular combination of parameters (current, geometry and external fields), all attainable in present experiments, which produces a 3D magnetic trap.

Effects of the inhomogeneity of the 2DEG on the trapping potential are also reported in this chapter. At low temperatures, the current flow in a 2DEG is not uniform due to the interaction of the electrons with the ionized-donor layer. This affects the quality of the trapping potential, limiting its operation to distances larger than 1 μm. To illustrate this, the density profile of an 10^4 ^{87}Rb BEC in a Z-trap was calculated for different distances between the trap and the 2DEG plane. At distances of 1 μm, the inhomogeneities of the potential are strong enough to split a trapped BEC into several disconnected pieces, while above 5 μm the density modulations are below 10% (see Figure 4.3).

Despite the low current density that a 2DEG can support, and the strong modulation of the trapping potential at short distances, the use of 2DEGs as conductors for microtrapping can provide several advantages over normal metallic conductors, some of them briefly suggested below.

Semiconductor fabrication techniques like ion implantation, deep-etching or shallow-

etching [32] have sub-micrometre resolution, which could reduce the modulation of the trapping potential due to imperfect definition of the wire edges, as observed in [30, 60, 73, 114, 115]

Also, because the 2DEG is embedded within the semiconductor device, the nearest surface to the trapped atoms is left free, allowing additional elements of control to be fabricated on top. In addition, due to the long-life time of trapped states, the 2DEG based-trap could be used to store ultra-cold atoms, which are extracted later on to be used by independent atom-manipulation configurations. BEC microscopes could be made by fabricating both the trapping wires and the quantum electronic structure to be probed in the same 2DEG.

Several technical questions, like the thermal coupling of the conductors to the substrate required for heat dissipation or the stability of the trapping configuration with respect to fluctuations in the current have not been considered. Nevertheless, from the considerations presented here, we can conclude that a 2DEG in its high-mobility regime can be used to create potentials that are flexible enough to manipulate cold atoms in a similar way to that achieved using normal metals as conducting elements.

CHAPTER 5

Exploring 2DEGs with BEC microscopy

Magnetic field sensors, with unprecedented combinations of resolution ($\sim$ μm) and sensitivity ($\sim$ nT), have been recently demonstrated experimentally using atomic Bose-Einstein condensates [69, 110, 116, 117]. With these setups, a single measurement process is enough to determine one component of the magnetic field inside elongated regions of area ~ 100 μm $\times$ 1 μm [69, 110, 117] . By combining high resolution-sensitivity and large area sampling with a single-shot, BEC-Magnetic Field Microscopy (BEC-MFM) has emerged as a promising tool to perform measurements in regimes inaccessible to other magnetic sensors like SQUIDs, Hall probes, atomic magnetometers or magnetic force microscopes [69].

On the other hand, semiconductor systems have been used extensively to study the boundary between classical and quantum dynamics as the system size becomes comparable to the carrier de Broglie wavelength. Current-voltage characteristics measured under controlled conditions of temperature and external applied electric and/or magnetic fields, provide evidence of a wide range of quantum phenomena including quantum Hall Effects, weak localization, universal conductance fluctuations and quantization of conductance. Such effects are revealed when the dimensions of the system are comparable to one of the carriers characteristics lengths scales: free-path, thermal wavelength or Fermi wavelength for example [96].

This chapter describes how a BEC-MFM can be used to study the structure and operation of heterostructures containing a 2DEG. We show that information can be obtained about electron transport in the 2DEG and the distribution of the donor impurities that create it. Section 5.1 contains a brief explanation of the operational principle of the BEC-MFM [69] and its properties. Section 5.2 explains how a BEC-MFM setup can

be employed to perform measurements of the quantized conductance in Quantum Point Contacts (QPC) defined in a high-mobility 2DEG. Section 5.3 shows that the magnetic field produced by a current through a 2DEG can be measured by a BEC-MFM, providing information about the distribution of ionized donors inside the heterojunction. Finally, Section 5.4 presents a summary of the relevant findings described in this Chapter with emphasis on further applications to be developed.

5.1 BEC Magnetic Field Microscopy (BEC-MFM)

The BEC-MFM technique is based on detecting density modulations of a Bose-Einstein condensate produced by an inhomogeneous magnetic field. Since the atomic cloud distributes according to the intensity of the magnetic field, inhomogeneities in the field translate into density modulations of the condensate, which can be detected by optical methods [30, 60].

Typically, the magnetic field in this systems is produced by two sources: a micro-trap setup (B_{trap}) (see Chapter 3), that fixes the location of the BEC and its sensitivity to inhomogeneities [22] and an inhomogeneous current or magnetization distribution (B_{probed}), which generates the magnetic field to be probed. The total trapping potential becomes corrugated, producing an atomic distribution with density modulations proportional to the intensity of the corrugation relative to the condensate chemical potential ($\Delta\eta/\eta \sim \mu_B B_{\text{probed}}/\mu$).

To quantify the effect that an inhomogeneous magnetic field distribution has on a typical trapping potential, consider a trap made by combining the magnetic field produced by a single current carrying wire ($\boldsymbol{B}_{\text{Wire}} = (0, B_{\text{Wire},y}, B_{\text{Wire},z})$) and an externally applied uniform bias-offset field ($\boldsymbol{B}_{\text{Bias,offset}} = (B_{\text{offset}}, B_{\text{Bias}}, 0)$), as shown in Figure 3.5. This combination produces the magnetic field distribution:

$$\boldsymbol{B}_{\text{trap}} = (B_{\text{offset}}, B_{\text{Bias}} + B_{\text{Wire},y}, B_{\text{Wire},z}) \tag{5.1}$$

A magnetic trap with approximate cylindrical symmetry is produced if the bias field is orientated to compensate the magnetic field produced by the wire. The axis of the resulting trap becomes parallel to the current carrying wire, and located at a distance z_0 given by the condition:

$$B_{\text{Bias}} + B_{\text{Wire},y}(z_0) = 0 \tag{5.2}$$

Now consider a single current element $\Delta\boldsymbol{j} = (\Delta j_x, \Delta j_y, 0)$, like the shown in Figure 5.1, located at the origin of coordinates, just below the trap axis. The magnetic field produced by this element of current is:

$$\begin{aligned} \Delta\boldsymbol{B}(z) &= (\Delta B_x, \Delta B_y, 0) \\ &= \frac{\mu_0}{4\pi}\frac{dxdy}{z^2}(\Delta j_y, -\Delta j_x, 0) \end{aligned} \tag{5.3}$$

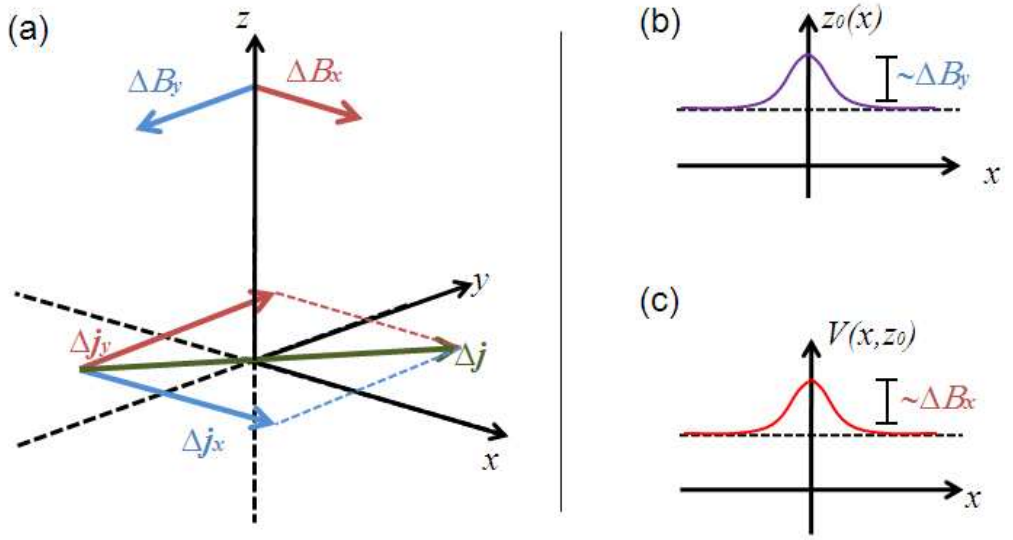

Figure 5.1: (a) Magnetic field components produced by a small current element. The tiny magnetic field generated by $\Delta \boldsymbol{j}$ modifies: (b) the trap position through the component along the bias field (blue arrows) and (c) the bottom of the trap (the potential energy at the minimum) by affecting the applied offset field (red arrows).

where $dxdy$ is the area occupied by the current element. This additional magnetic field affects the shape and position of the trap in a small region directly above the current element position. The new trap position z_0' is defined by the condition:

$$B_{\text{bias}} + B_{\text{Wire},y}(z_0') + \Delta B_y(z_0') = 0 \tag{5.4}$$

Performing a first order Taylor expansion around the original trapping position, this produces:

$$\begin{aligned} B_{\text{bias}} + B_{\text{Wire},y}(z_0) + \partial_z B_{\text{Wire},y}|_{z_0}\,(z_0' - z_0) \\ +\Delta B_y(z_0) + \partial_z \Delta B_y|_{z_0}\,(z_0' - z_0) = 0 \end{aligned} \tag{5.5}$$

Defining $\Delta z_0 = (z_0' - z_0)$ and noticing that $\partial_z B_{\text{Wire},y} \gg \partial_z \Delta B_y$ [1], the shift of the trapping position is:

$$\Delta z_0 = -\frac{\Delta B_y(z_0)}{\partial_z B_{\text{Wire},y}} \tag{5.6}$$

Finally, combining Eqs. (3.10), (5.3) and (5.6), the relative shift of the trap axis is:

$$\frac{\Delta z_0}{z_0} = \frac{\Delta j_x}{z_0^3}\frac{\mu_0}{4\pi} dxdy \frac{1}{\omega_z}\sqrt{\frac{m_F g_F \mu_B}{m B_{\text{offset}}}} \tag{5.7}$$

where ω_z is the trap frequency. In situations of interest, the change of the trap position is of the order of several Bohr radii and, therefore, it can be neglected.

[1] This inequality is satisfied if $|\Delta \boldsymbol{j}| \ll |\boldsymbol{j}_{\text{wire}}|$

The presence of the small current element $\Delta \boldsymbol{j}$ also affects the shape of the trap: the magnetic energy of an atom with magnetic moment μ, trapped just above the current element, becomes[2]:

$$\begin{aligned} E_0' &= \mu(B_{\text{offset}} + \Delta B_x) \\ E_0' &= E_0 + \mu \Delta B_x \end{aligned} \tag{5.8}$$

Combining Eqs. (5.3) and (5.8), the relative shift of the trap minimum is:

$$\frac{\Delta E}{E_0} = \frac{\Delta B_x}{B_{\text{offset}}} = \frac{\Delta j_y}{z^2} \frac{\mu_0}{4\pi} dx dy \frac{1}{B_{\text{offset}}} \tag{5.9}$$

where $\Delta E = E_0' - E_0$. Wildermuth *et al.* [118] demonstrated an ^{87}Rb-based magnetometric setup sensitive to relative inhomogeneities of order $\Delta E/E_0 \sim 4 \times 10^{-6}$. Based on the fact that the sensitivity is increased by reducing the scattering length of the interatomic interaction (see Eq. (5.13), below), they also proposed that using a condensate of ^{133}Cs and adjusting its atomic scattering length through a Feshbach resonance, the sensitivity can be improved up to two orders of magnitude. ^{133}Cs is a good candidate to improve the sensitivity, because there is a resonant change in its scattering length at a magnetic field of only ~ 17 G, which can be made compatible with the presence of the microtrap potential.

Although the working principle for magnetometry is independent of the shape of the trapping potential, elongated geometries containing needle-shaped condensates have been preferred by experimental groups. This trapping shape has a double advantage: first, it allows large area sampling with a single measurement process and second, the simplicity of the relation between the magnetic field distribution along the trap axis and the atomic linear density of quasi-1D condensates simplifies the analysis of the data obtained [69, 110, 116, 117]. In the Thomas-Fermi approximation, the 1D density ($\eta_{1\text{D}}$) is related to the intensity of the magnetic field by:

$$\mu_{1\text{D}} - m_F g_F \mu_B \left|\mathbf{B}(x)\right| = \hbar \omega_\perp \sqrt{1 + 4 a_s \eta_{1\text{D}}(x)} \tag{5.10}$$

where $\omega_\perp$ is the frequency in the transverse direction and the effective 1D chemical potential $\mu_{1\text{D}}$ is fixed by the total number of condensed particles, the scattering length and the trap shape [119].

The sensitivity of the magnetic BEC microscope can be evaluated using Eq. (5.10). In the mean field regime where $4 a_s \eta_{1\text{D}}(x) \gg 1$, a small current element produces a change in the density of:

$$\Delta \eta_{1\text{D}} = \frac{m_F g_F \mu_B \Delta B_x}{2 \hbar \omega_\perp a_s} \tag{5.11}$$

If a measurement of the density is performed with resolution Δx_0, then the difference in the number of atoms detected compared with the unperturbed trap is:

$$\Delta N = \frac{m_F g_F \mu_B \Delta B_x \Delta x_0}{2 \hbar \omega_\perp a_s} \tag{5.12}$$

[2] Here, it is assumed that the projection of the atomic moment is not modified by the small perturbing magnetic field, $\Delta \boldsymbol{B}$.

Now examine the above calculation as follows: if ΔN is the minimal atom number resolved by an imaging system with resolution Δx_0, the smallest variation in the magnetic field that can be registered is:

$$\Delta B = \frac{2\hbar^2 a_s}{m m_F g_F \mu_B} \frac{\Delta N}{\ell_0^2 \Delta x_0} \tag{5.13}$$

where ℓ_0 is the size of the condensate along the strong trapping direction [69]. This expression indicates that the sensitivity can be adjusted to the level of the inhomogeneities to be probed by manipulating the trapping potential, the atom-atom interaction strength, or both.

Two regimes of sensitivity can be identified in Eq. (5.13), depending on the spatial resolution of the magnetic microscope [118]. They are shown in Figure 5.2. In the first case, if ℓ_0 is smaller than the resolution of the imagining system, then the sensitivity has a strong dependence on the spatial resolution, $\sim 1/\Delta x_0^3$. Nowadays, the achievable optical resolution is typically in the range $(0.5 - 10)$ μm, corresponding to transverse frequencies of $(464.73 - 7.299)$ Hz ($(303.99 - 4.775)$ Hz) for a ^{87}Rb (^{133}Cs) condensate.

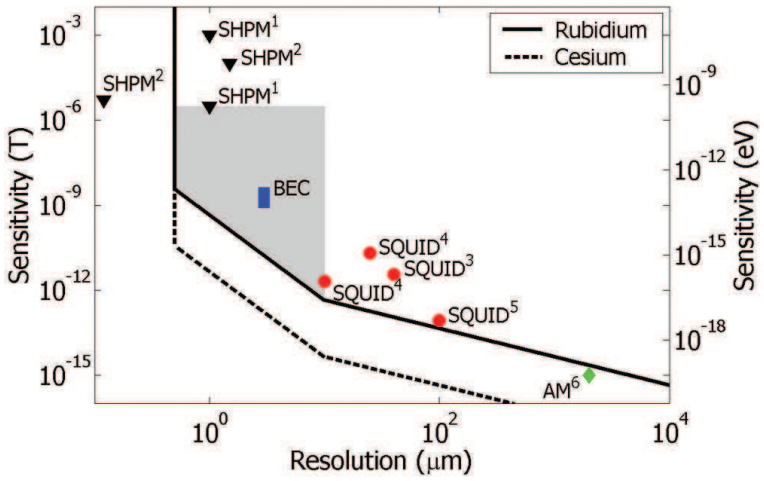

Figure 5.2: Figure taken from Wildermuth, *et al.* [118]. Sensitivity vs. spatial resolution for BEC-MFM. Dotted line corresponds to the estimated sensitivity of a ^{133}Cs BEC with a scattering length of 0.1 nm. The shaded region indicates the sensitivity-resolution range accessible by the setup reported in the same reference, using an ^{87}Rb condensate. The field sensitivity vs. resolution of modern magnetic microscopes are shown for comparison.

The second regime corresponds to trapping geometries where the size of the ground state along the transverse direction is bigger than the optical resolution. For this case, the spatial resolution in the transverse direction is given by $\ell_0 = \sqrt{\hbar/m\omega_\perp}$, and is set by the imaging system along the weak trapping axis. The sensitivity can be improved only by reducing the imaging resolution and scales as $\sim 1/\Delta x_0$. This second regime

corresponds to traps with frequencies of the order or smaller than ~ 1 Hz, which are technically challenging and difficult to realize [69].

The magnetic field microscope demonstrated by Wildermuth, *et al.* has a resolution of 3 μm and sensitivity of 4 nT [118]. Better sensitivities could be obtained by manipulating the atomic scattering length through the Feshbach resonance mechanism. For example, the atomic scattering length of ^{133}Cs can be adjusted to ~ 0.1 nm by controlling the offset magnetic field at the mG level [118], which would allow a sensitivity of the order of ~ 10 pT, i.e., three orders of magnitude better than attained so far [69, 118].

The magnetic sensor described here can be used to study the internal structure of materials and the dynamics of electron transport in conducting systems [118]. For example, the distribution of electric current through a metallic film has been reconstructed from measurements of the magnetic field produced [22, 110, 118]. The same idea is applied in the next two sections to study the current flow through a typical high-mobility 2DEG.

5.2 Detection of quantization of conductance in QPCs

The transport properties of a 2DEG depend on several length scales: the mean free path, ℓ_{free}, the coherence length, ℓ_ϕ, the de Broglie wavelength, λ_F and the size of the sample, L. The first two are limited by imperfections in the crystalline structure of the semiconducting layers and the electron-phonon interaction. At very low temperature, the electron-phonon interaction is strongly suppressed and the only remaining scattering mechanism is associated with the lack of periodicity of the system. Additionally, the carriers move ballistically if the size of the sample is smaller than the mean free path. Further reduction of the sample's size, making it comparable to the carriers' de Broglie wavelength (or Fermi wavelength), enhances the role of the quantization of modes, associated with the geometry of the sample, on the electron transport properties.

In a Quantum Point Contact (QPC) electrons move through a channel smaller than the mean-free path and the coherence length, and whose width is comparable with the Fermi wavelength. In this section we suggest how the quantized conductance of a QPC can be studied with the field microscopy techniques described in the previous section.

5.2.1 Quantized conductance of a 2D rectangular conductor

When a difference of potential (V) is applied between the ends of a conductor, an electric current (I) flow through it. Ohm's law relates both quantities in a linear form:

$$I = GV \tag{5.14}$$

where G is the system's conductance.

The conductance of a 2D rectangular conductor of length L, along the direction of current flow and with W, is given by:

$$G = \frac{\sigma W}{L} \tag{5.15}$$

where the conductivity σ is independent of the shape of the conductor [96].

Eq. (5.15) indicates that as the length of the conductor is reduced, the conductance should increase without limit. In contrast, measurements performed with QPCs defined in a 2DEG demonstrated that G approaches a finite value when the length of the conductor becomes shorter than the carrier mean free path (see B. J. van Wess *et al.* [120] and D. Wharam *et al.* [121]). Along with this observation, discrete jumps in the conductance, of size $G_c = \frac{2e^2}{h}$, occur as the width (W) of the QPC is varied.

Both characteristics [95, 96], finite conductance and its quantization, are consequences of the discrete nature of the electronic energy spectrum in a bounded region. This dominates the transport properties when the system's dimensions are comparable with the carrier's de Broglie wavelength, and smaller than the mean-free path and the coherence length, as discussed above.

Confining geometries in a 2DEG act like waveguides for electrons, causing quantization of the propagating modes (see Fig. 5.3(a) and (b)). The simplest case consists of a rectangular region with hard wall boundary conditions, for which the energy of the motion in the transverse direction to the conductor's length is quantized according to:

$$E_\ell = \frac{h^2}{2m^*}\frac{n^2}{4W^4}, \qquad \lambda_\ell = \frac{2W}{n} \tag{5.16}$$

where m^* the carrier effective mass and $n = 1, 2, 3 \ldots$ [96].

Since only modes with energy smaller than the carrier's Fermi level (E_F) are populated, the total number of occupied modes can be modified either by changing E_F or the structure of the energy spectrum, Eq. (5.16), as illustrated in Figure 5.3 (a). In this simple example, the number of transverse occupied modes, M, in the rectangular region is approximately:

$$M \simeq \text{int}\left[\frac{W}{\lambda_F/2}\right] \tag{5.17}$$

where λ_F is the Fermi wavelength.

If the rectangular conductor connects two electron reservoirs with different electrochemical potential ($\Delta\mu = \mu_L - \mu_R$), as illustrated in Figure 5.3(b), and assuming that the electrons enter and leave the conductor without reflecting from the contacts, the conductance of the system is given by [96]:

$$\frac{eI}{\Delta\mu} = G = \frac{2e^2}{h}M \tag{5.18}$$

where M is the number of open modes in the central region [95, 96]. This equation explains the quantization of conductance observed by B. J. van Wess *et al.* [120] and D. Wharam *et al.* [121], shown in Figure 5.3(d).

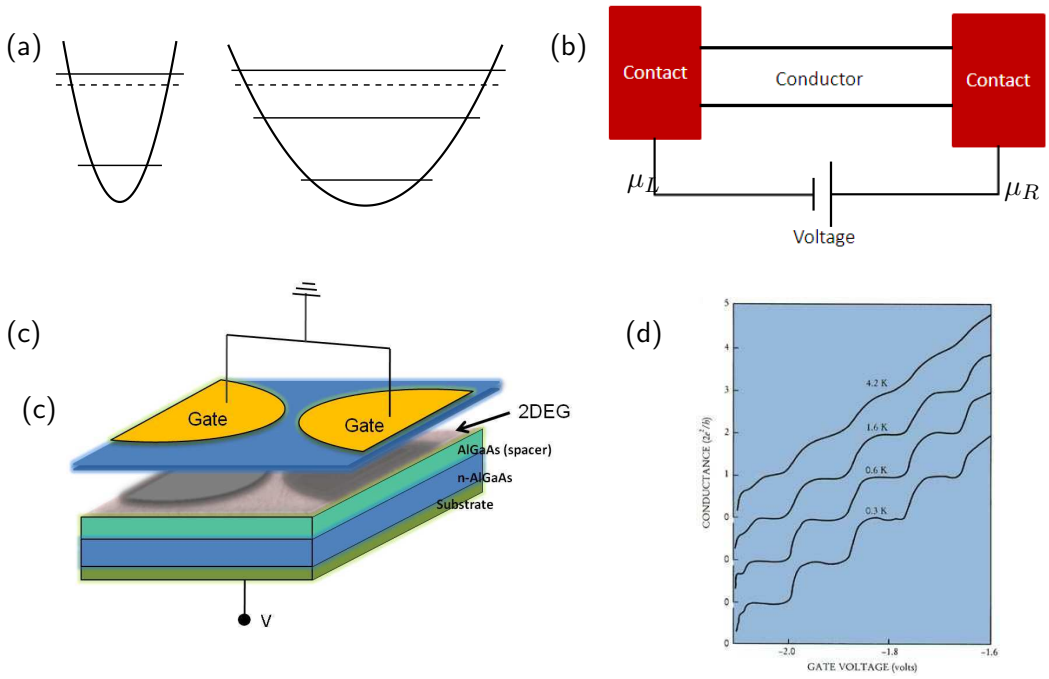

Figure 5.3: (a) Sketch showing how the abrupt change of the occupied modes in a QPC occurs. The number of modes below the Fermi level (dashed line) change abruptly by modifying the potential energy. (b) Conductor sandwiched between two contacts with an applied bias voltage equal to $\mu_L - \mu_R$. The harmonic potential shown in panel (a) describe the electron confining in the transverse direction of the conductor. (c) Schematic diagram showing a QPC formed by depleting a 2DEG. (d) Conductance versus gate voltage (which controls W) in a 2DEG at different temperatures. Quantized jumps of the conductance are due to changes in the occupancy of the energy levels (from [120].)

A Quantum Point contact (QPC) is an approximated experimental realization of the system described above. It consists of a thin constriction connecting two wide electrically-conducting regions in a 2DEG and whose width is comparable to the electron wavelength. Such a constriction can be produced by applying a negative voltage to an appropriate shaped layer of metallic material deposited on top of the cap layer of a heterojunction, as schematically shown in see Figure 5.3 (c) [96]. This setup is particularly convenient because the constriction width can be controlled via the intensity of the negative voltage, allowing control over the number of open modes (for electron transport) between the side regions.

In a 2DEG like that considered here (see Table 2.2), the quantization of the conductance would be observable when the electrons are forced to pass through a constriction a few tens of nm wide [96, 100, 122]. The current flow in the QPC depends on the voltage applied between the regions connected. To estimate this quantity, consider a QPC with ~ 5 open channels, and an applied voltage of 0.5 mV across the constriction;

this would produce a current of the order $\Delta j_x \sim 2.6$ A/m. Table 5.1 indicates a set of parameters of a QPC modelled as a rectangular region in the 2DEG we are using as a model.

QPC parameters	
Width	~ 20 nm
Length	$\sim 0.1 - 0.5$ μm
Fermi wavelength	~ 40 nm
Open modes	~ 50 per μm

Table 5.1: Properties of a typical QPC modelled as a small rectangular conducting region.

Electron flow through QPCs has been studied in the quantum conductance [122] and Quantum Hall regimes [123] confirming the mode occupation interpretation briefly reviewed here.

5.2.2 Detection of quantization of conductance with a BEC-MFM

The magnetic field generated by electron flow through a thin constriction in a 2DEG (noted as B_{QPC}) can produce a localized modulation of the density in a neighbouring BEC. We now establish the conditions needed to make such a modulation observable by a magnetic BEC microscope.

Suppose a magnetic trap holds a BEC near a current carrying QPC. The effect of B_{QPC} on the microtrap is maximized by an appropriate orientation of the trapping setup with respect to the current flow to be probed. As shown in Section 5.1 (specifically Eq. (5.8)), the trapping potential is mainly affected by the component of the perturbing magnetic field *parallel* to the trap axis[3] as shown in Figure 5.1(c), produced by a current orthogonal to this axis.

A relative orthogonal orientation between the trapping wire and the current flow in the semiconductor structure results in an offset magnetic field, B_{offset}, parallel (anti-parallel) to B_{QPC}. In this configuration, the trapping potential develops a small barrier (dimple) (see Figure 5.1(c)) whose height (depth) is proportional to the current in the semiconductor structure I_{QPC}. As a consequence of this perturbation on the trapping potential, the condensate becomes less (more) dense at the position of the barrier (dimple).

[3] The effect on the *position* of the trap can be neglected. Using a set of typical values for the trapping setup and the QPC condition, Eq. (5.7) produces:

$$\frac{\Delta z_0}{z_0} \sim 1 \times 10^{-5}$$

Assuming a working distance for the BEC-MFM of $z_0 \sim 10^{-6}$ m, the displacement of the trapping position becomes smaller than the atomic radius ($\Delta z_0 \sim 0.1$ Å).

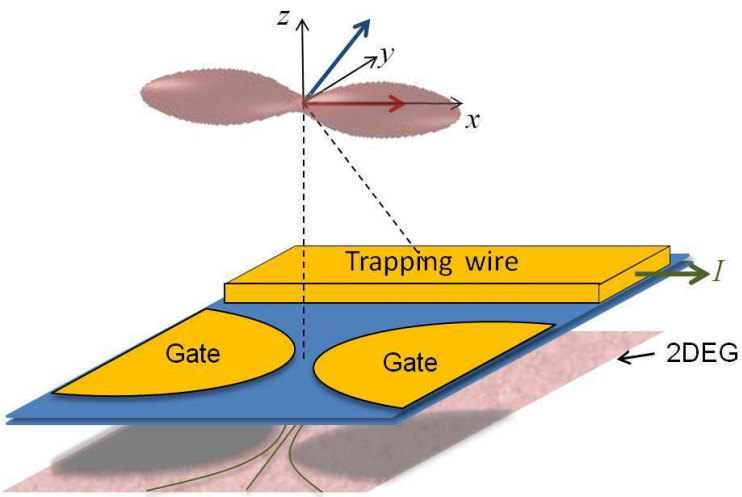

Figure 5.4: Schematic of a magnetic BEC microscope set to detect quantized changes in the conductance of a QPC. The trapping potential is generated by a current carrying Z-shaped wire (bent arms not shown) with external bias and offset fields. The trap axis (along the x-direction) is oriented orthogonal to the current flow in the QPC (along the y-direction, on average) so that the magnetic field generated by the QPC current has a large effect on the condensate. Continuous lines In the lower layer represent the electron flow through the constriction and the shadows correspond to regions in the 2DEG depleted by the voltage applied to the gates.

This is schematically shown in Figure 5.4

Consider the QPC as a rectangular region with the dimensions and properties indicated in Table 5.1. Figure 5.5 shows the intensity of the magnetic field produced by $I_{\text{QPC}} = 0.038$ μA as function of the perpendicular distance from the QPC's centre, which is given by Eq. (3.17).

In order to establish the conditions needed to detect the small magnetic field B_{QPC} and its quantized jumps, three aspects should be considered: the range of operation of a typical magnetic BEC sensor, the intensity of the magnetic field produced and the trapping and resolution characteristics.

Regarding the range of atom-surface distances offered by a magnetic BEC microscope, notice that due to the presence of an atom-surface attractive potential (Casimir-Polder potential), BEC-MFM can only operate at a distance between the tested source and the condensate larger than 1 μm [118]. A typical BEC-MFM setup can be set to work in the range of distances $1 - 5$ μm from the surface [22].

The sensitivity required for a magnetic field sensor to detect quantized conductance is set by the intensity of the magnetic field, B_{QPC}, whose value depends on the distance to the source. For a QPC with the properties considered above, and with a voltage of

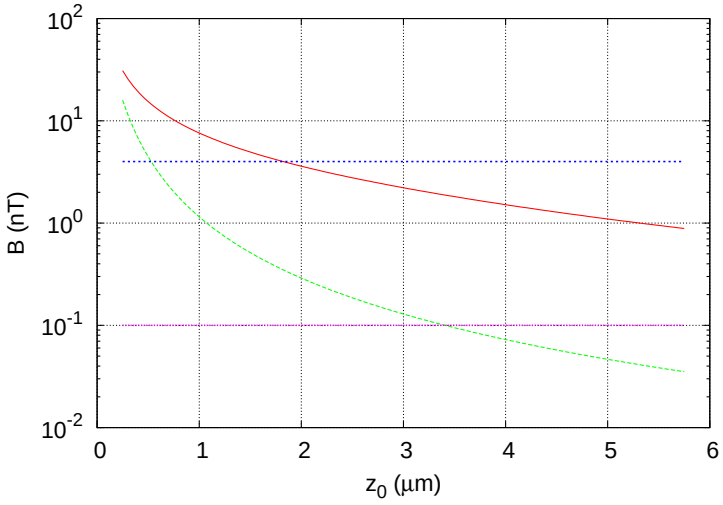

Figure 5.5: Magnetic field due to current through a rectangular sample of 2DEG with a single occupied mode ($W = 21.82$ nm) and lengths 300 nm (dashed curve) and 10 μm (solid curve), as a function of the perpendicular distance, z_0. Upper and lower horizontal lines correspond to the detection sensitivity levels of ^{87}Rb and ^{133}Cs condensates, respectively [69, 118].

0.5 mV applied, the magnetic field produced would have an intensity of the order of $B_{\text{QPC}} \sim 0.129$ nT at a distance of 3μm.

Finally, assume that the BEC is prepared in a trap with transverse frequency ~ 300Hz and imaged with a spatial resolution of $\Delta x_0 = 1$ μm and atom sensitivity of $\Delta N \sim 5$ atoms. It follows from Eq. (5.13) that detecting jumps of conductance, via the corresponding magnetic field change $B_{\text{QPC}} \sim 0.129$ nT, can be done if the condensate comprises an atomic species with a scattering length of $a_s \sim 0.5$ nm$= 10a_0$.

Trapping setup	
Shape	Z
Width (W)	100 μm
Length (L)	1000 μm
Current	213.8 mA
Bias Field	12.9 G
Offset Field	30 G
Position(z_0)	3 μm
Frequencies	$(4.32, 267.1, 272.4)$ Hz

Table 5.2: Parameters of the magnetic trap suitable to measure the quantization of conductance in a QPC.

Natural scattering lengths for alkali atoms are usually larger than $15a_0 \sim 1$ nm [40]. Smaller scattering lengths can, however, be achieved by using the Feshbach resonance mechanism. Cesium is a good candidate to be used as a field sensor since its scattering length becomes zero at a low magnetic field of 17 G [69, 118]. Near this zero crossing, the scattering length scales linearly with a slope ~ 6 nm/G, requiring mG control to obtain a scattering length in the desired range $a_s \sim 0.1$ nm .

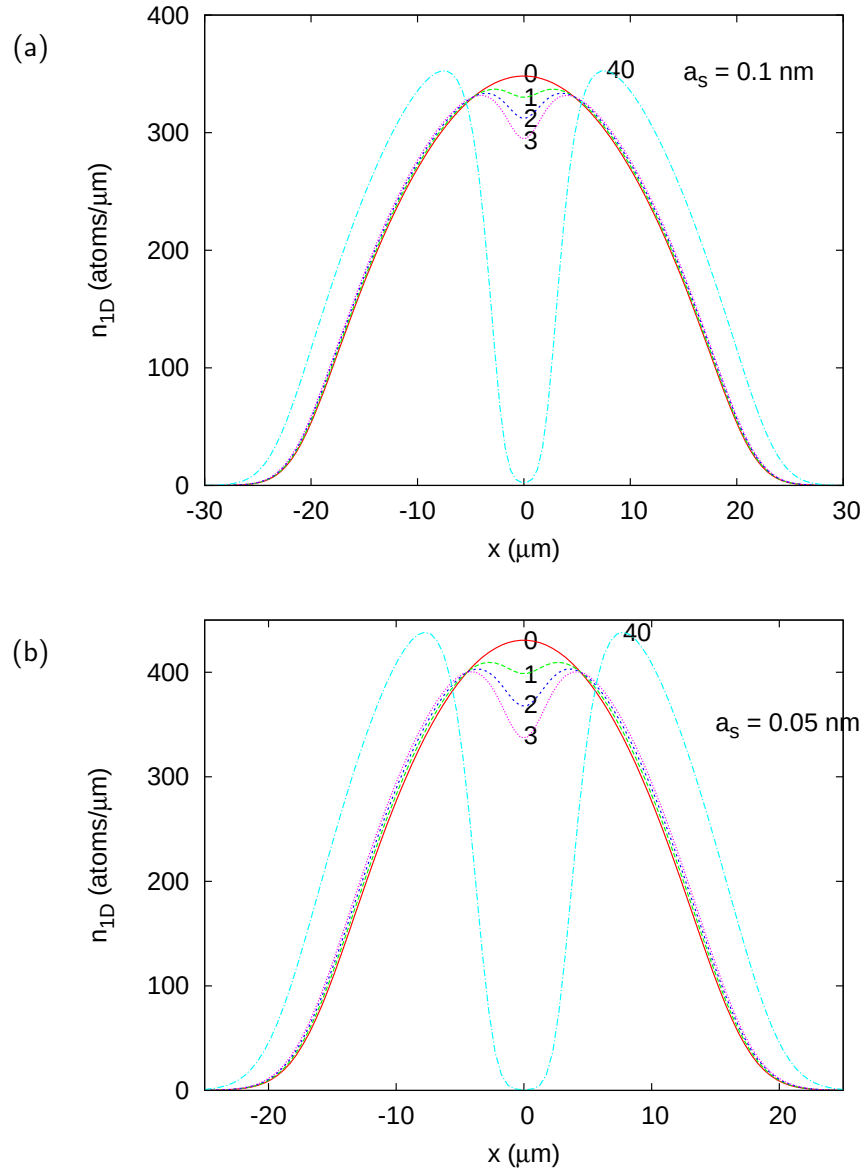

Figure 5.6: Density profiles for 10000 ^{133}Cs atoms with (a) $a_s = 0.1$ nm (b) $a_s = 0.05$ nm. The centre of the trapping potential is positioned at 3 μm from a rectangular conductor of dimensions 0.3 nm $\times M\lambda_F/2$, with $M = 0, 1, 2, 3$ and 40 being the number of open modes, carrying a current of $\sim M \times 0.038$ μA. The trapping potential is built by superposing the magnetic field produced by the QPC (Figure 5.5) and the trap created by the setup in Table 5.2. The depth of the central dimple increases with the number of open modes.

Further reduction of the scattering length results in a more sensitive magnetometer. Figure 5.6 shows the calculated ground state of a 10000 ^{133}Cs atom BEC trapped at $z_0 = 3.0$ μm from a thin and short rectangular conductor (simulating the QPC), carrying a small current $I_{\text{QPC}} \sim 0.038$ μA/mode. The exact distribution of magnetic field was calculated for a trap comprising the traditional Z-shaped current carrying wire plus bias and offset magnetic fields using the parameters shown in Table 5.2 In the absence of current through the QPC, the potential energy near the bottom of the trap can be approximated by a harmonic potential of frequencies $(4.32, 267.1, 272.4)$ Hz along each of the three spatial directions. As can be seen, each time a new transverse mode in the conducting region is occupied, a variation in the density of the condensate on the level of $\sim 10\%$ is produced. Relative changes of this size are easily observable by present imaging systems used in BEC-MFM [80].

5.3 Detection of long-range order in the donor distribution of heterostructures

Doped heterojunctions with a conducting layer embedded have great technological value. Their transport properties depend on the composition of the sample, which can be precisely controlled under modern fabrication conditions and can be manipulated through externally applied electric and magnetic fields.

At low temperatures, the electrical behaviour of a 2DEG is determined mainly by the charge distribution inside the heterojunction [100], which is difficult to measure due to the impossibility of having direct access to either the free carriers or the donors. One way to probe the distribution, however, is to perturb locally the carrier density by coupling capacitively the tip of a scanning probe microscope (SPM) to the sample [112]. Then, measurements of the conductance provide information about the charge density directly below the tip [112]. With this technique, the electron density and its flow in a 2DEG have been observed with resolution better than 10×10 nm^2, in samples of lateral size up to a few hundred of μm [112, 123]. A high resolution image of a large sample area can be produced by performing many measurement procedures placing the sensing tip at different positions above the sample.

This section shows that the BEC-MFM, described in Section 5.1, provides a good alternative to determine features of the donor distribution involving micrometre length scales, with a single measurement shot. This result is based on numerical evaluation of the magnetic field produced by electron flow in a high mobility 2DEG and of the resulting density profile of a BEC held by a trap near the 2DEG.

5.3.1 Inhomogeneous magnetic field produced by a current in a 2DEG

At low temperatures, when the electron-phonon interaction is suppressed, electrons in the 2DEG are deflected, usually at small angles, by their interaction with ionized donors. The Coulomb interaction between ionized donors and free charges in a 2DEG is screened by the electron-electron Coulomb interaction. In the linear screening regime, where the effect of the ionized-donors on the 2DEG is weak, the screened potential is given by Eq. (2.2) [102].

Although neutral donors in a heterojunction deposit randomly during the fabrication process, the distribution of ionized donors acquires a nanometre-scale correlation length when they donate the electrons to form the 2DEG, that depends, among other factors, on the temperature and illumination conditions under which that process occur. The screened potential, Eq. (2.2), would only reflect properties of the donor distribution if the distance between the donor and 2DEG layers is smaller than this correlation length.

Deflection of the carriers' paths is determined by the gradient of Φ_{screened} in Eq. (2.2), and imprints information about the correlation of the donor distribution in the magnetic field produced. Signatures of the correlation of the donor distribution on the magnetic field would survive up to distances smaller than its correlation length, due to the suppression of features with length scale λ according to $\sim \exp(-2\pi z/\lambda)$ in Eq. (2.2).

The magnetic BEC microscope, described previously in this chapter, can detect magnetic fields at distances larger than 1 μm from its sources, which is much larger than the correlation length of the donor distribution in a heterojunction, typically a few hundred nanometres [124]. As a consequence, considering an uncorrelated distribution of ionized donors is enough to evaluate the effects of interest here.

Consider the non-uniform contribution to the current flow, $\Delta\boldsymbol{j}(\boldsymbol{r})$, i.e. originating from fluctuations in the donor distribution. The current flow generated by a voltage applied in the plane of the 2DEG has a non-uniform component, $\Delta\boldsymbol{j}(\boldsymbol{r})$, originating from the inhomogeneity of the donor distribution. This component is given by the gradient of the screened donor potential Eq. (2.2):

$$\Delta\boldsymbol{j}(\boldsymbol{r}) = -\sigma\boldsymbol{\nabla}\Phi_{\text{screened}}(\boldsymbol{r}) \tag{5.19}$$

where σ is the conductivity of the 2DEG.

In a typical heterojunction, the electron-donor potential has features with a length scale of ~ 100 nm, which is comparable to the distance between the 2DEG and the donors. The amplitude of those features is $\lesssim 10\%$ of the Fermi energy, typically $\Delta\Phi \sim 1.0$ meV. Consequently, from Eq. (5.19), the intensity of inhomogeneities of the current are $|\Delta\boldsymbol{j}| = 1$ A/m for a sample with $\sigma = 2.58 \times 10^{-4}\ \Omega^{-1}$.

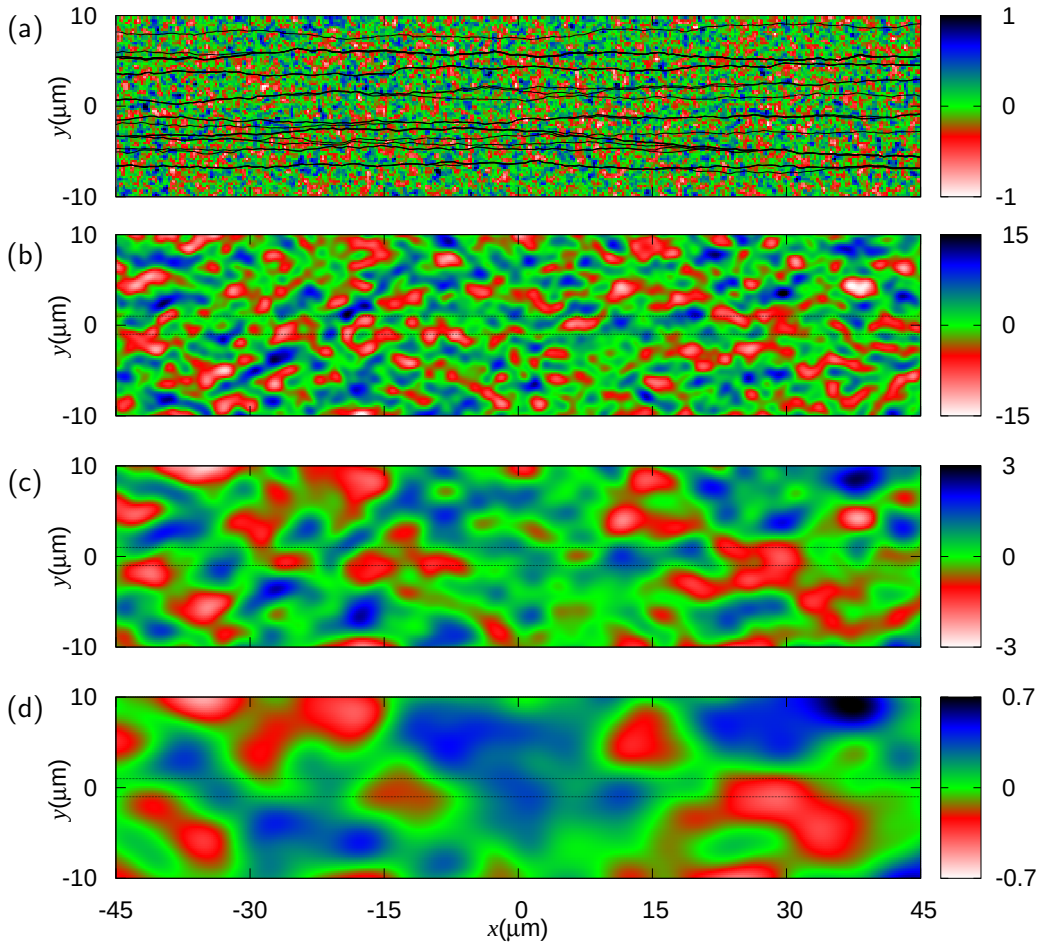

Figure 5.7: (a) Screened electron-donor potential within a typical 2DEG (parameters given in Table No. 2.2) and current flow lines (black). (b)-(d) Component of the magnetic field along the y-direction (parallel to the mean current direction) (in nT) calculated from Eq. (5.19) at (b) 1 μm, (c) 3 μm and (d) 5 μm above a 2DEG sample. For this calculation, the 2DEG is assumed to have a conductivity of $\sigma = 2.58 \times 10^{-4}\ \Omega^{-1}$.

The magnetic field produced by this current has inhomogeneities whose intensity and length scale depend on the distance to the 2DEG. Figure 5.7 shows the component of this inhomogeneous magnetic field along the $x-$axis, i.e. in the plane of the 2DEG and parallel to the electric field (x) corresponding to the applied voltage (see Appendix A for details about how this calculation was done). As explained in Section 5.2, the density of a neighbouring BEC trapped by a Z-trap configuration oriented along the $x-$axis would be modulated by the x component of the inhomogeneous magnetic field (the one which is parallel or anti-parallel to B_{offset}).

As the distance to the 2DEG increases, the amplitude of the magnetic field inhomogeneities decay and their profile becomes smoothed. Similar behaviour has been

observed in several experiments where the magnetic field produced by current-carrying metallic films is mapped from the density modulations of a BEC held next to it [22, 110, 116, 117, 118]. To analyse those experiments, calculation of the magnetic field produced by current confined in a plane were performed (see Section 5.3.3). These calculations successfully explain the general trend of the magnetic field intensity and have revealed interesting long-range structure in the pattern of current flow in metals. We now consider how a BEC-MFM would respond to the magnetic field above and current distribution within a 2DEG.

The magnetic field has features with a typical length scale comparable to the distance from the BEC to the 2DEG. This is because fluctuations with a length scale λ in the plane of the 2DEG decrease exponentially such that very fast fluctuations do not reach the BEC. Next section show that the amplitude of the inhomogeneities of the magnetic field produced by a current flow through the 2DEG considered here are large enough to be detected by an appropriate BEC-MFM setup.

5.3.2 Density modulations of a BEC trapped next to a current carrying 2DEG

To prove the feasibility of measuring the inhomogeneous magnetic field produced by a current-carrying 2DEG, consider a typical BEC magnetic microscope setup holding a condensate next to the 2DEG. Figure 5.7 suggests that the microscope will require a sensitivity of ~ 1 nT. Assuming that a ^{87}Rb condensate is imaged with an isotropic resolution of 1 μm, such sensitivity can be easily reached with an atom number resolution of $\Delta N \sim 12$.

Three factors impose a micrometre scale limit for the resolution: the minimum distance at which a BEC can be held from a surface, the exponential decay of the magnetic field produced by a planar current (see Section 5.3.3), and the resolution of optical imaging, which falls in the range of $(0.5 - 10)$ μm. Figure 5.8 shows a schematic diagram of a setup intended to measure the inhomogeneities of the magnetic field produced by a current-carrying 2DEG [118].

Suppose the condensate is trapped by a Z-wire setup (see Section 3.11) where the current and external magnetic fields are adjusted to locate the trap at different heights from the 2DEG, in which a small inhomogeneous current $\boldsymbol{j}_{\text{2DEG}}$ flows. Table 5.3 specifies precise combinations of parameters needed to create a trap 5 μm, 3 μm and 1 μm above the heterostructure, using a trap configuration as shown in Figure 3.11, with a central wire of dimensions $L \times W = 1.5$ mm $\times$ 100 μm. If the condensate is positioned far from the edges of the trapping wires, but close to the 2DEG, the modulation of the condensate density would be determined only by inhomogeneities in the 2DEG, and be proportional to $\boldsymbol{j}_{\text{2DEG}}$, with imperfections of the wire edges having a negligible effect [22].

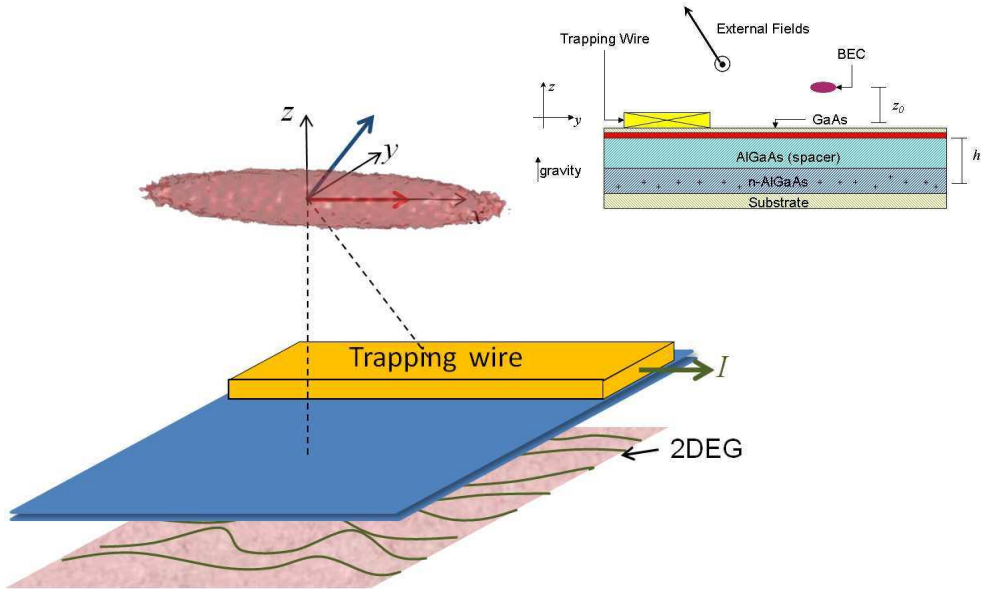

Figure 5.8: The inhomogeneous magnetic field produced by a current-carrying 2DEG modulates the density of a BEC held nearby in a microtrap. Controlling the external magnetic fields allows precise positioning of the condensate and adjustment of its sensitivity.

Trapping setup				
z_0(μm)	B_{offset} (G)	B_{Bias} (G)	Current (mA)	$(w_x, w_y, w_z)/2\pi$ (Hz)
1	20	12.98	209.54	$(2.46, 499.54, 500.00)$
3	20	12.70	210.22	$(3.00, 499.54, 500.00)$
5	20	12.45	211.56	$(3.47, 499.54, 500.00)$

Table 5.3: Parameters of the magnetic trap used to measure the inhomogeneous magnetic field produced by a current-carrying 2DEG.

To quantify how the presence of a current in the 2DEG affects the density of the condensate, we evaluate the density profile of a condensate comprising 10^4 ^{87}Rb atoms. We did this by calculating the ground state of the atomic system using an imaginary-time evolution of the Gross-Pitaevskii equation (1.27) (see Appendix A).

The magnetic field distribution that determines the potential energy, Eq. (1.31), is given by the trapping setup together with the magnetic field produced by the current distribution $\boldsymbol{j}_{\text{2DEG}}$, Eq. (5.19). The first contribution, the harmonic potential trapping, can be evaluated (in an approximate way) by splitting the Z-wire into three rectangular sections and applying Eq. (3.17) to each one of them.

The contribution coming from the current in the 2DEG is evaluated for a sample of dimensions ~ 3 mm $\times$ 3 mm. The current distribution, $\boldsymbol{j}_{\text{2DEG}}$, is determined by a

combination of Eqs. (2.2) and (5.19), whilst the magnetic field produced is calculated by numerical integration of the Biot-Savart law over the full sample area.

Computationally, the last mentioned task is the most difficult to perform. This is because the magnetic field should be evaluated in a 3D volume, with a spatial resolution high enough to allow a precise integration of the Gross-Pitaevskii equation. This numerical work produces the density distribution of the condensate in the combined magnetic field, which, when integrated along the transverse plane ($y - z$) direction, gives the density profile along the trap axis ($\eta(x)$). This result is shown in Figure 5.9 for different distances between the 2DEG and the BEC. In this figure, we also present the change of the atom density relative to the unperturbed ground state ($(\eta - \eta_0)/\eta_0 \times 100$), in the central region of the BEC (see insets and zoom).

The lowest density modulation so far detected using a BEC-MFM is around 5% [22, 110]. This suggests that, from the results presented in Figure 5.9, the inhomogeneous magnetic field produced by the current in the 2DEG is strong enough to be detected by a condensate held at a distance between 1 μm and 3 μm from the 2DEG. When this distance is 5 μm, the modulation of the density falls just below the present detection limit.

We find clear correspondence between the magnetic field and atom density modulations are evident at distances $z_0 = 5$ μm and $z_0 = 3$ μm, where the positions where $\Delta B_x = 0$ points (Figs. 5.7 (a),(b)) along the trap axis coincide with those where $\Delta\eta = 0$ (Figs. 5.9 (a), (b)), but when the cloud extension in the transverse direction is comparable with the length scale of the inhomogeneities, as occurs at $z_0 = 1$ μm, this correspondence is weaker (compare upper panel in Fig. 5.9(c) and 5.7(c)).

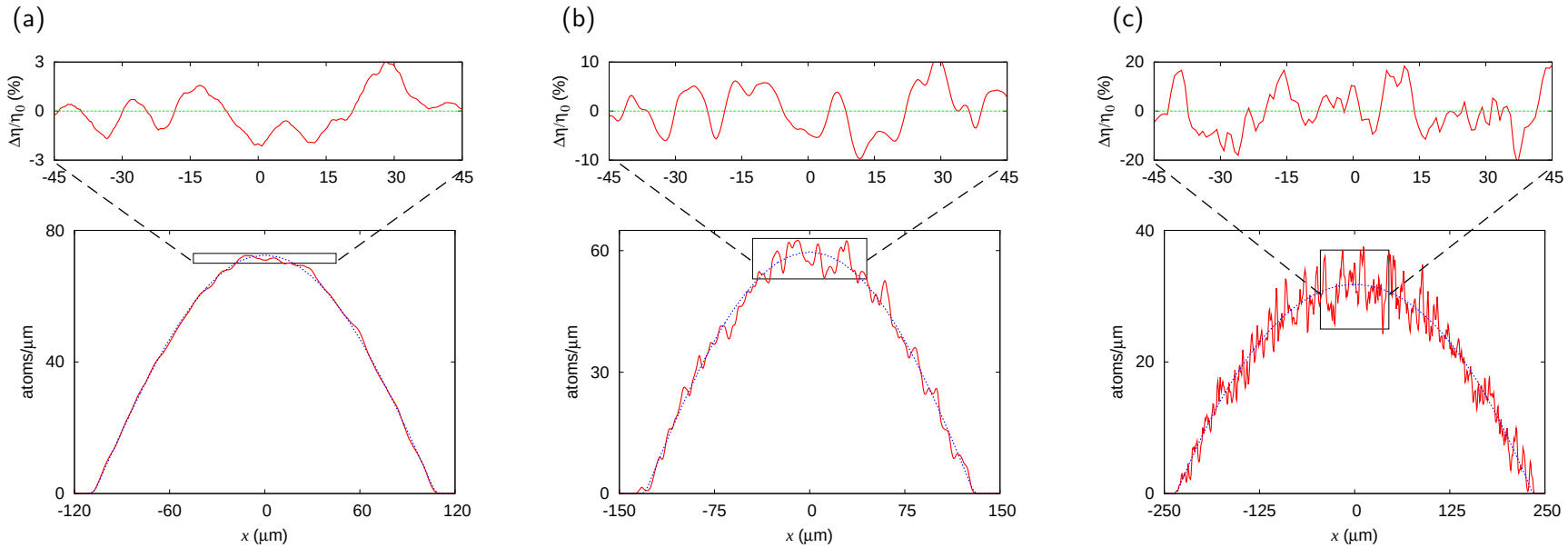

Figure 5.9: Calculated density profiles of a ^{87}Rb BEC containing 10^4 atoms (red line), held at different distances from a current-carrying 2DEG. Detailed parameters of the trapping potential are shown in Table 5.2. The position of the trap corresponds to (a) 5 μm, (b) 3 μm and (c) 1 μm. The local relative density modulation is shown for the central region in each case (upper panels). Blue lines (green lines) in lower (upper) panels corresponds to the ground state in absence of trap corrugation.

5.3.3 Relation between the donor statistics and the inhomogeneous magnetic field above a 2DEG

Now, we turn our attention to the relation between the magnetic field inhomogeneities and the underlying donor distribution. Combining Eq. (2.2) and the fact that the magnetic field produced by a current distribution confined in a two dimensional region can be obtained from its 2D Fourier transform [125] (see Appendix B), then $B_x(x; z_0)$ along the trap axis is given by:

$$B_x(x, z_0) = \frac{\mu_0 \sigma e}{4\epsilon\epsilon_0} \int d^2k \frac{k_y \ \eta_d(\boldsymbol{k})}{k + k_s} e^{-k(d+z_0)} e^{-ik_x x} \tag{5.20}$$

where $\boldsymbol{k} = (k_x, k_y)$, η_d is defined in Section 2.3 and d is the donor-2DEG distance.

Eq. (5.20) reveals two key results. First, the intensity of the magnetic field is proportional to the conductance of the 2DEG and depends critically on the donor distribution, whose Fourier transform is $\eta_d(\boldsymbol{k})$. Second, the magnetic field is sensitive to fluctuations in the donor distribution with length scales larger than the distance between the source of the fluctuation, i.e. the donor layer, and the trap position $(h + z_0)$ (see the real exponential factor in Eq. (5.20)).

The above statements imply that information about the statistical distribution of the donors can be obtained from measurements of the magnetic field produced by a current through the heterostructure. To illustrate this point, we consider the mean-square average of B_x along the trap axis, $\langle B_x^2 \rangle$, and the power spectral density, $D_{k_x}(z_0)$, of B_x versus position along the trap axis, x, at height z_0. It follows from Eq. (5.20) that (see Appendix B):

$$\langle B_x^2 \rangle = \left(\frac{\mu_0 \sigma e}{4\epsilon\epsilon_0} \right)^2 \int d^2k \frac{k_y^2 e^{-2k(d+z_0)}}{(k + k_s)^2} S(\boldsymbol{k}), \quad \text{and} \tag{5.21}$$

$$D_{k_x}(z_0) = \left(\frac{\mu_0 e \sigma}{4\epsilon\epsilon_0} \right)^2 \frac{1}{\langle B_x^2 \rangle} \int dk_y \frac{k_y^2 e^{-2k(d+z_0)}}{(k + k_s)^2} S(\boldsymbol{k}) \tag{5.22}$$

respectively, where $\langle\rangle$ indicates averaging along the trap axis and $S(\boldsymbol{k})$ corresponds to the spectral power of the donor density, defined by [1]:

$$\langle \eta_d(\boldsymbol{k}) \eta_d(\boldsymbol{k'}) \rangle = S(\boldsymbol{k}) \delta(\boldsymbol{k} + \boldsymbol{k'}) \tag{5.23}$$

The way that $\langle B_x^2 \rangle$ decays with the distance to the magnetic field source is directly related to the statistical properties of the current distribution that produces the inhomogeneous magnetic field (see [30, 80] and references therein). Fig. 5.10(a) shows $\langle B_x^2 \rangle$ given by Eq. (5.21) (red line) corresponding to an uncorrelated random distribution of donors with $S(\boldsymbol{k}) \sim \langle \bar{\eta}_d^2 \rangle$. In this case, we have verified numerically that the decay of $\langle B_x^2 \rangle$ is given by a power law which fits to $\sim 1/z^4$ (cyan line in Figure 5.10(a)).

This scaling law is different from that predicted for the roughness associated with imperfection of the wires' edges or surface [80], which gives to $\langle B_x^2 \rangle \sim 1/z^5$ (green

line in Fig. 5.10(a)). The difference originates from the statistical properties of the systems. In the case of the 2DEG considered here, the sources of inhomogeneity of the magnetic field are distributed randomly and without correlation, while the irregularities of the wires' edges have a Gaussian distribution with a characteristic length scale of a few ~ 100 μm [30].

To illustrate the dependence of $\langle B_x^2 \rangle$ on the nature of the donor distribution, we use Eq. (5.21) to calculate $\langle B_x^2 \rangle$ for two correlation relations:

$$\text{exponential, which: } \langle \eta_d(\boldsymbol{r})\eta_d(\boldsymbol{r'})\rangle = \bar{\eta}_d^2 e^{-|\boldsymbol{r}-\boldsymbol{r'}|/\lambda_c} \rightarrow S(\boldsymbol{k}) \sim \lambda_c^2/(k^2+\lambda_c^{-2})^{3/2},$$

$$\text{periodic modulation, which: } \eta_d(\boldsymbol{r}) \sim \bar{\eta}_d + \Delta\eta_d \sin(2\pi x/\lambda_p) \rightarrow S(\boldsymbol{k}) \sim \delta(k_x - 2\pi/\lambda_p)$$

The length scales for correlation are λ_c and λ_p for the exponential and periodic cases, respectively. Plots of $\langle B_x^2 \rangle$ versus z_0 are shown in Figures 5.11(a) and 5.11(b). The exponentially correlated donor distribution produces a slow decay (blue and green lines in Fig. 2.5(a), corresponding to $\lambda_c = 49$ μm and 12 μm, respectively) with a rate depending on the correlation length λ_c. The harmonically correlated distribution presents a nearly exponential decay (blue line in Fig. 5.11(b)). In Figs. 5.10(a) and 5.11, scaling laws $\sim z^{-4}$ and $\sim z^{-5}$ are shown for comparison (red and cyan lines).

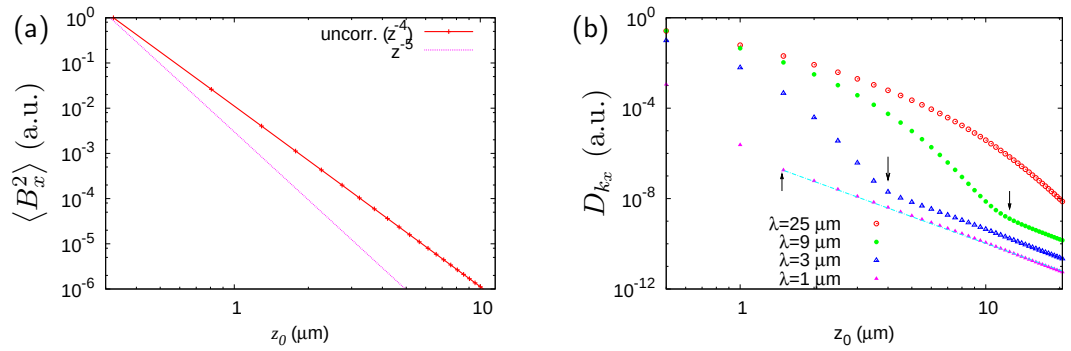

Figure 5.10: (a). Normalised mean-square average of the magnetic field as a function of the height above the 2DEG, for a random uncorrelated distribution of donors (red line). The cyan line corresponds to the $\sim z^{-5}$ scaling. (b) Spectral power density of the magnetic field roughness at different distances from the 2DEG corresponding to four wavelengths, from bottom to top, $\lambda_c = 1, 3, 9$ and 25 μm. For this case, the random donor distribution is uncorrelated.

The spectral power density of the inhomogeneous magnetic field ($D_{k_x}(z)$) also provides information about the donor distribution. Fig. 5.10(b) shows $D_{k_x}(z)$ for an uncorrelated donor distribution and for different $k_x = 2\pi/\lambda_x$ values, where, from bottom to top, $\lambda_x = 1, 3, 9$ and 25 μm. Similar to previous observations above metallic samples [117], at distances larger than the corresponding wavelength, $\lambda_x \sim 2\pi/k_x$, the spectral power density decays in an algebraic way, at a rate independent of k_x (dashed line). Also, an abrupt change in the decay rate occurs at distances comparable with

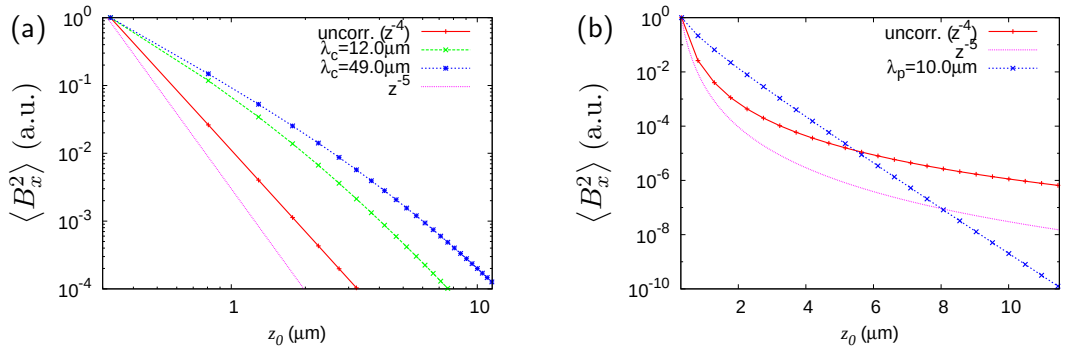

Figure 5.11: (a) Normalised mean-square average of the magnetic field as function of the heigh above the 2DEG, for exponentially correlated donor distribution, with correlation length of $\lambda_c = 12.0$ μm (green line) and $\lambda_c = 49.0$ μm (blue line). For comparison, the uncorrelated case and the z^{-5} scaling laws are shown (red and cyan lines, respectively). Notice the axis are in log-log scale. (b) The blue line represents the normalised mean-square average of the magnetic field as function of the heigh above the 2DEG, for a harmonically modulated donor distribution, with period of $\lambda_p = 10.0$ μm. As in panel (a), the uncorrelated case and the z^{-5} scaling laws are shown for comparison (see text). Notice the axis are in linear-log scale.

$2\pi/k_x$ (arrows in Fig. 5.10(b)). The position of this kink and its variation with k_x provide additional information to characterize the donor distribution.

External fields, change of the temperature or illumination of the sample are other mechanisms that produce changes in the distribution of ionized donors [100]. Our calculations indicate that such changes can be determined by detecting and analysing the magnetic field produced by a current in the 2DEG. As an specific example, consider that the sample is illuminated by an optical diffraction pattern, which produces periodic modulation of the ionized donor distribution with a period of a few micrometre. As shown in Figure 5.11(b), in comparison with the uncorrelated case, a change in both the intensity and the decay rate of the inhomogeneous magnetic field would be observed (see Appendix B).

The shortest working atom-surface distance and the optical resolution are both ~ 1 μm, with sub-micrometre features being inaccessible to present experiments. This implies that, since donors in a heterostructure are randomly distributed with typical correlation lengths of a few hundreds of nanometres (~ 100 nm) [126], only global characteristics of the distribution would be accessible by state-of-the-art BEC based microscopy techniques. This technical limitation is expected to be overcome as the field of BEC-MFM develops and its operation can be extended to sub-micrometre distances.

The following procedure could be used to determine the statistical properties of the donor distribution, using the results shown in this section: First, measure the magnetic

field distribution in the $x-y$ plane at different distances from the 2DEG. Second, evaluate the mean square fluctuations, power spectral density, and other moments of the magnetic field distribution, as a function of the distance to the 2DEG. Finally, by inverting equations like (5.22), the properties of the distribution can be determined.

As a final remark, notice that BEC-MFM could enable functional imaging of 2DEG systems by imaging, for example, the response of the 2DEG under a thermal cycle, illumination or back-gate voltages. In addition, the procedure suggested here has the advantage of causing a negligible perturbation on the semiconductor, while the measurement is done. This is in contrast to the Scanning Probe Microscope method widely used [112], where local modifications of the 2DEG properties are key to obtaining an image of the electron density of the 2DEG.

5.4 Summary and Discussion

This Chapter shows how BEC magnetic microscopy can be used to study features of heterojunctions containing a 2D conducting layer. In the situations presented, the QPC and the infinite 2DEG sample, a nearby BEC close to those devices, exhibits density modulations that depend on the characteristics of the current flow in the 2DEG. All of the simulations presented were performed using experimentally accessible parameters and therefore demonstrate the feasibility of the systems and experiments proposed.

The magnetic field produced by a current-carrying 2DEG depends on the electric transport properties and/or the statistical distribution of ionized donors within the heterojunction. In the case of a QPC, the magnetic field is weak and quantized in units determined by the underlying quantized conductance and the applied voltage.

For a current-carrying 2DEG, the characteristics of the distribution of ionized donors is imprinted in the mean-square amplitude of the magnetic field inhomogeneities, $\langle B_x^2 \rangle$, in particular the rate at which these fluctuations decay with distance from the 2DEG. The spectrum of the magnetic field's spatial fluctuations can also be related to the properties of the ionized donor distribution through Eq. (5.22).

Within the resolution of the microscopy technique, measurements of the magnetic field can be used to probe the current flow in the 2DEG and the distribution of ionized donors in the heterojunction. Such studies can be performed under different conditions of illumination, temperature and external magnetic fields, thus revealing how the 2DEG responds to changes in these parameters.

Instead of thinking of the condensate as a probe of the 2DEG, the magnetic field produced by semiconducting devices may also control or modify the dynamics of the condensate. For example, the random nature of the distribution of ionized donors can be used to produce random atomic potentials whose features can be controlled by tem-

perature or illumination of the sample.

As a final proposal, the magnetic field generated by arrays of QPCs and other quantum structures defined in the 2DEG may also be used to control the behaviour of the BEC. For example, Figure 5.5 shows that the cloud can be split by controlling the number of open modes in the QPC. The density of the condensate could also be modulated as by setting up an array of QPCs near the BEC, which would mimic the action of an optical lattice, but enable the width and depth of individual walls to be controlled. The possibility to reach nanometre control over condensates is another feature that could be implemented by using semiconductor devices in atom-chip configurations. Finally, applications could also exploit the ballistic nature of the electron motion in the 2DEG, which would help to reduce fabrication-related imperfections.

CHAPTER 6

Bose-Einstein condensates in 1D geometries

Creating semiconductor-cold-atoms hybrid systems, where electrons in the semiconductor and atoms in the BEC are sensibly coupled each other, requires a full understanding of the properties of both systems. Bearing in mind that typically micro-traps are produced with an elongated geometry, this Chapter presents a calculation of the phase correlation of BEC in elongated geometries.

The physics in low-dimensional systems can be fundamentally different from those presented by usual three-dimensional cases. In particular, in Bose gases, the coherence properties and characteristics of thermodynamic phase transitions are affected by the dimensionality of the system. An example of this is the well known Mermin-Wagner-Hohenber theorem [127, 128], which establishes the impossibility of off-diagonal long-range coherence (defined below) in homogeneous one-dimensional (1D) Bose gases at all temperatures and in two-dimensional (2D) Bose gases at any non-zero temperature [129]. The impossibility of long-range coherence is due to the enhancement of the phase fluctuations in the system, induced, in turn, by changes in the density of states and spectrum originating from the geometrical constrictions imposed on the gas.

Low-dimensional degenerate Bose gases can be experimentally realized by lowering the mean-field interaction energy in a 3D condensate below the energy splitting of the quantised levels along one or two spatial directions [129]. Such a situation can be produced by modulating a 3D condensate with one-dimensional or two-dimensional optical lattices and applying selective evaporative cooling to deplete particular wells [130, 131, 132]. In general, quasi-2D and quasi-1D degenerate gases are produced inside very asymmetric traps, where the motion along one or two spatial directions, respectively, requires an energy larger than the accessible thermal energy.

Microtrapping setups, like those described in Chapters 3 and 4, produce harmonic traps with approximate axial symmetry and a large aspect ratio between the frequencies along the axial and the transverse directions (see Table 4.3). For this reason, in order to develop hybrid solid-state - BEC systems, where the dynamics of the atoms and solid are mutually dependent, it is essential to know in detail the properties of such quasi-1D degenerate gases. An example of the relevance of such studies is the evidence that the lack of complete phase coherence along elongated clouds can be exploited to improve the sensitivity of interferometric setups [133, 134].

The phase coherence properties of low-dimensional degenerate gases continues to attract great interest both experimentally [20, 135, 136] and theoretically [129, 137, 138, 139, 140, 141]. This chapter presents a numerical study of the phase correlation function in quasi-1D Bose-Einstein condensates, focusing on a qualitative description of the results for different regimes. General definitions of the correlation function and its properties in Bose gases are presented in Section 6.1. Section 6.2 presents the derivation of the effective 1D non-linear equation proposed by A. Muñoz-Mateo and V. Delgado [142], which can be used to describe condensed (or quasi-condensed) Bose gases in different regimes of transverse confinement [142, 143].

The central result of this chapter is presented in Section 6.3. This is the use of the Muñoz-Delgado effective 1D equation to obtain the low-energy excitation modes of the Bose gas, and evaluate the phase correlation function in different regimes of confinement, as defined by Menotti *et. al* [143]. Our results are compared with analytic expressions by Petrov, *et al* [138, 139], corresponding to two extreme regimes of confinement. Finally, Section 6.4 summarizes the findings of this chapter.

6.1 Low-dimensional Bose gases

Consider a particle of mass m trapped in a 3D harmonic potential, where the frequency along one or two spatial directions is much larger than along the remaining direction. The motion along the directions of strong confinement is almost completely constrained if the total energy of the particle is smaller than the splitting of the energy levels along those directions in the trap. In a gas at temperature T, the thermal motion has an average energy of $k_B T$, and therefore such constriction is achieved if $\hbar\omega_i \gg k_B T$. Surprisingly, this condition is independent of the strength of the inter-atomic interactions if the potential is harmonic [40] .

Features of thermodynamic phase transitions depend on system dimensionality [1]. For a Bose gas, this is due to the dependence of the density of states with the spatial dimension occupied by it. To illustrate this point explicitly, consider a uniform gas of density η_{2D} with non-interacting particles of mass m moving in a 2D plane of area A.

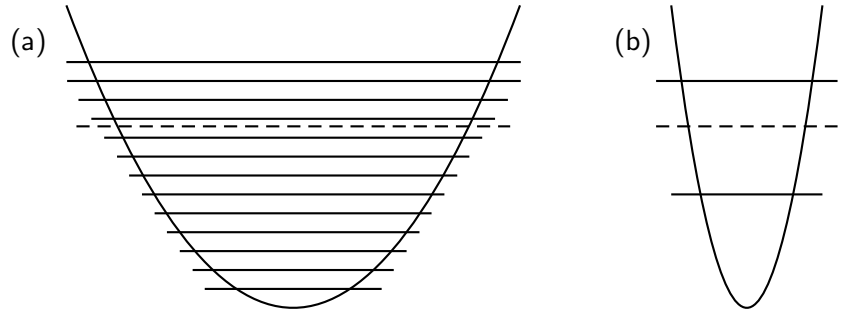

Figure 6.1: Schematic diagram illustrating how the motion along one spatial direction can be constrained by increasing the strength of the potential along it. The dashed line indicates the Fermi level or chemical potential and solid lines indicate the energy levels of the trap. When the level splitting is small ((a)), transitions between these levels are easier to perform than when the splitting is large ((b)).

The density of states in this case is given by [96]:

$$g_{2D}(E)dE = \frac{1}{2}\frac{Am}{\pi\hbar^2}dE \tag{6.1}$$

Substituting this result into the equation of state Eq. (1.4), the condition relating the chemical potential and the total number of particles, equivalent to Eq. (1.6) for the 3D gas, becomes:

$$\eta_{2D}\lambda^2 = -\ln(1-\exp(\mu/k_BT)) \tag{6.2}$$

For any temperature and density, Eq. (6.7) can be satisfied if the chemical potential is given by:

$$\mu = kT\ln(1-\exp(-T/T_{2D})) \tag{6.3}$$

where

$$T_{2D} = \frac{2\pi\hbar^2\eta_{2D}}{mk} \tag{6.4}$$

is the so called temperature of degeneracy. Notice that, in contrast to the 3D case (Eqs. (1.6)-(1.9)), the chemical potential $\mu(T)$ is analytic for all $T \neq 0$, with a monotonic increase with decreasing temperature [144].

Note that there is no need to separate out the particles occupying the zero momentum state, as done for the 3D case in Chapter 1. The occupation number of this state becomes of the order of the total number of particles, N, if the temperature satisfies $T < T_{2D}/\log N$, which goes to zero in the thermodynamic limit ($N \to \infty, A \to \infty, N/A = \eta_{2D}$). This implies that at any non-zero temperature, Bose-Einstein condensation of a uniform 2D system cannot occur in the limit of a large system.

A similar situation occurs for the non-interacting boson gas confined to a one-dimensional box of length L. In this case, the density of states is [96]:

$$g_{1D}(E)dE = \frac{Lm^{1/2}}{\pi\hbar 2^{1/2}E^{1/2}}dE \tag{6.5}$$

and the degeneracy parameter is $\eta_{1D}\lambda_T = (T/T_{1D})^{1/2}$, with

$$T_{1D} = \frac{\hbar^2}{mk_B}\eta_{1D}^2. \tag{6.6}$$

The corresponding relation between the total number of particles and the chemical potential in the quantum degeneracy regime is:

$$\mu = -\frac{\pi k_B T}{(\eta_{1D}\lambda_T)^2} \tag{6.7}$$

The chemical potential, μ, is a continuous function of the density and the temperature of the system, demonstrating the absence of a thermodynamic transition in the uniform 1D ideal Bose gas [40]. Similar to the 2D case, the zero momentum state becomes macroscopically occupied if the temperature satisfies $T \ll T_{1D}/N$, which goes to zero in the thermodynamic limit.

These two examples illustrate how the dimensionality of a Bose gas affects its behaviour at low temperature. In particular, the presence of a Bose-Einstein condensed phase, in terms of a macroscopic occupation of a single-particle state, is ruled out for the uniform 2D and 1D gases. This simple picture is modified by the presence of interactions between particles and a confining potential. This can be explained more clearly by considering the BEC in terms of the one-particle reduced density matrix introduced in Chapter 1.

6.1.1 Phase correlations in low-dimensional Bose gases

The Bose-Einstein condensate transition is characterized by the appearance of a coherent state, occupied by a macroscopic fraction of the particles in the system. These concepts, coherence and macroscopic occupation, can be defined in terms of the non-diagonal elements of the density matrix and its eigenvalues/eigenfunctions, respectively (see Section 1.1.1), which allows an unambiguous identification of the single-particle state occupied by particles in an interacting system.

The condition of long-range coherence, characteristic of the condensed phase, implies that the non-diagonal elements of the density matrix are different from zero. The one body density matrix can be calculated in the long range limit using the macroscopic representation of the field operator ($\hat{\Psi}(\boldsymbol{r},t)$ in Eq. (1.18)) in terms of its modulus and phase [2], which, in the time-independent case, is:

$$\hat{\Psi}(\boldsymbol{r}) = \sqrt{\eta_0(\boldsymbol{r})}e^{i\hat{S}(\boldsymbol{r})}, \tag{6.8}$$

where $\eta_0(\boldsymbol{r})$ is the condensate density and $\hat{S}$ is the phase operator of the field. With this, the one-particle density matrix, Eq. (1.14), becomes:

$$\rho_{(1)}(\boldsymbol{r},\boldsymbol{r'}) = \sqrt{\phi_0(\boldsymbol{r})\phi_0^*(\boldsymbol{r'})}\langle e^{i(\hat{S}(\boldsymbol{r})-\hat{S}(\boldsymbol{r'}))}\rangle \tag{6.9}$$

Off-diagonal long-range coherence occurs when:

$$\lim_{|\boldsymbol{r}-\boldsymbol{r'}|\to L} \rho_{(1)}(\boldsymbol{r},\boldsymbol{r'}) \neq 0$$

where L is the linear dimension of the system. In this limit, the density matrix is dominated by the exponential factor, which, assuming a Gaussian probability distribution for the occurrence of phase fluctuations, becomes [2]:

$$\left\langle e^{[\hat{S}(\boldsymbol{r})-\hat{S}(\boldsymbol{r'})]} \right\rangle = e^{\langle[\hat{S}(\boldsymbol{r})-\hat{S}(\boldsymbol{r'})]^2/2\rangle}. \tag{6.10}$$

The argument of the exponential factor can be expressed in terms of the phase fluctuation and correlation functions as follows:

$$\frac{1}{2}\langle[\hat{S}(\boldsymbol{r})-\hat{S}(\boldsymbol{r'})]^2\rangle = \frac{1}{2}\langle\hat{S}(\boldsymbol{r})^2\rangle + \frac{1}{2}\langle\hat{S}(\boldsymbol{r'})^2\rangle - \langle\hat{S}(\boldsymbol{r})\hat{S}(\boldsymbol{r'})\rangle \tag{6.11}$$

which, as consequence of the average, in the case of an homogenous system becomes:

$$\frac{1}{2}\langle[\hat{S}(\boldsymbol{r})-\hat{S}(\boldsymbol{r'})]^2\rangle = \langle\hat{S}(\boldsymbol{r})^2\rangle - \langle\hat{S}(\boldsymbol{r})\hat{S}(\boldsymbol{r'})\rangle \tag{6.12}$$

This shows that the phase correlation function, $\chi(\boldsymbol{r},\boldsymbol{r'}) = \langle\hat{S}(\boldsymbol{r})\hat{S}(\boldsymbol{r'})\rangle$, is the quantity dominating the long-range coherence. For example, a linear dependence $\chi(\boldsymbol{r},\boldsymbol{r'}) \sim |\boldsymbol{r}-\boldsymbol{r'}|/\ell_S$, corresponds to an exponential decay of the density matrix within a length scale ℓ_S and if the size of the system is such that $\ell_S > L$, then the system shows long-range coherence.

To evaluate explicitly the correlation function $\chi(\boldsymbol{r},\boldsymbol{r'})$, it is useful to write the phase operator in terms of the excitations of the system (defined in Eq. 1.15) [145, 146]:

$$\hat{S}(\boldsymbol{r}) = (4\eta_0(\boldsymbol{r}))^{-1/2}\sum_{j=1}^{\infty}\left(f_j^+(\boldsymbol{r})\hat{\phi}_j + (f_j^+(\boldsymbol{r}))^*\hat{\phi}_j^\dagger\right) \tag{6.13}$$

where $\hat{\phi}_j$ is the annihilation operator of the excitation with quantum numbers j and energy ϵ_j (see Section 1.1), f_j^+ the symmetric combination of the u_j and v_j Bogoliubov-de Gennes modes (see Appendix C).

Expansion of Eq. (6.13) allows us to write the phase correlation function in the form:

$$\left\langle\hat{S}(\boldsymbol{r})\hat{S}(\boldsymbol{r'})\right\rangle = \sum_{j=1}^{\infty}\left[\frac{f_j^+(\boldsymbol{r})}{(4\eta_0(\boldsymbol{r}))^{1/2}}\frac{f_j^+(\boldsymbol{r'})}{(4\eta_0(\boldsymbol{r'}))^{1/2}}\right](1+2N_j) \tag{6.14}$$

where $N_j = (e^{\epsilon_j/kT}-1)^{-1}$ is the Bose-Einstein occupation number of the excitations in thermal equilibrium.

To identify the role of dimensionality on the coherence properties of the atom cloud, consider a D-dimensional uniform interacting gas in the thermodynamic limit[1]. In this

[1] The thermodynamic limit of the uniform system consists of taking the volume and the total number of particle to both approach infinity i.e. $N, V^D \to \infty$ whilst the density is kept constant ($\eta = N/V^D = \eta_0$).

case, the energy and wave-function of the excitation modes with small momentum, p, correspond to [2, 40] :

$$\epsilon(\boldsymbol{p}) = cp \tag{6.15}$$

$$f^{+}_{\boldsymbol{p}}(\boldsymbol{r}) = \frac{1}{\sqrt{2V^D}}\left(\frac{mc}{\eta_0 p}\right)^{1/2} e^{i\boldsymbol{p}\cdot\boldsymbol{r}} \tag{6.16}$$

The previous result is valid for $p < p_{\mathsf{max}}$, where p_{max} is a cut-off momentum, which specifies the validity limit of the hydrodynamic approach, underlying Eq. (6.8) [2].

In addition, by taking the thermodynamic limit, the discrete summation in Eq. (6.14) should be replaced by an integral over the momentum space:

$$\sum_{j=1}^{\infty} \rightarrow \frac{V^D}{(2\pi\hbar)^D}\int d^D p \tag{6.17}$$

where V^D is the corresponding volume in the D-dimensional space. Considering a temperature high enough that the Bose distribution can be approximated by the classical distribution, $N(\boldsymbol{p}) = kT/cp$, the phase correlation function becomes:

$$\left\langle \hat{S}(\boldsymbol{r})\hat{S}(\boldsymbol{r'})\right\rangle = \frac{mc}{\eta_0}\frac{1}{(2\pi\hbar)^D}\int d^D p \frac{e^{i\boldsymbol{p}\cdot\boldsymbol{s}}}{p}\left(1+\frac{2kT}{cp}\right) \tag{6.18}$$

where $\boldsymbol{s} = \boldsymbol{r} - \boldsymbol{r'}$. This integral depends on the dimensionality of the system through the volume element in the corresponding momentum space $d^D p$. In the long-range limit ($s \rightarrow \infty$), the thermal contribution produces the following correlation functions [2, 40]:

$$\left\langle \hat{S}(\boldsymbol{r})\hat{S}(\boldsymbol{r'})\right\rangle_{\mathsf{3D}} \simeq \frac{kTm}{4\pi\hbar^2\eta_0}\frac{1}{s} \tag{6.19}$$

$$\left\langle \hat{S}(\boldsymbol{r})\hat{S}(\boldsymbol{r'})\right\rangle_{\mathsf{2D}} \simeq \frac{2T}{T_{2D}}\ln(s/s_m), \quad \text{with } s_m \sim \hbar/p_{\mathsf{max}} \tag{6.20}$$

$$\left\langle \hat{S}(x)\hat{S}(x')\right\rangle_{\mathsf{1D}} \simeq \frac{mkT}{\eta_0\hbar^2}s \tag{6.21}$$

The divergent behaviour of the phase correlation when $s \rightarrow \infty$, eliminates the long-range order of the one-particle density matrix in the 2D and 1D cases. This can be seen by substituting Eqs. (6.19)-(6.21) into Eq. (6.9), which yields:

$$\rho_{(1),\mathsf{3D}}(\boldsymbol{r},\boldsymbol{r'}) \rightarrow (\eta_0^{\mathsf{1D}})^2 \tag{6.22}$$

$$\rho_{(1),\mathsf{2D}}(\boldsymbol{r},\boldsymbol{r'}) \rightarrow (\eta_0^{\eta_{\mathsf{2D}}})^2\left(\frac{s_m}{s}\right)^{T/T_{2D}} \tag{6.23}$$

$$\rho_{(1),\mathsf{1D}}(r,r') \rightarrow (\eta_0^{\mathsf{1D}})^2 e^{(mk_BT/\eta_{1D}\hbar^2)|s|/2} \tag{6.24}$$

At finite temperatures, the off-diagonal elements of the density matrix for the 2D and 1D cases tend to zero as $s \rightarrow \infty$, demonstrating the impossibility of Bose-Einstein condensation for those cases. Notice that in the 2D case, the decay of non-diagonal elements of the density matrix is intermediate between that of the BEC, Eq. (6.22),

and that of a normal system [2]. The distance over which the 2D system is still phase correlated can be estimated from Eq. (6.23), to be:

$$L_S^{2D} \sim s_m e^{T_{2D}/2T} \tag{6.25}$$

For the one dimensional situation, the density matrix decays exponentially and defines a coherence length of:

$$L_S^{1D} = \frac{1}{\eta_0^{1D}} \frac{T_{1D}}{T} \tag{6.26}$$

These results prove that the existence of long-range order in uniform ideal Bose gases depends on the dimensionality of the system. This picture is modified substantially by the presence of a confining potential acting over the particles and making the system non-uniform [144]. In particular, if the system size is smaller than the coherence lengths Eqs. (6.25) and (6.26), the off-diagonal long-range order is recovered, allowing, at low enough temperature, the collapse of the particles into a single coherent state forming a BEC.

To conclude this section, Table 6.1 summarizes the statements about the existence/non-existence of Bose-Einstein condensation in different dimensions and in the presence of interactions. In the case of $T \neq 0$, the possibility of BEC is defined as the existence of a finite temperature below which the condition of long-range coherence is satisfied.

	$T = 0, g = 0$	$T \neq 0, g = 0$	$T = 0, g > 0$	$T \neq 0, g > 0$
1D	No	No	No	No
2D	yes	No	yes	No
3D	yes	yes	yes	yes

Table 6.1: Presence of off-diagonal long-range coherence in Bose gases under different conditions of temperature and interparticle interaction. If the system is confined to a finite region of the space, off-diagonal order is always possible.

6.2 BEC in an elongated trap (quasi-1D Bose gas)

Consider a degenerate Bose gas trapped by a harmonic potential with axial symmetry along the x axis:

$$V(x, \boldsymbol{r}_\perp) = \frac{m\omega_x^2 x^2}{2} + \frac{m\omega_\perp^2 \boldsymbol{r}_\perp^2}{2} \tag{6.27}$$

where $\boldsymbol{r}_\perp = (y, z)$ is a 2D vector position in the yz plane (transverse plane).

The frequencies of the potential energy determine the time scales in corresponding subspaces. In a highly asymmetric situation ($\omega_\perp \gg \omega_x$) the degrees of freedom in the transverse direction (indicated by the symbol $\perp$) adjust instantaneously to an equilibrium

configuration compatible with the state along the axial direction (indicated by the letter x) [142, 147]. The condensate wave function can, therefore, be approximated by a factorized form:

$$\psi_0(\boldsymbol{r},t) = \varphi(\boldsymbol{r}_\perp, \eta_{1\mathrm{D}}(x,t))\phi(x,t) \tag{6.28}$$

where $\eta_{1D}(x)$ is the 1D density along the x axis, normalized to the total number of particles:

$$\eta_{1\mathrm{D}}(x,t) = N\int |\psi_0(\boldsymbol{r},t)|^2 d\boldsymbol{r}_\perp = N|\phi(x,t)|^2 \tag{6.29}$$

and the transverse factor is normalized to unity:

$$1 = \int |\varphi(\boldsymbol{r}_\perp, \eta_{1\mathrm{D}}(x,t))|^2 d\boldsymbol{r}_\perp \tag{6.30}$$

Substituting this ansatz into the Gross-Pitaevskii equation, Eq. (1.27), yields:

$$\left(i\hbar\partial_t\phi + \frac{\hbar^2}{2m}\frac{d^2\phi}{dx^2} - \frac{m\omega_x^2x^2}{2}\phi\right)\varphi = \left(-\frac{\hbar^2}{2m}\nabla_\perp^2\varphi + \frac{m\omega_\perp^2\boldsymbol{r}_\perp^2}{2}\varphi + \frac{4\pi\hbar^2a}{m}\eta_{1\mathrm{D}}|\varphi|^2\varphi\right)\phi \tag{6.31}$$

where the spatial and time variations of $\varphi(\boldsymbol{r}_\perp, \eta_{1\mathrm{D}}(x,t))$ induced by the axial density $\phi(x,t)$ have been neglected.

Multiplying Eq. (6.31) by φ^* and integrating with respect to the transverse coordinates produces:

$$i\hbar\partial_t\phi = -\frac{\hbar^2}{2m}\frac{d^2\phi}{dx^2} + \frac{m\omega_x^2x^2}{2}\phi + \mu_\perp(\eta_{1\mathrm{D}})\phi \tag{6.32}$$

with

$$\mu_\perp(\eta_{1\mathrm{D}}) = \int \varphi^*\left(-\frac{\hbar^2}{2m}\nabla_\perp^2 + \frac{m\omega_\perp^2\boldsymbol{r}_\perp^2}{2} + \frac{4\pi\hbar^2a}{m}\eta_{1\mathrm{D}}|\varphi|^2\right)\varphi d\boldsymbol{r}_\perp \tag{6.33}$$

Inserting Eq. (6.32) into Eq. (6.31), gives an equation for the transverse wave-function:

$$\mu_\perp(\eta_{1\mathrm{D}})\varphi = \hat{H}_{\mathrm{eff}}\varphi \tag{6.34}$$

$$\mu_\perp(\eta_{1\mathrm{D}})\varphi = \left(-\frac{\hbar^2}{2m}\nabla_\perp + \frac{m\omega_\perp^2\boldsymbol{r}_\perp^2}{2} + \frac{4\pi\hbar^2a}{m}\eta_{1\mathrm{D}}|\varphi|^2\right)\varphi \tag{6.35}$$

where, we have defined $\hat{H}_{\mathrm{eff}}$, the nonlinear Hamiltonian characteristics of the effective mode, as follows:

$$\hat{H}_{\mathrm{eff}} = \left(-\frac{\hbar^2}{2m}\nabla_\perp + \frac{m\omega_\perp^2\boldsymbol{r}_\perp^2}{2} + \frac{4\pi\hbar^2a}{m}\eta_{1\mathrm{D}}|\varphi|^2\right) \tag{6.36}$$

Equation (6.35) is an equilibrium Gross-Pitaevskii equation for the transverse factor of the condensate wave-function, which depends parametrically on the 1D density $\eta_{1\mathrm{D}}$. Equation (6.32) is useful as far as Eq. (6.35) can be solved for φ, which can be done approximately in two extreme cases.

Firstly, the 1D mean-field regime is defined when the non-linear term in Eq. (6.35), $\sim |\varphi|^2$, is small compared with other terms contributing to $\mu_\perp$. In this case, the non-linear contribution can be treated as a perturbation of the linear part of the equation,

which coincides with a non-interacting 2D harmonic oscillator. The zero order wave function corresponds, therefore, to the Gaussian ground state of the transverse harmonic oscillator:

$$\varphi(\boldsymbol{r}_\perp) = \frac{1}{(\pi a_\perp^2)^{1/2}} e^{-|\boldsymbol{r}_\perp|^2/2a_\perp^2} \tag{6.37}$$

and the first order corrected to the chemical potential, given by the expected value Eq. (6.33), results in:

$$\mu(\eta_{1D}) = \hbar\omega_\perp + 2\hbar\omega_\perp a\eta_{1D} \tag{6.38}$$

This regime occurs whenever the chemical potential is smaller than the energy splitting of modes corresponding to the transverse confining potential, i.e., $\mu \lesssim \hbar\omega_\perp$.

The second situation is called the 3D cigar-shaped regime, and occurs in the opposite limit, i.e., when the nonlinear contribution is the dominating factor in Eq. (6.35). In this case, neglecting the kinetic energy contribution, a Thomas-Fermi approximation provides the transverse wave-function:

$$|\varphi(\boldsymbol{r}_\perp)|^2 = \frac{m}{4\pi\hbar^2 a\eta_{1D}} \frac{2\mu_\perp(\eta_{1D}) - m\omega_\perp^2|\boldsymbol{r}_\perp|^2}{2} \tag{6.39}$$

Using this approximation in Eq. (6.33), produces the chemical potential:

$$\mu_\perp(\eta_{1D}) = 2\hbar\omega_\perp\sqrt{a\eta_{1D}} \qquad \text{3D-cigar regime} \tag{6.40}$$

According to Menotti and Stringari [143], the different regimes of transverse confinement can be characterized by the dimensionless combination:

$$\lambda = N\frac{\omega_x}{\omega_\perp}\frac{a}{a_\perp} \tag{6.41}$$

where λ is known as the cross-over parameter. Eq. (6.41) produces the phase diagram in Figure 6.2. If $(N\omega_x a)/(\omega_\perp a_\perp) \gg 1$ many configurations of the harmonic oscillator in the transverse direction are excited, corresponding to the 3D-cigar regime. In the opposite limit, $(N\omega_x a)/(\omega_\perp a_\perp) \ll 1$, all particles occupy the ground state of the transverse potential and the system is in the 1D mean-field regime.

It is interesting to find an approximate solution to Eq. (6.32) valid for the cross-over between these two regimes. This can be done by noticing that the exact solution of Eq. (6.35) minimizes the chemical potential functional Eq. (6.33). As a consequence, an approximate solution for φ can be obtained by applying a variational approach to minimize the functional Eq. (6.33) [142]. A convenient trial function consists of the harmonic ground state for the transverse plane, using its width as a variational parameter:

$$\varphi(\boldsymbol{r}_\perp) = \frac{1}{(\pi^{1/2}(\Gamma a_\perp)^2)^{1/2}} e^{-|\boldsymbol{r}_\perp|^2/2(\Gamma a_\perp)^2} \tag{6.42}$$

The chemical potential functional is minimized by this function when its width is scaled by the factor [142]:

$$\Gamma = (1 + 4aN|\phi|^2)^{1/4} \tag{6.43}$$

Combining Eqs. (6.42), (6.43) and (6.33) yields:

$$\mu_\perp(\eta_{1D}) = \hbar\omega_\perp\sqrt{1+4a\eta_{1D}} \tag{6.44}$$

A very interesting feature of this resulting chemical potential is that, by taking the corresponding limits, it reproduces the result for both the 1D mean-field (Eq. (6.38)) and the 3D-cigar (Eq. (6.40)) regimes.

An effective 1D equation for the axial factor of the wave function can be obtained by substituting Eq. (6.44) into Eq. (6.32):

$$i\hbar\partial_t\phi = -\frac{\hbar^2}{2m}\frac{d^2\phi}{dx^2} + \frac{m\omega_x x^2}{2}\phi + \hbar\omega_\perp\sqrt{1+4a\eta_{1D}}\phi \tag{6.45}$$

This equation includes approximately the effects due to the transverse degrees of freedom. Muñoz and Delgado [142, 147, 148] have shown that Eq. (6.45) describes the equilibrium configuration and dynamics of the lowest-energy modes of an elongated degenerate Bose gas, with a precision comparable to the full 3D GPE Eq. (1.27). In addition to this, the remarkable feature of reproducing both the 1D mean-field and 3D-cigar-shaped limits, motivates us to use Eq. (6.45) for evaluating the phase correlation properties of quasi-1D degenerate Bose gases in the cross-over regime (see Figure 6.2).

6.3 Low-energy modes and Phase correlation in quasi-1D degenerate Bose gases

The phase coherent properties of low-temperature Bose gases in the 1D mean-field and the 3D-cigar regimes, have been studied by Petrov, *et. al* [138, 144, 139]. They consider a chemical potential much larger than the splitting of the energy levels of the axial trapping potential ($\mu \gg \hbar\omega_x$), such that a Thomas-Fermi approximation can be applied to obtain the density profile in terms of polynomials of x.

In the 1D mean-field regime, where the transverse function corresponds to a Gaussian profile, Eq. (6.37), the low-energy excitation energies and modes are given by [138]:

$$\epsilon_j = \hbar\omega_x\sqrt{j(j+1)/2} \tag{6.46}$$

$$f_j^+ = \left(\frac{j+1/2}{R_{\mathsf{TF}}^{\mathsf{1D}}}\right)^{1/2}\left\{\frac{2\mu}{\epsilon_j}\left[1-\frac{x^2}{(R_{\mathsf{TF}}^{\mathsf{1D}})^2}\right]\right\}^{1/2} P_j(x/R_{\mathsf{TF}}^{\mathsf{1D}}) \tag{6.47}$$

where $P_j(x/R_{\mathsf{TF}})$ ($j = 1, 2, 3, \ldots$) are Legendre polynomials, and the Thomas-Fermi radius is defined by

$$R_{\mathsf{TF},x} = \sqrt{\frac{2\mu}{m\omega_x^2}} \tag{6.48}$$

In the 3D-cigar regime, where the transverse function corresponds to an inverted parabola

(Eq. (6.39)), the low-energy excitations/modes are [139]:

$$\epsilon_j = \hbar\omega_x\sqrt{j(j+3)/4} \tag{6.49}$$

$$f_j^+ = \left[\frac{(j+2)(2j+3)g\eta_0}{4\pi(j+1)R_{\mathsf{TF},\perp}^2 R_{\mathsf{TF},x}\epsilon_j}\right]^{1/2} P_j^{(1,1)}(x/R_{\mathsf{TF}}^{\mathsf{3D}}) \tag{6.50}$$

where

$$R_{\mathsf{TF},\perp} = \sqrt{\frac{2\mu}{m\omega_\perp^2}}; \quad R_{\mathsf{TF},x} = \sqrt{\frac{2\mu}{m\omega_x^2}} \tag{6.51}$$

Notice that in both cases, the energy spectrum, $\{\epsilon_j,\ j = 1, 2, \ldots\}$, is independent of the number of particles N, the strength of the transverse confinement and of the interparticle interaction, g.

In the 1D mean-field regime, a direct calculation of the temperature dependence of the mean-square phase difference with respect to the cloud centre, $\left\langle[\hat{S}(0) - \hat{S}(x)]^2\right\rangle$, made by combining Eqs. (6.13) and (6.47), produces [138]:

$$\left\langle[\hat{S}(0) - \hat{S}(x)]^2\right\rangle = \frac{4T\mu}{3T_{1\mathsf{D}}\hbar\omega_x}\left[\ln\frac{R_{\mathsf{TF},x} - x}{R_{\mathsf{TF},x} + x}\right] \tag{6.52}$$

the temperature, T_ϕ, at which Eq 6.52 is of the order unity at $x \sim R_{\mathsf{TF},x}$ is given by:

$$T_\phi = T_{1\mathsf{D}}\frac{\hbar\omega_x}{k_B\mu} \tag{6.53}$$

For the 3D-cigar regime, an explicit expression equivalent to 6.52 cannot be obtained. Nevertheless, it can be probed that in this regime, $\left\langle[\hat{S}(0) - \hat{S}(x)]^2\right\rangle$ obeys a universal function of the form:

$$\frac{\left\langle[\hat{S}(0) - \hat{S}(x)]^2\right\rangle}{\delta_R^2} = f(0, x/R_{\mathsf{TF},x}) \tag{6.54}$$

$$\delta_R^2 \approx \frac{T}{T_c}\frac{a^{2/5}m^{1/5}\omega_\perp^{22/15}}{N^{4/15}\omega_x^{19/15}} \tag{6.55}$$

with f independent of system details. The presence of axial phase fluctuations is governed by the parameter δ_R^2, which becomes close to unity above the temperature:

$$T_\phi^3 D = 15(\hbar\omega_z)^2 N/32\mu \tag{6.56}$$

The 1D mean-field and the 3D-cigar regimes define, each one, natural temperatures scales above which such fluctuations become relevant. In this thesis, Eqs. (6.53) and (6.56) are used as temperature scales in corresponding regimes, whilst for the cross-over, the temperature scale have been arbitrarily chosen as Eq. (6.53).

For the cross-over between these two regimes, Eq. (6.45) can be used to evaluate the low-energy energy spectrum and the corresponding fluctuations of the phase for

the condensate wave-function. This is achieved by linearizing this equation around small deviations from an equilibrium configuration ϕ_0, resulting in a set of Bogoliubov-de Gennes equations (see details in Appendix C). The mode spectrum is obtained numerically by solving the eigen-problem:

$$\epsilon_j \begin{pmatrix} u_j \\ v_j \end{pmatrix} = \begin{pmatrix} \mathcal{L} & -|\phi_0|^2\dot{\zeta}_0 \\ |\phi_0|^2\dot{\zeta}_0 & -\mathcal{L} \end{pmatrix} \begin{pmatrix} u_j \\ v_j \end{pmatrix} \tag{6.57}$$

where:

$$\mathcal{L} = -\frac{\hbar^2}{2m}\frac{d^2}{dx^2} + V(x) - \mu + \dot{\zeta}_0|\phi_0|^2 + \zeta_0 \tag{6.58}$$

with

$$\begin{aligned} \zeta_0 &= \hbar\omega_\perp\sqrt{1+4a\eta_{1D}^0} \\ \dot{\zeta}_0 &= \hbar\omega_\perp\frac{2a\eta_{1D}^0}{\sqrt{1+4a\eta_{1D}^0}} \end{aligned}$$

The Bogoliubov-de Gennes equation (6.57) depends on the equilibrium condensate wave-function, ϕ_0, and on the nonlinear term of the effective equation and its variation with respect to $\eta_{1D}^0 = N|\phi_0|^2$, ζ_0 and $\dot{\zeta}_0$ respectively. Each eigen-energy, ϵ_j, have associated a pair of functions, u_j and v_j, corresponding to the positive and negative Fourier components in the time domain. Density and phase fluctuations can be expressed in terms of the antisymmetric and symmetric combinations, $f_j^- = u_j - v_j$ and $f_j^+ = u_j + v_j$, respectively [144]. At low temperatures, $T \ll T_\phi$, the density fluctuations are small and $f_j^- \to 0$, making possible the wave-function factorization Eq. (6.8) [144] and leaving as the only relevant modes the symmetric combination f_j^+ [144].

With the energy spectrum and their corresponding wave-functions f_j^+, we can evaluate the mean square of the phase difference between two positions, Eqs. (6.12)- (6.14). The trap centre, $\boldsymbol{r} = 0$, is a convenient reference point, and therefore, we evaluate the phase correlation function relative to it: $\left\langle[\Delta\hat{S}(x)]^2\right\rangle = \left\langle[\hat{S}(0) - \hat{S}(x)]^2\right\rangle$, which follows from Eq. (6.12). We have performed these calculations exploring the phase space of transverse confinement shown in Figure 6.2 (see Table 6.2, using the parameters corresponding to the points labelled A–G in the same figure. These numerical results are then compared with the analytical predictions given by Petrov, *et. al* [138, 139], obtained applying Eqs. (6.47) and (6.50) (see Figures 6.6 and 6.7, below).

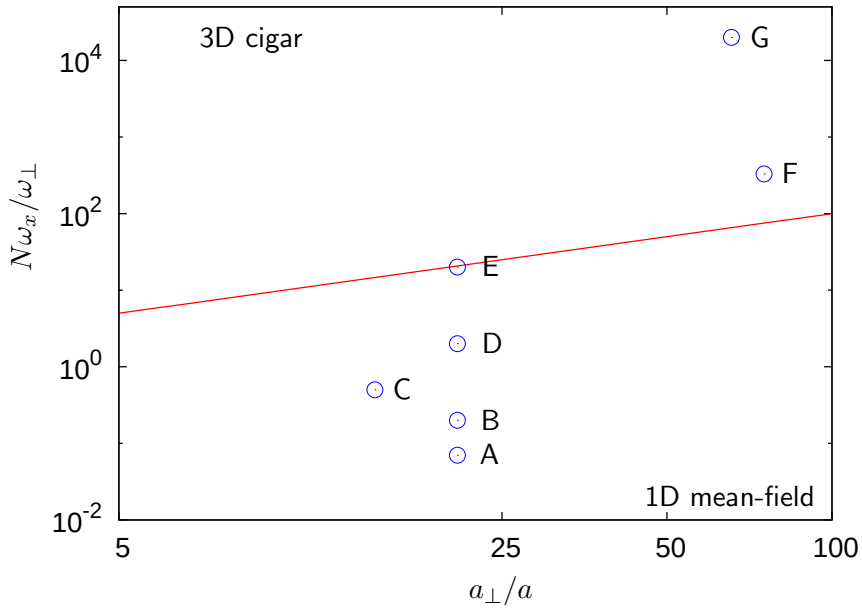

Figure 6.2: Phase diagram defining the different regimes of transverse confinement in a quasi-1D Bose gas. The line corresponds to $N\omega_x/\omega_\perp = a_\perp/a$, marking the cross-over between the 1D mean-field and the 3D-cigar regimes. The circles, labelled A-G, indicates the cases studied in section 6.3 (see Table 6.2)

To facilitate comparison between the results corresponding to different regime, a convention of colours is used in all figures in this chapter: red lines correspond to results obtained from the 1D effective equation (Eq. (6.45)), green lines to the 1D mean-field regime and blue lines to the 3D-mean field regime.

Case	N	$\omega_x/2\pi$ (Hz)	$\omega_t/2\pi$ (Hz)	λ	$(\mu - \hbar\omega_\perp)/(\hbar\omega_x)$
A	70	10	10000	0.00338	23.31
B	200	10	10000	0.00965	46.6
C	200	50	20000	0.03412	42.6
D	2000	10	10000	0.09650	207.5
E	20000	10	10000	0.965498	837.7
F	50000	5	760	4.37542	289
G	10^6	20	1000	305.15228	255.15

Table 6.2: Parameters of the configurations used to evaluate the excitation modes. In all cases we consider a gas of ^{87}Rb atoms, whose s-wave scattering length is $a_s = 5.2$ nm. The chemical potential and ground state were obtained by solving numerically Eq. (6.45) (see Appendix A).

6.3.1 Density profile

Figures 6.3 and 6.4 show the density profiles calculated for the parameters specified in Table 6.2. Three different profiles were obtained for each of the cases A–G, corresponding to: (a) an imaginary-time evolution of the 1D effective equation Eq. (6.45) (η_{EE}), (b) the Thomas-Fermi profile of the 1D mean-field regime η_{1D}, and (c) the Thomas-Fermi profile of the 3D-cigar regime η_{3D}

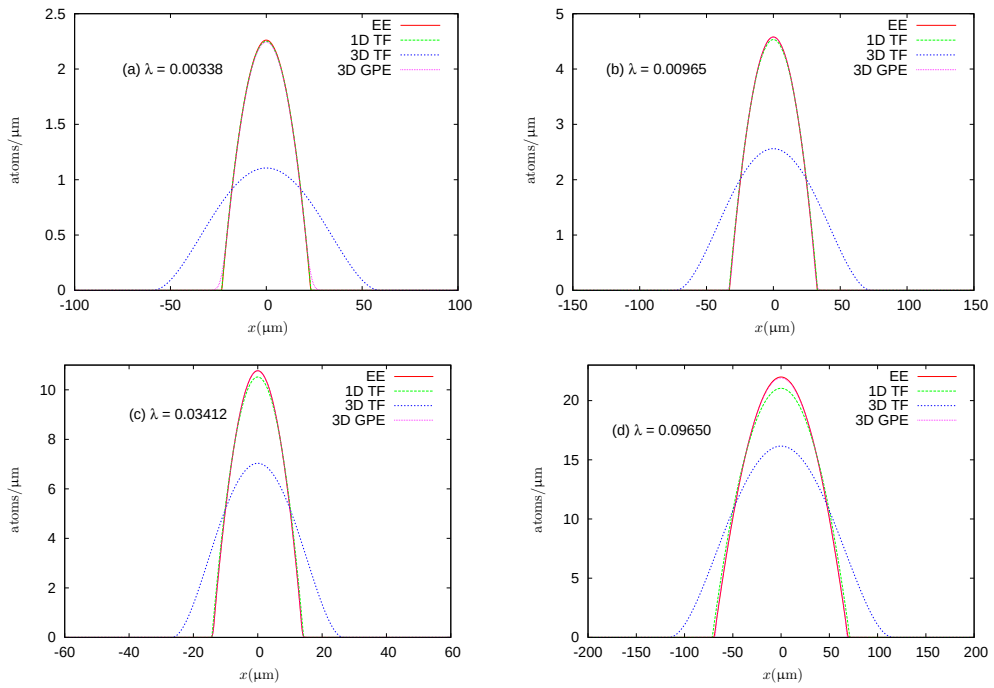

Figure 6.3: Density profiles calculated for cases A–D specified in Table 6.2. For A–C, the density profiles given by Eq. (6.45) (red line, EE) and by the Thomas-Fermi approximation in the 1D mean-field regime (green line, 1D TF) are almost indistinguishable. In D, these two predictions have a different peak density, but are similar in shape. All these cases are far from the 3D-cigar regime (blue curve, 3D TF) and, therefore, the density profiles predicted by Eq. (6.60) (blue line) are appreciably different from the other results. In all cases, the cyan line corresponds to the ground state of the full 3D GPE equation (Eq. (1.27)).

For the 1D mean-field and 3D cigar regimes, the density profiles are given by :

$$\eta_{\mathsf{1D}}(x) = \frac{2\mu_{\mathsf{TF}}^{\mathsf{1D}} - m\omega_x^2 x^2}{4\hbar\omega_\perp a} \tag{6.59}$$

$$\eta_{\mathsf{3D}}(x) = \frac{\mu_{\mathsf{TF}}^{\mathsf{3D}} m}{8\hbar^2 a} R_{\mathsf{TF},\perp}^2 \left(1 - \frac{x^2}{R_{\mathsf{TF},\mathsf{x}}^2}\right)^2 \tag{6.60}$$

respectively, where the widths of the cloud are defined according to Eqs. (6.48) and

(6.51) and the chemical potentials satisfy:

$$\mu_{\mathsf{TF}}^{\mathsf{1D}} = \left(\frac{3}{2}aN\hbar\omega_\perp\sqrt{\frac{m\omega_x^2}{2}}\right)^{2/3} \text{ and } \mu_{\mathsf{TF}}^{\mathsf{3D}} = \left(\frac{15}{4}(\hbar\omega_\perp)^2 Na\sqrt{\frac{m\omega_x^2}{2}}\right)^{2/5} \tag{6.61}$$

Cases A–D lies below the cross-over line in Figure 6.2, with increasing cross-over parameter ($\lambda_{\mathsf{A}} = 0.00338 \rightarrow \lambda_{\mathsf{D}} = 0.0965$). Correspondingly, the difference between the density profiles resulting from the 1D effective equation (η_{EE}) and from the 1D mean-field approximation (η_{1D}), increases with increasing lambda λ, being almost indistinguishable for small values (Cases A–C, red and green lines in Figure 6.3(a)–(c)). In these cases, the 3D-cigar approximation cannot be applied because the non-linear term is not very large ($4a\eta_{\mathsf{1D}} \ll 1$) and, consequently, the profile predicted in this approximation is quite different from the other two calculations (blue line in Figure 6.3(a)–(d)).

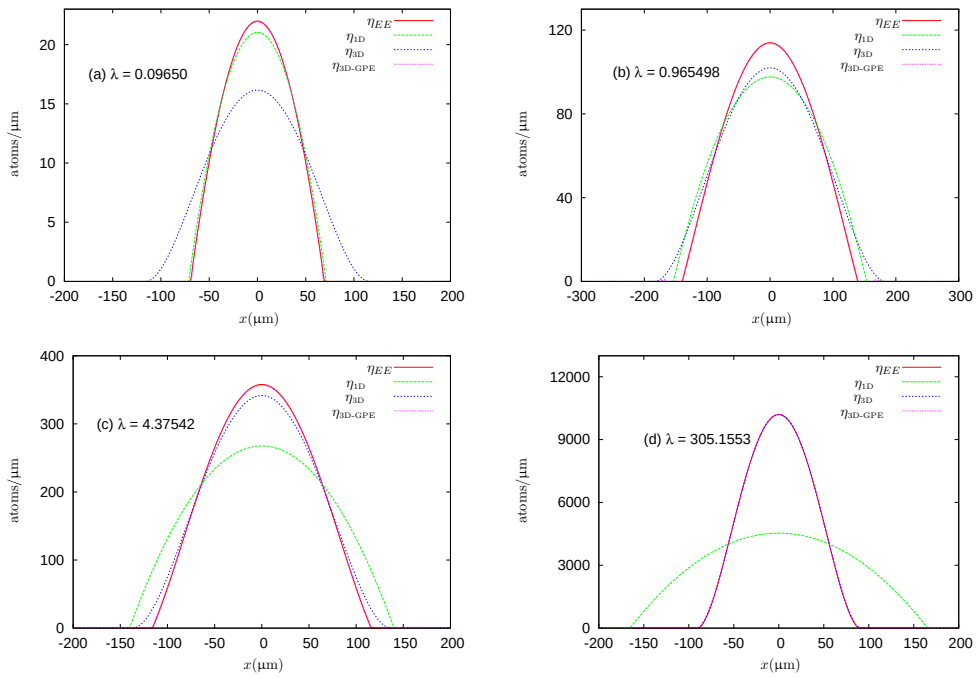

Figure 6.4: Density profiles calculated for cases D–G specified in Table 6.2, showing a smooth transformation between the 1D mean-field (green curves, 1D TF) and the 3D-cigar regimes (blue curves, 3D TF). The density profile becomes more 3D-cigar-like as λ increases. This sequence of figures, demonstrate how the 1D mean-field approximation (green line, 1D TF) becomes progressively less effective to describe the density profile of the system, and the opposite with respect to the 3D-cigar approximation (blue curve, 3D TF). In all cases, the cyan line corresponds to the ground state of the full 3D GPE equation (Eq. (1.27)).

Case E corresponds to the crossover regime. Predictions of the 1D mean-field and 3D-cigar regimes are similar (green and blue lines in Figure 6.4(b)) but differ appreciably

from the 1D effective field equation (red line in Figure 6.4(b)). In case F, the cross-over parameter is not too big ($\lambda_{\mathrm{D}} = 4.37$) and the density profiles corresponding to the 1D effective equation is close to that predicted by the 3D-cigar regime (red and blue lines in Figure (6.4(c)), respectively).

Case G has a large cross-over parameter, $\lambda_{\mathrm{F}} = 305.15$, and, not surprisingly, the density profile predicted by the 3D-cigar regime (η_{3D}) and by the 1D effective equation η_{EE} are indistinguishable, whilst the 1D mean-field prediction becomes ineffective for this case.

These results show how the effective theory, Eq. (6.45), is able to reproduce the smooth transformation of the density profile, from the 1D mean-field to the 3D-cigar regimes, as the cross-over parameter is increased.

6.3.2 Excitation spectrum (Bogoliubov modes)

The Thomas-Fermi approximation can be used whenever the chemical potential is much larger than the separation of the energy levels in the trapping potential ($\mu \gg \hbar\omega_x, \hbar\omega_\perp$). When such criteria is not satisfied, the excitation spectrum is not well represented either by Eq. (6.47) or Eq. (6.50). Instead, Eq. (6.45) can be used to obtain (numerically) the excitation spectrum for such situations, as well as for the crossover between the 1D mean field and the 3D-cigar regimes.

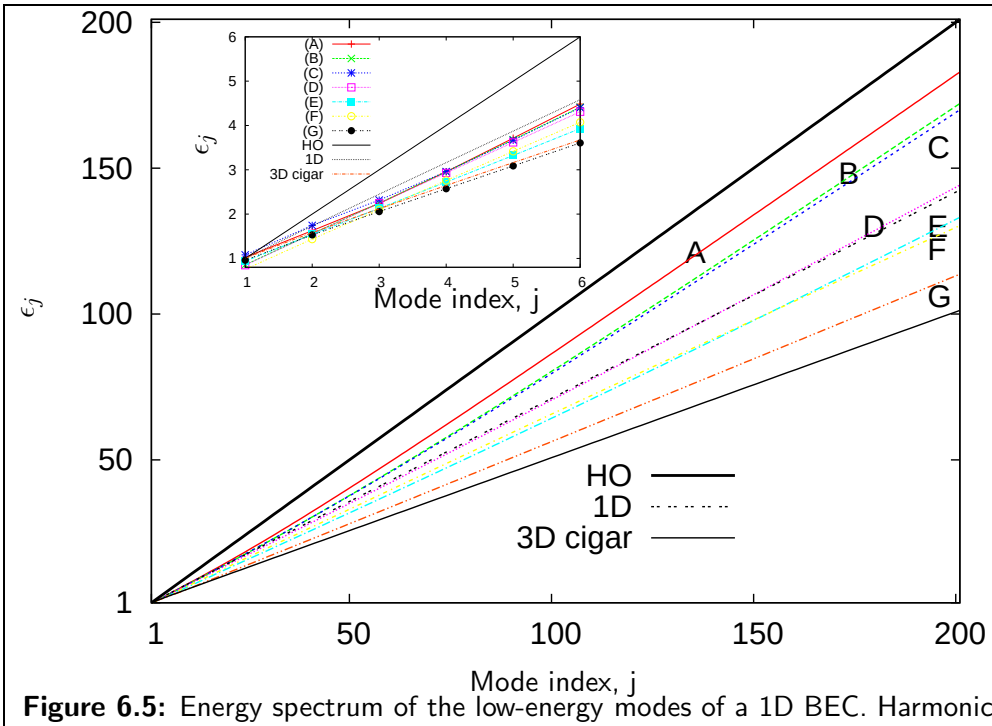

Figure 6.5: Energy spectrum of the low-energy modes of a 1D BEC. Harmonic oscillator, 1D mean-field and 3D cigar regimes correspond to thick, dotted and thin black lines, respectively. Other lines corresponds to the configurations specified in Table 6.2.

Figure 6.5 shows the energy spectrum of excitations for the cases defined in Table 6.2. With the exception of the very low-energy modes (inset in Figure 6.5), for all the cases studied, the low-energy spectrum is approximately linear with respect to the mode number, $\epsilon \sim \alpha j$. The largest slope, α, corresponds to the non-interacting case (harmonic oscillator, thick black line in Figure 6.5) while the smallest α corresponds to the 3D-cigar regime (thin black line in Figure 6.5). The excitation spectrum corresponding to the 1D mean-field regime falls in between these two situations (dashed black line in Figure 6.5).

We have found cases where, although the Thomas-Fermi approximation produces the correct shape of the density profile, the energy spectrum has a harmonic-oscillator-like structure with a slope, α_{HO}, satisfying $\alpha_{\mathrm{HO}} > \alpha > \alpha_{\mathrm{1D}}$, and is not well represented by Eq. (6.47). This typically occurs when the chemical potential is just a few tens of $\hbar\omega_x$ (Cases A, B and C in Table 6.2, red, green and blue lines in Figure 6.5, respectively.).

In Case D, the chemical potential is $\sim 200 \times \hbar\omega_x$, but still smaller than the energy splitting along the transverse direction ($\sim 1000\hbar\omega_x$). Consequently, this case corresponds to the 1D mean-field regime, where a Thomas-Fermi approximation can be applied in the axial direction, while the wave-function in the transverse plane looks like the ground state of the transverse potential. The corresponding spectrum to this case (cyan line in Figure 6.5), is well approximated by Eq. (6.47), despite the density profile starting to deviate from the 1D mean-field prediction (see Figure 6.3(d)).

In Cases E and F, there are several hundred axial levels below the chemical potential and the Thomas-Fermi approximation can be safely applied. These cases are close to the cross-over regime and the spectra for these cases lies between those corresponding to the 1D mean-field or the 3D-cigar regimes (see sea-blue and yellow lines in Figure 6.5).

The excitation spectrum in case G, which has a large cross-over parameter ($\lambda \sim 300$) and a density profile that is well described by the 3D-cigar regime, is not accurately described by the 3D-cigar regime (Eq. (6.50)). However, in Figure 6.5 the slope of the spectrum, α, decreases as λ is made bigger and bigger, indicating a transition between the 1D mean-field and the 3D-cigar regimes.

Figures 6.6 and 6.7 show some modes for the cases defined in Table 6.2, determined by solving the Bogoliubov equations corresponding to Eq. (6.45) (red curves), the 1D mean-field Eq. (6.47) (green curves) and the 3D-cigar Eq. (6.50) (blue curves). The spatial width of the excitations corresponds to that of the density profile, and, as a consequence, the 1D mean-field excitations approximate the results of the Bogoliubov analysis (Eq. (6.45)) in Cases A–D. In the cross-over region, we can observe how the corresponding Bogoliubov excitations approach those associated with the 3D-cigar regime (Eq. (6.50)). It is interesting to notice that in Cases A–C, where the slope of the excitation spectrum, α, is between the non-interacting case and the 1D mean-field regimes, corresponding high energy modes are wider than the condensate, reflecting the non-interacting character of the spectrum and cannot be reproduced by results Eqs. (6.47) and (6.50).

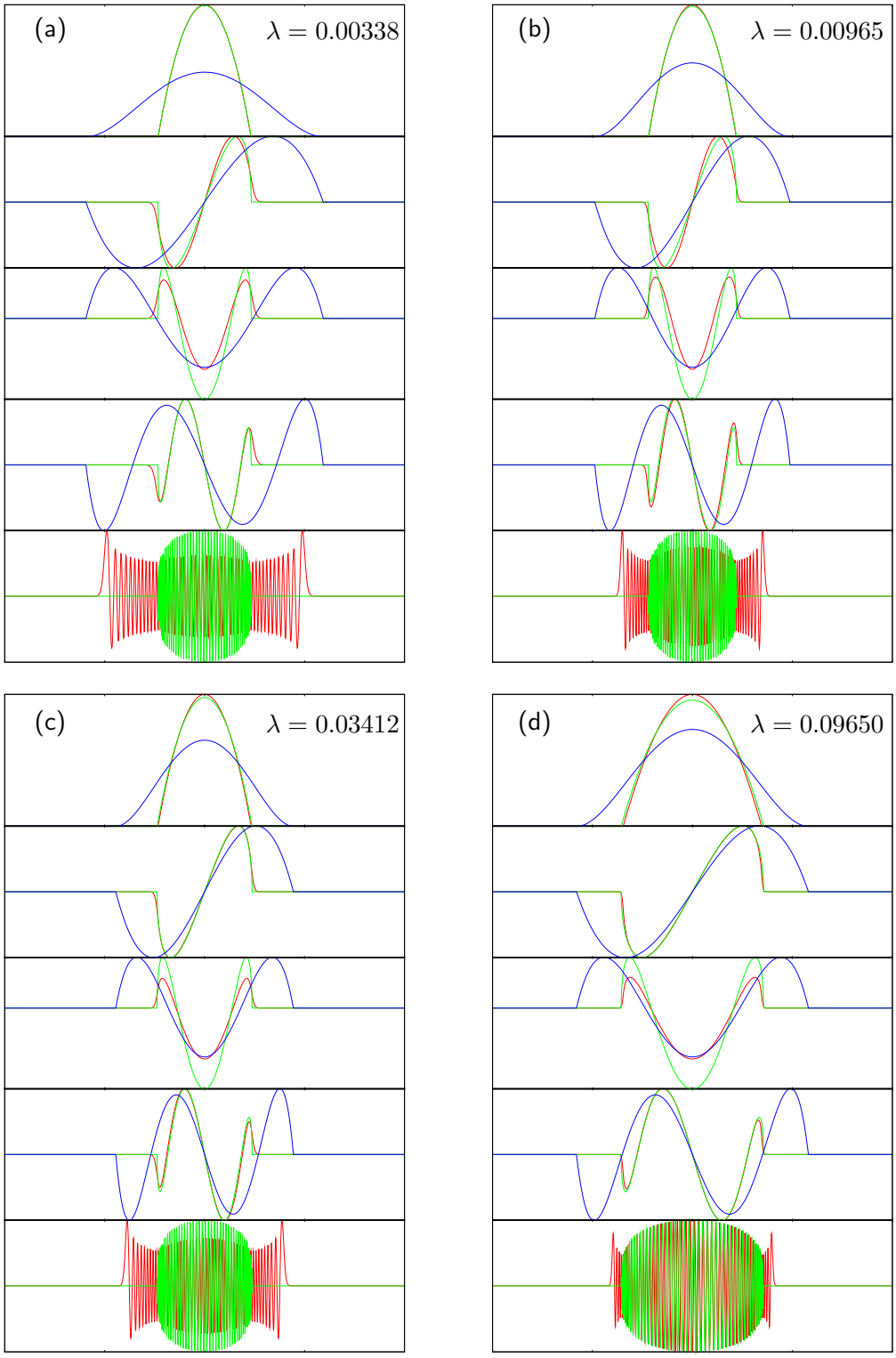

Figure 6.6: f_j^+ modes corresponding to (a) $\lambda = 0.00338$, (b) $\lambda = 0.00965$, (c) $\lambda = 0.03412$ and (d) $\lambda = 0.09650$ (d). Each panel, from top to bottom, shows the modes $j = 0, 1, 2, 3$ and 75. The colour convention is described in the text. For clarity, in all panes at the bottom, the line corresponding to the 3D cigar regime is omitted.

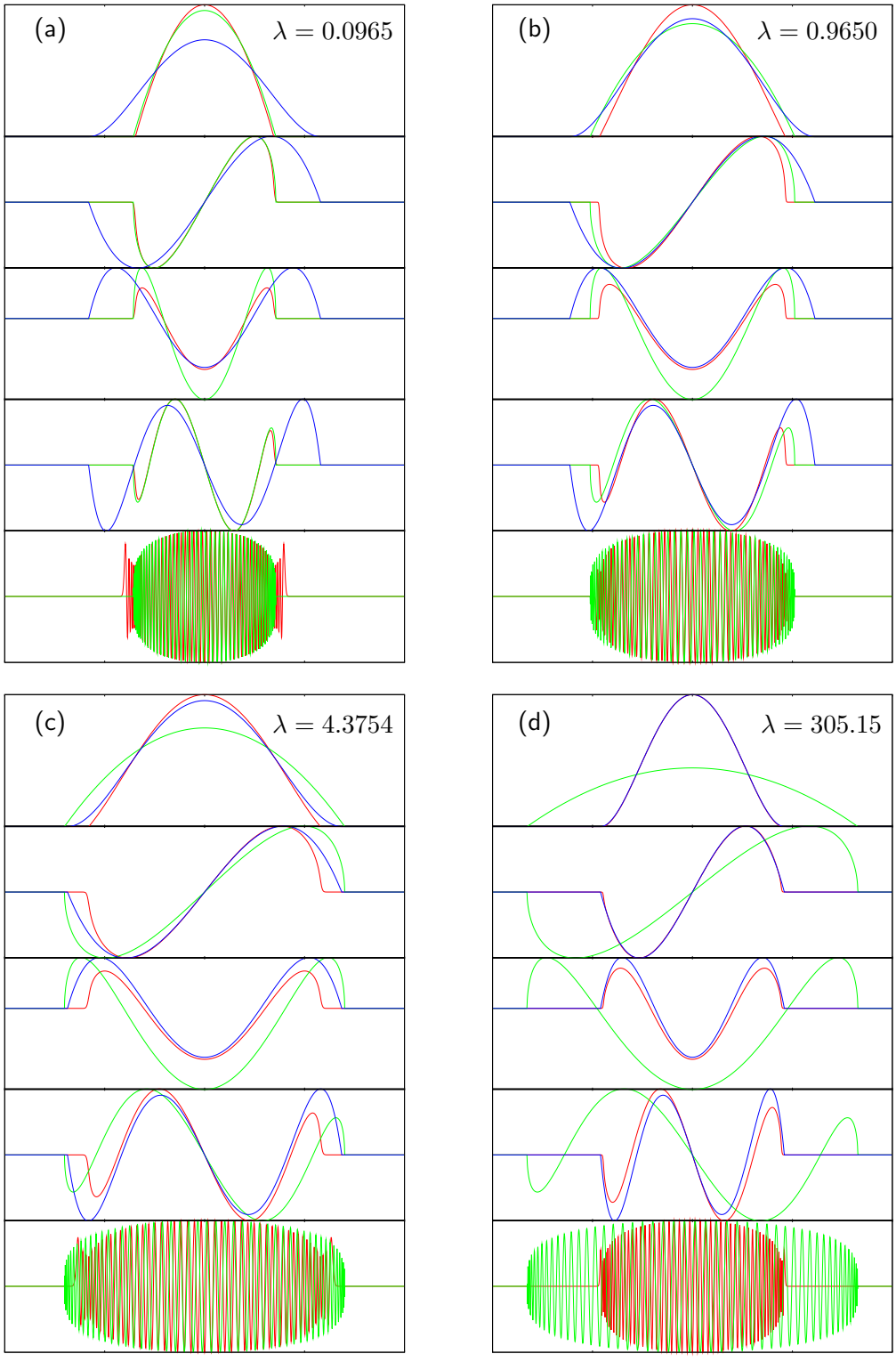

Figure 6.7: f_j^+ modes for $\lambda = 0.0965$ (a), $\lambda = 0.9650$ (b), $\lambda = 4.3754$ (c) and $\lambda = 305.15$ (d). Each panel, from top to bottom, shows the modes $j = 0, 1, 2, 3$ and 75. The colour convention is described in the text. For clarity, in all panes at the bottom, the line corresponding to the 3D cigar regime is omitted.

6.3.3 Phase Fluctuations and correlations in 1D degenerate Bose gas

Expressing the phase operator in terms of the low-energy excitations is a convenient way to quantify the phase correlation in elongated degenerate Bose gases. The one-dimensional version of Eq. (6.13) corresponds to:

$$\hat{S}(x) = [4\eta_0(x)]^{-1/2} \sum_{j=1}^{\infty} f_j^+(x)\hat{\phi}_j + (f_j^+(x))^* \hat{\phi}_j^\dagger \tag{6.62}$$

As indicated by Eqs. (6.9) and (6.10), the long-range behaviour of the non-diagonal elements of the density matrix is dominated by the mean square of the difference of the phase between two points along the condensate, in this case $\left\langle [\Delta\hat{S}(x,x')]^2 \right\rangle = \left\langle [\hat{S}(x) - \hat{S}(x')]^2 \right\rangle$. Taking into account the bosonic character of the operators $\hat{\phi}_j$ and the definition of the phase operator in terms of the excitations (Eq. (6.62)), the mean-square phase difference can be written as follows [2]:

$$\left\langle [\Delta\hat{S}(x,x')]^2 \right\rangle = \sum_j^{\infty} \left[\frac{f_j^+(x)}{[4\eta_0(x)]^{1/2}} - \frac{f_j^+(x')}{[4\eta_0(x')]^{1/2}} \right]^2 (1 + 2N_j) \tag{6.63}$$

where N_j is the thermal occupation of mode j:

$$N_j = \frac{1}{(e^{\epsilon_j/kT} - 1)} \tag{6.64}$$

Eq. (6.63) has two contributions. The quantum contribution corresponds to the temperature independent term. The contribution associated with thermal fluctuations depends on the thermal occupation number of the excitation modes. These two terms are evaluated for Cases A–G in Table 6.2 by the three approaches shown before: (a) a numerical solution of the Bogoliubov equations associated with Eq. (6.45) (see Appendix C), (b) using the excitations for the 1D mean-field regime, Eq. (6.47), and (c) using the excitations for the 3D-cigar regime, Eq. (6.50).

The results presented in the next section are shown as functions of a dimensionless unit of length x/R, where R is the cloud width corresponding to each approximation.

Quantum Fluctuations

Figures 6.8 and 6.9 present the quantum contribution to $\left\langle [\Delta\hat{S}(x)]^2 \right\rangle$ for the cases specified in Table 6.2. All three approaches, the 1D effective equation (red curves), the 1D mean-field regime (green curves) and the 3D-cigar regime (blue curves), produce $\left\langle [\Delta\hat{S}(x)]^2 \right\rangle$ versus x/R plots with three distinct regions. Near the cloud centre ($x = 0$), there is an approximate logarithmic (fast) increase ($\sim \ln(x/\ell_c)$). Then, the growth becomes linear along a region whose extension depends on the system parameters. Finally, near the edge of the cloud, the phase correlation grows exponentially.

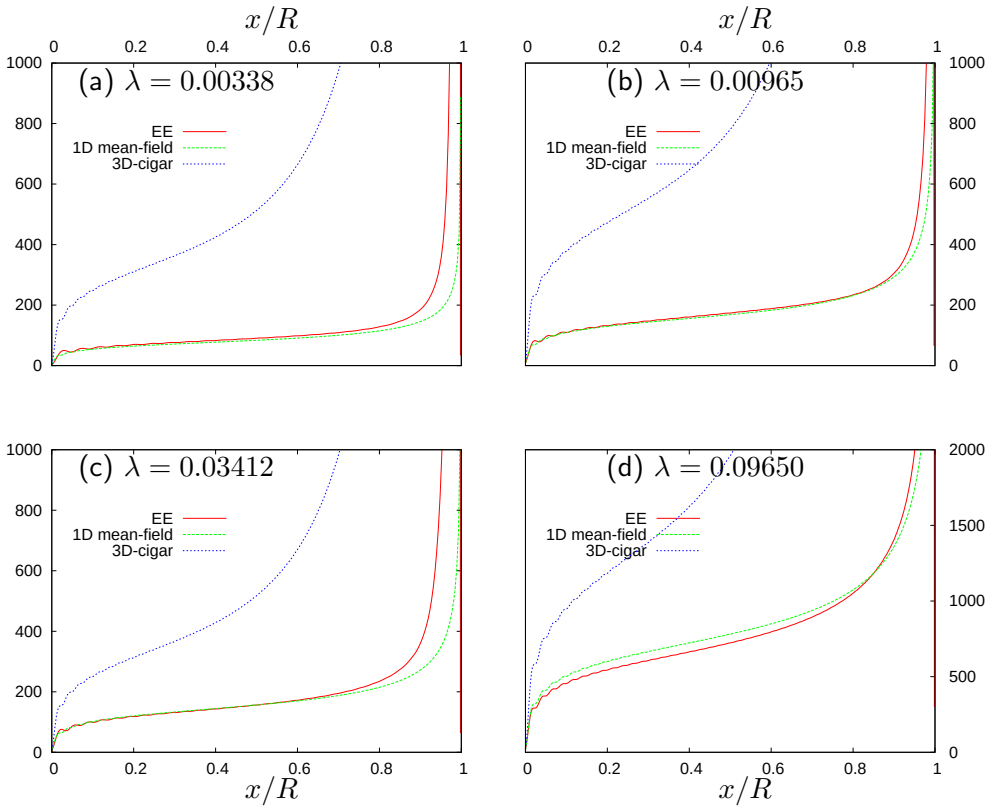

Figure 6.8: Phase correlation function (vertical axes) for Cases A-D in Table 6.2, versus distance to the trap centre. In all these cases, the function $\left\langle (\Delta\hat{S}(x))^2 \right\rangle$ corresponding to the effective equation (red curves, Eq. (6.45)) is very close to that resulting from the 1D mean-field approximation (green curves) in the Thomas-Fermi regime. Blue curves are calculated in the 3D-cigar regime.

According to Petrov *et. al* [138, 139], the phase correlation, in both the 1D mean-field and the 3D-cigar regimes, is given by universal functions of the form:

$$\left\langle [\Delta\hat{S}(x)]^2 \right\rangle = \beta(\mu) f(x/R), \tag{6.65}$$

where R is the width of the cloud (Eq. (6.48) and (6.51)), β is a factor that depends on the number of particles and the trapping configuration, and the function $f(x/L)$ is a independent of the details of the system like the trap frequencies, number of atoms and scattering length.

The results in Figures. 6.8 and 6.9 show that the 1D effective model produces phase correlations with the form of Eq. (6.65), with a corresponding universal form $f_{\mathsf{EE}}(x/L)$, only for configurations whose spectrum lies between the Harmonic oscillator and the 1D mean-field regimes (see Figure 6.5), such as Cases A–C in Table 6.2. The previous statement can be proven by scaling the results in Figure 6.9 (red curves) to a common scale, whereupon it becomes evident that all red curves correspond to the same

function, $f_{\mathrm{EE}}(x/L)$, multiplied by a different factor. Figure 6.10(a) compares the forms of $f_{\mathrm{EE}}(x/L)$ (red curve), $f_{\mathrm{1D}}(x/L)$ (green curve) and $f_{\mathrm{3D}}(x/L)$ (blue curve), all of them numerically evaluated, and scaled to have the same value at $x = 0.42$ (this position can be arbitrarily chosen, without appreciable change in the scaled functions). In this plot, the different regions of phase correlation variation are indicated and the corresponding fitted functions are also plotted.

Observe that the function $f_{\mathrm{EE}}(x/L)$ (red curve) is similar to that corresponding to the 1D mean-field (green curve), differing only near the edge of the cloud, where the excitation modes also differ, as mentioned previously. It is worth noting that the regions with logarithmic and linear growth of the phase correlation function have almost the same sizes and functional dependence for both $f_{\mathrm{EE}}(x/L)$ and $f_{\mathrm{1D}}(x/L)$.

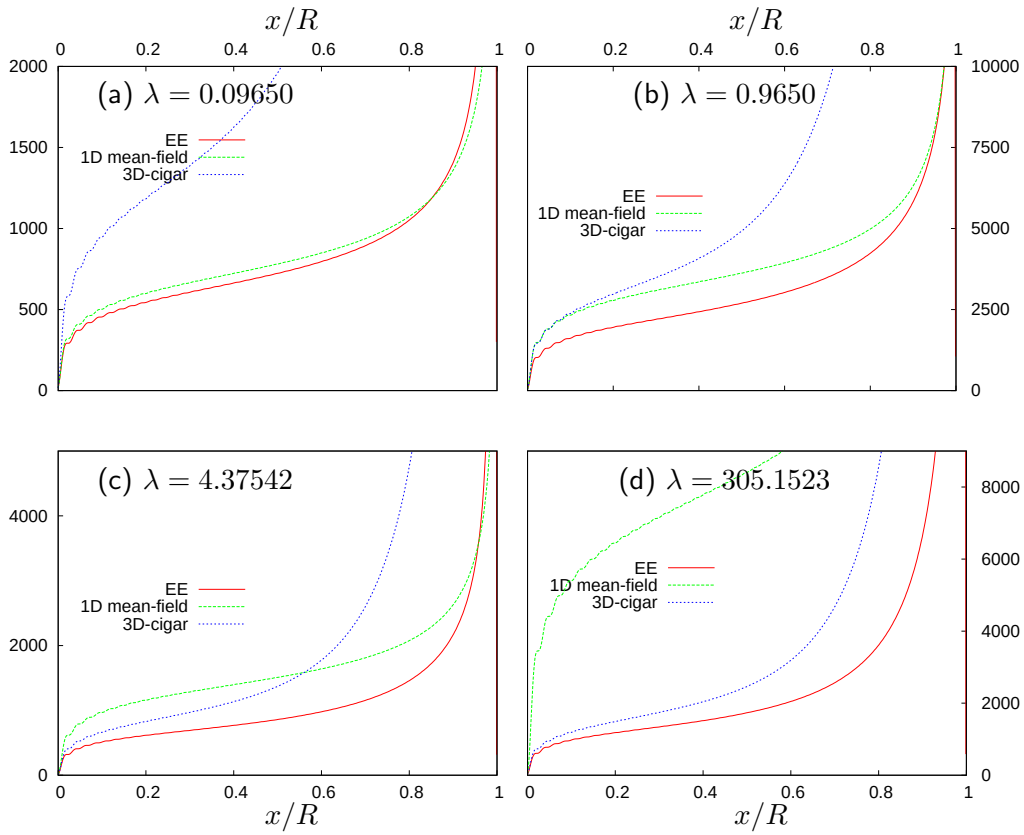

Figure 6.9: Phase correlation (vertical axes) for Cases D–G in Table 6.2, versus distance to the trap centre. For cases E–G, a transition between the 1D mean-field and the 3D-cigar regimes can be observed, as the blue curve (3D-cigar regime) approaches to the red one (Effective equation), while, simultaneously, the green curve (1D mean-field) moves away from the effective equation prediction.

Case D in Table 6.2 has a spectrum coinciding with that predicted in the 1D mean-field regime. In this case, the phase correlation functions corresponding to the 1D mean-field regime (green curve in Fig. 6.9(D)) and the 1D effective equation (red curve

in Fig. 6.9(D)) are very close, due to the similarity of the excitation modes in both cases (see Figs. 6.7).

When the energy level spectrum lies in the cross-over region, it is not possible to identify a universal function for the phase correlation calculated from the excitations of the effective model Eq. (6.45) (red curves in Fig. 6.9). For these cases, although three regions with similar features can still be identified, the width of each one depends on the particular system under consideration (see Figure 6.10(b)).

The evolution of the mean square of the phase difference during the transition between the 1D mean-field and the 3D-cigar regimes is explored in Figure 6.10(b). The first region, where a fast increase occurs ($\sim \ln(x/\ell_c)$), has about the same length in all cases, while the width of the region with linear growth reduces as the system approaches the 3D-cigar regime.

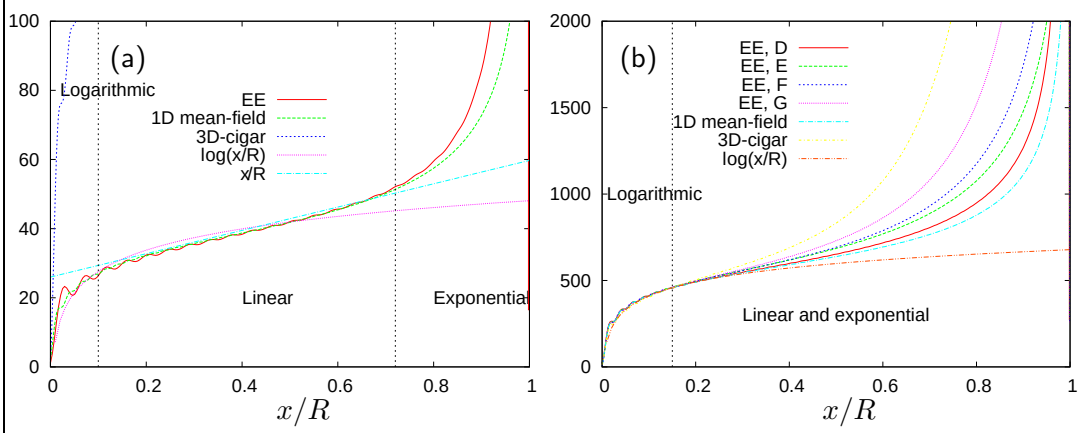

Figure 6.10: Scaled $\left\langle (\Delta\hat{S}(x))^2 \right\rangle$ (vertical axes) versus x/R. (a) Cases A–C in Table 6.2 (red curve, only one case shown for clarity). The scaling factor is chosen to obtain, in all cases, the same value at $x = 0.42$. In all cases, after scaling, all functions coincide with a universal function $f(x/L)$. The scaled 1D mean-field (green curve) and 3D-cigar (blue curve) predictions are also shown, along with the best logarithmic (cyan curve) and linear (light blue) fits, in the corresponding regions. (b) Corresponding to cases D–G in Table 6.2, the 1D mean-field and 3D-cigar predictions. Three regions of variation can be defined, whose width depends on the particular situation considered, such that, in contrast to panel (a), no universal function can be defined.

Thermal Fluctuations

Result for the thermal contribution to the mean square phase difference are shown in Figures 6.11, 6.12 and 6.13. For comparison, the quantum contribution is also shown, demonstrating that this contribution is much smaller than the thermal one.

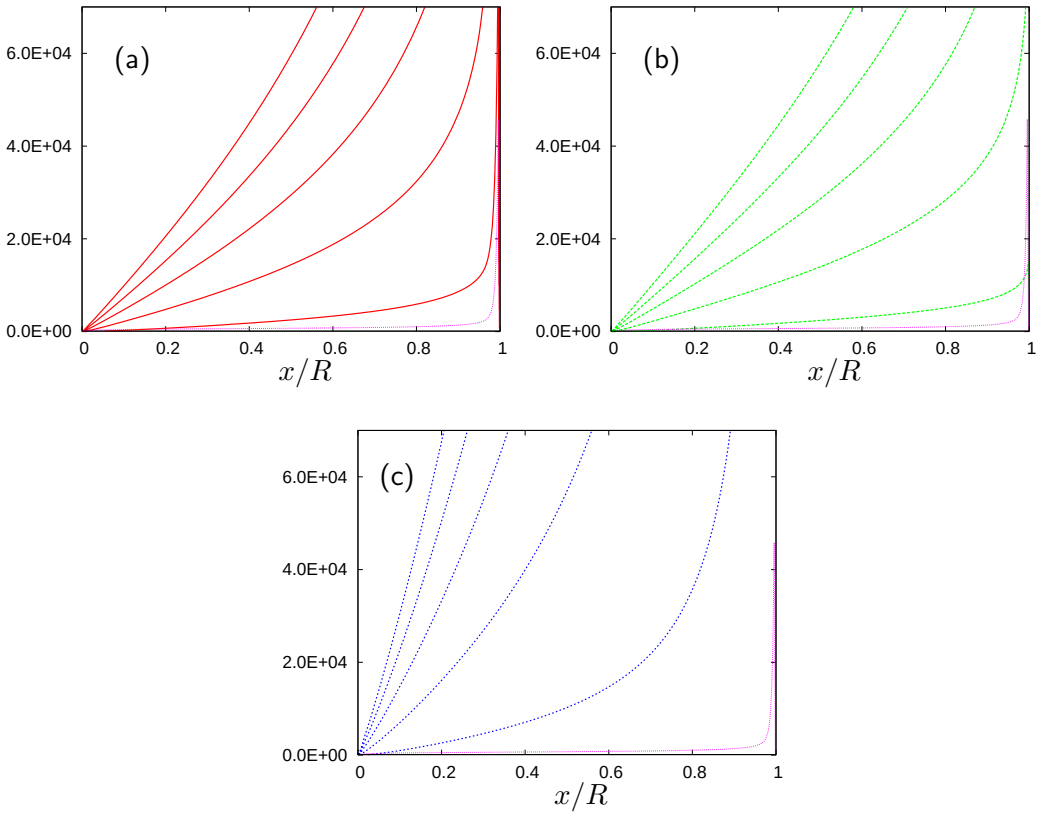

Figure 6.11: Thermal contribution to $\left\langle [\Delta\hat{S}(x)]^2 \right\rangle$ for Case D, obtained using different approaches: (a) the 1D effective equation. (b) the 1D mean-field approximation and (c) the 3D-cigar approximation. All figures show curves corresponding (from bottom to top) to the temperatures 0 (cyan curve), T_ϕ, $5T_\phi, 10T_\phi, 15T_\phi$ and $20T_\phi$. In all cases, $\left\langle (\Delta\hat{S})^2 \right\rangle$ can be factorized in the form $\beta(T)f(x/L)$, with a common $f(x/L)$ that depends on the approach used

Figure 6.11 shows $\left\langle [\Delta\hat{S}(x)]^2 \right\rangle$ for different temperatures, corresponding to case D. All other cases have, qualitatively, the same characteristics. The 1D mean-field and 3D-cigar predictions (panels (b) and (c) of Figure 6.11, respectively) follow universal functions given by Eq. (6.65), in which β now also depends on the temperature. In contrast, the effective model Eq. (6.45), produces a dependence of the form:

$$\left\langle [\Delta\hat{S}(x)]^2 \right\rangle = \beta(\mu, \lambda, T) f(\mu, \xi, x/L), \tag{6.66}$$

where ξ depends on the details of the trapping potential, and f is a function which does not depend on the temperature of the system, but does depend on the system details such as the trap geometry or the number of particles (Figure 6.11(a)).

Similar to the quantum contributions, when the excitation spectrum is between the harmonic oscillator and the 1D mean-field regimes (case A, B and C), the mean square phase difference given by the effective equation (6.45) is similar to that produced by

the 1D mean-field in the Thomas-Fermi approximation. This can be observed in the sequence of Figures 6.12(a)-(d), where a small difference between the red and green curve is seen.

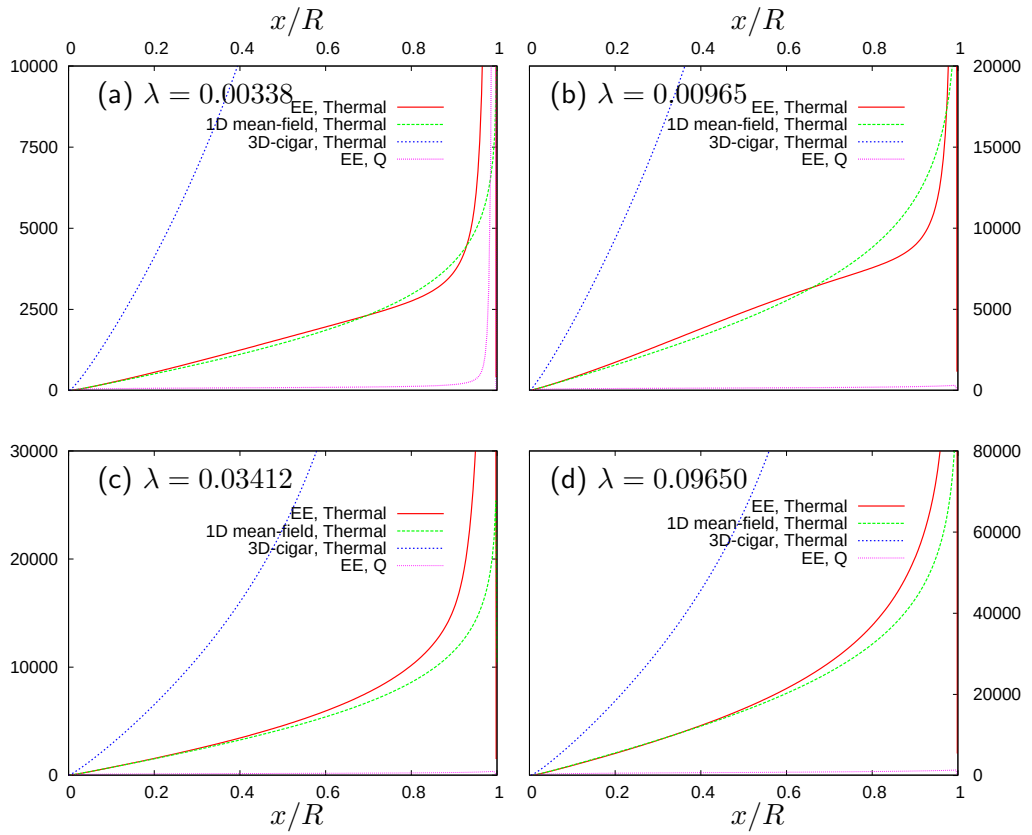

Figure 6.12: Thermal contribution to $\left\langle [\Delta \hat{S}(x)]^2 \right\rangle$ corresponding to cases A–D (panels (a)-(d) respectively). In all these cases, the results corresponding to the 1D mean-field approximation (green curves) and the 1D effective equation (red curves) are similar, and differ significantly only near the edge of the cloud ($x/R \sim 1$).

In all cases, two regions can be defined. One where the phase correlation grows linearly with the distance to the centre of the cloud and a second where fast growth occurs. The widths of these regions, as well as the rate of growth, depend on the specific system considered and its temperature. Figure 6.13 shows a transition between the 1D mean field and the 3D-cigar regimes as the dimensional parameter, λ, is increased, similar to our observations for the quantum contribution (Figure 6.9). In the first panel, $\left\langle [\Delta \hat{S}]^2 \right\rangle$ is close to the prediction of the 1D mean-field regime and gradually it becomes similar to the the 3D-cigar prediction.

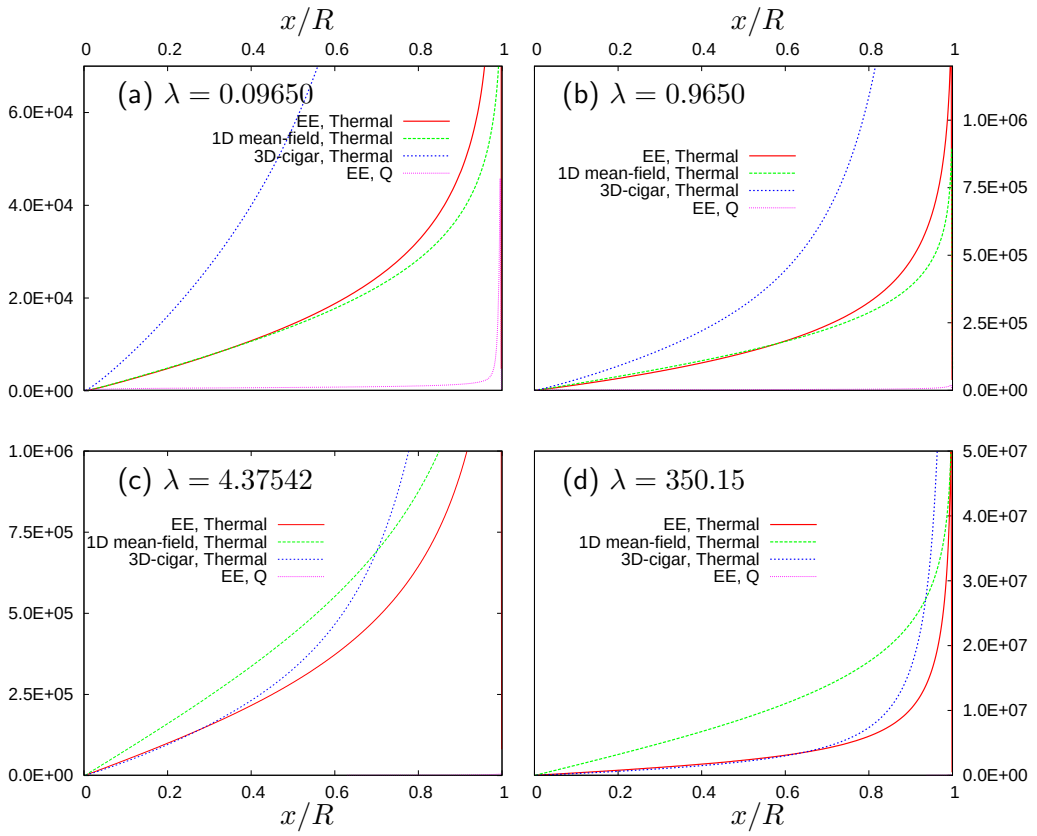

Figure 6.13: Thermal contribution to $\left\langle [\Delta \hat{S}(x)]^2 \right\rangle$ corresponding to Cases D–G defined in Table 6.2 (panels (a)–(d) respectively). This set of plots shows that the 1D effective equations (red curve) reproduces a smooth transition between the 1D mean-field (green curves) and the 3D-cigar (blue curves). In all cases, the cyan curve corresponds to the quantum contribution.

6.4 Summary

This chapter presents some characteristics of low-dimensional degenerate Bose gases (BEC or condensate), with particular emphasis on the so-called quasi-1D regime. This regime is achieved by imposing an asymmetric trapping potential, with a very strong confinement along two of the three spatial directions in 3D.

We consider a 3D harmonic potential with cylindrical symmetry, characterized by the frequencies along the transverse, $\omega_\perp$, and axial directions, ω_x, with $\omega_\perp \gg \omega_x$. In this situation, two extreme regimes can be defined: (a) when the trap in the transverse direction is so high that the condensate only populates the lowest state in the transverse direction (1D mean-field regime) and (b) when there are many levels occupied along both the transverse and axial directions, such that a Thomas-Fermi approximation can be applied in all spatial directions (3D-cigar regime).

The density of states and excitation spectrum of the condensate depend on the trap-

ping potential, affecting the spatial correlation of the wave-function of the condensate [40, 2]. For the two regimes mentioned, 1D mean-field and 3D-cigar, there are analytical expressions for the spectrum, excitation modes and phase correlation of the condensate wave-function (Eq. 6.63), in the Thomas-Fermi approximation [138, 139] .

Muñoz and Delgado have proven that a simple one-dimensional equation, Eq. (6.45), can be use to evaluate the density profile and the low-energy dynamics of the condensate, with the same accuracy than a full 3D Gross-Pitaevskii simulation. Their 1D equation remains valid in the cross-over between the 1D mean-field and the 3D-cigar regimes, characterized by a dimensionless parameter $\lambda = N(\omega_x a)/(\omega_\perp a_\perp)$ [143, 147].

This effective equation is used to evaluate the density profile, the excitation modes and the mean-square phase difference, $\left\langle (\Delta\hat{S}(x))^2 \right\rangle$, for configurations A–G indicated in Table 6.2. These calculations show how the properties of the quasi-1D condensate change as the system crosses from the 1D mean-field to the 3D-cigar regimes.

We have compared the density profile given by the equilibrium state of the Eq. (6.45) with the equilibrium state of a 3D-GPE. The comparison is favourable and probes the accuracy of the effective equation for this calculation. Cases A–G indicated in Table 6.2 can be classified in three groups (according to their dimensionless parameter, λ).

To the first group belongs cases A–C. All of them have a dimensional parameter $\lambda \ll 1$, and therefore, lie in the 1D mean-field regime. In these cases, despite the chemical potential being just a few orders of magnitude higher than the energy quantum of the trap in the axial direction (i.e. $\hbar\omega_x$), the density profile is well approximated by a Thomas-Fermi approximation of the 1D mean-field (Figure 6.3). In contrast, the spectrum of excitations does not follows the rule given by the 1D mean-field approximation ($\epsilon_j = \hbar\omega_x\sqrt{j(j+1)/2}$) (Figure 6.5). The reason for this behaviour is the low number of particles, which makes the spectrum have a non-interacting character, corresponding to the harmonic oscillator dispersion relation. This is shown in figure 6.5, where, for large j, the slope of the dispersion relation, $\epsilon_j = \alpha j$, corresponding to these cases satisfies $\alpha_{\mathsf{HO}} > \alpha > \alpha_{\mathsf{1D}}$.

In this group, the 1D effective equation and the 1D mean-field predictions of the wave-functions for the low energy excitations only differ slightly near the edges of the cloud, which is expected because of the failure of the Thomas-Fermi approximation involved in the 1D mean-field result. For high energy modes, the difference becomes appreciable; the spatial extension of the modes according to the 1D effective equation can be larger than the condensate size, while the Thomas-Fermi approximation of the 1D mean-field case rules out this possibility by definition (see Figure 6.6).

Also for Cases A–C corresponding to this group, the quantum and thermal contributions to $\left\langle [\Delta\hat{S}(x)]^2 \right\rangle$ predicted by the spectrum of the effective equation and by the 1D mean-field are similar but, again, differ close to the edges of the cloud. The quantum contribution reveals three spatial regions of variation: logarithmic growth, lineal

growth and exponential growth. The length of each region is the same for all cases (see Figure 6.10(a)), i.e., is independent of λ, and satisfies the universal form of Eq. (6.65). Similarly, in the thermal contribution, two regions can be distinguished: linear and exponential growths, but in this case the extension of these depends on the system having the form of Eq. (6.66).

The second group has a single member, Case D in Table 6.2, which, according to its dimensional parameter, lies in the 1D mean-field regime. In fact, the density profile, excitation spectrum and $\left\langle [\Delta\hat{S}(x)]^2 \right\rangle$ determined from the effective equation and the 1D mean-field regime differ only near the edges of cloud, again as a consequence of the Thomas-Fermi approximation used in the second method.

The last group is formed by Cases E, F and G. According to their dimensional parameters, λ, they lie in the cross-over region between the 1D mean-field and the 3D-cigar regimes. Comparing the density profiles, it can be observed how the effective equation predictions move away from the 1D mean-field and get close to the 3D-cigar regime. A similar transition occurs in the energy level spectrum (Figure 6.5) and excitations modes (Figure 6.4), and in both the quantum an thermal contributions to $\left\langle (\Delta\hat{S}(x))^2 \right\rangle$ (Figures 6.10(b) and 6.13). The same regions of variation with the distance to the cloud centre can be observed as in Cases A–C, but the length of each one depends on λ, as shown by Eq. (6.66). Respect to the thermal contribution to the phase fluctuations, it should be highlighted that it cannot be described by a universal function, in contrast to cases in the first group.

In the sequence of figures presented in this chapter, we have shown how the 1D effective equation Eq. 6.45 produces a a smooth transition between the 1D mean-field and the 3D-cigar regimes. This can be see by noticing that for $\lambda \ll 1$ the red and green curves are similar, and as λ is increased, the green curves (1D mean-field predictions) move away from the red ones (effective equation predictions), while the blue curves (3D-cigar predictions) move closer to the red curves.

CHAPTER 7

Outlook and directions for future work

Recent experimental and theoretical work has highlighted the great potential of magnetically trapped dilute atomic gases in the Bose-Einstein condensed phase, for developing applications and to study fundamental physics [26]. The degenerate regime can be reached by isolating the gas from uncontrollable perturbations, making this an ideal system to test the validity of fundamental concepts in quantum physics like the spin-statistics theorem, spontaneous symmetry breaking, coherence, quantum phase transitions, etc. [2, 40]. In addition, the effect that an external perturbation has on the degenerate gas can be exploited in a two way: first, as a tool to understand the source of the perturbation and second to perform controlled transformations of the gas itself. The BEC magnetic field microscope [117, 125] corresponds to the first situation, while several examples of atomic micro-manipulation with magnetic surface traps illustrate the second possibility [26, 61].

A standard setup generically called an "atom chip", is being used by many experimental groups to manipulate atomic BECs [26]. It consists of a set of controllable magnetic field sources mounted on a surface. Good conducting materials (like copper, gold and silver) are preferred as the sources of magnetic field, mainly because they support large current densities, therefore, producing low Joule heating, which can be dissipated fast enough to avoid destruction of the system components. Large currents produce strong and stable confining potentials, desirable to develop fast dynamics and perform several operations during the BECs life-time. Proof of principle setups of several applications have been already developed, including atomic guides, beam splitters, coherent manipulation and interferometry experiments [26].

Nowadays, the cold atom community is beginning to study different materials replacing the conducting wires in the atom chip. So far, few of these systems have been explored, including ferromagnetic magnetic traps and lattice experiments [90], superconductor atom chips (recent experiments reported in [94]), a proposal of magnetic trapping with carbon-nano-tubes [88], considerations of using alloys as conducting elements [86] and materials with anisotropic conductivity [87]. Until now, the possible advantages of the production of the atom chip, and of the properties of the materials are largely unexploited experimentally. The list of alternatives (or complements) to metals also includes graphene, semiconducting ferromagnets, and all the set of semiconducting devices such as quantum dots, quantum wires or nano-resonators which have not being used so far in any experiment to control the BEC in a direct form.

This thesis explores the coupling of an atomic Bose-Einstein condensate to a high-mobility two-dimensional electron gas, through the magnetic field generated by a current in the 2DEG. Two simple observations motivate studying this combination of systems: due to its quasi-2D nature and its smaller conductance compared with a good conducting metal, the life-time of trapped states near a 2DEG is expected to be much larger than above a metallic slab. The second motivation is technical: structures over semiconducting devices can be patterned with high resolution (nm precision), potentially reducing significantly the modulation of the magnetic field profile due to geometrical imperfection of the patterns, which can limit the possibilities of operation and has been observed in many atom chip experiments [26, 80].

The magnetic field produced by a typical high-mobility 2DEG at cryogenic temperatures, can be used to trap the condensate. The trap produced can be easily located at distances between $1-10$ μm above the 2DEG, with a depth of a few tens of μK. This trap is weaker than most of the traps reported in experiments [26], but still strong enough to hold a typical BEC containing 10^4-10^5 atoms. Hybrid systems combining the magnetic field produced by a 2DEG and metal wires can improve the trapping conditions, keeping the advantages identified above of using a semiconducting device. On the other hand, the irregularities of the electron motion inside the 2DEG produces inhomogeneities of the magnetic field, which affect strongly the continuity of a trapped condensate when it is located at distances of the order of 1 μm from the surface. These results suggest that implementing trapping potentials using 2DEGs, or similar semiconducting devices, can open a new range of atom chip operation below 10μm, with the advantage of having atomic and coherence lifetimes limited only by collisions with background atoms.

The second problem considered in this thesis consists of using a BEC close to a 2DEG to probe the semiconducting system by sensing the irregularities of the magnetic field produced. Two examples of this situation are presented: determination of quantised conductance in a quantum point contact and determination of characteristics of the donor distribution in the heterojunction containing the 2DEG. In both cases, a simple model of the heterojunction provides a relationship between its structure and the mag-

netic field produced. The level of sensitivity needed to detect variations of the magnetic field due to changes in the conductance of a QPC can be reached by an atomic BEC with a small scattering length which can be set, e.g. by using a Feshbach resonance of ^{133}Cs.

In the second example, it was proven that the magnetic field profile can be used to extract information about the statistics of the donor distribution in the heterojunction. The development of such applications would present great advantages for the study of semiconductor materials. For example, the single shot character of the measurement, which means that a single experimental process can provide information about the heterojunction at different points within it. A second advantage is the non-perturbative character of this technique, in the sense that properties of the 2DEG are not appreciably changed by the presence of the BEC. A major disadvantage is the poor resolution of the technique compared with other imaging procedures [122]. A micrometre resolved image of the heterojunction is not enough to resolve all their details, which have a typical length scale of a few hundred nm, but can be useful to identify long-range correlations.

Because of its geometry, atoms chips usually create trapping potentials with extremely elongated geometries, placing the BEC into a quasi-1D regime [143]. Such low dimensional systems have phase coherence properties different from those observed in a 3D system, and whose understanding is needed to perform coherent manipulation of the condensates in applications such as the matter-wave interferometer [26]. In this thesis, we use the effective 1D equation proposed in [147], to evaluate the coherence properties of elongated BECs in different regimes of transverse confinement [143]: 1D mean-field, 3D-cigar and the crossover between these two extremes. Predictions of the correlation of the phase based on such an equation (Eq. (6.45)) show a smooth transition between the two extreme regimes, confirming the ability of the equation to describe, in addition to the density profile of elongated BEC, the low energy dynamics of the system [142, 147, 148].

Several directions of study can be pointed out. Apart from the examples mentioned above of atom chips using non-metallic wires, other material systems have been considered, including the coupling BECs to a forest of carbon nano-tubes [149] and using nano-magnets for trapping [150]. There is still a lot of room for research involving other materials, and in particular establishing how solid state devices and BEC can be coupled. As an example of what could be done to establish the possibilities for magnetic trapping offered by different materials, here we illustrate the case of semiconducting ferromagnets.

Trapping and manipulation of atoms using permanent magnets has been demonstrated by R. Gerritsma *et al.* [90], but such designs suffer from the inflexibility of having a fixed magnetization. Ferromagnetic semiconductors, or Dilute Magnetic Semiconductors (DMS), are materials whose magnetic properties can be changed by adjusting

the carrier concentration or applying stress through a piezoelectric structure [151]. This material seems adequate for implementing designs for cold atom manipulation with improved flexibility over the permanent magnet based setups.

Firstly, a suitable geometry should be established. Two slabs of material magnetized in the same direction, as shown in figure 7.1(a), plus externally applied bias (along z) and offset (along x) fields, constitute the simplest possible trapping configuration involving uniform magnetised material. In this configuration, trapping properties (position, depth and frequency) depend on the magnetization and distance between slabs centres. Figures 7.1(b) and (c) show typical values achievable with this setup.

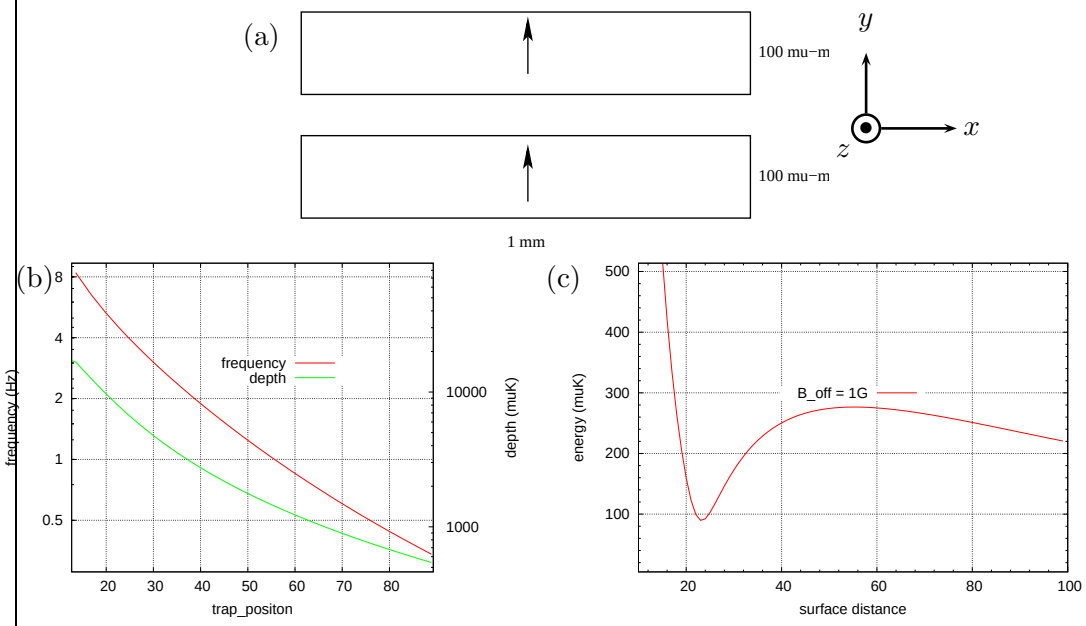

Figure 7.1: (a) Typical trap properties achievable with a couple of DMS slabs in a parallel configuration. (b) Trap properties for different trap positions. (c) Typical potential energy for an ^{87}Rb in presence of a setup like shown in (a)

The magnetization density of a DMS reaches just a few tens of kA/m [151], which means that in order to build a trap working in the micrometre region, the required dimensions of the slabs should be around one order of magnitude larger than the typical ones deposited for DMS (3 µm vs. 300 nm). Perhaps it is not impossible to grow DMS slabs with the required geometry, but it definitely is not a common task in the context of DMS. In addition, it seems difficult to incorporate a simple way to control the intensity and direction of the magnetic field. Advantages and implementation strategies for the design of setups for atom manipulation are open questions.

Apart from trapping, new materials can offer the possibility to couple with the BEC in such a way that they are, themselves, influenced by its presence. For example, we can think of applications where the density of free electrons in a semiconductor is modified by

the BEC, maybe due to the interaction between atomic and electron dipolar moments [79]. Also, improving the coherence properties, lifetime and control of cold atomic clouds could be achieved by integrating semiconductor devices in atom chips, opening a broad range of possibilities for both technological applications and fundamental research. Work in the direction of creating hybrid systems combining solid state devices and BECs is nowadays an open field which surely, in the near future, will bring us interesting applications and also new challenges.

APPENDIX A

Numerical solution of the GPE

This appendix describes how to produce a numerical solution of the Gross-Pitaevskii equation, Eq. (1.27), and in particular how to calculate the ground state configuration of a condensate described by the GPE. The presentation here follows mainly two bibliographic sources: the well known *Numerical recipes: The art of scientific computing* [152] and the PhD. thesis presented by Robin Scott [153], where many additional details can be found.

A.1 Operator splitting

The time splitting method, or method of fractional steps, is a procedure used for solving partial differential equations by combining several finite difference schemes [152]. Consider an operator $\mathcal{L}$ responsible of the time evolution of a function $u(x,t)$, according to the partial differential equation:

$$\partial_t u = \mathcal{L} u \tag{A.1}$$

where the spatial (x) and temporal (t) dependencies of both u and $\mathcal{L}$ are assumed but not explicitly indicated.

Suppose that $\mathcal{L}$ is a linear sum of M pieces, which act additively on u [152], i.e., the full operator $\mathcal{L}$ can be written as:

$$\mathcal{L} = \mathcal{L}_1 + \mathcal{L}_2 + \dots \tag{A.2}$$

and consider the set of equations with the form:

$$\partial_t u = \mathcal{L}_m u \tag{A.3}$$

with $m = 1, 2, \ldots, M$.

Let $\mathcal{U}_m$ be a scheme which solves approximately Eq. (A.3), by updating the function u in discrete time steps, from its value at a given time t to the next instant $t + \Delta t$. The M updating schemes, one corresponding to each contribution to the operator $\mathcal{L}$, perform a discrete time evolution of the variable u according to:

$$\begin{aligned} u^{t+\Delta t} &= \mathcal{U}_1(u^t, \Delta t) && \text{(A.4)} \\ u^{t+\Delta t} &= \mathcal{U}_2(u^t, \Delta t) && \text{(A.5)} \\ u^{t+\Delta t} &= \mathcal{U}_3(u^t, \Delta t) && \text{(A.6)} \\ &\vdots \end{aligned}$$

such that $\mathcal{U}_m$ is a discrete version of the individual operator $\mathcal{L}_m$.

Including *all* the terms of the original operator, $\mathcal{L}$, in each one of the updating schemes $\mathcal{U}_m$, and not only the m^{th} contribution, allows us to perform a complete updating sequence corresponding to the full operator. This procedure should follows the sequence [152]:

$$\begin{aligned} u^{t+\Delta t/m} &= \mathcal{U}_1(u^t, \Delta t/m) && \text{(A.7)} \\ u^{t+2\Delta t/m} &= \mathcal{U}_2(u^{t+\Delta t/m}, \Delta t/m) && \text{(A.8)} \\ &\cdots \\ u^{t+\Delta t} &= \mathcal{U}_m(u^{t+(m-1)\Delta t/m}, \Delta t/m) && \text{(A.9)} \end{aligned}$$

This combination of individual updating schemes provides the time evolution determined by the full operator $\mathcal{L}$.

A.2 Crank-Nicolson updating scheme.

Consider the Gross-Pitaevskii equation, Eq. (1.27), with an external potential of the form:

$$V(\boldsymbol{r}) = \sum_{i=1}^{D} V_i(x_i) \qquad \text{(A.10)}$$

where D is the spatial dimensionality of the system and $\boldsymbol{r} = (x_1, \ldots x_D)$ represents a spatial vector position. A potential energy of the form Eq. (A.10) implies that motion along each spatial direction contributes to $V(\boldsymbol{r})$. The simplest example of this kind of potential is the three dimensional harmonic potential with independent elastic constants along each spatial direction.

With this form of the potential, the GPE operator can be split into contributions corresponding to each spatial direction.

$$i\hbar\partial_t\psi = \sum_{i}^{D} \mathcal{L}_i\psi \qquad \text{(A.11)}$$

where the one-dimensional Gross-Pitaevskii operator (1D-GP), $\mathcal{L}_i$, has the form:

$$\mathcal{L}_i = -\frac{\hbar^2}{2m}\frac{\partial^2}{\partial x_i^2} + V_i(x_i) + \frac{1}{3}\frac{4\pi\hbar^2 a_s}{m}|\psi|^2 \tag{A.12}$$

For this form of potential energy, the operator splitting method,explained in the previous section, can be used to solve the GPE.

According to this method, the time-evolution of the condensate wave function is built by successive applications of updating schemes corresponding to each contribution to the GP operator, satisfying the Eq. (A.3). The non-integrability of the 1D-GP operator, Eq. (A.12), requires the use of numerical methods to evaluate the time-evolution of the condensate wave-function ψ. This is done by imposing a discretisation of the time and space coordinates in steps of Δt and Δx_i, respectively, and representing the wave-function, ψ, on such a grid of spatial points and evaluating its time-evolution at finite time steps [153].

By discretizing the time and space, the partial derivative operators in the GPE take the approximate form:

$$\begin{aligned} \partial_t\psi &\approx \frac{\psi_j^{t+\Delta t} - \psi_j^t}{\Delta t} \\ \partial_{x_i}\psi &\approx \frac{\psi_{j+1}^t - 2\psi_j^t + \psi_{j-1}^t}{(\Delta x_i)^2} \end{aligned} \tag{A.13}$$

where j indicates the position in the spatial grid.

Replacing directly the discrete versions of the differential operators, Eqs. (A.13), into the time evolution equation corresponding to the 1D-GP operator, Eq. (A.12), produces:

$$i\hbar\frac{\psi_j^{t+\Delta t} - \psi_j^t}{\Delta t} = -\frac{\hbar^2}{2m}\frac{\psi_{j+1}^t - 2\psi_j^t + \psi_{j-1}^t}{(\Delta x_i)^2} + (V_i^j + \frac{U_0}{3}|\psi_j^t|^2)\psi_j^t \tag{A.14}$$

where V_i^j indicates the i^{th} contribution to the potential energy evaluated at the j^{th} position in the spatial grid. Notice that using Eq. (A.14), the value of the wave function at the next instant of time, $\psi^{t+\Delta t}$, can be evaluated explicitly by its values corresponding to the previous instant of time, ψ^t. This procedure is known as an *explicit scheme*, since the wave-function in the new instant of time can be obtained explicitly from the wave function at previous instants.

On the other hand, the condensate wave function should satisfy the GPE at every instant of time. Therefore, with the same level of accuracy as Eq. (A.14), the right hand side of the GPE should be satisfied by the updated wave function, $\psi^{t+\Delta t}$:

$$i\hbar\frac{\psi_j^{t+\Delta t} - \psi_j^t}{\Delta t} = -\frac{\hbar^2}{2m}\frac{\psi_{j+1}^{t+\Delta t} - 2\psi_j^{t+\Delta t} + \psi_{j-1}^{t+\Delta t}}{(\Delta x_i)^2} + (V_i^j + \frac{U_0}{3}|\psi_j^{t+\Delta t}|^2)\psi_j^{t+\Delta t} \tag{A.15}$$

In contrast with Eq. (A.14), this last equation cannot be solved explicitly for the updated wave-function. In Eq. (A.15), there is a mixture of the wave-function evaluated at

different grid points, at the instant of time $t + \Delta t$, which are precisely the unknown variables. This is an example of an *implicit scheme*, where the future wave-function is determined by the relation of its values at different positions.

According to Robin Scott [153]:

> "Both schemes (explicit and implicit) have the disadvantage that different sides of the equations are centred at different times. Specifically, the left-hand side of the explicit scheme is centred at time $t + \frac{\Delta t}{2}$, while the right-hand side is centred at time t. The left-hand side of the implicit scheme is also centred at time $t + \frac{\Delta t}{2}$ but the right-hand side is centred at time $t + \Delta t$."

To solve this inconsistency, it is enough to take an average of the explicit and implicit schemes, producing what is known as the *Crank-Nicolson* method, with the finite difference equation:

$$i\hbar\frac{\psi_j^{t+\Delta t}-\psi_j^t}{\Delta t} = -\frac{\hbar^2}{2m}\frac{\psi_{j+1}^{t+\Delta t}-2\psi_j^{t+\Delta t}+\psi_{j-1}^{t+\Delta t}+\psi_{j+1}^t-2\psi_j^t+\psi_{j-1}^t}{(\Delta x_i)^2} + \left(V_j+\frac{U_0}{3}|\psi_j^{t+\Delta t}|^2\right)\psi_j^{t+\Delta t}+\left(V_j+\frac{U_0}{3}|\psi_j^t|^2\right)\psi_j^t \quad \text{(A.16)}$$

Reorganising Eq. (A.16) by separating the updated bits of the form $\psi_j^{t+\Delta t}$, from the old ones, ψ_j^t, this equation can be written as:

$$\psi_j^{t+\Delta t}\left(1+2\beta+\alpha\left(\frac{U_0}{3}|\psi_j^{t+\Delta t}|^2+V_j\right)\right)-\beta\psi_{j+1}^{t+\Delta t}-\beta\psi_{j-1}^{t+\Delta t} = \psi_j^t\left(1-2\beta-\alpha\left(\frac{U_0}{3}|\psi_j^t|^2+V_j\right)\right)+\beta\psi_{j+1}^t+\beta\psi_{j-1}^t \quad \text{(A.17)}$$

with

$$\alpha = i\frac{\hbar\Delta t}{2\hbar} \text{ and } \beta = \frac{i\hbar\Delta t}{2m(\Delta x_i)^2} \quad \text{(A.18)}$$

Finally, Eq. (A.17) is conveniently written in the matrix form:

$$\begin{pmatrix} 1+\xi_j^{t+\Delta t} & -\beta & \cdots & & & \\ -\beta & 1+\xi_{j+1}^{t+\Delta t} & -\beta & 0 & \cdots & \\ 0 & -\beta & 1+\xi_{j+2}^{t+\Delta t} & -\beta & 0 & \cdots \\ 0 & 0 & -\beta & 1+\xi_{j+3}^{t+\Delta t} & -\beta & 0 \\ \vdots & \vdots & & & & \end{pmatrix}\begin{pmatrix}\psi_j^{t+\Delta t}\\ \psi_{j+1}^{t+\Delta t}\\ \psi_{j+2}^{t+\Delta t}\\ \psi_{j+3}^{t+\Delta t}\\ \vdots\end{pmatrix} = \begin{pmatrix} 1+\xi_j^t & -\beta & \cdots & & & \\ -\beta & 1-\xi_{j+1}^t & -\beta & 0 & \cdots & \\ 0 & -\beta & 1-\xi_{j+2}^t & -\beta & 0 & \cdots \\ 0 & 0 & -\beta & 1-\xi_{j+3}^t & -\beta & 0 \\ \vdots & \vdots & & & & \end{pmatrix}\begin{pmatrix}\psi_j^t\\ \psi_{j+1}^t\\ \psi_{j+2}^t\\ \psi_{j+3}^t\\ \vdots\end{pmatrix} \quad \text{(A.19)}$$

where

$$\xi_j^t = 2\beta + \alpha\left(\frac{U_0}{3}|\psi_j^t|^2 + V_i^j\right) \tag{A.20}$$

The right hand side of Eq. (A.19) can evaluated explicitly since it depends entirely on the known function ψ_j^t. In contrast, the diagonal elements of the matrix on the left-hand side (LHS) depend on the updated function,$\psi_j^{t+\Delta t}$, which is unknown, and therefore they cannot be explicitly calculated. A way to resolve this issue consists of using the old function, ψ_j^t, to evaluate the matrix entries and then estimate the updated function. This first estimation of $\psi_j^{t+\Delta t}$ is used to evaluate the LHS matrix, and then solved again to find a new updated function. This procedure should be repeated iteratively until it reaches convergence, which sounds worse than it is in practice, since usually just two iterations are enough to obtain an updated function with good accuracy [153].

According to the time-splitting method, a complete time evolution of the full GPE is obtained by applying the scheme indicated by the tridiagonal Eq. (A.19) for each spatial direction, but including the pieces of the operator $\mathcal{L}$ corresponding to the other spatial directions. In practice, this means that Eq. (A.20) should be replaced by:

$$\xi_j^t = 2\beta + \alpha(U_0|\psi_j^t|^2) + V_j) \tag{A.21}$$

with V_j being the total potential energy at position j in the grid and not just the contribution corresponding to the spatial coordinate involved in the momentum operator.

The tridiagonal form of the problem Eq. (A.19) is conserved for each direction if the wave-function is stored according to the order of the grid along the corresponding direction. This requires that between applications of the updating scheme along different directions, the vector ψ_j should be reorganised. See [153] for details about the reorganisation sequence.

Finally, it should be mentioned that the boundary conditions over the wave-function should be carefully taken into account when building the tridiagonal matrices in Eq. (A.19).

A.3 Imaginary-time evolution of the GPE

Consider a generalised Schrödinger equation:

$$i\hbar\partial_t\psi = \mathcal{L}\psi \tag{A.22}$$

with $\mathcal{L}$ a Hermitian operator. Replacing the time variable by the complex quantity $-it$, converts the wave-equation Eq. (A.22) into a diffusion equation, which can be used to obtain equilibrium configurations.

Formally, the real-time evolution of a general Schrödinger equation is given by:

$$|\psi(t)\rangle = e^{-i\hat{\mathcal{L}}t/\hbar}|\psi(t=0)\rangle \tag{A.23}$$

Using the set of eigen-states of the operator $\hat{\mathcal{L}}$, satisfying $\hat{\mathcal{L}}\,|\phi_j\rangle = \epsilon_j\,|\phi_j\rangle$, any initial condition can be expanded as:

$$|\psi(t=0)\rangle = \sum \psi_j\,|\phi_j\rangle \tag{A.24}$$

and therefore, the time evolution takes the form

$$|\psi(t)\rangle = \sum_j e^{-i\epsilon_j t/\hbar}\psi_j\,|\phi_j\rangle \tag{A.25}$$

Performing the change $t \to -it$, the time evolution of each component of the state becomes a decaying exponential. After a given evolution period, the whole wave-function decreases in amplitude as consequence of the non-conservation of the norm introduced by the ficticious i factor. The components corresponding to excitations states decay faster than the associated with the ground state of the system (lowest eigen-energy). To avoid the wave-function going to zero after prolongated evolution, a renormalization should be realized periodically. The result of this processes is the suppression of all components except the one corresponding to the lowest energy state [153].

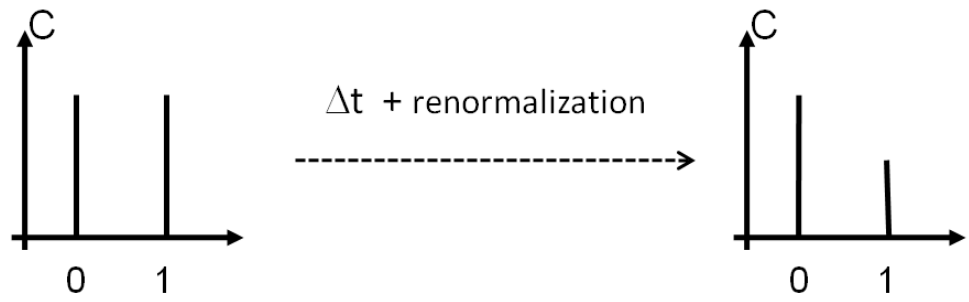

Figure A.1: Sketch of how the imaginary time evolution of an initial state eliminates the high energy components.

Figure A.1 illustrates an example of how the composition of the initial states changes as the imaginary-time evolution occurs. Panel (a)p shows a representation of the coefficients of the initial state: $|\psi(t=0)\rangle = \frac{1}{\sqrt{2}}\,|0\rangle + \frac{1}{\sqrt{2}}\,|1\rangle$, where the states have energies satisfying $\epsilon_0 < \epsilon_1$. After a period of imaginary time evolution and renormalisation, the coefficients of the superposition transform as shown in the panel to the right. After repeated evolution and renormalization processes, the component corresponding to the higher energy vanishes.

APPENDIX B

Magnetic field due to a 2D distribution of currents

This appendix shows how the magnetic field produced by a two-dimensional current flow can be obtained in terms of the Fourier transform of the distribution. A straightforward application of such relation allows us to obtain the magnetic field produced by a current flowing in a 2DEG and the donor distribution in the hetero-junction, Eq. (5.20).

This direct relation between the magnetic field and the donor distribution can be used to establish the relation between the statistics properties of those two quantities, as illustrated by Eqs. (5.21) and (5.22).

This appendix follows the definitions of ensemble average and correlation function by Kerson Huang in [1].

B.1 Magnetic field in terms of the Fourier Transform of the current density

This section follows the presentation in Ref. [125]. Consider a thin conducting layer lying in the $x-y$ plane and carrying a time-independent current density $\boldsymbol{j} = (j_x, j_y)$. This current density represents the charge passing through a transverse section of the 2D plane, per unit of time and "area" of the transverse section. In 2D a transverse section corresponds to a line and therefore, the current considered here, $\boldsymbol{j}$, is in units of $\frac{charge}{length \times time}$.

The Biot-Savart law relates the magnetic field with its sources according to:

$$\boldsymbol{B}(\boldsymbol{r}) = \frac{\mu_0}{4\pi} \int \frac{\boldsymbol{j}(\boldsymbol{r'}) \times (\boldsymbol{r} - \boldsymbol{r'})}{|\boldsymbol{r} - \boldsymbol{r'}|^3} d^2\boldsymbol{r'} \tag{B.1}$$

where μ_0 is the permeability of the vacuum, $\boldsymbol{r} = (x, y, z)$, $\boldsymbol{r'}$ is a position vector in the plane of the conductor and the integral is performed over the complete region where the current flows.

After examining each component of the magnetic field given by Eq. (B.1), the Biot-Savart law can be interpreted as a convolution of the current density with the weighting function $(\boldsymbol{r} - \boldsymbol{r'})/|\boldsymbol{r} - \boldsymbol{r'}|^3$. For example, consider the x-component of the magnetic field, which, according to Eq. (B.1), is given by:

$$B_x(\boldsymbol{r}) = \frac{\mu_0}{4\pi} z \int \frac{j_y(\boldsymbol{r'})(x - x')}{((x - x')^2 + (y - y')^2 + z^2)^{3/2}} dx'dy' \tag{B.2}$$

The convolution theorem establishes a relation between the Fourier Transform of the convoluted function and the weighting factor [152]. In the present case, the convoluted function corresponds to the current density components while the weighting factor is given by the components of $\sim \frac{(\boldsymbol{r}-\boldsymbol{r'})}{|\boldsymbol{r}-\boldsymbol{r'}|^3}$) [152], according to Eq. (B.1) Applied to Eq. (B.2), this theorem reads out as:

$$b_x(\boldsymbol{k}, z) = g(\boldsymbol{k}, z) j_y(\boldsymbol{k}) \tag{B.3}$$

where $\boldsymbol{k} = (k_x, k_y)$, $b_x(\boldsymbol{k}, z)$ and $j_y(\boldsymbol{k})$ are the 2D Fourier transforms of the magnetic field and current density, respectively, and $g(\boldsymbol{k}, z)$ is the 2D Fourier transform of the factor multiplying the current density in Eq. (B.2):

$$g(\boldsymbol{k}, z) = \frac{\mu_0}{2} e^{-kz} \tag{B.4}$$

where $k = \sqrt{k_x^2 + k_y^2}$ [125]

Similar results can be obtained for the y and z components of the magnetic field, which are summarised as follows [125]:

$$b_x(k_x, k_y, z) = \frac{\mu_0}{2} e^{-kz} j_y(k_x, k_y) \tag{B.5}$$

$$b_y(k_x, k_y, z) = -\frac{\mu_0}{2} e^{-kz} j_x(k_x, k_y) \tag{B.6}$$

$$b_z(k_x, k_y, z) = i\frac{\mu_0}{2} e^{-kz} \left(\frac{k_y}{k} j_x(k_x, k_y) - \frac{k_x}{k} j_y(k_x, k_y) \right) \tag{B.7}$$

B.2 Derivation of Equation (5.20)

Equation (5.20) establishes the relation between the magnetic field produced by a current in a 2DEG, and the distribution of donors in the hetero-junction.

Consider a typical hetero-junction containing a 2DEG whose electrons come from a thin layer of dopant. As explained in Chapter 2, the electron-electron Coulomb repulsion screens the electrostatic potential due to the ionized donors. In the linear screening

regime [96], the total electrostatic potential is given by Eq. (2.2):

$$\Phi_{\text{screened}}(\boldsymbol{r'}) = \frac{e^2}{4\pi\epsilon\epsilon_0}\int e^{-kd}\frac{\eta_d(\boldsymbol{k})e^{i\boldsymbol{k}\cdot\boldsymbol{r'}}}{k+k_s}d\boldsymbol{k} \tag{B.8}$$

where d is the separation between the donor layer and the 2DEG plane, $\boldsymbol{k} = (k_x, k_y)$, $\eta_d(\boldsymbol{k})$ is the 2D Fourier Transform of the donor density $\eta_d(\boldsymbol{r'})$, $\boldsymbol{r'}$ is a vector position in the 2DEG plane, ϵ is the relative permittivity of GaAs and

$$k_s = \frac{e^2 m_e^*}{2\epsilon\epsilon_0\pi\hbar^2}$$

is the screening wave vector, with m_e^* the electron effective mass.

The inhomogeneous component of the current flow occurring when a small uniform electric field is applied to the 2DEG, is determined by the gradient of Eq. (B.8):

$$\boldsymbol{j}(\boldsymbol{r'}) = -\sigma\vec{\nabla}\frac{\Phi(\boldsymbol{r})}{e} \tag{B.9}$$

where σ is the 2D conductivity of the layer, which has units of $\frac{charge}{length\times time}\frac{charge\times length}{energy}$

When converting Eq. (B.9) to k-space, the derivative operator becomes a multiplication by the corresponding wave-vector component. Therefore, in k-space, the inhomogeneous contribution to the current density, Eq. (B.9), becomes:

$$\boldsymbol{j}(\boldsymbol{k}) = -\sigma\frac{\Phi(\boldsymbol{k})}{e}\boldsymbol{k} \tag{B.10}$$

Combining this last equation with the screened potential, Φ, given by Eq. (B.8), the Fourier Transform of the inhomogeneous components of the current in the 2DEG is obtained:

$$\boldsymbol{j}(\boldsymbol{k}) = \sigma\ \boldsymbol{k}\ \frac{e}{2\epsilon\epsilon_0}e^{-kd}\frac{\eta_d(\boldsymbol{k})}{k+k_s} \tag{B.11}$$

The Fourier components of the x-component of the magnetic field produced by this current, can be evaluated by applying the convolution theorem Eq. (B.5), which yields:

$$b_x(\boldsymbol{k}, z) = \frac{\mu_0}{2}e^{-kz}\sigma k_y\frac{e}{2\epsilon\epsilon_0}e^{-kd}\frac{\eta_d(\boldsymbol{k})}{k+k_s} \tag{B.12}$$

Finally, an inverse Fourier transform over Eq. (B.12) produces the magnetic field distribution in real space:

$$B_x(\boldsymbol{r}) = \frac{\mu_0\sigma e}{4\epsilon\epsilon_0}\int d^2\boldsymbol{k}\ k_y\frac{\eta_d(\boldsymbol{k})}{k+k_s}e^{-k(d+z)}e^{i\boldsymbol{k}\cdot\boldsymbol{r}} \tag{B.13}$$

which, along the x-axis ($y = 0$) becomes:

$$B_x(x, z) = \frac{\mu_0\sigma e}{4\epsilon\epsilon_0}\int d^2\boldsymbol{k}\ k_y\frac{\eta_d(\boldsymbol{k})}{k+k_s}e^{-k(d+z)}e^{ik_x x} \tag{B.14}$$

coinciding with Eq. (5.20).

B.3 Derivation of Eqs. (5.21) and (5.22)

Eq. (B.14) establishes a direct relation between the statistical distribution of the donors in the hetero-junction containing the 2DEG and the inhomogeneous magnetic field produced when a small current flows inside it.

This equation also can provide a relation between the statical properties of these two quantities. A simple example is the self-correlation of the component of the magnetic field along the x-axis, given by:

$$\left\langle B_x(x,z)B_x(x',z)\right\rangle = \left(\frac{\mu_0\sigma e}{4\epsilon\epsilon_0}\right)^2 \int\int d^2\boldsymbol{k}d^2\boldsymbol{k'}\ k_y k'_y \frac{\langle\eta_d(\boldsymbol{k})\eta_d(\boldsymbol{k'})\rangle}{(k+k_s)(k'+k_s)} \times e^{-(k+k')(d+z)}e^{ik_x x+k'_x x'} \quad \text{(B.15)}$$

where the correlation of the donor density distribution, in momentum space, can be identified.

Assuming that the donor distribution, $\eta_d(\boldsymbol{r'})$, belongs to an stationary ensemble with probabilities independent of the origin of coordinates, then the correlation function of the density distribution satisfies:

$$\left\langle \eta_d(\boldsymbol{r'})\eta_d(\boldsymbol{r'}+\Delta\boldsymbol{r'})\right\rangle = C(\Delta\boldsymbol{r'}) \quad \text{(B.16)}$$

i.e. it depends only on the relative distance between the points.

This relation implies that, in the momentum representation, the auto-correlation function of the donor density satisfy the standard relation [1]:

$$\left\langle \eta_d(\boldsymbol{k})\eta(\boldsymbol{k'})\right\rangle = S(\boldsymbol{k})\delta(\boldsymbol{k}+\boldsymbol{k'}) \quad \text{(B.17)}$$

where $S(\boldsymbol{k})$ is the spectral density of the donor density distribution. Using this equation in Eq. (B.15) eliminates one of the integrals and yields:

$$\left\langle B_x(x,z)B_x(x',z)\right\rangle = \left(\frac{\mu_0\sigma e}{4\epsilon\epsilon_0}\right)^2 \int d^2\boldsymbol{k}\ k_y^2 \frac{S(\boldsymbol{k})}{(k+k_s)^2} e^{-2k(d+z)}e^{ik_x(x-x')} \quad \text{(B.18)}$$

The mean-square of the magnetic field can be obtained by taking $x = x'$ in Eq. (B.18):

$$\left\langle B_x^2(z)\right\rangle = \left(\frac{\mu_0\sigma e}{4\epsilon\epsilon_0}\right)^2 \int d^2\boldsymbol{k}\ k_y^2 \frac{S(\boldsymbol{k})}{(k+k_s)^2} e^{-2k(d+z)} \quad \text{(B.19)}$$

which corresponds to Eq. (5.21)

The spectral power of the magnetic field $B_x(x,z)$, considered as a function of x, can be defined as [1]:

$$D_{k_x}(z) = \frac{1}{2\pi}\frac{1}{\langle B_x^2(z)\rangle}\int d(x-x')\left\langle B_x(x,z)B_x(x',z)\right\rangle e^{-ik_x(x-x')} \quad \text{(B.20)}$$

Therefore, applying Eq. (B.18), $D_{k_x}(z)$ can be written in the form:

$$D_{k_x}(z) = \left(\frac{\mu_0 \sigma e}{4\epsilon\epsilon_0}\right)^2 \frac{1}{\langle B_x^2(z)\rangle} \int dk_y \frac{k_y^2 e^{-2k(d+z)}}{(k+k_s^2)} S(\boldsymbol{k}) \tag{B.21}$$

corresponding to Eq. (5.22).

The averages considered here correspond to ensemble averages, i.e. averages over different realizations of the donor distribution. According to the ergodic hypothesis, valid for a stationary ensemble [1], the average in Eq. (B.15) is equivalent to an average over real space, meaning that a single measurement of the magnetic field along the x-axis, can be used to determine the statistical properties here mentioned.

APPENDIX C

Bogoliubov - de Gennes modes for the 1D effective model of a quasi-1D degenerate Bose gas

In a Bose-Einstein condensate, the small amplitude oscillations around a stationary configuration are described by the Bogoliubov - de Gennes equations. These can be obtained by linearising the Gross-Pitaevskii equation around a small deviation from the equilibrium configuration.

Here we consider a 1D generalised Gross-Pitaevskii equation with arbitrary non-linear dependence on the condensate density, $\eta_{1D} = |\psi|^2$:

$$i\hbar\partial_t\psi = -\frac{\hbar^2}{2m}\partial_x^2\psi + V(x)\psi + \zeta(\eta_{1D})\psi \tag{C.1}$$

where ψ is normalised to the total number of particles, N, according to:

$$\int |\psi|^2 dx = N \tag{C.2}$$

An equilibrium configuration, ψ_0, satisfies the time independent non-linear Schrödinger equation:

$$\mu\psi_0 = -\frac{\hbar^2}{2m}\partial_x^2\psi_0 + V(x)\psi_0 + \zeta(\eta_{1D}^0)\psi_0 \tag{C.3}$$

where μ is the chemical potential.

The time evolution of a small deviation from the equilibrium configuration can be studied by writing the condensate wave-function in the form:

$$\psi(x,t) = (\psi_0(x) + \epsilon\delta\psi(x,t))e^{-i\mu t} \tag{C.4}$$

The Taylor expansion of the non-linear function $\zeta(\eta_{1D})$, around the equilibrium configuration ψ_0 has the form:

$$\zeta(\eta_{1D}) = \zeta(\eta_{1D}^0) + \epsilon \left.\frac{\partial \zeta}{\partial \eta_{1D}}\right|_{\eta_{1D}^0} \psi_0(\delta\psi + \delta\psi^*) \tag{C.5}$$

where we have considered the particular case of ψ_0 as a real function.

Using this expansion, the fact that ψ_0 satisfies Eq. (C.3), and keeping only first order terms in ϵ, the linear deviation satisfies:

$$i\partial_t \delta\psi = -\frac{\hbar}{2m}\partial_x^2 \delta\psi + \psi_0^2 \dot{\zeta}_0(\delta\psi + \delta\psi^*) + (\zeta_0 - \mu)\delta\psi \tag{C.6}$$

where

$$\begin{aligned} \zeta_0 &= \zeta(\eta_{1D}^0) \\ \dot{\zeta}_0 &= \left.\frac{\partial \zeta}{\partial \eta_{1D}}\right|_{\eta_{1D}^0} \end{aligned}$$

The excitation modes of the system can be obtained by expanding the linear deviation of the condensate function in Fourier components of frequency ω_j:

$$\delta\phi = \sum_j u_j(x) e^{-i\omega_j t} - v_j^*(x) e^{i\omega_j t} \tag{C.7}$$

As result of replacing expansion Eq. (C.7) into Eq. (C.6) and separating out the positive and negative frequency factors, a set of two coupled equations for the coefficients $u_j(x)$ and $v_j(x)$ is produced:

$$\hbar\omega_j u_j = -\frac{\hbar^2}{2m}\frac{d^2 u_j}{dx} + (V(x) - \mu)u_j + |\psi_0|^2 \dot{\zeta}_0(u_j - v_j) + \zeta_0 v_j \tag{C.8}$$

$$-\hbar\omega_j v_j = -\frac{\hbar^2}{2m}\frac{d^2 v_j}{dx} + (V(x) - \mu)v_j + |\psi_0|^2 \dot{\zeta}_0(u_j - v_j) + \zeta_0 u_j \tag{C.9}$$

These coupled equations are known as the Bogoliubov-de Gennes equations and can be written in the matrix form:

$$\hbar\omega_j \begin{pmatrix} u_j \\ v_j \end{pmatrix} = \begin{pmatrix} \mathcal{L} & -|\psi_0|^2\dot{\zeta}_0 \\ |\psi_0|^2\dot{\zeta}_0 & -\mathcal{L} \end{pmatrix} \begin{pmatrix} u_j \\ v_j \end{pmatrix} \tag{C.10}$$

where

$$\mathcal{L} = -\frac{\hbar^2}{2m}\frac{d^2}{dx^2} + V(x) - \mu + \dot{\zeta}_0|\psi_0|^2 + \zeta_0 \tag{C.11}$$

In this form, the Bogoliubov-de Gennes equations correspond to a eigen-problem for the matrix at the right hand side of Eq. (C.10). For an arbitrary external potential $V(x)$ and non-linear function, ζ, numerical solutions to this equation can be found by expanding the matrix in a complete basis of functions, $\{\phi_j(x), j = 1, \ldots\}$, satisfying the ortho-normality condition:

$$\int dx \phi_j^*(x)\phi_i(x) = \delta_{ij} \tag{C.12}$$

The $u_j(x)$ and $v_j(x)$ functions can be expanded as:

$$u_j(x) = \sum_n u_j^n \phi_n(x) \tag{C.13}$$

$$v_j(x) = \sum_n v_j^n \phi_n(x) \tag{C.14}$$

and, the matrix in Eq. (C.10) can be written as:

$$\begin{pmatrix} \mathcal{L}_{nm} & -(|\psi_0|^2\dot{\zeta}_0)_{nm} \\ (|\psi_0|^2\dot{\zeta}_0)_{nm} & -\mathcal{L}_{nm} \end{pmatrix} \tag{C.15}$$

with

$$\mathcal{L}_{nm} = \int dx \phi_m^* \mathcal{L} \phi_n \tag{C.16}$$

$$(|\psi_0|^2\dot{\zeta}_0)_{nm} = \int dx \phi_m^* (|\psi_0|^2\dot{\zeta}_0) \phi_n \tag{C.17}$$

In this thesis we have chosen a discrete spatial representation for the functions $u_j(x)$ and $v_j(x)$, i.e., they are represented by a vector containing the value of the functions at points of a regular grid spaced by Δx, in a region of length L

With this representation, the action of the operator $\mathcal{L}$ over an arbitrary function, f, is given by:

$$\mathcal{L}[f] = -\frac{\hbar^2}{2m}\frac{f_{k+1} - 2f_k + f_{k-1}}{\Delta x^2} + (V_k - \mu + \zeta_{0,k} + |\psi_{0,k}|^2\dot{\zeta}_{0,k})f_k \tag{C.18}$$

where the subindex k indicates the value of the corresponding function at position k in the spatial grid.

Finally, the matrix representation of operators $\mathcal{L}$ and $|\psi_0|^2\dot{\zeta}_0$ becomes:

$$\mathcal{L} = \begin{pmatrix} g_k + \frac{1}{\Delta x} & -\frac{1}{2\Delta x} & 0 & \cdots & & \\ -\frac{1}{2\Delta x} & g_{k+1} + \frac{1}{\Delta x} & -\frac{1}{2\Delta x} & 0 & \cdots & \\ 0 & -\frac{1}{2\Delta x} & g_{k+2} + \frac{1}{\Delta x} & -\frac{1}{2\Delta x} & 0 & \cdots \\ 0 & 0 & -\frac{1}{2\Delta x} & g_{k+3} + \frac{1}{\Delta x} & -\frac{1}{2\Delta x} & 0 \quad \cdots \\ \vdots & \vdots & & & & \end{pmatrix} \tag{C.19}$$

$$|\psi_0|^2\dot{g}_0 = \begin{pmatrix} |\psi_{0,i}|^2\dot{\zeta}_{0,k} & 0 & \cdots & & & \\ 0 & |\psi_{0,i}|^2\dot{\zeta}_{0,k+1} & 0 & \cdots & & \\ 0 & 0 & |\psi_{0,i}|^2\dot{\zeta}_{0,k+2} & 0 & \cdots & \\ 0 & 0 & 0 & |\psi_{0,i}|^2\dot{\zeta}_{0,k+3} & 0 & \cdots \\ \vdots & \vdots & \vdots & \vdots & \ddots & \end{pmatrix} \tag{C.20}$$

Results in Chapter 6 were obtained by solving the eigen-problem of the matrix Eq. (C.15), composed by the sub-matrices Eqs. (C.19) and (C.20). The ground state of the condensate was calculated by an imaginary-time propagation of the GPE, as explained in Appendix A. For each case presented, the size of the region where the Bogoliubov modes are evaluated is taken at least two times the extension of the condensate. In addition, the size of the space of the grid was taken smaller than the healing length at the peak density of the condensate. The eigenstates of the matrix were calculated by a standard LAPACK subroutine (see http://www.netlib.org/lapack/).

List of publications

- G. Sinuco-Leon, T. M. Fromhold, Using ultra-cold atoms to probe density correlations in two-dimensional electron gases, *in preparation*
- G. Sinuco-Leon, T. M. Fromhold, Trapping ultra-cold atoms using high mobility Two Dimensional Electron gases, *in preparation*
- T.E. Judd, R.G. Scott, G. Sinuco, T.W.A. Montgomery, A.M. Martin and T.M. Fromhold, Zone-plate focusing of Bose-Einstein condensates for atom optics and erasable high-speed lithography of quantum electronic components, to be published in New Journal of Physics

Presentations

- Using ultra-cold atoms to determine long-range density correlation in two-dimensional electron gases. Oral presentation, CMMP09, University of Warwick, December 2009, Warwick- UK.
- Ultra-cold atoms based determination of long-range density correlation in Two-dimensional electron gases. Poster, FINESS 2009, September 2009, Durham - United Kingdom
- Magnetic field fluctuations above a Two-Dimensional Electron gas. Oral presentation in the CQ-Seminar, Universität Tübingen, November 2008, Tübingen - Germany

Bibliography

[1] Kerson Huang. *Introduction to statistical physics*. Taylor & Francis, 2001.

[2] Lev Pitaevskii and Sandro Stringari. *Bose-Einstein Condensation*. Oxford Science Publications, 2008.

[3] M. H. Anderson, J. R. Ensher, and M. R. Matthews. Observation of Bose-Einstein Condensation in a Dilute Atomic Vapor. *Science*, 269:198–201, 1995.

[4] K. B. Davis, M. O. Mewes, M. R. Andrews, N. J. van Druten, D. S. Durfee, D. M. Kurn, and W Ketterle. Bose-Einstein Condensation in a Gas of Sodium Atoms. *Phys. Rev. Lett.*, 75:3969–3973, 1995.

[5] C. C. Bradley, C. A. Sackett, J. J. Tollett, and R. G. Hulet. Evidence of Bose-Einstein Condensation in an Atomic Gas with Attractive Interactions. *Phys. Rev. Lett.*, 75(9):1687–1690, Aug 1995.

[6] Mark W. Keller, Ali L. Eichenberger, John M. Martinis, and Neil M. Zimmerman. A Capacitance Standard Based on Counting Electrons. *Science*, 285:1706, 1999.

[7] M. R. Andrews, C. G. Townsend, H.-J. Miesner, D. S. Durfee, D. M. Kurn, and W. Ketterle. Observation of Interference Between Two Bose Condensates. *Science*, 275:637, 1997.

[8] K. W. Madison, F. Chevy, W. Wohlleben, and J. Dalibard. Vortex Formation in a Stirred Bose-Einstein Condensate. *Phys. Rev. Lett.*, 84(5):806–809, Jan 2000.

[9] J. R. Abo-Shaeer, C. Raman, J. M. Vogels, and W. Ketterle. Observation of Vortex Lattices in Bose-Einstein Condensates. *Science*, 292:476, 2001.

[10] I. Coddington, P. Engels, V. Schweikhard, and E. A. Cornell. Observation of Tkachenko Oscillations in Rapidly Rotating Bose-Einstein Condensates. *Phys. Rev. Lett.*, 91(10):100402, Sep 2003.

[11] William C. Stwalley. Stability of Spin-Aligned Hydrogen at Low Temperatures and High Magnetic Fields: New Field-Dependent Scattering Resonances and Predissociations. *Phys. Rev. Lett.*, 37(24):1628–1631, Dec 1976.

[12] S. Inouye, M. R. Andrews, J. Stenger, H.-J. Miesner, D. M. Stamper-Kurn, and W. Ketterle. Observation of Feshbach resonances in a BoseEinstein condensate. *Nature*, 392:151, 1998.

[13] J. Kinast, S. L. Hemmer, M. E. Gehm, A. Turlapov, and J. E. Thomas. Evidence for Superfluidity in a Resonantly Interacting Fermi Gas. *Phys. Rev. Lett.*, 92(15):150402, Apr 2004.

[14] M. Bartenstein, A. Altmeyer, S. Riedl, S. Jochim, C. Chin, J. Hecker Denschlag, and R. Grimm. Collective Excitations of a Degenerate Gas at the BEC-BCS Crossover. *Phys. Rev. Lett.*, 92(20):203201, May 2004.

[15] M. W. Zwierlein, J. R. Abo-Shaeer, A. Schirotzek, C. H. Schunck, and W. Ketterle. Vortices and superfluidity in a strongly interacting Fermi gas. *Nature*, 435:1047, 2005.

[16] T. A. Pasquini, Y. Shin, C. Sanner, M. Saba, A. Schirotzek, D. E. Pritchard, and W. Ketterle. Quantum Reflection from a Solid Surface at Normal Incidence. *Phys. Rev. Lett.*, 93(22):223201, Nov 2004.

[17] S. Burger, K. Bongs, S. Dettmer, W. Ertmer, K. Sengstock, A. Sanpera, G. V. Shlyapnikov, and M. Lewenstein. Dark Solitons in Bose-Einstein Condensates. *Phys. Rev. Lett.*, 83(25):5198–5201, Dec 1999.

[18] J. Denschlag, J. E. Simsarian, D. L. Feder, Charles W. Clark, L. A. Collins, J. Cubizolles, L. Deng, E. W. Hagley, K. Helmerson, W. P. Reinhardt, S. L. Rolston, B. I. Schneider, and W. D. Phillips. Generating Solitons by Phase Engineering of a Bose-Einstein Condensate. *Science*, 287:97, 2000.

[19] B. P. Anderson, P. C. Haljan, C. A. Regal, D. L. Feder, L. A. Collins, C. W. Clark, and E. A. Cornell. Watching Dark Solitons Decay into Vortex Rings in a Bose-Einstein Condensate. *Phys. Rev. Lett.*, 86(14):2926–2929, Apr 2001.

[20] Z. Hadzibabic, P. Krüger, M. Cheneau, B. Battelier, and J. Dalibard. Berezinskii–Kosterlitz–Thouless crossover in a trapped atomic gas. *Nature*, 441(7097):1118–1121, 2006.

[21] Ying-Ju Wang, Dana Z. Anderson, Victor M. Bright, Eric A. Cornell, Quentin Diot, Tetsuo Kishimoto, Mara Prentiss, R. A. Saravanan, Stephen R. Segal, and Saijun Wu. Atom Michelson Interferometer on a Chip using a Bose-Einstein Condensate. *Phys. Rev. Lett.*, 94(9):090405, Mar 2005.

[22] J. Fortágh, H. Ott, S. Kraft, A. Günther, and C. Zimmermann. Potential roughness near lithographically fabricated atom chips. *Phys. Rev. A*, 76:063621, 2007.

[23] Philipp Treutlein, Peter Hommelhoff, Tilo Steinmetz, Theodor W. Hänsch, and Jakob Reichel. Coherence in Microchip Traps. *Phys. Rev. Lett.*, 92(20):203005, May 2004.

[24] Luca Fontanesi, Michiel Wouters, and Vincenzo Savona. Superfluid to Bose-Glass Transition in a 1D Weakly Interacting Bose Gas. *Phys. Rev. Lett.*, 103:030403, 2009.

[25] J. I. Cirac and P. Zoller. Quantum Computations with Cold Trapped Ions. *Phys. Rev. Lett.*, 74(20):4091–4094, May 1995.

[26] J. Fortágh and C. Zimmermann. Magnetic microtraps for ultracold atoms. *Rev. Mod. Phys.*, 79:235, 2007.

[27] Ron Folman, Peter Krüger, Jörg Schmiedmayer, Johannes Denschlag, and Carsten Henkel. Microscopic Atom Optics: From wires to an Atom Chip. *Adv. Atom. Mol. and Opt. Phys.*, 48:263, 2002.

[28] P. K. Rekdal, S. Scheel, P. L. Knight, and E. A. Hinds. Thermal spin flips in atom chips. *Phys. Rev. A*, 70(1):013811, Jul 2004.

[29] Yu-ju Lin, Igor Teper, Cheng Chin, and Vladan Vuletić. Impact of the Casimir-Polder Potential and Johnson Noise on Bose-Einstein Condensate Stability Near Surfaces. *Phys. Rev. Lett.*, 92(5):050404, Feb 2004.

[30] Daw-Wei Wang, Mikhail D. Lukin, and Eugene Demler. Disordered Bose-Einstein Condensates in Quasi-One-Dimensional Magnetic Microtraps. *Phys. Rev. Lett.*, 92:076802, 2004.

[31] C. Henkel, S. Pötting, and M. Wilkens. Loss and Heating of particles in small and noisy traps. *Appl. Phys. B*, 69:379, 1999.

[32] J. H. Davies. Electronic states in narrow semiconducting wires near threshold. *Semicond. Sci. Technol.*, 3:995, 1988.

[33] F. London. The λ-phenomenon of liquid helium and the Bose-Einstein degeneracy. *Nature*, 141:643–644, 1938.

[34] L. D. Landau. *J. Phys. USSR*, 5:71, 1941.

[35] L. D. Landau. *J. Phys. USSR*, 11:91, 1947.

[36] N. N. Bogoliubov. *J. Phys. USR*, 11:23, 1947.

[37] L. D. Landau and E. M. Lifshitz. *Statistical Physics part 2*. Pergamon Press, 1991.

[38] O. Penrose. *Philos. Mag.*, 42:1371, 1951.

[39] O. Penrose and L. Onsager. Bose-Einstein Condensation and Liquid Helium. *Phys. Rev.*, 104:576, 1956.

[40] C. J. Pethick and H. Smith. *Bose-Einstein Condenstation in Diluite Gases*. Cambridge, 2008.

[41] S.A. Gardiner. (Quantum) Chaos in BECs. *J. Mod. Optics*, 49:1971, 2002. cond-mat/0202380.

[42] N. P. Proukakis and B Jackson. Finite Temperature Models of Bose-Einstein Condensation. *J. Phys. B*, 41:203002, 2008.

[43] Wolfgang Ketterle and N. J. van Druten. Bose-Einstein condensation of a finite number of particles trapped in one or three dimensions. *Phys. Rev. A*, 54:656–660, 1996.

[44] N. J. van Druten and Wolfgang Ketterle. Two-Step Condensation of the Ideal Bose Gas in Highly Anisotropic Traps. *Phys. Rev. Lett.*, 79:549, 1997.

[45] Anthony J. Leggett. Bose-Einstein condensation in the alkali gases: Some fundamental concepts. *Rev. Mod. Phys.*, 73(2):307–356, Apr 2001.

[46] V. I. Yukalov. Bose-Einstein condensation and gauge symmetry breaking. *Laser Phys. Lett.*, 4:632, 2007.

[47] Franco Dalfovo, Stefano Giorgini, Lev P. Pitaevskii, and Sandro Stringari. Theory of Bose-Einstein condensation in trapped gases. *Rev. Mod. Phys.*, 71:463–512, 1999.

[48] E. L. Raab, M. Prentiss, Alex Cable, Steven Chu, and D. E. Pritchard. Trapping of neutral sodium atoms with radiation pressure. *Phys. Rev. Lett.*, 59(23):2631–2634, Dec 1987.

[49] W. H. Wing. *Prog. Quantum Electron.*, 8:181, 1984.

[50] J. Reichel. Microchip traps and Bose-Einstein condensation. *App. Phys. B*, 74:469–487, 2002.

[51] J.H. Thywissen, M. Olshanii, G. Zabow, M. Drndić, KS Johnson, RM Westervelt, and M. Prentiss. Microfabricated magnetic waveguides for neutral atoms. *Eur. Phys. J. D*, 7(3):361–367, 1999.

[52] József Fortágh, Sebastian Kraft, Andreas Günther, Christian Trück, Philipp Wicke, and Claus Zimmermann. Perspectives of ultracold atoms trapped in magnetic micro potentials. *Opt. Comm.*, 243:45, 2004.

[53] B. Damski, J. Zakrzewski, L. Santos, P. Zoller, and M. Lewenstein. Atomic Bose and Anderson Glasses in Optical Lattices. *Phys. Rev. Lett.*, 91(8):080403, Aug 2003.

[54] W. Hänsel, J. Reichel, P. Hommelhoff, and T. W. Hänsch. Trapped-atom interferometer in a magnetic microtrap. *Phys. Rev. A*, 64(6):063607, Nov 2001.

[55] T. A. Pasquini, M. Saba, G.-B. Jo, Y. Shin, W. Ketterle, and D. E. Pritchard. Low Velocity Quantum Reflection of Bose-Einstein Condensates. *Phys. Rev. Lett.*, 97:093201, 2006.

[56] A. Günther, S. Kraft, M. Kemmler, D. Koelle, R. Kleiner, C. Zimmermann, and J. Fortágh. Diffraction of a Bose-Einstein Condensate from a Magnetic Lattice on a Microchip. *Phys. Rev. Lett.*, 95(17):170405, Oct 2005.

[57] A. Günther, S. Kraft, C. Zimmermann, and J. Fortágh. Atom Interferometer Based on Phase Coherent Splitting of Bose-Einstein Condensates with an Integrated Magnetic Grating. *Phys. Rev. Lett.*, 98:140403, (2007).

[58] C. Monroe, D. M. Meekhof, B. E. King, W. M. Itano, and D. J. Wineland. Demonstration of a Fundamental Quantum Logic Gate. *Phys. Rev. Lett.*, 75(25):4714–4717, Dec 1995.

[59] D. P. DiVicenzo. The Physical Implementation of Quantum Computation. *Fortschr. Phys.*, 48:771, 2000.

[60] J. Fortágh, H. Ott, S. Kraft, A. Günther, and C. Zimmermann. Surface effects in magnetic microtraps. *Phys. Rev. A*, 66(4):041604, Oct 2002.

[61] J. Reichel, W. Hänsel, and T. W. Hänsch. Atomic Micromanipulation with Magnetic Surface Traps. *Phys. Rev. Lett.*, 83(17):3398–3401, Oct 1999.

[62] W. Hänsel, P. Hommelhoff, T. W. Hänsch, and J. Reichel. Bose-Einstein condensation on a microelectronic chip. *Nature*, 413:498, 2001.

[63] H. Ott, J. Fortágh, G. Schlotterbeck, A. Grossmann, and C. Zimmermann. Bose-Einstein Condensation in a Surface Microtrap. *Phys. Rev. Lett.*, 87(23):230401, Nov 2001.

[64] M. D. Barrett, J. A. Sauer, and M. S. Chapman. All-Optical Formation of an Atomic Bose-Einstein Condensate. *Phys. Rev. Lett.*, 87(1):010404, Jun 2001.

[65] A. Günther, M. Kemmler, S. Kraft, C. J. Vale, C. Zimmermann, and J. Fortágh. Combined chips for atom optics. *Phys. Rev. A*, 71(6):063619, Jun 2005.

[66] S. Whitlock, R. Gerritsma, T. Fernholz, and R. J. C. Spreeuw. Two-dimensional array of microtraps with atomic shift register on a chip. *New J. Phys.*, 11:023021, 2009.

[67] Donatella Cassettari, Björn Hessmo, Ron Folman, Thomas Maier, and Jörg Schmiedmayer. Beam Splitter for Guided Atoms. *Phys. Rev. Lett.*, 85(26):5483–5487, Dec 2000.

[68] W. Hänsel, J. Reichel, P. Hommelhoff, and T. W. Hänsch. Magnetic Conveyor Belt for Transporting and Merging Trapped Atom Clouds. *Phys. Rev. Lett.*, 86(4):608–611, Jan 2001.

[69] Wildermuth Sthephan. *One-dimensional Bose-Einstein condensates in micro-traps*. PhD thesis, Ruperto-Carola University of Heidelberg, 2005.

[70] D. Cassettari, A. Chenet, R. Folman, A. Haase, B. Hessmo, P. Krger, T. Maier, S. Schneider, T. Calarco, and J. Schmiedmayer. Micromanipulation of neutral atoms with nanofabricated structures. *Appl. Phys. B*, 70:721, 2000.

[71] B. P. Anderson and M. A. Kasevich. Loading a vapor-cell magneto-optic trap using light-induced atom desorption. *Phys. Rev. A*, 63(2):023404, 2001.

[72] T Montgomery, T. M. Fromhold, and T. Judd. Private communication, University of Nottingham.

[73] S. Kraft, A. Günther, H. Ott, D. Wharam, C Zimmermann, and J. Fortágh. Anomalous longitudinal magnetic field near the surface of copper conductors. *J. Phys. B*, 35:L469, 2002.

[74] Erika Andersson, Tommaso Calarco, Ron Folman, Mauritz Andersson, Björn Hessmo, and Jörg Schmiedmayer. Multimode Interferometer for Guided Matter Waves. *Phys. Rev. Lett.*, 88:100401, 2002.

[75] T Müller, X Wu, A Mohan, A Eyvazov, Y Wu, and R Dumke. Towards a guided atom interferometer based on a superconducting atom chip. *New J. Phys. 10*, 10:073006, 2008.

[76] James A. Stickney and Alex A. Zozulya. Wave-function recombination instability in cold-atom interferometers. *Phys. Rev. A*, 66(5):053601, Nov 2002.

[77] A. Günther, S. Kraft, C. Zimmermann, and J. Fortágh. Atom Interferometer Based on Phase Coherent Splitting of Bose-Einstein Condensates with an Integrated Magnetic Grating. *Phys. Rev. Lett.*, 98(14):140403, Apr 2007.

[78] Judd T. E., Scott R. G., and Fromhold T. M. Atom-chip diffraction of Bose-Einstein condensates: The role of interatomic interactions. *Phys. Rev. A*, 78:053623, 2008.

[79] T. E. Judd, R. G. Scott, G. Sinuco, T.W.A. Montgomery, A.M. Martin, P. Krüger, and T.M. Fromhold. Zone-plate focusing of Bose-Einstein condensates for atom optics and erasable high-speed lithography of quantum electronic components. *cond-mat.quant-gas/0912.1846*.

[80] T. Schumm, J. Estve, C. Figl, J.-B. Trebbia, C. Aussibal, H. Nguyen, D. Mailly, I. Bouchoule, C. I. Westbrook, and A. Aspect. Atom chips in the real world: the effects of wire corrugation. *Eur. Phys. J. D*, 32:171, 2005.

[81] L. Della Pietra, S. Aigner, C. von Hagen, Sönke Groth, I Bar-Joseph, H. J. Lezec, and J. Schmiedmayer. Designing potentials by sculpturing wires. *Phys. Rev. A*, 75:063604, 2007.

[82] G. S. Agarwal. Quantum electrodynamics in the presence of dielectrics and conductors. I. Electromagnetic-field response functions and black-body fluctuations in finite geometries. *Phys. Rev. A*, 11:230, 1975.

[83] C. Henkel. Magnetostatic field noise near metallic surfaces. *Eur. Phys. J. D*, 35:59, 2005.

[84] D. M. Harber, J. M. McGuirk, J. M. Obrecht, and E. A. Cornell. Thermally Induced Losses in Ultra-Cold Atoms Magnetically Trapped Near Room-Temperature Surfaces. *J. Low Temp. Phys.*, 133:229, 2003.

[85] S. Scheel, P. K. Rekdal, P. L. Knight, and E. A. Hinds. Atomic spin decoherence near conducting and superconducting films. *Phys. Rev. A 72, 042901 (2005) (4 pages)*, 72:042901, 2005.

[86] V. Dikovsky, Y. Japha, C. Henkel, and R. Folman. Reduction of magnetic noise in atom chips by material optimization. *Eur. Phys. J. D*, 35:87, 2005.

[87] T. David, Y. Japha, V. Dikovsky, R. Salem, C. Henkel, R. Folman, and Ben-Gurion. Magnetic interactions of cold atoms with anisotropic conductors. *Eur. Phys. J. D*, 48:331, 2008.

[88] P. G. Petrov, S Machluf, S. Younis, R. Macaluso, T. David, B. Hadad, Y. Japha, M. Keil, E. Joselevich, and R. Folman. Trapping cold atoms using surface-grown carbon nanotubes. *Phys. Rev. A*, 79:043403, 2009.

[89] T. Fernholz, R. Gerritsma, S. Whitlock, I Barb, and R. J. C. Spreeuw. Fully permanent magnet atom chip for Bose-Einstein condensation. *Phys. Rev. A*, 77:033409, 2008.

[90] R. Gerritsma, S. Whitlock, T. Fernholz, H. Schlatter, J. A. Luigjes, J.-U. Thiele, J. B. Goedkoop, and R. J. C. Spreeuw. Lattice of microtraps for ultracold atoms based on patterned magnetic films. *Phys. Rev. A 76, 033408 (2007)*, 76:033408, 2007.

[91] Bo-Sture K. Skagerstam, Ulrich Hohenester, Asier Eiguren, and Per Kristian Rekdal. Spin Decoherence in Superconducting Atom Chips. *Phys. Rev. Lett.*, 97:070401, 2006.

[92] T. Nirrengarten, A. Qarry, C. Roux, A. Emmert, G. Nogues, M. Brune, J.-M. Raimond, and S. Haroche. Realization of a Superconducting Atom Chip. *Phys. Rev. Lett.*, 97:200405, 2006.

[93] C. Roux, A. Emmert, A. Lupascu, T. Nirrengarten, G. Nogues, M. Brune, J.-M. Raimond, and S. Haroche. Bose-Einstein condensation on a superconducting atom chip. *Eur. Phys. Lett.*, 81:56004, 2008.

[94] D Cano, B. Kasch, H. Hattermann, R. Kleiner, C. Zimmermann, D. Koelle, and J. Fortágh. Meissner effect in superconducting microtraps. *Phys. Rev. Lett.*, 101:183006, 2008.

[95] J. H. Davies. *The physics of low-dimensional semiconductors*. Cambridge University Press, 1999.

[96] S. Datta. *Electronic Transport in Mesoscopic Systems*. Cambridge University Press, 1997.

[97] C. Kittel. *Introduction to Solid State Physics*. New York: Wiley, 2005.

[98] M. J. Kelly. *Low-dimensional semiconductors*. Oxford Science Publications, 1995.

[99] T. J. Drummond, W. Kopp, H. Morkoc, and M. Keever. Transport in modulation-doped structures ($Al_xGa_{1-x}As$/GaAs) and correlations with Monte Carlo calculations (GaAs). *Appl. Phys. Lett.*, 41:277, 1982.

[100] G. Bastard. *Wave mechanics applied to semiconductor heterostructures*. Les Editions de Physique, 1988.

[101] A. Endo and Y. Iye. Harmonic Content of strain-induced Potential modulation in unidirectional lateral superlattices. *J. Phys. Soc. Jpn.*, 74:2797, 2005.

[102] A. L. Efros, F. G. Pikus, and V. G. Burnett. Density of states of a two-dimensional electron gas in a long-range random potential. *Phys. Rev. B*, 47(4):2233–2243, Jan 1993.

[103] W. Gao N. Liu and J. Yin. Magnetic guiding of cold neutral atoms using a V-shaped current-carrying conductor. *Eur. Phys. J. D*, 19:137, 2002.

[104] T.J. Davis. 2D magnetic traps for ultra-cold atoms: a simple theory using complex numbers. *Eur. Phys. J. D*, 18:27, 2002.

[105] C. V. Sukumar and D. M. Brink. Spin-flip transitions in a magnetic trap. *Phys. Rev. A*, 56(3):2451–2454, Sep 1997.

[106] B. Lev. Fabrication of micro-magnetic traps for cold neutral atoms. *Quantum Inf. Comput.*, 3:450, 2003.

[107] S. Groth, P. Krüger, S. Wildermuth, R. Folman, T. Fernholz, J. Schmiedmayer, D. Mahalu, and I. Bar-Joseph. Atom chips: Fabrication and thermal properties. *Appl. Phys. Lett.*, 85:2980, 2004.

[108] T. Varpula and T. Poutanen. Magnetic field fluctuations arising from thermal motion of electric charge in conductors. *J. Appl. Phys.*, 55:4015, 1984.

[109] B. Zhang and C. Henkel. Magnetic noise around metallic microstructures. *Journal of Applied Physics*, 102:084907, 2007.

[110] S. Aigner, L. Della Pietra, Y. Japha, O. Entin-Wohlman, T. David, R. Salem, R. Folman, and J. Schmiedmayer. Long-Range order in electronic transport through disordered metal films. *Science*, 319:1226, 2008.

[111] Mark A. Topinga, Robert M. Westervelt, and Eric J. Heller. Imaging Electron Flow. *Physics Today*, December:47, 2003.

[112] M. A. Topinka, B. J. LeRoy, S. E. J. Shaw, E. J. Heller, R. M. Westervelt, K. D. Maranowski, and A. C. Gossard. Imaging Coherent Electron Flow from a Quantum Point Contact. *Science*, 289:2323, 2000.

[113] J.-B. Trebbia, C. L. Garrido Alzar, R. Cornelussen, C. I. Westbrook, and I. Bouchoule. Roughness Suppression via Rapid Current Modulation on an Atom Chip. *Phys. Rev. Lett.*, 98:263201, 2007.

[114] A. E. Leanhardt, A. P. Chikkatur, D. Kielpinski, Y. Shin, T. L. Gustavson, W. Ketterle, and D. E. Pritchard. Propagation of Bose-Einstein Condensates in a Magnetic Waveguide. *Phys. Rev. Lett.*, 89(4):040401, Jul 2002.

[115] A. E. Leanhardt, Y. Shin, A. P. Chikkatur, D. Kielpinski, W. Ketterle, and D. E. Pritchard. Bose-Einstein Condensates near a Microfabricated Surface. *Phys. Rev. Lett.*, 90(10):100404, Mar 2003.

[116] Jones M P A, Vale C J, Sahagun D, Hall B V, Eberlein C C, B. E. Sauer, K Furusawa, D. Richardson, and E. A. Hinds. Cold atoms probe the magnetic field near a wire. *J. Phys. B.*, 37:L15, 2004.

[117] P. Krüger, S. Wildermuth, S. Hofferberth, A. L. Mauritz, S. Groth, I Bar-Joseph, and J. Schmiedmayer. Cold atoms close to surfaces: measuring magnetic field roughness and disorder potentials. *J. Phys.: Conf. Ser.*, 19:56, 2005.

[118] S. Wildermuth, S. Hofferberth, S. Lesanovsky, S. Groth, S. Krüger, J. Schmiedmayer, and I. Bar-Joseph. Sensing electric and magnetic fields with Bose-Einstein condensates. *Appl. Phys. Lett.*, 88:264103, 2006.

[119] F. Gerbier. Quasi-1D Bose-Einstein condensates in the dimensional crossover regime. *Eurphys. Lett.*, 66:771, 2004.

[120] B. J. van Wees, H. van Houten, C. W. J. Beenakker, J. G. Williamson, L. P. Kouwenhoven, D. van der Marel, and C. T. Foxon. Quantized conductance of point contacts in a two-dimensional electron gas. *Phys. Rev. Lett.*, 60(9):848–850, Feb 1988.

[121] D. A. Wharam, T. J. Thornton, R Newbury, M. Pepper, H. Ahmed, J. E. F. Frost, D. G. Hasko, D. C. Peacock, D. A. Ritchie, and G. A. C. Jones. One-dimensional transport and the quantisation of the ballistic resistance. *J. Phys. C*, 21:L209, 1988.

[122] M. A. Topinka, B. J. LeRoy, R. M. Westervelt, S. E. J. Shaw, R. Fleischmann, E. J. Heller, K. D. Maranowski, and A. C. Gossard. Coherent branched flow in a two-dimensional electron gas. *Nature*, 410:183, 2001.

[123] N. Aoki, C. R. da Cunha, R. Akis, D. K. Ferry, and Y. Ochiai. Imaging of integer quantum Hall edge state in a quantum point contact via scanning gate microscopy. *Phys. Rev. B*, 72(15):155327, Oct 2005.

[124] R. Grill and G. H. Döhler. Effect of charged donor correlation and Wigner liquid formation on the transport properties of a two-dimensional electron gas in modulation δ-doped heterojunctions. *Phys. Rev. B*, 59(16):10769–10777, Apr 1999.

[125] B. Roth, N. Sepulveda, and J. Wikswo. Using a magnetometer to image a two-dimensional current distribution. *J. Appl. Phys.*, 65:361, 1989.

[126] T. Palm. Effects of remote impurity scattering including donor correlations in a branching electron waveguide. *Phys. Rev. B*, 52:11284, 1995.

[127] N. D. Mermin and H. Wagner. Absence of Ferromagnetism or Antiferromagnetism in One- or Two-Dimensional Isotropic Heisenberg Models. *Phys. Rev. Lett.*, 17(22):1133–1136, Nov 1966.

[128] P. C. Hohenberg. Existence of Long-Range Order in One and Two Dimensions. *Phys. Rev.*, 158(2):383–386, Jun 1967.

[129] U. Al Khawaja, J. O. Andersen, N. P. Proukakis, and H. T. C Stoof. Low dimensional Bose gases. *Phys. Rev. A*, 66(1):013615, Jul 2002.

[130] A. Görlitz, J. M. Vogels, A. E. Leanhardt, C. Raman, T. L. Gustavson, J. R. Abo-Shaeer, A. P. Chikkatur, S. Gupta, S. Inouye, T. Rosenband, and W. Ketterle. Realization of Bose-Einstein Condensates in Lower Dimensions. *Phys. Rev. Lett.*, 87(13):130402, Sep 2001.

[131] Sabine Stock, Zoran Hadzibabic, Baptiste Battelier, Marc Cheneau, and Jean Dalibard. Observation of Phase Defects in Quasi-Two-Dimensional Bose-Einstein Condensates. *Phys. Rev. Lett.*, 95(19):190403, Nov 2005.

[132] P. Krüger, Z. Hadzibabic, and J. Dalibard. Critical point of an interacting two-dimensional atomic Bose gas. *Phys. Rev. Lett.*, 99(4):040402, 2007.

[133] G. B. Jo, J. H. Choi, C. A. Christensen, Y. R. Lee, T. A. Pasquini, W. Ketterle, and D. E. Pritchard. Matter-wave interferometry with phase fluctuating Bose-Einstein condensates. *Phys. Rev. Lett.*, 99(24):240406, 2007.

[134] R. G. Scott, D. A. W.. Hutchinson, T. E. Judd, and T. M. Fromhold. Quantifying finite-temperature effects in atom-chip interferometry of Bose-Einstein condensates. *Phys. Rev. A*, 79:063624, 2009.

[135] S. Dettmer, D. Hellweg, P. Ryytty, J. J. Arlt, W. Ertmer, K. Sengstock, D. S. Petrov, G. V. Shlyapnikov, H. Kreutzmann, L. Santos, and M. Lewenstein. Observation of Phase Fluctuations in Elongated Bose-Einstein Condensates. *Phys. Rev. Lett.*, 87(16):160406, Oct 2001.

[136] S. Richard, F. Gerbier, J. H. Thywissen, M. Hugbart, P. Bouyer, and A. Aspect. Momentum Spectroscopy of 1D Phase Fluctuations in Bose-Einstein Condensates. *Phys. Rev. Lett.*, 91(1):010405, Jul 2003.

[137] D. S. Petrov, M. Holzmann, and G. V. Shlyapnikov. Bose-Einstein Condensation in Quasi-2D Trapped Gases. *Phys. Rev. Lett.*, 84(12):2551–2555, Mar 2000.

[138] D. S. Petrov, G. V. Shlyapnikov, and J. T. M. Walraven. Regimes of Quantum Degeneracy in Trapped 1D Gases. *Phys. Rev. Lett.*, 85(18):3745–3749, Oct 2000.

[139] D. S. Petrov, G. V. Shlyapnikov, and J. T. M. Walraven. Phase-Fluctuating 3D Bose-Einstein Condensates in Elongated Traps. *Phys. Rev. Lett.*, 87(5):050404, Jul 2001.

[140] J. O. Andersen, U. Al Khawaja, and H. T. C. Stoof. Phase Fluctuations in Atomic Bose Gases. *Phys. Rev. Lett.*, 88(7):070407, Feb 2002.

[141] R. N. Bisset, M. J. Davis, T. P. Simula, and P. B. Blakie. Quasi-condensation and coherence in the quasi-two-dimensional trapped Bose gas. *Phys. Rev. A*, 79:033626, 2009.

[142] A. Munoz Mateo and V. Delgado. Effective one-dimensional dynamics of elongated Bose-Einstein condensates. *Annals of Physics*, 324:709, 2009.

[143] Chiara Menotti and Sandro Stringari. Collective oscillations of a one-dimensional trapped Bose-Einstein gas. *Phys. Rev. A*, 66(4):043610, Oct 2002.

[144] D. S. Petrov, D. M. Gangardt, and G. V. Shlyapnikov. Low-dimensional trapped gases:. *J. Phys IV France*, 116:5, 2004.

[145] Alexander L. Fetter and Daniel Rokhsar. Excited states of a dilute Bose-Einstein condensate in a harmonic trap. *Phys. Rev. A*, 57(2):1191–1201, Feb 1998.

[146] S. I. Shevchenko. *Soc. J. Low Temp. Phys*, 18:223, 1992.

[147] A. Muoz Mateo and V. Delgado. Effective mean-field equations for cigar-shaped and disk-shaped Bose-Einstein condensates. *Phys. Rev. A*, 77:013617, 2008.

[148] A. Muñoz Mateo and V. Delgado. Ground-state properties of trapped Bose-Einstein condensates: Extension of the Thomas-Fermi approximation. *Phys. Rev. A*, 75:063610, 2007.

[149] B. Grüner, M. Jag, A. Stibor, G. Visanescu, M. Häffner, D. Kern, A. Günther, and J. Fortágh. Integrated Atom Detector Based on Field Ionization near Carbon Nanotubes. *cond-mat.quant-gas/0911.1329 Phys. Rev. A*, 80:063422, 2009.

[150] D. A. Allwood, T. Schrefl, G. Hrkac, I. G. Hughes, and C. S. Adams. Mobile atom traps using magnetic nanowires. *Appl. Phys. Lett.*, 89:014102, 2006.

[151] I Stolichnov, S.W.E Riester, H.J. Trodahl, N. Setter, A.W. Rushforth, K.W. Edmonds, R.P. Campion, C.T. Foxon, B.L. Gallagher, and T. Jungwirth. Nonvolatile ferroelectric control of ferromagnetism in (Ga,Mn)As. *Nature Materials*, 7:464, 2008.

[152] W.H. Press, S.A. Teukolsky, W.T. Vetterling, and B.P. Flannery. *Numerical recipes: The art of Scientific computing*. Cambridge Univ. Press Cambridge MA, USA:, 2007.

[153] Robin George Scott. *Cold atoms in optical lattices*. PhD thesis, School of Physics and Astronomy, University of Nottingham., 2003.